



The
University
Of
Sheffield.

3D printing polymer - ceramic composites for orbital floor reconstruction

Thesis submitted to the University of Sheffield
for the degree of Doctor of Philosophy

By:

Maha Omran

School of Clinical Dentistry
The University of Sheffield

February 2021

Acknowledgments

I would like to take this opportunity to express my sincere gratitude to my supervisors, Professor Cheryl Miller, Dr Rob Moorehead and Dr Candice Majewski for being very patient with me, their guidance throughout my project and their continuous encouragement.

I am forever grateful to my collaborators, Dr Caroline Harrison, Dr Joey Shepherd and Mr Iain Varley for their invaluable advice and constant support during my PhD.

A massive thank you to my colleagues, friends and the staff at the School of Clinical Dentistry. A special thank you to Amnael Orozco, Beatriz Monteiro, Danilo Villanueva, George Bullock and Alex Bolger. I would also like to thank my colleagues and the staff at the Centre of Advanced Additive Manufacture (AdAM) especially Wendy Birtwistle, Kurt Bonser, Ryan Brown and James Wingham.

Thank you to University of Sheffield for their financial support as part of institutional commitment to the EPSRC Centre for Innovative Manufacturing in Medical Devices (MeDe Innovation) grant: EP/K029592/1.

Lastly, I would like to express my gratitude to my mother, Khalid, Maya and Waleed for their love and encouragement.

Abstract

The delicate structure of the orbital floor makes it prone to fractures. Implants are often used to repair fractures, -which are tailored to the estimated defect size and shape by surgeons. Deficiencies in shaping or positioning may require additional surgeries to correct or remove the implant, as can infections and other postoperative complications.

Additive Manufacturing (AM) processes can produce complex geometries, and therefore present an opportunity to address some of these deficiencies. However, this requires knowledge of suitable materials and of their behaviour in the chosen AM process; this is the focus of this thesis.

The processability of polymer-ceramic composites with antimicrobial properties were investigated on laser sintering (LS) and high speed sintering (HSS) as they can produce parts with a high accuracy and a rough surface finish to encourage osseointegration. Polyamide 12 (PA12) was chosen as it is an ideal polymer for these processes, hydroxyapatite (HA), due to its osteoconductive properties and zinc (Zn), which is known to possess antimicrobial properties.

The processability of varying compositions of HA:PA12 and 2:98 wt% Zn:PA12 composites were initially investigated separately. It was found that the upper limit for processing HA:PA12 differed (20:80 for LS and 40:60 for HSS) while the 2:98 wt% Zn:PA12 composition was successfully processed on both LS and HSS.

Analysis proved the presence of well distributed additives after processing, indicating that samples are likely to exhibit osteoconductive and antimicrobial properties. The addition of the additives increased the porosity and the specific surface area, more so for HSS than LS samples. However, there was a decrease in the tensile and flexural properties of the samples with the addition of the additives. Overall, the LS samples had higher mechanical properties than HSS samples, nonetheless, both processes produced samples with similar flexibility to the natural orbital floor bone^{1, 2} with potentially enough strength for orbital reconstruction applications.

Cell viability tests showed that all the HA:PA12 samples were biocompatible and the 2:98 wt% Zn:PA12 samples proved to be effective against *Staphylococcus aureus*. However, when the materials were combined (Zn:HA:PA12) both the LS and HSS samples that contained Zn, showed cytotoxic effects against MG 63 cells. In conclusion, both processes have shown a potential in the fabrication of polymer-ceramic composites with antimicrobials for orbital floor reconstruction application however further work is required to investigate whether there is an optimal Zn:HA:PA12 ratio that has a bacteriostatic effect and is biocompatible.

Contents

Acknowledgments	II
Abstract	III
1 Introduction	1
1.1 Background	1
1.2 Aims and objectives	3
2 Literature review	4
2.1 Bone	5
2.1.1 Bone healing	8
2.2 The orbit and orbital floor fractures	10
2.3 Surgical repair of orbital floor fractures	11
2.3.1 Orbital floor surgery.....	13
2.3.2 Implant materials for orbital floor reconstruction.....	14
2.4 Post operative complications and possible preventions	26
2.4.1 Prevention/ treatment of bacterial infections	26
2.4.2 Improving implant stability	30
2.4.3 Increasing restoration accuracy	31
2.5 Additive manufacture	32
2.5.1 Types of additive manufacture technologies	33
2.5.2 Additive manufacture of bioceramics.....	40
2.5.3 Summary and manufacturing technique selection	46
2.6 Polymer processing	47
2.6.1 Polyamide 12.....	48
2.6.2 Compositing polyamide 12	49
2.7 Factors that influence the mechanical properties in laser sintering and high speed sintering	51
2.7.1 Energy density.....	51
2.7.2 Part location and orientation in the build platform.....	53
2.8 Summary	54
3 Material and Method	56
3.1 Material selection	56
3.1.1 Base polymer	56
3.1.2 Bioactive material	57
3.1.3 Antimicrobial agent.....	57
3.1.4 Compositions	58

3.1.5	Powder preparation.....	59
3.2	Powder characterisation	59
3.2.1	Powder morphology.....	59
3.2.2	Thermal analysis.....	60
3.3	Design of test samples.....	62
3.4	Part fabrication	64
3.4.1	Laser sintering.....	64
3.4.2	HSS parameters.....	66
3.5	Effect on the physical and mechanical properties	68
3.5.1	Dimensional accuracy	68
3.5.2	Additive distribution	69
3.5.3	Surface area analysis.....	70
3.5.4	Characterisation of crystal structure.....	72
3.5.5	Tensile properties	72
3.5.6	Flexural properties	73
3.6	Effect of steam sterilisation on the mechanical properties of PA12	73
3.7	Effect on the biocompatibility	77
3.7.1	Cell seeding density.....	78
3.7.2	Cell viability and DNA quantification.....	79
3.8	Effect on the antibacterial properties	81
3.8.1	Bacterial culture preparation.....	81
3.1.1	Assessing bacterial growth.....	81
3.9	Data analyses	83
4	<i>Results and discussion: bioactive ceramic: polymer compositions</i>	<i>84</i>
4.1	Processability	85
4.1.1	Powder morphology.....	85
4.1.2	Thermal analysis.....	86
4.2	Printability	88
4.2.1	Laser sintering.....	89
4.2.2	High speed sintering.....	91
4.3	Effect on the physical and mechanical properties	92
4.3.1	Dimensional accuracy	92
4.3.2	Surface topography analysis	95
4.3.3	Additive distribution	101
4.3.4	Surface area analysis.....	103
4.3.5	Characterisation of crystal structure.....	105
4.3.6	Tensile properties	108
4.3.7	Flexural properties	115
4.4	Effect of steam sterilisation on the mechanical properties of polyamide 12	117
4.5	Effect on the Biocompatibility	123
4.5.1	Cell seeding density.....	124
4.5.2	Cell viability and DNA quantification.....	126
4.6	Summary and composite selection	132
5	<i>Results and discussion: antimicrobial: polymer compositions</i>	<i>135</i>

5.1	Processability of zinc: polyamide 12 composites	135
5.1.1	Powder morphology.....	136
5.1.2	Thermal analysis.....	137
5.2	Printability	138
5.2.1	Laser sintering.....	139
5.2.2	High speed sintering.....	140
5.3	Effect of Zn on the physical and mechanical properties	140
5.3.1	Dimensional accuracy	141
5.3.2	Surface topography analysis	143
5.3.3	Characterisation of crystal structure.....	145
5.3.4	Tensile properties	149
	152
5.3.5	Flexural properties	154
5.4	Evaluation of antibacterial properties of Zn:PA12 parts.....	156
5.5	Summary.....	158
6	<i>Results and discussion: antimicrobial: bioactive ceramic: polymer compositions....</i>	160
6.1	Processability	160
6.1.1	Thermal analysis.....	161
6.2	Printability	162
6.2.1	Laser sintering.....	163
6.2.2	High speed sintering.....	164
6.3	Effect on the physical and mechanical properties	164
6.3.1	Dimensional accuracy	165
6.3.2	Surface topography analysis	167
6.3.3	Characterisation of crystal structure.....	173
6.3.4	Tensile properties	174
6.3.5	Flexural properties	180
6.4	Evaluate the antimicrobial properties of Zn:HA:PA12	182
6.5	Effect on the biocompatibility	185
6.6	Summary.....	189
7	<i>Summary discussion and conclusions</i>	191
7.1	Processability on LS and HSS	191
7.2	Additive distribution, porosity and specific surface area.....	192
7.3	Mechanical properties	192
7.4	Sterilisability	193
7.5	Chemical composition	193
7.6	Antimicrobial capabilities.....	194
7.7	Biocompatibility.....	194
7.8	Future work	197
8	<i>Outputs.....</i>	199

8.1	Publication	199
8.2	Conferences	199
8.3	Awards.....	200
9	References	201
10	Appendix A	234

List of Figures

Figure 2.1.	(a) The dense outer shell shows the macrostructure of cortical bone while the porous bone inside the dense outer shell is the cancellous bone; (b) Microstructure of osteon units; (c) Nanostructure of collagen fibres made up of collagen fibrils ⁵	5
Figure 2.2	Schematic diagram of the for walls of the orbit.....	10
Figure 2.3.	Computer tomography (CT) scan of an orbital floor fracture ³¹	12
Figure 2.4.	The arrow points towards a porous Medpor® sheet placed over an orbital fracture ⁵⁷	18
Figure 2.5	Silicone implant removal post migration. (Personal communication I. Varley, MD, in 24/10/ 2017).	19
Figure 2.6.	Polyetheretherketone (PEEK) orbital floor implant (Personal communication I. Varley, MD, in 24/10/ 2017).....	22
Figure 2.7.	Schematic diagram of a stereolithographic (SLA) process.	34
Figure 2.8.	Computer aided design (CAD) model of an orbital floor implant.	35
Figure 2.9.	Schematic representation of 3D direct ink writing (DIW) process.....	36
Figure 2.10.	Schematic diagram of a Fused deposition modelling (FDM) process.....	37
Figure 2.11.	Schematic diagram of a laser sintering (LS) process.	38
Figure 2.12.	Schematic diagram of a high speed sintering (HSS) process.....	39
Figure 3.1.	A standard differential scanning calorimetry (DSC) curve for polyamide 12 (PA12). The first peak is the crystallisation peak while the second peak is the melting peak. The area in the middle is the sintering. Window also known as the processing window ²⁰⁰	61
Figure 3.2.	Computer aided design (CAD) models showing the dimensions (mm) of (A) discs, (B) tensile test bars and (C) three-point bend bars.....	63
Figure 3.3.	LS build set up.	65
Figure 3.4	High speed sintering build set up.....	67
Figure 3.5	Overview of the effect of steam autoclave experiment protocol. The *m was taken due to an 18 h delay between autoclaving and tensile testing.....	76
Figure 3.6	Agar plate dilutions for colony counting.	82
Figure 4.1.	Secondary electron (SE)- Scanning electron microscopy (SEM) micrographs of (a) polyamide 12 and (b) hydroxyapatite powders.	85

Figure 4.2. Differential scanning calorimeter (DSC) curves of hydroxyapatite: polyamide 12 (HA:PA12) powder compositions, where $T_{C_{onset}}$ is crystallisation temperature onset and $T_{m_{onset}}$ is melting temperature onset	87
Figure 4.3. Laser sintered tensile test bars made of different wt% of hydroxyapatite: polyamide 12 (HA:PA12). Scale bar= 10p coin.	89
Figure 4.4. High speed sintered tensile test bars made of different wt% of hydroxyapatite: polyamide 12 (HA:PA12). Scale bar= 10p coin.	91
Figure 4.5. Backscattered electron (BSE)- Scanning electron microscopy (SEM) micrographs of laser sintered discs composed of different wt% hydroxyapatite: polyamide 12 (HA:PA12) taken at x100 and x1000 magnifications.	96
Figure 4.6. Backscattered electron (BSE)- Scanning electron microscopy (SEM) micrographs of high speed sintered discs composed of different wt% of hydroxyapatite: polyamide 12 (HA:PA12) taken at x100 and x1000 magnifications.	99
Figure 4.7. 2D cross-sectional images of laser sintered samples composed of different wt% of hydroxyapatite: polyamide 12 (HA:PA12) obtained by micro-CT scanning. Scale bar= 2 mm.	101
Figure 4.8. 2D cross-sectional images of high speed sintered samples composed of different wt% of hydroxyapatite: polyamide 12 (HA:PA12) obtained by micro-CT scanning. Scale bar= 2 mm.	102
Figure 4.9. Powder X-ray diffraction (XRD) patterns of polyamide 12 (PA12) and hydroxyapatite. (HA) before 3d printing. The XRD pattern of HA is presented with Miller indices (hkl) showing crystal family of planes for each diffraction peak.....	106
Figure 4.10. XRD patterns of laser sintered discs composed of different wt % of hydroxyapatite: polyamide 12 (HA:PA12). Where Δ represents PA12 and \blacksquare represents HA.....	107
Figure 4.11. XRD patterns of high speed sintered discs composed of different wt % of hydroxyapatite: polyamide 12 (HA:PA12). Where Δ represents PA12 and \blacksquare represents HA.....	107
Figure 4.12. The tensile properties: (a) Young's modulus (E), (b) Ultimate tensile strength (σ_{UTS}) and elongation at break (ϵ_{max}) of laser sintered samples composed of different wt% hydroxyapatite: polyamide 12 (HA:PA12). Error bars: \pm SD, n=5. Statistical analysis using one way ANOVA with Tukey's multiple comparison. Statistical significance * p<0.05.	109
Figure 4.13. The tensile properties: (a) Young's modulus (E), (b) Ultimate tensile strength (σ_{UTS}) and elongation at break (ϵ_{max}) of high speed sintered samples composed of different wt% hydroxyapatite: polyamide 12 (HA:PA12). Error bars: \pm SD, n=5. Statistical analysis using one way ANOVA with Tukey's multiple comparison. Statistical significance * p<0.05.	112
Figure 4.14. Flexural modulus of (a) laser sintered and (b) high speed sintered samples composed of different wt% hydroxyapatite: polyamide 12 (HA:PA12) Error bars: \pm SD, n=5. Statistical analysis using one way ANOVA with Tukey's multiple comparison. Statistical significance * p<0.05.	115
Figure 4.15. The tensile properties: (a) Young's modulus (E), (b) Ultimate tensile strength (σ_{UTS}) and elongation at break (ϵ_{max}) of laser sintered polyamide 12 (PA12) samples for all combinations of conditioning and drying. Error bars: \pm SD, n=5. Statistical analysis using one way ANOVA with Tukey's multiple comparison. Statistical significance * p<0.05.	119

Figure 4.16. Effect of water content on (a) Young’s modulus (E), (b) Ultimate tensile strength (σ_{UTS}) and (c) Elongation at break (ϵ_{max}). The measurement of the goodness of fit is shown by the linear fit with the calculated R^2 . There was a strong correlation between the water content and σ_{UTS} and a moderate correlation between water content and E as well as ϵ_{max} 122

Figure 4.17. Light microscopy of MG 63 cells cultured on tissue culture plastic (TCPS) at different cell densities for 7 days. By day 4, the wells with 30,000 cells or more had reached 100% confluency. The images were acquired at 100x magnification. The images here are a representative of 3 images acquired per sample. Scalebar= 400 μ m and is the same for all images. 124

Figure 4.18. Cell viability (MG 63: PrestoBlue™) of laser sintered samples composed of hydroxyapatite: polyamide 12 (HA: PA12) at different weight percentages (wt %). 0:100 HA: PA12 was used as control. Tissue culture plastic (TCPS) was used for comparison. N=1, n=3. Error bars: \pm SD. Statistical analysis using one-way ANOVA. Statistical significance * $p < 0.05$ 127

Figure 4.19. DNA content as indication of cell number on laser sintered samples composed of hydroxyapatite: polyamide 12 (HA:PA12) at different weight percentages (wt%) after 7 days of culture. 0:100 HA: PA12 was used as control. Tissue culture plastic (TCPS) was used for comparison. N=1, n=3. Error bars: \pm SD. Statistical analysis using one way ANOVA. Statistical significance * $p < 0.05$ 128

Figure 4.20. Cell viability (MG 63: PrestoBlue™) of high speed sintered (HSS) samples composed of hydroxyapatite: polyamide 12 (HA: PA12) at different weight percentages (wt %). 0:100 HA: PA12 was used as control. Tissue culture plastic (TCPS) was used for comparison. N=1, n=3. Error bars: \pm SD. Statistical analysis using one way ANOVA. Statistical significance * $p < 0.05$ 130

Figure 4.21. DNA content as indication of cell number high speed sintered (HSS) samples composed of hydroxyapatite: polyamide 12 (HA:PA12) at different weight percentages (wt%) after 7 days. 0:100 HA: PA12 was used as control. Tissue culture plastic (TCPS) was used for comparison. N=1, n=3. Error bars: \pm SD. Statistical analysis using one way ANOVA. Statistical significance * $p < 0.05$ 132

Figure 5.1. Secondary electron (SE)- Scanning electron microscopy (SEM)micrographs of zinc (Zn) powder taken at x1000 magnification. 136

Figure 5.2. Differential scanning calorimeter (DSC) curves of 2:98 wt% zinc: polyamide 12 (Zn:PA12) powder. 137

Figure 5.3. Laser sintered tensile test bars made of 0:100 and 2:98 wt% zinc: polyamide 12 (Zn:PA12). Scale bar= 20p coin. 139

Figure 5.4. High speed sintered tensile test bars made of 0:100 and 2:98 wt% zinc: polyamide 12 (Zn:PA12). Scale bar= 20p coin. 140

Figure 5.5. Backscattered electron (BSE)- Scanning electron Scanning electron microscopy (SEM) micrographs of laser sintered discs composed of 2:98 wt% zinc: polyamide 12 (Zn:PA12) taken at x100 and x1000 magnifications. 143

Figure 5.6. Backscattered electron (BSE)- Scanning electron Scanning electron microscopy (SEM) micrographs of high speed sintered discs composed 2:98 wt% zinc: polyamide 12 (Zn:PA12) and 0:100 wt% Zn:PA12 used as comparison. The micrographs were taken at x100 and x1000 magnifications. 144

Figure 5.7. Powder X-ray diffraction (XRD) patterns of zinc (Zn) before 3d printing. The XRD pattern of Zn is presented with Miller indices (hkl) showing crystal family of planes for each diffraction peak.	146
Figure 5.8. X-ray diffraction (XRD) patterns of laser sintered discs composed of 2:98 wt% zinc: polyamide 12 (Zn:PA12). Where Δ represents PA12 and \circ represents Zn.....	147
Figure 5.9. X-ray diffraction (XRD) patterns of high speed sintered discs composed of 2:98 wt% zinc: polyamide 12 (Zn:PA12). Where Δ represents PA12 and \circ represents Zn... ..	147
Figure 5.10. The tensile properties: (a) Young's modulus (E), (b) Ultimate tensile strength (σ_{UTS}) and elongation at break (ϵ_{max}) of laser sintered samples composed of 0:100 and 2:98 wt% zinc: polyamide 12 (Zn:PA12). Error bars: \pm SD, n=5. Statistical analysis using an unpaired T-test. Statistical significance * p<0.05.....	149
Figure 5.11. The tensile properties: (a) Young's modulus (E), (b) Ultimate tensile strength (σ_{UTS}) and elongation at break (ϵ_{max}) of laser sintered samples composed of 0:100 and 2:98 wt% zinc: polyamide 12 (Zn:PA12). Error bars: \pm SD, n=5. Statistical analysis using an unpaired T-test. Statistical significance * p<0.05.....	152
Figure 5.12. Flexural modulus of (a) laser sintered and (b) high speed sintered samples composed of 0:100 and 2:98 wt% zinc: polyamide 12 (Zn:PA12). Error bars: \pm SD, n=5. Statistical analysis using unpaired T-test. Statistical significance * p<0.05.....	154
Figure 5.13. Number of viable Staphylococcus aureus (S. aureus) attached to laser sintered discs composed of 0:100 and 2:98 wt% zinc: polyamide 12 (Zn:PA12) after 24 h incubation. N=1, n=3. Error bars \pm SD. Statistical analysis using unpaired T-test. Statistical significance * p<0.05.	156
Figure 5.14. Number of viable Staphylococcus aureus (S. aureus) attached to high speed sintered discs composed of 0:100 and 2:98 wt% zinc: polyamide 12 (Zn:PA12) after 24 h incubation. N=1, n=3. Error bars \pm SD. Statistical analysis using unpaired T-test. Statistical significance * p<0.05.	157
Figure 6.1. Differential scanning calorimeter (DSC) curves of zinc: hydroxyapatite: polyamide 12 (Zn:HA:PA12) powder compositions.	161
Figure 6.2. Laser sintered tensile test bars composed of 0:100 and 2:19.6:78.4 wt% of zinc: hydroxyapatite: polyamide 12. Scale bar= 20 p coin.	163
Figure 6.3. High speed sintered tensile test bars composed of 0:100 and 2:39.2:58.8 wt% of zinc: hydroxyapatite: polyamide 12. Scale bar= 20 p coin.	164
Figure 6.4. Backscattered electrons (BSE)- Scanning electron microscopy (SEM) micrographs of laser sintered discs composed of 2:19.6:78.4 wt% zinc: hydroxyapatite: polyamide 12 (Zn:HA:PA12). Taken at x500 and x1000 magnifications.	167
Figure 6.5. Energy Dispersive X-ray (EDX)- Scanning electron microscopy (SEM) analysis of laser sintered 2:19.6:78.4 wt% zinc: hydroxyapatite: polyamide 12 (Zn:HA:PA12).	169
Figure 6.6. Backscattered electron (BSE)- Scanning electron Scanning electron microscopy (SEM) micrographs of high speed sintered discs composed of different wt% zinc: hydroxyapatite: polyamide 12 (Zn:HA:PA12). Taken at x500 and x1000 magnifications.	170
Figure 6.7. Energy Dispersive X-ray (EDX)- Scanning electron microscopy (SEM) analysis of high speed sintered 2:39.2:58.8 wt% zinc: hydroxyapatite: polyamide 12 (Zn:HA:PA12). The arrow points towards the area being analysed.....	172

Figure 6.8. Powder X-ray diffraction (XRD) patterns of laser sintered 2:19.6:78.4 wt% zinc: hydroxyapatite: polyamide 12 (Zn:HA:PA12) and high speed sintered 2:39.2:58.8 wt% Zn:HA:PA12. Where Δ represents PA12, \blacksquare represents HA and \circ represents Zn.	173
Figure 6.9. The tensile properties: (a) Young's modulus (E), (b) Ultimate tensile strength (σ_{UTS}) and elongation at break (ϵ_{max}) of laser sintered samples composed of different wt% zinc: hydroxyapatite: polyamide 12 (Zn:HA:PA12). Error bars: \pm SD, n=5. Statistical analysis using an unpaired T-test.	175
Figure 6.10. The tensile properties: (a) Young's modulus (E), (b) Ultimate tensile strength (σ_{UTS}) and elongation at break (ϵ_{max}) of high speed sintered samples composed of different wt% zinc: hydroxyapatite: polyamide 12 (Zn:HA:PA12). Error bars: \pm SD, n=5. Statistical analysis using an unpaired T-test.	178
Figure 6.11. Flexural modulus of (a) laser sintered and (b) high speed sintered samples composed of different wt% of zinc: hydroxyapatite: polyamide 12 (Zn:HA:PA12). Error bars: \pm SD, n=5. Statistical analysis using one way ANOVA with Tukey's multiple comparison.	180
Figure 6.12. Number of viable Staphylococcus aureus attached to laser sintered discs composed of zinc: hydroxyapatite: polyamide 12 (Zn:HA:PA12) at different weight percentages (wt%) after 24 h incubation. N=1, n=3. Error bars \pm SD. Statistical analysis using one way ANOVA with Tukey's multiple comparison. Statistical significance * p<0.05.	183
Figure 6.13. Number of viable Staphylococcus aureus attached to high speed sintered discs composed of zinc: hydroxyapatite: polyamide 12 (Zn:HA:PA12) at different weight percentages (wt%) after 24 h incubation. N=1, n=3. Error bars \pm SD. Statistical analysis using one way ANOVA with Tukey's multiple comparison. Statistical significance * p<0.05.	184
Figure 6.14. Cell viability (MG 63: PrestoBlue™) of laser sintered samples composed of zinc: hydroxyapatite: polyamide 12 (Zn:HA:PA12) at different weight percentages (wt %). 0:0:100 HA: PA12 was used as control. N=3, n=3. Error bars: \pm SD. Statistical analysis using one way ANOVA with Tukey's multiple comparison. Statistical significance * p<0.05.	186
Figure 6.15. Cell viability (MG 63: PrestoBlue™) of high speed sintered samples composed of zinc: hydroxyapatite: polyamide 12 (Zn:HA:PA12) at different weight percentages (wt %). 0:0:100 HA: PA12 was used as control. N=3, n=3. Error bars: \pm SD. Statistical analysis using one way ANOVA with Tukey's multiple comparison. Statistical significance * p<0.05.	188

List of tables

Table 4.1. Melt characteristics of hydroxyapatite: polyamide 12 (HA:PA12) powder compositions.	87
Table 4.2. Part dimensions of 3-point bend bars composed of different wt% of hydroxyapatite: polyamide 12 (HA:PA12). The expected values were defined in the CAD model. The measurements were conducted on 5 samples.	93

Table 4.3. Part dimensions of high speed sintered 3-point bend bars composed of different wt% of hydroxyapatite: polyamide 12 (HA:PA12). The expected values were defined in the CAD model. The measurements were conducted on 5 samples.	94
Table 4.4. Brunauer-Emmett-Teller (BET) nitrogen adsorption measurements of the specific surface area of laser sintered and high speed sintered samples composed of different wt% of hydroxyapatite: polyamide 12 (HA:PA12).	104
Table 4.5. Tensile properties for laser sintered samples composed of different wt% of hydroxyapatite: polyamide 12.	110
Table 4.6 Tensile properties for high speed sintered samples composed of different wt% of hydroxyapatite: polyamide 12 (HA:PA12).	113
Table 4.7. Flexural modulus values for laser sintered and high speed sintered samples composed of different wt% of hydroxyapatite: polyamide 12 (HA:PA12).	116
Table 4.8. The values for the measured tensile properties of all combinations of conditioning and drying.	120
Table 4.9. Measured water content during testing.	121
Table 5.1. Melting and crystallisation onset temperatures of 2:98 wt% zinc: polyamide 12 (Zn:PA12) powder with pure PA12 for comparison.	137
Table 5.2. Part dimensions of laser sintered 3-point bend bars composed of 0:100 and 2:98 wt% zinc: polyamide 12 (Zn:PA12). The expected values were defined in the CAD model. The measurements were conducted on 5 samples.	141
Table 5.3. Part dimensions of high speed sintered 3-point bend bars composed of 0:100 and 2:98 wt% zinc: polyamide 12 (Zn:PA12). The expected values were defined in the CAD model. The measurements were conducted on 5 samples.	142
Table 5.4. Tensile properties for laser sintered samples composed of 0:100 and 2:98 wt% zinc: polyamide 12 (Zn:PA12).	150
Table 5.5. Tensile properties for high speed sintered samples composed of 0:100 and 2:98 wt% zinc: polyamide 12 (Zn:PA12).	153
Table 5.6. Flexural modulus values for laser sintered and high speed sintered samples composed of 0:100 and 2:98 wt% zinc: polyamide 12 (Zn:PA12).	154
Table 6.1. Melting and crystallisation onset temperatures of zinc: hydroxyapatite: polyamide 12 (Zn:HA:PA12) powder compositions.	161
Table 6.2. Part dimensions of laser sintered 3-point bend bars composed of different wt% of zinc: hydroxyapatite: polyamide 12 (Zn:HA:PA12). The expected values were defined in the CAD model. The measurements were conducted on 5 samples.	165
Table 6.3. Part dimensions of high speed sintered 3-point bend bars composed of different wt% of zinc: hydroxyapatite: polyamide 12 (Zn:HA:PA12). The expected values were defined in the CAD model. The measurements were conducted on 5 samples.	166
Table 6.4. Tensile properties for laser sintered samples composed of different wt% zinc: hydroxyapatite: polyamide 12 (Zn:HA:PA12).	176
Table 6.5. Tensile properties for high speed sintered samples composed of different wt% zinc: hydroxyapatite: polyamide 12 (Zn:HA:PA12).	179
Table 6.6. Flexural modulus values for laser sintered and high speed sintered samples composed of different wt% zinc: hydroxyapatite: polyamide 12 (Zn:HA:PA12).	181

List of abbreviations

3D	Three Dimensions
a-PC	Aliphatic- Polycarbonate
ALP	Alkaline Phosphatase
AM	Additive Manufacture
BET	Brunauer-Emmett-Teller
BG	Bioactive Glass
BIC	Bone-to-Implant Contact
BMPs	Bone Morphogenic Proteins
BSE	Backscattered Electron
BSI	British Standards Institution
BT	Bed Temperature
CAD	Computer-Aided Design
CaP	Calcium Phosphates
CT	Computer Tomography
DIW	Direct Ink Writing
DLP	Digital Light Processing
DNA	Deoxyribonucleic Acid
DPM	Degree of Particle Melt
DSC	Differential Scanning Calorimetry
DTA	Differential Thermal Analysis
<i>E. coli</i>	<i>Escherichia coli</i>
ECM	Extra Cellular Matrix
EDX	Energy Dispersive X-ray
FCS	Fetal Calf Serum
FCU	Colony Forming Units
FDM	Fused Deposition Modelling
HA	Hydroxyapatite
HDPE	high-Density Polyethylene
HSS	High Speed Sintering
LCM	Lithography-based Ceramic Manufacturing
LG	L-Glutamine
LP	Laser Power
LS	Laser Sintering
MicroCT	MicroComputed Tomography
MRI	Magnetic Resonance Imaging
MSCs	Mesenchymal Stem Cells
NEAA	Non-Essential Amino Acids
P/S	Penicillin-Streptomycin
PA	Polyamide
PA12	Polyamide 12
PBS	Phosphate-Buffered Saline
PCL	Polycaprolactone

PDO	Polydioxanone
PEEK	Polyetheretherketone
PEKK	Polyetherketoneketone
PGA	Polyglycolic Acid
PLA	Poly(lactic Acid)
PLGA	Poly(lactide-co-glycolide)
PLLA	Poly(L-lactide)
PMMA	Polymethyl Methacrylate
PSI	Patient Specific Implants
PVA	Poly(vinyl alcohol)
RNA	Ribonucleic Acid
ROS	Reactive Oxygen Species
S. aureus	Staphylococcus Aureus
S. epidermidis	Staphylococcus Epidermidis
SE	Secondary Electron
SEM	Scanning Electron Microscope
SLA	Stereolithography
SLM	Selective Laser Melting
STL	Standard Tessellation Language
T _c	Crystallization Temperature
T _{Conset}	Onset of Crystallisation Temperature
TCP	Tricalcium Phosphate
TCPS	Tissue Culture Plastic
T _g	Glass Transition Temperature
T _m	Melting Temperature
T _{monset}	Onset of Melting Temperature
UV	Ultraviolet
XRD	X-Ray Diffraction

1 Introduction

1.1 Background

Sport injuries, interpersonal violence, and motor vehicle accidents are the most common causes of orbital floor fractures. Some orbital fractures require surgical intervention, and most times an implant is needed to reconstruct the orbital anatomy. Many materials have been used for the reconstruction of the orbital floor including bone grafts, polyether ether ketone (PEEK), and titanium mesh. These materials have been successful to a certain degree, but still have some drawbacks and limitations including potential implant malalignment, implant migration, and high infection rates.

Laser sintering (LS) and high speed sintering (HSS) are powder-base additive manufacturing (AM) techniques that have the potential to fabricate customisable implants based on patient scan data, aiming to reduce inaccuracies due to implant shaping *in-situ*. Polyamide 12 (PA12) is a polymer commonly used in LS and HSS due to its ideal processing properties. While biocompatible, PA12 is not osteoconductive, and this can limit bone regeneration and implant integration to the surrounding bone. Hydroxyapatite (HA), in contrast, is a widely used osteoconductive material, similar in composition to natural bone but it is a brittle material that cannot easily be used to produce complex structures. Using HA as an additive for PA12 can help overcome the brittleness of the ceramic while enhancing osteoconductive properties.

Introduction

Orbital floor implants are susceptible to bacterial infections due to the implants' possible exposure to the nasal/oral/pharyngeal mucosal cavities. An implant site infection usually requires an additional surgery, normally also requiring removal of the implant. Moreover, many of the bacterial infections that arise at these implant sites are resistant to one or more antibiotics. Therefore, it is a challenge to treat these infections, and preventing them is a priority. The addition of antimicrobial agents to implants has been found useful in reducing implant associated infections. Antimicrobial agents, such as zinc (Zn), have a different method of action to antibiotics which is less likely to promote resistance in bacteria. The incorporation of an antimicrobial agent to an orbital floor implant may be beneficial as it can decrease bacterial adhesion to the surface of the implants. This has the potential to reduce the need for a secondary surgery.

Introduction

1.2 Aims and objectives

The aim of this research was to investigate the potential use of powdered-polymer Additive Manufacturing processes (specifically laser sintering and high speed sintering) for orbital floor reconstruction applications.

The objectives:

- To investigate the processability of HA:PA12 composites from 5 to 40 wt% HA in order to establish whether there was an upper limit for the amount of HA which could physically be processed and the optimal HA:PA12 composition.
- To investigate any effects that HA may have on the physical, mechanical properties and biocompatibility of all HA:PA12 compositions which could be processed.
- To identify if steam autoclave has an effect on the mechanical properties of the base polymer (PA12).
- To investigate the processability of 2:98 wt% Zn:PA12 by LS and HSS.
- To investigate any effects that Zn may have on the physical, mechanical and antimicrobial properties of the 2:98 wt% Zn:PA12 samples which could be processed.
- To investigate the processability of Zn:HA:PA12 compositions by LS and HSS.
- To investigate any effects that the combination of the additives (Zn and HA) may have on the physical, mechanical and antimicrobial properties as well as the biocompatibility of the Zn:HA:PA12 samples which could be processed.

2 Literature review

Chapter 2 will begin by giving a background into bone: its composition, formation and development and the different types of bone healing. The anatomy of the orbit will be discussed in section 2.2 focusing on the orbit and orbital floor fractures as well as bone healing. Section 2.3 will discuss the surgical repair procedure of orbital floor repair and the variety of implantation materials that have been used for orbital floor reconstruction including their advantages and disadvantages. The common post operative complications are discussed, including ideas on how to prevent/ decrease the rate of these complications. Section 2.5 explores how additive manufacture (AM) techniques can be useful in the fabrication of patient specific orbital floor implants. The literature is reviewed to assess which AM technique has the most potential in the manufacture of ceramic-based materials suitable for orbital floor reconstruction applications. Section 2.7 focuses on factors that influence the mechanical properties of the parts produced by Laser sintering (LS) and high speed sintering (HSS). Following this, discussion focuses on the processing of polyamide 12 (PA12) and compositing PA12 with ceramics and antibacterial materials. This in turn leads into determination of the research gap related to the manufacture of patient specific ceramic-polymer composites with antibacterial properties for orbital floor reconstruction applications.

Chapter 2

2.1 Bone

Bone is a specialised, complex and highly organised connective tissue³. Its functions include protecting internal organs, providing structural support, facilitating movement, acting as a reservoir for cytokines and growth factors, and storing mineral content such as calcium and phosphorous^{4, 5}.

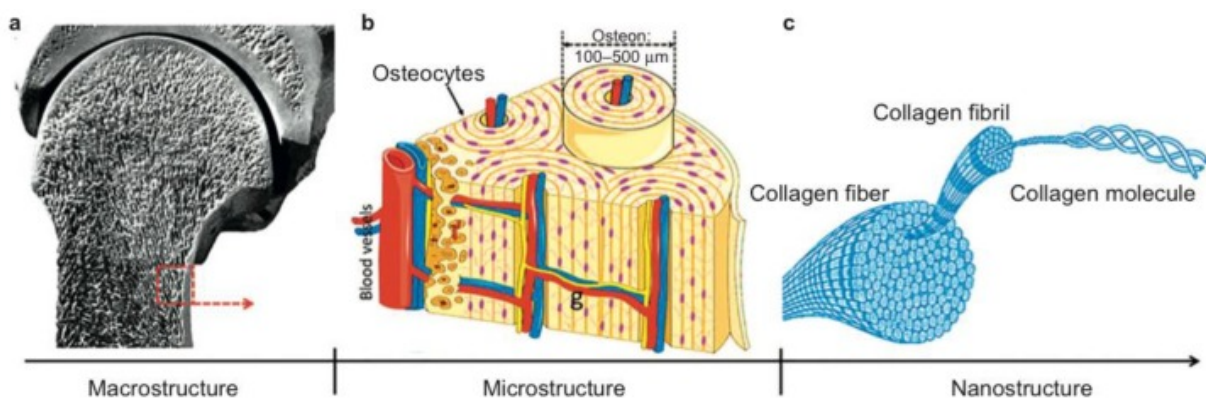


Figure 2.1. (a) The dense outer shell shows the macrostructure of cortical bone while the porous bone inside the dense outer shell is the cancellous bone; (b) Microstructure of osteon units; (c) Nanostructure of collagen fibres made up of collagen fibrils⁵.

The hierarchical organisation of bone is shown in Figure 2.1. Bone is made from two different osseous tissues known as cortical and cancellous bone⁶. Cortical bone makes up the outer wall of bones and is formed of osteons units known as Haversian systems. This compact bone makes up 80 % of the skeletal mass and is responsible for the support and protection of the skeleton. Cancellous bone is made up of interconnected framework of trabeculae (which makes up the remaining skeletal mass). It is less dense than cortical bone due to its porous/ spongy structure, and is responsible for metabolic functions and biomechanical functions⁵. Cortical bone has

Chapter 2

less than 10 % porosity while cancellous bone has a 50- 90% porosity⁷. Porosity is important as it permits vascular and neural supply. However, porosity leads to a decrease in the mechanical strength, Cortical bone has an ultimate strength between 50- 151 MPa^{8, 9} and a modulus between 7-30 GPa⁸⁻¹⁰. Cancellous bone has an ultimate strength of 0.1- 30 MPa and a modulus between 10 to 3000 MPa¹¹.

Bone is composed of inorganic and organic elements. The organic matrix contains fibrous protein and collagen while the inorganic matrix component is non-stoichiometric carbonated hydroxyapatite¹². Different bone types have a differing ratio of inorganic mineral, collagen and water, in a systematic way. The quantity of collagen stays fairly consistent while the calcium phosphate (CaP) content increases at the expense of the water content.

The mammalian skeleton is formed by two processes during the embryonic development; intramembranous ossification which produces the flat bones in the skull and the clavicle, and endochondral ossification, which is responsible for the development of most bones in the body¹³.

Intramembranous ossification takes place in the embryo, eight weeks after fertilisation. Mesenchymal stem cells multiply and condense into compact nodules. Some cells differentiate into capillaries while others alter their shape to become osteoblasts- cells that can synthesise and mineralise bone. Osteoblasts secrete osteoid, an unmineralized organic bone matrix made mostly from type 1 collagen. They soon become calcified thus hardening the bone matrix. Osteoblasts that are trapped in the calcified matrix differentiate into bone cells (osteocytes). Then, bony spicules are

Chapter 2

emitted from the region where ossification commenced. Compact mesenchymal cells surround the bony spicules to form the periosteum, a membrane that surrounds the bone. The cells under the periosteum differentiate into osteoblasts which deposit osteoid matrix parallel to the spicules, this causes many layers of bone to be formed¹⁴.

Endochondral ossification is an important process that takes place in foetal development for the production of long bones, it also takes place during the growth of long bones and during natural bone healing of fractures. Endochondral ossification commences with a pre-existing cartilage template which begins to calcify. An osteoid matrix is laid down by the osteoblast, on the outer part of the cartilage template, to form the trabecular bone, which provides structural support. The chondrocytes begin to grow and increase in size, they stop secreting collagen and start to secrete alkaline phosphatase, an enzyme critical in mineral deposition. The calcified cartilage formed is impermeable to diffusion of nutrients thus chondrocytes begin to undergo a programmed cell death known as apoptosis to leave small cavities. At the same time, a bud of cells originating from periosteum invades the calcified cartilage template initiating vascularisation. This allows for nutrients, osteoblasts and osteoclasts to enter the cavities to remodel the partially calcified cartilage into woven bone which is then remodelled into lamellar bone. The diaphysis (the central part of the long bone) elongates, inside the diaphysis is the medullary cavity, which contains bone marrow. Chondrocytes and cartilage continue to grow at the end of bone. Growth plates are formed between the epiphyseal and metaphyseal ossification centres that mediates bone growth. These plates disappear when the individual has stopped growing which is at around 13 to 18 years old¹⁴. However, bone is never fully developed as it continually renews itself.

Chapter 2

2.1.1 Bone healing

Bone is strong however it can fracture if external forces are applied in excess of its strength. Trauma such as sport injuries, interpersonal violence and motor vehicle accidents as well as medical conditions such as osteoporosis can lead to bone fractures. Fracture healing is a critical biological process. Bone has the capacity to self-repair certain micro-damaged bone fractures in order to fully restore the bone to its original condition. However, approximately 10 % of pathological fractures and defects will undergo delayed union which may progress to non-union¹⁵, where the bone cannot heal without further intervention¹⁶. These fracture repair interventions are divided into two types: primary and secondary fracture healing. Primary fracture healing, also known as direct fracture healing, occurs when there is direct contact between the fracture surfaces while secondary bone healing does not require direct contact of bone fractures.

Primary bone healing

Primary bone healing, also known as direct fracture healing, occurs through gap healing or contact healing. Contact healing can only take place when bone on one side of the cortex unites with bone on the other side of the cortex, the gap ends must be less than 0.01 mm and the strain in the interfragmentary region should be less than 2 % (the strain is increased with an increase in gap distance). Cutting cones, longitudinal cavities generated by osteoclasts, are later filled by bone formed by osteoblasts present at the back of each of these cutting cones. Bony union and restored Haversian systems are formed simultaneously. The Haversian systems

Chapter 2

permit blood vessels carrying osteoblastic precursors to penetrate. Direct remodelling allows the bridging osteons to later mature into lamellar bone¹⁷.

Harversian system remodelling and bony unions are not formed simultaneously in gap healing. The fracture site is filled with lamellar bone, but unlike contact healing, the lamellar bone is reorganised longitudinally by secondary osteonal reconstruction process. Mechanically weak lamellar bone, produced by osteoblasts, replaces the primary bone structure. This process takes 3 to 8 weeks until a secondary remodelling phase begins which follows a similar process to contact healing¹⁷.

Secondary bone healing

Secondary bone healing, also known as indirect fracture healing, is the most common form of fracture healing. It is slower than primary bone healing as it can take months or even years to fully heal. New bone is formed by both intramembranous and endochondral ossification^{12, 18}. A hematoma, a collection of blood outside a damaged blood vessel, develops at the fracture site in the first few days after the fracture. The injury initiates an inflammatory response which causes the hematoma to coagulate around and in between the fracture ends to form a template for callus formation. Mesenchymal stem cells (MSCs) are recruited, proliferated and differentiated into osteogenic cells in order to regenerate the bone. Once the primary hematoma is formed, a fibrin-rich granulation tissue develops where endochondral formation takes place in between the fracture ends and externally to the periosteal site, forming a soft callus and giving the structure stability. Simultaneously, adjacent to the fracture ends, intramembranous ossification creates a hard callus. Blood supply and adequate

Chapter 2

vascularisation are essential for successful fracture healing¹⁹. In order to allow for blood-vessel in growth, cells and extra matrices are removed at the repair site by chondrocyte apoptosis and cartilaginous degradation. The next step involves the mineralisation and resorption of the primary soft cartilaginous callus into hard bony callus¹⁷. The final stage is the remodelling phase, where the hard callus remodels into lamellar bone structure with central medullar cavity which restores the bone's structure and mechanical strength, which may take months or even years¹².

2.2 The orbit and orbital floor fractures

The two bony cavities that divide the upper facial skeleton from the middle face are Figure 2.2 known as the orbits. The purpose of these bones is to provide protection for what is inside the orbit which includes nerves, veins, extraocular muscles, arteries and the eye globe²⁰.

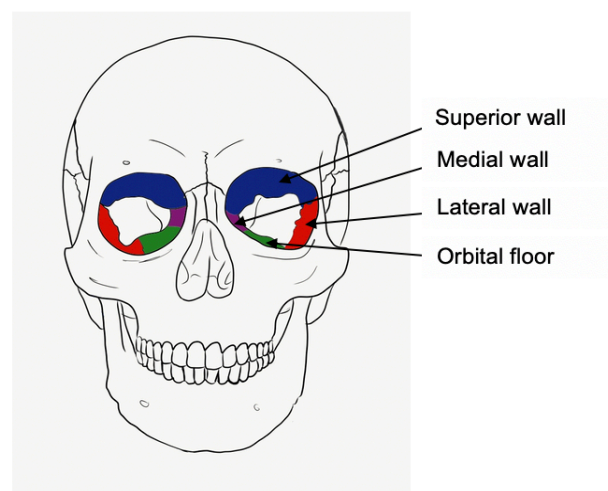


Figure 2.2 Schematic diagram of the four walls of the orbit.

Chapter 2

An orbit is composed of seven bones: frontal, zygomatic, maxillary, ethmoidal, sphenoid, lacrimal and palatine. It is divided into four walls which are covered with periosteum: the superior wall, the medial wall, the lateral wall and the orbital floor²¹, as shown in Figure 2.2. The superior wall is made up of the orbital plate of the frontal bone and the lesser wing of the sphenoid bone. The lateral wall is the thickest wall and is composed of the zygomatic and greater wing of the sphenoid. The medial wall is a thin wall composed of the frontal process of the maxilla, lacrimal, ethmoid and lesser wing of sphenoid. The orbital floor also has a thin structure, it is largely formed of the orbital plate of the maxilla as well as the small orbital process of palatine bone and orbital surface of zygomatic bone. The length of an adult orbital floor is 35 to 40 mm²² with a non-uniform thickness²³ ranging from 0.26 to 1.25 mm²⁴. Due to its thin structure and anatomical positioning, over the hollow maxillary sinus, it is more susceptible to fractures.

There are two main proposed mechanisms by which an orbital floor fracture occurs: buckling and hydraulic. The buckling theory suggests that a fracture occurs through a transmission of force to the orbital floor from a shock to the orbital rim. The hydraulic theory proposes that the fracture occurs through a transmission of force to the orbital floor through a shock to the eye globe²⁵.

2.3 Surgical repair of orbital floor fractures

A fracture in the orbital floor may create an opening into the maxillary sinuses and/ or the ethmoid where the orbital fat, muscles and tissue can become entrapped²⁶. This

Chapter 2

can result in complications such as diplopia; double vision²⁷, enophthalmos; a relative posterior displacement of the eye globe²⁸ and hypoglobus; a lowering of the globe²⁹.

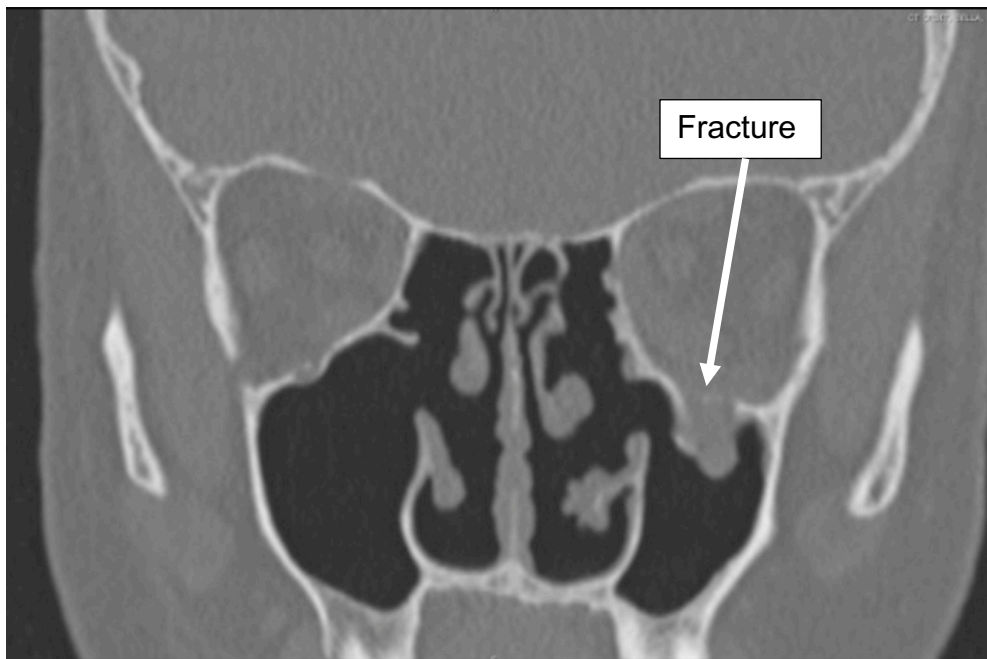


Figure 2.3. Computer tomography (CT) scan of an orbital floor fracture³¹.

There is much debate on the management and the treatment of orbital fractures, in particular on the topic of the indication for surgery. The majority of surgeons rely on the data acquired from computer tomography (CT) scans^{30, 31} (Figure 2.3) to assess what fracture they believe requires surgical intervention. Some fractures necessitate immediate surgery (within 24 hours), due to restricted eye motility which leads to pain, nausea or oculocardic reflex. Other patients are observed for two weeks or more, before any surgery is undertaken³². Some small fractures may heal alone by the formation of scar tissue. Early surgery is typically carried out 1 to 14 days after the incident. Patients with diplopia that is clinically unimproved with orbital tissue entrapment are treated within that timeframe. Large defects are managed at an early stage as studies have shown better functional results with early surgeries. Making a

Chapter 2

decision on when to treat small orbital defects is more challenging- some fractures may heal without surgery by the formation of scar tissue. Patients with small defects usually have adequate ocular motility with minimal displacement thus it is more difficult to estimate whether surgery is necessary as it is hard to foresee how the soft tissue will behave over time. It is therefore critical to observe these defects closely. This can take even more than two weeks before any surgery is indicated³².

2.3.1 Orbital floor surgery

An orbital floor surgery aims to restore the function of the orbital floor and the patient's aesthetic appearance by repairing the defect using an implantation material with adequate strength to support the orbital content which weigh between 37.80 to 51.03 g³³. Accessing the orbital floor can be done by making an incision transcutaneously through the lower eyelid, infrarorbital or via the transconjunctival approach. The latter is the preferred method as it offers the best visualisation of the orbital floor. In brief:

1. The surgeon makes an incision to gain access to the orbital floor, avoiding disruption of the lacrimal glands, infraorbital nerves, the optic nerves and the origin of the inferior oblique muscles.
2. Once the surgeon has gained access to the defect, the standard sized orbital floor implant is shaped by hand and trimmed to the estimated size and shape of the fracture, during the surgery.
3. After the implant is placed on the defect, it is fixed (certain materials require the use of screws to secure the implant in place), and subsequently the skin incision is closed up by sutures.

Chapter 2

4. To ensure eye mobility a forced duction test is performed³⁴ to test if tissue has been trapped beneath the implant. If the forced duction test fails, the incision is reopened to remove the implant in order to resize and reshape the material and then placed back on the defect and fixed in position.
5. The incision is closed again by stitching.

The total cost of the surgery ranges from \$25,586.26 to \$49,985.74³⁵ in the US, any complications can increase surgical time and thus surgical cost.

2.3.2 Implant materials for orbital floor reconstruction

Various materials have been used for orbital floor reconstruction surgery in the hope of accomplishing an optimal clinical outcome for patients³⁶. However, as of yet, an ideal implantation material remains elusive²⁶. The purpose of an orbital floor implant is to repair the defect while bringing the eye globe to its correct position and avoiding enophthalmos³⁶. This means there are a number of (often conflicting) performance requirements which are difficult to meet in a single material. Ideal orbital floor implant should be:

1. Biocompatible- which is defined as 'the capability of a finished and sterilized medical device to perform within an acceptable biological reaction in a clinical application³⁷. This is important as it allows the implant to integrate with the host tissue while avoiding negative responses³⁸.
2. Osteoconductive- to promote growth of natural bone on the surface and through the implant to increase implant stability and reduce implant migration³⁹.
3. High toughness- Orbital floor implants are non-loadbearing; the mechanical properties of orbital floor implants vary considerably between one another. It is

Chapter 2

important that an implant is tough enough to resist fractures and firm enough to support the orbital content.

4. Readily available- to accommodate for the increased demand³⁶.
5. Malleable or ideally custom- to fit the complex defect and regional anatomy for a more accurate restoration³⁶.
6. Antibacterial- to prevent bacterial infections.
7. Easily sterilised before use.

For many years bone grafts and in particular autografts were considered to be the 'gold standard'. However, various synthetic materials have been developed and are being used for orbital floor reconstruction. Their prices vary between \$70.25 up to \$7,718.00³⁵ per implant in the US. The materials used for orbital floor reconstruction are presented in this section (2.3.2).

Natural materials used for orbital floor repair

Bone grafts are commonly used in surgical procedures to regenerate bones. Autografts, allografts and xenografts are harvested from different sources.

Autografts are transplanted tissue from one part into another part of the body of the same individual. Cancellous bone, cortical bone and cortico-cancellous grafts are common autologous bone grafts. Autografts are most commonly harvested from the outer table of calvarium (skull), the maxillary bone and the mandibular cortex to treat orbital floor and medial wall fractures. These are often seen as the "gold standard" for bone grafting as they circumvent immunogenicity, which is defined as "*the ability of a molecule or a substance to provoke an immune response*"⁴⁰. They have ideal

Chapter 2

osteoconduction and osseointegration (direct bone-to-implant anchorage) properties which decreases the risk of implant migration and increases graft stability due to direct bone-to-implant contact. In addition, they have the ability to recruit immature cells to develop into pre-osteoblasts, known as osteoinduction⁴¹. Autografts are commonly used for children under the age of 8 to accommodate for growth of the orbital skeleton³⁴. Unlike the other bone grafts, autografts do not pose a risk of disease transmission, nonetheless, harvesting from another part of the body requires an additional operation. This is a disadvantage as it increases pain and donor site morbidity⁴². Another disadvantages of autografts includes poor drainage of fluids as well as their cumbersome properties, meaning that they cannot be easily tailored to match the shape of the orbital floor⁴³.

Allografts involve the transplantation of organs, cells and tissue from one person into another in the same species and can be harvested from cadavers or living donors making them more widely available than autografts. The drawbacks to allografts are the absence of viable cells, reducing its osteogenic potential and increasing viral transmutations and contaminations. In addition, they can increase immunological reactions that may prevent bone healing which can give rise to rejection⁴².

Xenografts are organs, tissues and cells transplanted from individuals of one species and implanted into a recipient from another species. These are commonly sourced from coral sources, porcine and bovine bone. Xenografts are readily available and are relatively inexpensive. When their antigenic properties are stabilized to avoid disease transmission, they partially lose their osteogenic and osteoinductive properties.

Chapter 2

Furthermore, their use can increase the transmission of infections and zoonotic diseases⁴².

Synthetic materials no longer in use or uncommonly used for orbital floor regeneration

Alloplastic synthetic biomaterials were developed to overcome the drawbacks of natural transplants such as autografts, allografts and xenografts. They can be made in different forms and possess a variety of properties⁴⁴. Various implantation materials have been used for orbital reconstruction however, many of these implantation materials are no longer in use or are uncommonly used due to high complication rates.

Bioactive glass (BG) have been used in bone reconstruction applications due to their ability to biodegrade over time while releasing calcium and silica ions that are believed to stimulate osteoprogenitor cells⁴⁵ however, highly reactive BGs degrade rapidly causing implant instability⁴⁶. In addition, because of its rigid nature, it is difficult to shape the implant making it challenging to achieve the precise shape and size required for successful orbital floor repair. Typically, BG implants are manufactured using conventional fabrication techniques. Conventional manufacturing techniques have been used for many years to produce orbital floor implants. These include subtractive and formative manufacturing⁴⁷⁻⁵⁰. Subtractive manufacturing uses processes such as milling or drilling techniques to remove material from a block for the desired shape to be achieved. Formative manufacturing, such as injection moulding, uses heat and pressure to obtain the desired shape of the object. Often, the use of traditional manufacturing techniques would require the use of multiple fabrication techniques to produce parts which can be expensive⁵¹. Studies investigating the use of BG implants

Chapter 2

found that they generally foreign body reaction however, the one of the most common post operative complication reported was diplopia (up to 61%)^{52, 53}. Diplopia followings surgical repair is commonly caused by several⁵⁴:

1. Failure to remove extraocular muscles and orbital tissue from the fracture site before implant placement.
2. Orbital tissue entrapment by the implant.
3. Implant adherence to the periosteum lining of the orbit leading to a phenomenon known as orbital adherence syndrome.
4. Neuromuscular damage, which can be caused by oversized implants.

In the case of a complication where the patient requires an additional surgery to re-position the implant, an addition \$13,042.41 is required in charges³⁵ in the US.

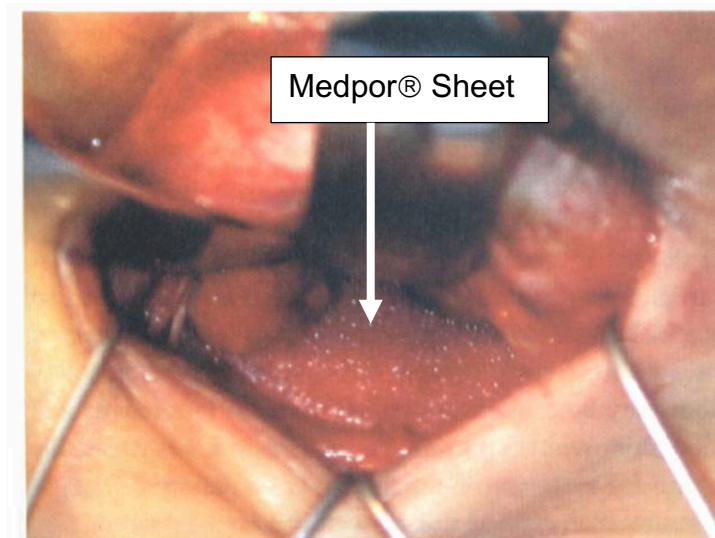


Figure 2.4. The arrow points towards a porous Medpor® sheet placed over an orbital fracture⁵⁷.

High-density polyethylene is used to produce porous polyethylene implants (PPE) for craniofacial defect restoration (Figure 2.4). It is biocompatible and its porous structure allows for vascularisation⁵⁵. Medpor® is a commercial PPE sheet with good

Chapter 2

mechanical strength and flexibility^{56, 57}. Nonetheless, it lacks rigidity and is not radiopaque, making it challenging to examine the implant using X-ray imaging. Like BG, Medpor® are manufactured using conventional fabrication techniques. Unlike BG implants, Medpor® implants do not typically cause post operative diplopia, nonetheless, complications such as implant fusion to the extraocular muscle or the fibroadipose tissue has been reported⁵⁸ making it more challenging to remove the implant in case of complications. In addition, it has been reported to have a relatively high infection rate (ranging from 1 % to 12.5 %)⁵⁹⁻⁶¹. A study found that the infection rate can be significantly reduced by soaking Medpor® implants in gentamycin solution before implantation⁶². However, implant fusion remains a challenge.

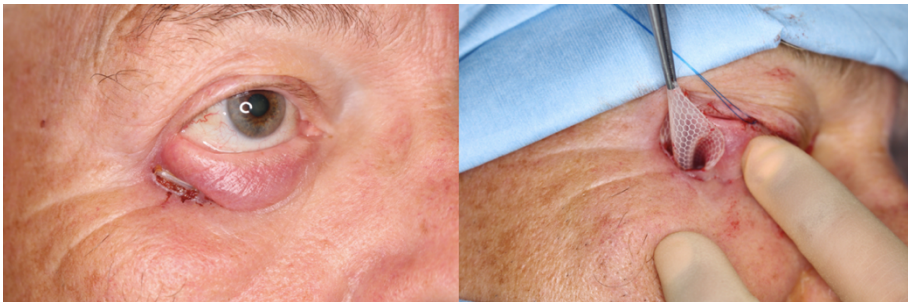


Figure 2.5 Silicone implant removal post migration. (Personal communication I. Varley, MD, in 24/10/ 2017).

Silicone implants and sheets are supple, inexpensive and provide sufficient mechanical stability to maintain the content of the orbit in big blowout fractures however its smooth surface may limit its application in bone reconstruction. Conventional fabrication techniques are typically employed to fabricate these implants. Implantation of silicone implants is relatively easy; however, it has a complication rate between 12 % to 13.8 %^{50, 63}, including implant migration (Figure

Chapter 2

2.5) and infections⁶³. Silicone implants are prone to develop a fibrous capsule around the implant. Certain fibrous capsules do not pose risk to the patient, thus if a complication occurs, it may not be extracted with the implant as it can provide sufficient mechanical strength to support the orbital content and obviate the need for a secondary implant. Nevertheless, if the fibrous capsule becomes very thick it can lead to orbital tissue entrapment or infections⁶⁴.

Polymethyl methacrylate (PMMA) is a biocompatible, non-immunogenetic and a cost effective polymer⁶⁵ but contain residual monomers that may leach out and result in toxic effects⁶⁶. Overall, PMMA is relatively bioinert so cannot osseointegrate with bone tissue⁶⁷. PMMA implants for orbital floor repair were manufactured by mixing PMMA powder with liquid reagent and is then moulding it into the desired shape. Patients who received PMMA implants had no surgical complications however, all the patients suffered from minor pain⁶⁸ which may have been caused by sharp edges from implant trimming and shaping procedure.

Polyamides (PA) has great mechanical properties and flexibility as well as biocompatibility and high resistance to body fluids, making it a great polymer for medical implants. However, PA's bioinert properties limits its applications. Commercially available PA implants (SupraFOIL® and Supramid®) for orbital floor applications are typically produced from PA6, manufactured by conventional fabrication processes. PA implants are 38 times less expensive than Medpor® implants⁶⁹ which is advantageous with the rise in medical costs, the use of reliable, safe, yet cost-effective materials is important. Nonetheless, one of the main reasons

Chapter 2

PA implants are uncommonly used in orbital floor repair due to post operative complications such as persistent enophthalmos⁶⁹ and infections^{70, 71}.

Synthetic materials currently used for orbital floor regeneration

Polydioxanone (PDO), a synthetic biomaterial, commonly used for the manufacture of sutures⁷² is biocompatible and is completely resorbable⁷³. However, like most polymers, it lacks biological functionality. Patients who have received conventionally fabricated PDO foil implants have shown bone ingrowth six months postoperatively⁷⁴. However, PDO is only used in small orbital floor defects (up to 1 cm²) as they do not offer sufficient stability to repair larger defects⁷⁴. Other post operative complications reported include (up to 24%) diplopia, persistent enophthalmos^{74, 75} and infections⁷⁶.

Polyglycolic acid (PGA) is another resorbable material frequently used in bone regeneration applications due to its excellent biocompatibility however, its fast degradation compromises its mechanical strength⁷⁷. An *in vitro* study carried out by Hatton *et al.*⁷⁸ investigated biodegradable PGA and reinforced silicone membranes for the repair of orbital floor fractures. The study found that cell adhesion was superior in PGA due to the increased surface area caused by its woven topography compared to the smooth collagen. This is advantageous as a higher surface area provides more attachment sites for cell adhesion and migration while the rough surface increases osteoblast differentiation⁷⁹. An *in vitro* study revealed up to 22% of patients who received PGA implants developed complications due to implant malalignment and 11% had infections⁸⁰.

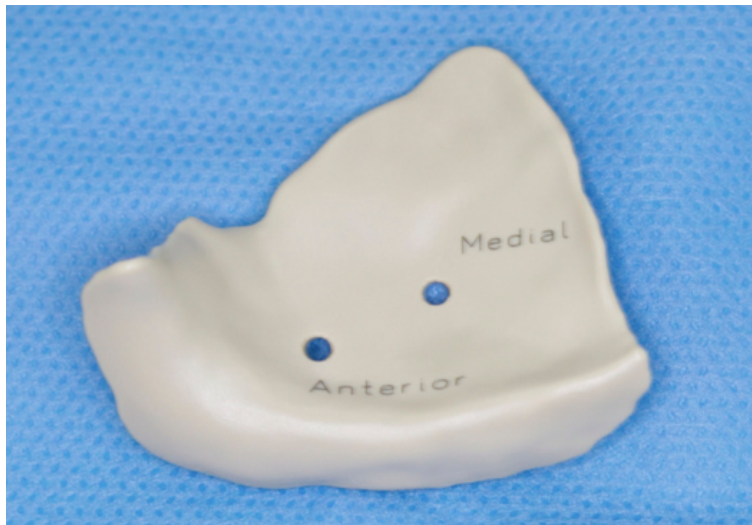


Figure 2.6. Polyetheretherketone (PEEK) orbital floor implant (Personal communication I. Varley, MD, in 24/10/ 2017).

Polymers such as polyetheretherketone (PEEK) (Figure 2.6) and polyetherketoneketone (PEKK) have recently gained a lot of interest due to their biocompatibility, radiopacity and a modulus of elasticity similar to that of cortical bone. In addition to its great biomechanical characteristics, PEKK has been reported to have significant antibacterial properties against gram-negative *Pseudomonas aeruginosa* compared to PEEK. The main limitation to PEEK and PEKK is their inability to bond to bone⁸¹. These implants have been generally manufactured using a block of extruded material⁸². However, recently, PEEK⁸³ and PEKK patient specific implants (PSI) have been manufactured using 3D printing. Patients who received patient specific PEEK implants did not experience post operative infections however up to 17.9% had post operative diplopia⁸⁴.

Titanium is commonly used in bone reconstruction applications due to its biocompatibility, osteointegration and excellent mechanical properties. Titanium mesh

Chapter 2

is one of the most commonly used materials for orbital repair and is typically manufactured by casting to standard sizes⁸⁵. One of the main drawbacks to casting is the lack of flexibility in designing complex structures. In addition, titanium mesh implants are expensive (81 times more expensive than SupraFOIL implants⁶⁹). Titanium mesh is trimmed and moulded to the estimated shape and size of the defect by the surgeon *In-situ*, despite careful trimming, sharp edges are common which can cause pain and discomfort to the patient⁸⁶. Overall, titanium mesh has low extrusion rate and is stable due to its ability to osseointegrate. Reported post operative complications include mild chronic infections and delayed enophthalmos⁸⁷. Due to the osseointegration capabilities of titanium if an infection occurs it may require implant extrusion which can result in loss of healthy bone. Like PEEK and PEKK more recent research has focused on the manufacture of patient specific titanium implants using 3D printing technologies. Selective laser melting (SLM) and electron-beam melting (EBM) have been used, where EBM has been reported to produce parts with lower residual stresses and with lower degree of contamination by gasses. Overall, 3D printing patient specific titanium implants can enhance anatomical alignment however, handling fine titanium powders is dangerous as they can be explosive. In addition, several post processing steps are required to reduce residual stresses and remove support structures. The final polishing step gives rise to a smooth surface⁸⁸ which is not desirable in bone reconstruction applications.

Summary

In summary, many materials have been used for orbital floor reconstruction applications. Table 2.1 shows the advantages and disadvantages of the different

Chapter 2

materials used for orbital floor repair. It is evident that some materials perform better than others however, all the materials have drawbacks as well as reported post operative complications. Post operative complications can lead to complications which can lead the patient to experience discomfort and pain and if an additional surgery is necessary, additional charges are required. Therefore, reducing post operative complications can improve patient satisfaction and reduce overall cost.

Table 2.1. Advantages and disadvantages of the various reconstruction materials used in orbital floor repair.

Material	Advantages	Disadvantages and implant complications
Autografts	<ul style="list-style-type: none"> • “Gold standard”⁴¹ • Circumvent immunogenicity⁴¹ • Osteoconduction and osseointegration properties⁴¹ 	<ul style="list-style-type: none"> • Increased pain⁴² • Donor site morbidity⁴² • Poor drainage⁴² • Cumbersome⁴³ • Limited availability
Allografts	<ul style="list-style-type: none"> • More widely available than autografts 	<ul style="list-style-type: none"> • Reduced osteogenic potential • Increase viral transmission and contamination • Increased immunological reactions⁴²
Xenografts	<ul style="list-style-type: none"> • Readily available • Inexpensive 	<ul style="list-style-type: none"> • Low osteogenic and osteoinductive properties⁴² • Increased transmission of zoonotic diseases⁴²
Bioactive glass	<ul style="list-style-type: none"> • Biocompatible • Biodegradable⁴⁵ • No foreign body reaction 	<ul style="list-style-type: none"> • Fast degradation can cause implant instability⁴⁶ • Rigid so is difficult to shape • Diplopia reported
PPE (Medpor®)	<ul style="list-style-type: none"> • Biocompatible • Porosity allows for vascularisation • Good mechanical strength^{56, 57} • Good flexibility^{56, 57} 	<ul style="list-style-type: none"> • Not radiopaque • Lacks rigidity • Implant fusion to extraocular muscles the fibroadipose tissue⁵⁸ • Infections reported⁵⁹⁻⁶¹

Chapter 2

	<ul style="list-style-type: none"> • No post operative diplopia reported 	
Silicone	<ul style="list-style-type: none"> • Biocompatible • Supple • Inexpensive • Sufficient mechanical strength • Relatively easy implantation 	<ul style="list-style-type: none"> • Smooth surface • Implant migration reported^{50, 63} • Implant infections reported^{50, 63}
PMMA	<ul style="list-style-type: none"> • Biocompatible • Non-immunogenetic • Inexpensive⁶⁵ • No surgical complication reported 	<ul style="list-style-type: none"> • Residual monomers may leach out and can be toxic⁶⁶ • Bioinert⁶⁷ • Patients experienced minor post operative pain⁶⁸
PA (SupraFOIL® and Supramid®)	<ul style="list-style-type: none"> • Biocompatible • Great mechanical properties • Good flexibility • High resistance to body fluids • inexpensive 	<ul style="list-style-type: none"> • Bioinert^{70, 71} • Persistent enophthalmos reported • Infections reported^{70, 71}
PDO	<ul style="list-style-type: none"> • Biocompatible • Completely resorbable⁷³ • Bone ingrowth reported six months post operatively⁷⁴ 	<ul style="list-style-type: none"> • Only used for small defects (up to 1 cm²)⁷⁴ • Diplopia reported^{74, 75} • Persistent enophthalmos reported • Infections reported^{74, 75, 76}
PGA	<ul style="list-style-type: none"> • Biocompatible • Resorbable⁷⁷ • Better cell adhesion than silicone⁷⁹ 	<ul style="list-style-type: none"> • Fast degradation comprising mechanical strength⁷⁷ • Implant migration reported⁸⁰ • Implant infections reported⁸⁰
PEEK and PEKK	<ul style="list-style-type: none"> • Biocompatible • Radiopaque • Modulus of elasticity similar to cortical bone • PEKK reported to have antibacterial properties • No post operative infections 	<ul style="list-style-type: none"> • Not osteoconductive⁸¹ • Diplopia reported⁸⁴

Titanium	<ul style="list-style-type: none">• Biocompatible• Osseointegration properties• Low extrusion rate• High implant stability	<ul style="list-style-type: none">• Expensive⁶⁹• Mild chronic infections reported• Delayed enophthalmos reported⁸⁷• Sharp edges⁸⁶• Implant extrusion may result in loss of healthy bone
----------	---	--

2.4 Post operative complications and possible preventions

The main post operative complications reported here (section 2.4) include post operative infections and migration, as well diplopia and presenting enophthalmos which may be caused by incorrectly sizing, shaping or positioning of the implant. As such, the major post operative considerations are prevention/treatment of infections, issues with implant stability, and the accuracy of the implants, each of which will be discussed here.

2.4.1 Prevention/ treatment of bacterial infections

Orbital floor bacterial infections are most commonly caused by *Staphylococcus aureus* (*S. aureus*), *Staphylococcus epidermidis* (*S. epidermidis*), *Serratia marcescens*, and *Pseudomonas aeruginosa*⁸⁹. The most common treatment for bacterial infections is antibiotic use. Antibiotics are separated into classes according to their mechanism of action; antibiotic targets include bacterial DNA synthesis, cell wall synthesis, protein synthesis and/or RNA synthesis⁹⁰. Constant bacterial mutation and transfer of bacterial DNA between cells gives rise to antibiotic resistance which allows bacteria to survive antibiotic treatment via different methods including production of enzymes that can degrade, modify or inactivate the antibiotics⁹¹, changing the targets of

Chapter 2

antibiotics as well as export the antibiotics entering the cell wall^{92, 93}. Bacterial resistance to antibiotics is an increasing global challenge; an estimated 70 % of bacterial infections are now resistant to at least one or more antibiotics⁹⁴. If an infection is persistent following placement of implants, a revision surgery is often required to remove the implant which is costly and has a reduced success rate. A lot of research has been conducted to study antimicrobial agents which are alternatives to 'traditional' antibiotics as they have great potential in fighting bacterial infections, and therefore decreasing the need for secondary surgeries. The use of metals as antimicrobial agents dates back to 1500 BP. Silver was commonly used by the Egyptians, Indians, Persian kings, Romans, Greeks and Phoenicians to disinfect water and preserve food⁹¹. Silver sutures were also invented to be used in surgical procedures to prevent infections⁹⁵. As well as silver, other metals including copper and zinc are also antimicrobial agents. The modes of action of metals and metal oxides differ from that of antibiotics, in that they alter the cellular processes of bacteria at a molecular and biochemical level which makes them promising against infections⁹⁶. Metals such as silver, copper and zinc are also antimicrobial agents. They can also be synthesised into metal oxide nanomaterials which have a higher surface area, leading to a greater particle surface reactivity⁹⁷.

Antimicrobial agents have proven to exhibit antimicrobial activity both in the macro and nano size. Antimicrobial agents such as metals and metal oxides have different mechanism of action to antibiotics. The mechanism of action is not well understood; however, it is believed that there are three general mechanisms.

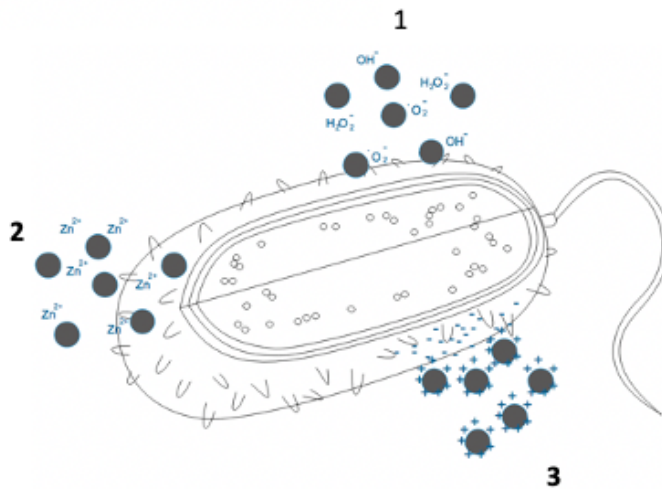


Figure 2.7. Different mechanisms of action of zinc oxide (ZnO) and zinc (Zn). (1) Formation of reactive oxygen species (ROS). (2) Release of antimicrobial ions. (3) Electrostatic forces between bacteria and ZnO nanoparticles causing damaging to bacterial cell membrane.

Figure 2.7 shows examples of the different mechanism of actions of antimicrobial agents using zinc and zinc oxide as an example. The same mechanisms are believed to be true for other antimicrobial metals such as silver and copper and their oxides. Figure 2.7 (1) represents the formation of reactive oxygen species (ROS). This mechanism is considered the main mechanism of action for the antibacterial activity of ZnO. ZnO is a semiconductor that can produce ROS. Electrons can move from the valence to the conduction band. When a free electron (e^-) moves to the conduction band, it gives rise to an electron hole (h^+) in the valence band. The positively charged valence band reacts with water creating $\cdot OH$ and H^+ . O_2 dissolves in the medium and becomes superoxide anion radicals ($O_2^{\cdot -}$). These radicals react with the H^+ to create (HO_2^{\cdot}). Hydrogen peroxide anions (HO_2^-) are subsequently created by the collision of

Chapter 2

free electrons collide with $\text{HO}_2\cdot$. Finally, H_2O_2 are formed when hydrogen peroxide anions react with hydrogen ions. As the bacteria is negatively charged the only molecule that can enter the bacteria is H_2O_2 . These molecules penetrate the cell membrane and cause damage to the cell⁹⁸. Reactive oxygen species are only believed to be produced by zinc oxide and not by zinc. Figure 2.7 (2) shows the release of bacteriostatic ions, in this case Zn^{2+} , which happens when a metal or metal oxide is placed in a medium with a microorganism. The ions penetrate into the bacteria and inactivate their enzymes⁹⁹. Figure 2.7 (3) shows the third theoretical mechanism of action which works by electrostatic forces between the positively charged ions and negatively charged bacteria causing tight bond between the microorganism and the metal oxide.

Silver-based wound dressings are commonly used to treat chronic skin and soft tissue infections such as diabetic foot ulcers. Many medical devices, including some heart valves and catheters are manufactured from silver impregnated polymers to inhibit the formation of bacterial biofilm. However, a prolonged exposure to silver can cause a non-life-threatening condition known as argyria. It can lead to an irreversible blue-grey skin colouring caused by the deposition of silver sulphide precipitates and silver selenide in the skin¹⁰⁰. Copper is an effective antibacterial, antiviral and antifungal agent¹⁰¹. Zinc is an antimicrobial agent frequently used in dentistry in products such as toothpaste and mouthwash, and in control of dental plaque. In addition, zinc is an important trace element found in the body. It has a vital role in the development, formation, mineralisation and maintenance of healthy bone and been found to tightly osseointegrate and enhance cell adhesion¹⁰², increasing implant stability and hence

Chapter 2

preventing migration¹⁰³. Therefore, zinc is selected as the antibacterial material for this project.

2.4.2 Improving implant stability

Implant migration is commonly caused due to the lack of implant stability. Implant migration can lead to further complications which often require a secondary operation to remove the migrated implant and possibly insert a new implant. There are several ways by which implant stability can be increased including the use of screw fixations to mechanically fix the implant in position or the use of porous osteoconductive materials to achieve a direct anchorage and contact between the implant and bone. Screws, specifically titanium screws are used frequently in orbital floor reconstruction surgery to fix the implant to the orbital rim. The advantages to screw fixation is the high mechanical strength, the osseointegrate properties and lack of foreign body reaction¹⁰⁴. However, screw loosening remains a problem^{64, 105} which does not only lead to poor implant fixation but can also lead to further complications such as infections¹⁰⁶.

Bioceramics, are widely used for bone regeneration due to their excellent biocompatibility and osteoconductive properties. They permit the formation of a more stable bond with the surrounding bone without the need for screw fixation¹⁰⁷. Bioactive materials are defined as materials that will dissolve slightly to promote formation of a biological apatite layer before forming a direct chemical bond with the bone¹⁰⁸. It is reported that 60 % of commercial bone graft substitutes include ceramics, mainly calcium phosphates (CaP) and bioactive glasses¹⁰⁹. HA and tricalcium phosphate

Chapter 2

(TCP) are types of CaP ceramics. CaPs exhibits great cell adhesion, excellent biocompatibility, osteoconductive properties and are similar in composition to the natural bone tissue mineral¹¹⁰. Hydroxyapatite (HA), $\text{Ca}_{10}(\text{PO}_4)_6(\text{OH})_2$, is a material closely associated to the natural bone apatite. It is the inorganic element which makes up 65 % of bone. The rest is made up by the organic matrix. HA has been used extensively as an artificial bone substitute due to its biocompatibility, osseointegration, osteoconduction and bioactivity. At the bone-implant interface, HA forms a bond with the bone through a carbonated calcium-deficient apatite layer. This provides the implant with stabilisation, reducing implant migration¹¹¹. It has been found to possess superior surface interaction properties and physiochemical interactions than the other CaPs¹¹⁰. TCP was found to have a bioresorption rate that is high and unpredictable¹¹¹. HA is the most stable CaP, as it has a decreased solubility in physiological environment defined by pH, temperature and body fluids to support bone mineralisation^{51, 112}. Therefore, the bioceramic selected for this study is HA.

2.4.3 Increasing restoration accuracy

Incorrectly shaping or positioning the implant can hinder the accuracy of the restoration which can lead to complications such as diplopia and enophthalmos. As mentioned in section 2.3.2, currently more research is being conducted on the fabrication of patient specific orbital floor implants in order to increase the accuracy of restoration. However, materials currently used for orbital floor reconstruction, such as PEEK and titanium, are not bioactive. Additive manufacture (AM) has the potential of fabricating complex patient specific implants from patient scan data. In addition, part of the advantage of AM is the ability of adding bioactive and antibacterial materials to

Chapter 2

improve implant stability and decrease infections, respectively. Even though, AM has many advantages it is important to bear in mind that AM will not eliminate the need for traditional fabrication techniques. Nonetheless it is predicted to revolutionise niche markets¹¹³.

Based on this information this PhD will investigate the potential of AM to address all three of these post operative issues by producing orbital floor implants that are both antibacterial and encourage cell/bone growth, in patient-specific geometries.

2.5 Additive manufacture

AM is defined by ASTM F2792 as ‘a process of joining materials to make objects from three-dimensional (3D) model data, usually layer upon layer, as opposed to subtractive manufacturing methodologies’¹¹⁴. In the past, AM was mainly used to develop prototype models, nonetheless, the applications of AM expanded as the technology continued to improve allowing fabrication of a variety of materials at a higher accuracy and speed. The medical industry is using AM in many different ways including the production of patient-specific anatomical models, surgical instrumentation, prosthetics and implants. In 2011, one of the most researched fields addressing 3D printing for surgical applications was for craniofacial reconstruction¹¹⁵. The production of 3D printed patient-specific implants for craniofacial reconstruction has gained a lot of attention in literature as it does not only offer better cosmesis but can reduce surgical time as well as provide precise adaption to the implantation site⁸². AM technology has improved immensely over the past years however, its applications

Chapter 2

remain limited. Some main limitations include part size, surface finish and quality variation from one machine to another¹¹⁶.

2.5.1 Types of additive manufacture technologies

There are various AM technologies developed to process metals, polymers, ceramics and plastics. These have several fundamental steps in common:

- A computer aided design (CAD) is produced using a 3D modelling software. Some printers require the design of support structures for overhanging holes or edges to keep them in the aimed position.
- The geometry of the 3D model is defined using a built-in-tessellation algorithm which covers the surface of the part with triangular mesh to create a simple boundary representation. This is then stored in Standard Tessellation Language (STL) format, a standard file format for 3D objects commonly used in AM systems. When this is used in combination with a 3D slicer (to slice the mesh into a series of parallel cross sections¹¹⁷), it forms the printing instructions for the 3D printer to fabricate the part.
- The object is printed layer by layer according to the STL file.
- The completed part is removed and post processed to obtain the final end product. This may include the removal of support structures.

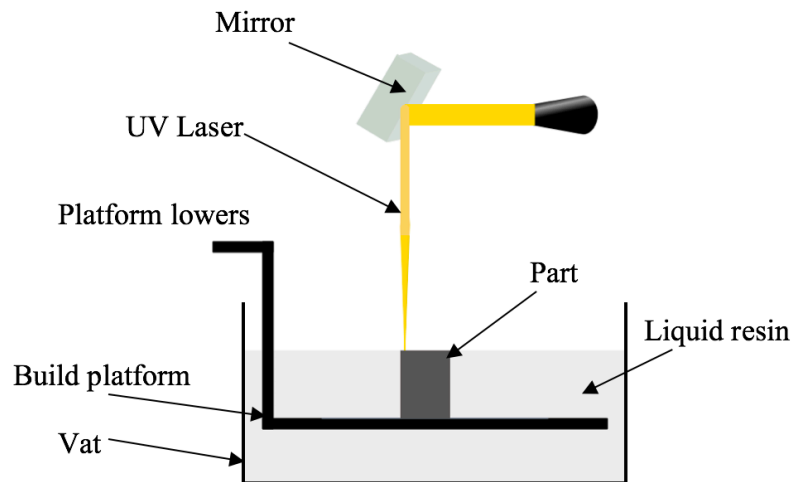


Figure 2.7. Schematic diagram of a stereolithographic (SLA) process.

Figure 2.7 shows a simple schematic diagram of a stereolithography (SLA) process. SLA, a liquid-based AM technique, using a photocurable liquid resin as the raw material. An ultraviolet (UV) laser traces each layer according to the CAD model and polymerises the polymer, causing the resin to solidify, whilst the area around the part remains a liquid. Subsequently, the platform drops down by one-layer thickness and another layer of liquid resin is spread on top of the solidified part. The process is repeated, curing the layers on top of each other. This is repeated until the full part is manufactured¹¹⁸.

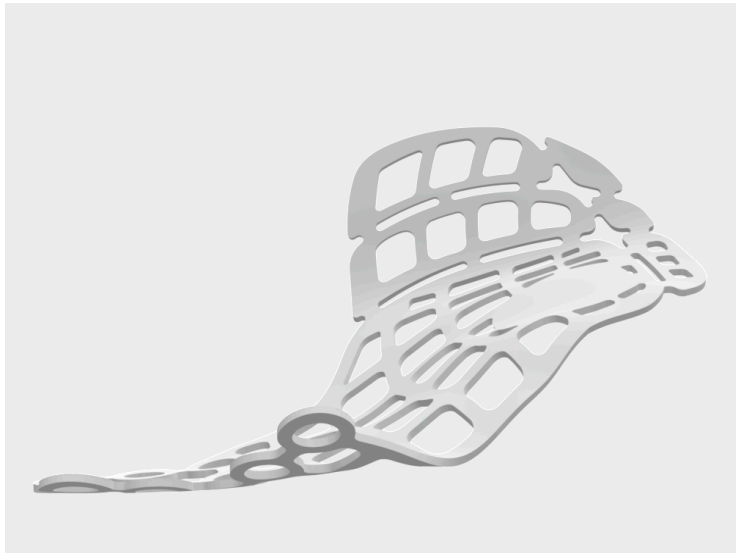


Figure 2.8. Computer aided design (CAD) model of an orbital floor implant.

SLA possesses a very high resolution, the precision of this technique can reach 20 μm and thus, being capable of fabricating highly accurate structures¹¹⁹. Complex parts, such as those needed for orbital floor reconstruction, require support structures for printability as they often have overhangs and bridges (Figure 2.8). This has several disadvantages including: additional time to remove the support structures, constraints on the geometric freedom as the supports need to be manually removed therefore, hand/ tool access is critical. The addition of support structures increases printing time which increases energy costs and in wasted feed stock as most support materials are non-recyclable¹²⁰. Digital light processing (DLP), a “sister technology” to SLA, uses a projector to flash an image of a layer over the build platform, curing all points simultaneously, resulting in a faster processing time and can potentially reduce cost. SLA is mostly used for the manufacture of diagnostic models, surgical simulation and treatment models¹²¹. The SLA parts are not commonly used in the body because most photocurable resins available have been shown to have cytotoxic effects on cells if any residues remain on the sample^{122, 123}.

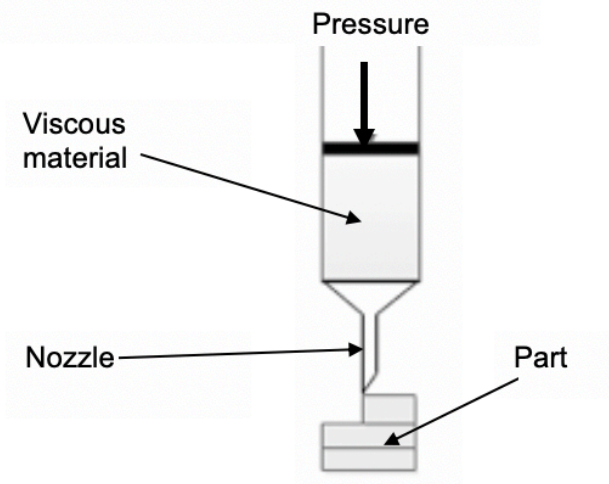


Figure 2.9. Schematic representation of 3D direct ink writing (DIW) process.

3D direct ink writing (DIW), also known as robocasting, is another liquid-based AM technique. A schematic representation of DIW is shown by Figure 2.9. DIW is mainly used to produce ceramic parts as a higher density can be loaded compared with both in micro- and nano-scale compared to powder-based techniques¹²⁴. A paste or a viscous material is extruded through an inkjet print head layer by layer at a constant rate and at a specific pressure. Once one layer is complete, the bed moves down by one layer. Another layer of viscous material is dispensed on top of the existing layer until the part is completed¹²⁵.

This technique is both cheaper and faster than photocuring and does not require support structures. It is often used to print bioceramic scaffolds for bone regeneration applications¹²⁶. However, the parts produced generally have low resolution and mechanical properties¹²⁷.

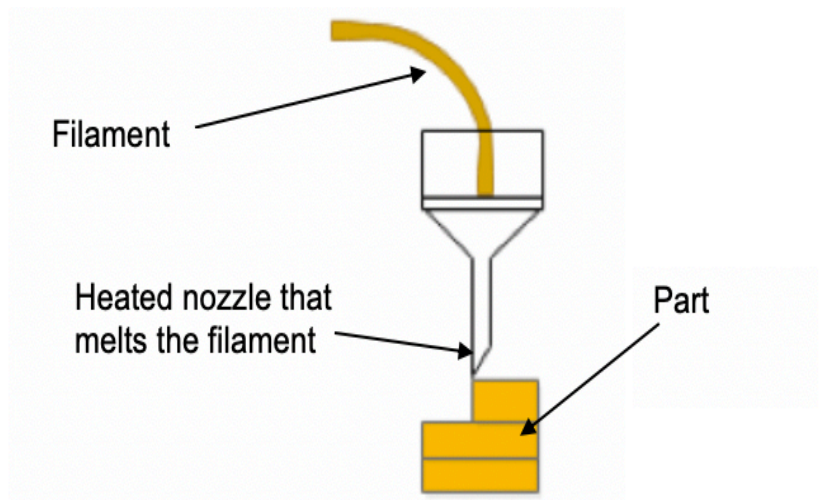


Figure 2.10. Schematic diagram of a Fused deposition modelling (FDM) process.

A schematic diagram of a fused deposition modelling (FDM) system is shown in Figure 2.10. Materials such as thermoplastic polymers filaments are commonly used in FDM. Metals and ceramics alone cannot be processed on FDM due to their higher melting temperature, therefore they are mixed with polymer binders to make filament feedstock¹²⁸. The filament feedstock moves through an extrusion nozzle and builds the model layer by layer. The extrusion nozzle operates in the x and y direction while the bed gets lowered in the z direction¹¹⁸.

The advantage of FDM is its cost effectiveness and ease of operation. In addition, parts produced typically have good strength. Then the polymer binder can be removed to obtain just the ceramic or the metal part. However this usually results in defects and voids¹²⁹, decreasing the mechanical properties of the part. FDM is typically used for the fabrication of geometrically simple surgical models that do not require a high level of detail¹³⁰.

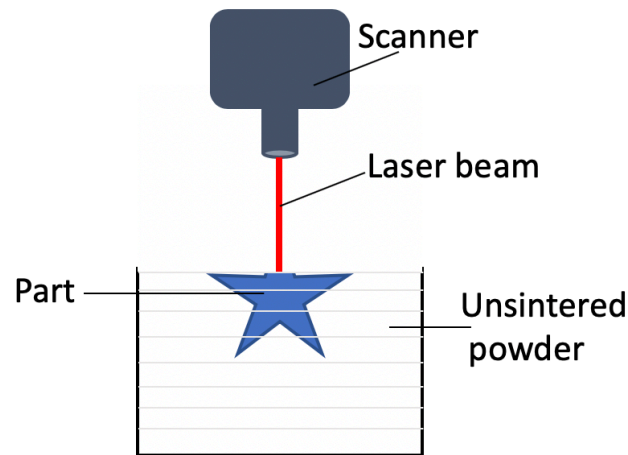


Figure 2.11. Schematic diagram of a laser sintering (LS) process.

Laser Sintering (LS) is typically used to process thermoplastic powders. A schematic diagram of LS is shown in Figure 2.11. A thin layer of fresh powder is spread on the build platform, from left to right with a re-coater blade. The excess powder goes into the powder collector chamber on the other side. A CO₂ laser scans the build platform according to the sliced STL file and fuses the powder in those specific areas. The powder that was not sintered around the part acts as support. The build platform moves down one layer and the re-coater blade on the right spreads a fresh layer of powder on the build platform, the laser scans the new layer, and this process is repeated until the part is complete¹³¹.

LS produces parts with a high resolution and good mechanical properties^{118, 132}. LS is carried out in an inert atmosphere using argon or nitrogen to circumvent oxidation of the polymer during sintering, leading to a reduction in internal stresses therefore no additional supports are required in LS¹³³. The main drawback to LS is the expensive

Chapter 2

equipment which can cost from \$100,000 for industrial LS printers compared to industrial FDM printers are available from \$15,000¹³⁴. Due to its high accuracy typically, LS is used to fabricate geometrically complex structures¹³⁵ which can have a huge potential in the manufacture of patient-specific orbital floor implants.

High speed sintering

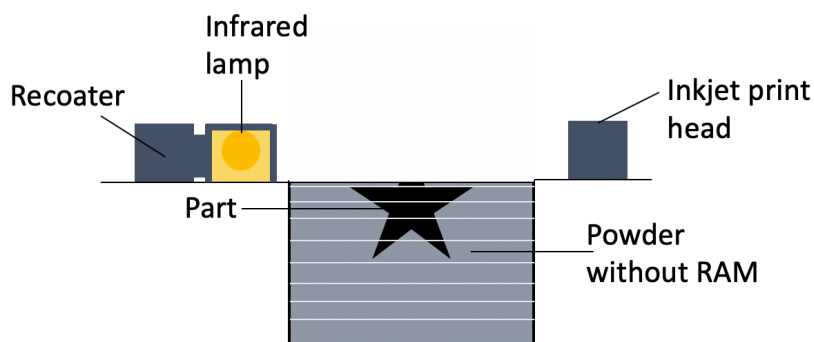


Figure 2.12. Schematic diagram of a high speed sintering (HSS) process.

High speed sintering (HSS) developed at the University of Loughborough¹³⁶, is a promising technique that is currently in the development stage (not commercially available). A schematic diagram of an HSS system is shown in Figure 2.12. Like LS, it is mainly used for processing thermoplastic powders. HSS and LS are similar powder-based AM techniques that differ in the way sintering is initiated¹³⁷. To sinter powders, HSS uses an inkjet print head to lay Radiation Absorbing Material (RAM) on the powder surface. Subsequently, an IR lamp passes over the powder build bed and the powders sprayed with the RAM ink absorb enough IR energy to selectively sinter the powders¹³⁸. The powder in the feed is heated to prevent cold powder being

Chapter 2

deposited on the build bed. The temperature of the bed is kept below the melting temperature of the material¹³⁷.

Similar to LS, it can also produce complex structures with the additional benefit of reducing machine costs and processing time¹³⁹. As this is a prototype it may affect the accuracy of the prints in addition as there is not much research on biocompatibility of the ink used in HSS. Nonetheless, this technique can be potentially useful in the manufacture of patient-specific implants at a faster rate and potentially reduced cost.

2.5.2 Additive manufacture of bioceramics

AM of complex patient specific implants from bioceramics has gained a lot of interest over the past couple of decades. Unlike materials such as polymers and metals, ceramics are more challenging to process due to their brittle nature and high processing temperature. This section (2.5.2) will explore the different printing systems that offer printing of bioceramics and will discuss the advantages and limitations of each technique.

Stereolithography

SLA of ceramics is challenging, as most of these materials are not photocurable. Research has been conducted on the combination of ceramics such as silica, silicon nitride, alumina and HA with photocurable resin^{132, 140-145}. The appropriate rheological properties, suspension viscosity and long-term stability, are important criteria for successful part printing on SLA. It is important that the additive remains

Chapter 2

homogeneously distributed throughout the resin for a period of hours to days to ensure consistent properties. It has been reported that the addition of the ceramic increases the viscosity exponentially, which can lead to a reduction or an inhibition in the flow of resin. Current SLA technology can process materials at 10s of Pa•s and a shear rate of 1000 s^{-1} ¹³². In addition, part shrinkage and a decrease in density are common drawbacks for SLA of ceramics which in turn leads to a decrease in the mechanical properties. Typically, volume shrinkage can be compensated for by software compensation technology, however, the software has to be further developed to accurately calculate this data for parts with a complex geometry¹⁴⁴. Research has found that the polymerization process is significantly affected by the light scattering from the ceramic particles within the suspension, despite the ceramic particles being transparent to UV irradiation¹⁴⁶. This phenomenon also effects the dimensional accuracy of the parts. Though SLA has a great potential in manufacturing custom implants with a high resolution, currently, due to the scarce number of biocompatible photocurable resin, its use is limited in the biomedical field.

Digital light processing

Ceramic printing on DLP was commercialised by Lithoz GmbH and is known as lithography-based ceramic manufacturing (LCM). LCM produces highly dense parts from materials such as zirconia, alumina and TCP¹⁴⁷. A recent study by Schmidleithner *et al.*¹⁴⁸ conducted an *In vitro* investigation on murine preosteoclast MC3T3-E1 cells suspended on TCP parts. It showed that there was an increase in alkaline phosphatase (ALP) activity over 14 days. However, the structure of bone is different between animals and humans which can influence the bone's composition,

Chapter 2

remodelling, healing and signalling pathways, thus, interspecies differences can make data extrapolation challenging¹⁴⁹. This technique has a potential in manufacturing highly dense ceramic parts with a high surface finish and a high resolution. Though, like SLA, the limitation in biocompatible photocurable resin remains an issue.

Direct ink writing

There are four important factors to bear in mind when DIW ceramic-slurries: the percentage of solids in the ink, the rheological properties of the paste, the rate of dispersion of the ink from the nozzle and the ink's drying kinetics^{125, 150}.

Originally, ceramic-based slurries were combined with minimal organic content (<1 wt%) to use as feedstock on DIW. The ink is usually composed of roughly 50 to 60 vol% ceramic powder, a dispersant to help spread the ceramic in the aqueous solution^{151, 152}, less than 1 % organic content which acts as the additive and 35 to 50 % water or another volatile solvent. The main drawback to DIW is the use of organic content. This is because residual traces might still be present despite post processing which can give rise to an adverse toxic effects *in vitro* and provoke inflammatory responses *in vivo*¹⁵³

To avoid the use of organic content and increase the flexibility of the specimens, Maazouz *et al.*¹⁵⁴ manufactured alpha-TCP and gelatine reactive slurries. The study found that the crosslinked bovine gelatine increased the compressive strength and elastic modulus of the scaffold than the non-crosslinked gelatine. Longer-cultures revealed that the crosslinked gelatine samples had higher cell proliferation and

Chapter 2

adhesion nonetheless, the values were significantly lower than the tissue culture plastic (TCPS) control. The measured specific surface area was $24.85 \pm 0.02 \text{ m}^2/\text{g}$. BioOss®, a commercial bovine bone substitute with high osteoconductive properties, has been found to have a specific surface area ranging between 60 up to $100 \text{ m}^2/\text{g}$ ¹⁵⁵⁻¹⁵⁸ which means that it has a larger surface area to absorb more proteins to induce bone differentiation. A limitation to this technique is that to prevent gelation the gelatine has to be kept at temperatures higher than $30 \text{ }^\circ\text{C}$ ¹⁵⁹, therefore printing the material may be challenging without additional equipment such as a heating jacket to keep the syringe at the desired temperature.

Fused deposition modelling

Research has been conducted on the combination of bioinert polymer with bioactive ceramic to fabricate composite filaments^{8, 160}. Studies have also been conducted on the combination of biodegradable polymers such as polylactic acid (PLA), polycaprolactone (PCL) and poly(lactide-co-glycolide) (PLGA) with biodegradable ceramics for biomedical application¹⁶¹⁻¹⁶⁴. A study comparing *in vivo* performance of titanium cage implants for spinal fusion applications with FDM PCL-TCP implants in sheep models found that at 12 months both implants had similar fusion rate and the PCL-TCP showed superior bone ingrowth and more homogeneous bone distribution¹⁶⁵. Composites such as PCL/HA^{163, 166} and PCL/ PLA/ HA¹⁶⁷ have been successfully used in FDM however, this technique still has its limitations such as only thermoplastic materials can be used, typically the parts produced have low surface roughness which is not advantageous as surface modification or coating may be required in addition, it is challenging to achieve micro porosity which is necessary for

Chapter 2

cell ingrowth and vascularisation¹¹⁹. An additional drawback of FDM is the poor surface quality caused by the 'staircase' effect which is a result of the layer deposition¹⁶⁸. The staircase effect cannot be completely eliminated, however it can be improved by optimising the processing parameters¹⁶⁹. Post processing is typically required to remove the staircase effect, which may lead to a decrease in part accuracy.

Laser sintering

Ceramic parts have been fabricated on LS has been proven to have a potential in manufacturing bone scaffolds with a high resolution and high-quality surface finish. However, processing ceramics on LS is difficult as ceramic have a high melting temperature therefore, they are typically combined or coated with materials that have a lower melting temperature. Physically blended or coated ceramics with polymers such as PEEK¹⁵³, poly(vinyl alcohol) (PVA)¹⁷⁰, PCL¹⁷¹, high density poly ethylene (HDPE)^{172, 173}, poly(L-lactide) PLLA¹⁷⁴, Aliphatic- polycarbonate (a-PC)¹⁷⁵ and polyamide (PA)¹⁷⁶⁻¹⁷⁹ have been produced on LS. Several studies have combined HA and PA12^{177, 179}. PA12 is commonly used in LS as it had the desirable thermal properties. The part produced had relatively low mechanical properties because the studies used low processing temperatures such as 132 and 140 °C and low laser powers of 4 and 5 W. The bed temperature and the laser powder used in the studies were very low which may have caused insufficient melting between the powder particles which can lead to low mechanical properties. Shrinkage is a well-known phenomenon, in LS. The shrinkage varies from one material to another and can affect the part accuracy. Shrinkage rates are lower in amorphous polymers as the molecular chains are arranged in a random manner. Nonetheless, amorphous polymers are not

Chapter 2

frequently used in LS and HSS because they do not have a fixed melting peak therefore, the polymer transitions into a liquid more gradually, producing parts which are partially dense with potential layer deposition issues¹⁸⁰. Typically, experimental prints are undertaken to calibrate the machines and calculate the shrinkage compensation in order to rescale the original CAD model.

2.5.3 Summary and manufacturing technique selection

Table 2.2. Advantages and disadvantages of various AM techniques in possessing bioceramic materials.

AM techniques	Advantages	Disadvantages
SLA and DLP	<ul style="list-style-type: none"> • Parts produces with a high resolution • Parts have good strength 	<ul style="list-style-type: none"> • The need for support structures • There is a scarce number of biocompatible photocurable resin • Most ceramics are not photocurable • Ceramics have been found to affect the polymerisation process which in turn effects part accuracy.
DIW	<ul style="list-style-type: none"> • Cost effective • Fast process compared to SLA, DLP, LS and HSS • Does not require support structures 	<ul style="list-style-type: none"> • Low resolution • Low mechanical properties • May use organic content which may leave residual traces that may provoke an inflammatory response • Gelatin reactive slurries that do not require organic content have to be processed quickly to prevent gelation
FDM	<ul style="list-style-type: none"> • Cost effective • Easy to operate • Fast process compared to SLA, DLP, LS and HSS • Parts have good strength 	<ul style="list-style-type: none"> • Only thermoplastic polymers and wax can be used • Parts typically have low surface roughness • Poor surface quality • Nozzle blockage
LS and HSS	<ul style="list-style-type: none"> • Parts produces with a high resolution • Does not require support material • Rough surfaces to encourage bone ingrowth • Parts have good strength 	<ul style="list-style-type: none"> • Expensive equipment • Limited number of polymers can be processed

Chapter 2

Table 2.2 shows the advantages and disadvantages of various AM techniques for processing bioceramics. Despite some efforts, there's no perfectly suitable biocompatible orbital floor implant material that is osteoconductive, antimicrobial and patient specific, therefore, this project aims to investigate this further. Powder-based AM systems, LS and HSS, were selected because they can produce parts with a high accuracy, a rough surface finish which can encourage osseointegration and do not require support structures thus reducing waste. Therefore, these techniques have a promising potential in the fabrication of orbital floor implants.

2.6 Polymer processing

There is a wide range of sinterable polymers including thermoplastic polymers such as polypropylene (PP), polyethylene (PE), PCL as well as high performance polymers such as PEEK and amorphous polymers such as polycarbonate (PC), polystyrene (PS) and PMMA¹⁸¹. Thermoplastic polymers can be subdivided into amorphous and semi-crystalline. The molecular chains of amorphous polymers are arranged in a random manner while semi-crystalline polymers are 50 to 60 % ordered and the rest are in an amorphous state. The difference in molecular chain arrangement causes amorphous and semi-crystalline polymers to have significantly different thermal properties¹⁸². The thermal properties of a polymer are critical in LS and HSS as they are both heat transfer processes where polymer particles are heated rapidly and then cooled naturally to form solid parts¹⁸². Semi-crystalline PA11 and PA12 account for 95 % of LS polymer powder material market¹⁸³ as they possess the desired thermal and physical properties for successful sintering. Flowability of the powder is very much dependent on the shape and size of each particle. A spherical powder shape and a

Chapter 2

powder size between 20 to 80 μm ensures better flowability and a superior packing density which in turn, gives rise to greater part density thus leading to superior mechanical properties¹⁸⁴. One of the main reasons that commercial PA12 is readily used is that it has the spherical shape and an optimal particle size ensuring good processability. Therefore, PA12 was selected as the base polymer for this project.

2.6.1 Polyamide 12

PA12 is extensively used in LS and HSS because it has the desirable extrinsic and intrinsic properties for LS and HSS. It has a large sintering window (gap between melting temperature and crystallisation temperature), allowing it to stay stable despite the fluctuation of heat during the sintering process. PA12 is a thermoplastic polymer which becomes softer when exposed to heat and solidify upon cooling. When PA12 particles are heated, they undergo thermal transition such as melting and crystallisation. The consolidation process of semi-crystalline PA12 occurs above their melting temperature (T_m). PA12 have a sharp melting peak therefore, when sufficient heat energy is absorbed by the particles, the polymer rapidly changes into a viscous liquid. Sintering necks are formed between particles and if enough heat energy is absorbed, particles fully melt and overlap with the previous layer. Upon cooling below T_m , polymer crystals grow from a nucleation centre to form lamellar stacks of spherulites. When PA12 is heated from room temperature to its melting point, it undergoes a crystal to crystal transition known as the Brill transition¹⁸⁵. At room temperature, the molecular chains of PA12 form hydrogen bonded sheets which are stacked together using weak Van der Waals forces. The molecular chains are arranged into a trans-zigzag conformation to form a triclinic lattice. At melting point,

Chapter 2

the triclinic phase of PA12 is replaced by a pseudo-hexagonal crystalline structure. This phenomenon can be observed by X-ray diffraction (XRD). PA12 at room temperature shows two distinct peaks at d -spacing of 0.44 nm and 0.37 nm, which are typical for the triclinic lattice. Upon melting, the two peaks merge into a single peak at d -spacing of 0.42 nm, a representative of the less stable pseudo-hexagonal unit cell¹⁸⁶. This phase transition can cause shrinkage during the formation of crystalline regions, but it increases part density.

2.6.2 Compositing polyamide 12

While PA12 may have various benefits such as being an ideal material to process on LS and HSS, it is bioinert and is not amicrobial. As mentioned in section 2.5.2, various studies have investigated the processability of HA and PA12 to increase the osteoconductive properties of the material. Generally, the parts produced were processed at relatively low processing temperatures and laser power which in turn resulted in parts with low mechanical properties. Therefore, it would be interesting to investigate increasing the processing parameters in order to increase the degree of particle melt (DPM) to improve the mechanical properties of the parts.

Kamarajan *et al.* investigated the *in vitro* and *in vivo* cell viability and cytotoxicity on 5 and 10 wt% HA:PA12 LS scaffolds¹⁸⁷. The cell viability results revealed that all the samples were biocompatible and did not cause any cytotoxicity. The test results for the alkaline phosphatase (ALP) assay showed that the scaffolds containing HA had lower ALP enzyme activity level at day 4 and 7 than the TCPS control. However, at day 10, there was no statistical difference between the samples and the control. The

Chapter 2

low levels of ALP may be due the type of cells used. MG 63 cells are known to express lower ALP activity than primary human cells¹⁸⁸. Alizarin red staining was used to test for calcium mineralisation. The results showed that after 28 days the samples with HA were more intensely stained, an indication for a higher calcium content. Calcium is a nutrient commonly associated with the formation and metabolism of bone however, in this study this stain may not be very useful as the samples with HA contains calcium, therefore the increase of HA content will increase calcium concentration. The control used was a PA12 scaffold, which does not contain calcium and is therefore not a useful control. Other techniques could have been used such as Sirius Red to stain total collagen tissue present on the scaffolds¹⁸⁹. The *in vivo* test conducted in rat models suggest that after 7 weeks of implantation the rat with PA12 implant had an inflammatory response, but no inflammatory response was observed in the rat with the 10 wt% HA:PA12. The PA12 implants showed the presence of plasma cells, fibroblasts, neutrophils and scattered inflammatory infiltrate. The 10 wt% HA:PA12 implant showed the presence of fibroblasts, scattered macrophages, plasma cells and a small number of neutrophils. Neutrophils are the first cells attracted to the site of injury and are key mediators of the inflammatory response which is the first step in secondary bone healing. Even though there was no inflammatory response in the rat model with the 10 wt% HA:PA12 implant, the literature highlighted that orbital floor implants are more prone to infections due to the implant's exposure to the nasal/oral/pharyngeal mucosal cavities. This can potentially be prevented by adding an antibacterial agent to the polymer-ceramic composite.

As of yet high speed sintering of polymers with HA remains a novel technique. This is also true for laser sintering and high speed sintering of polymers with antimicrobial

Chapter 2

properties. Therefore, there is a gap in the research to explore the processability of these materials on HSS which can produce implants that can potentially be used for orbital floor reconstruction applications. A study conducted by Turner *et al.*¹⁹⁰ introduced a new approach of combining 1 % antimicrobial agent (silver-based additive) with a polymer powder (PA12) to process on laser sintering. Currently, there are no published research on the laser sintering or high speed sintering of polymer-ceramic implants with antimicrobial properties. As mentioned in section 2.4.1, Zn was chosen as the antimicrobial agents in this study due to their ability to aid in the bone formation process, improving cell adhesion and osseointegration properties however, as of yet there has been no literature reporting the LS or HSS of Zn/PA12 composites.

2.7 Factors that influence the mechanical properties in laser sintering and high speed sintering

Even though the orbital floor is non-load bearing, the material must possess sufficient strength to support the eye globe and orbital content and withstand any handling forces during the implantation procedure. The printing parameters and the part orientation within the build must be kept constant as they have an effect on the mechanical properties of the parts. Section 2.7.1 and 2.7.2 discuss how the energy density, as well as the part location and orientation of the parts within the build, respectively, have an influence on the mechanical properties of the parts in LS and HSS.

2.7.1 Energy density

Chapter 2

The energy density input plays an important role in powder-based AM. A higher sample density can be achieved by increasing the energy density input to the optimal setting¹⁹¹. The energy density is the intensity of the energy being delivered to the particles. The energy density (J/mm^2) is commonly calculated using (Equation 2.1, where P represents the laser or lamp power (W), v is the laser beam or lamp speed (mm/s) and h is the hatch distance or heated length of the lamp (mm)^{191, 192}.

$$\text{Energy density} = \frac{P}{v \times h}$$

(Equation 2.1.)

Increasing the energy input results in higher degree of particle melt (DPM) as it enables larger particles to melt complete leading to higher sample densities. A study conducted by Majewski *et al.*¹⁹³ which investigated how the mechanical properties are effected by DPM in LS, revealed that increasing the DPM increased the tensile strength and elongation at break of the samples. Increasing the laser power and reducing the scan speed are a few ways to increase the DPM. However, delivering an excessive amount of energy to the particles can cause the smaller polymer particles to combust. Large particles often require more laser energy to melt than the small particles, results in complete melting of the small particles and incomplete melting of the large particles. Leading to what is known as ‘cored’ spherulites¹⁹³⁻¹⁹⁶. An advantage to the ‘cored’ spherulites in this research is that it can lead to surface irregularities which in turn lead to a higher degree of surface roughness. Implants with a textured surface have been found to be superior for bone reconstruction applications because they have an increased surface area which can increase bone-to-implant

Chapter 2

contact (BIC)¹⁹⁷⁻¹⁹⁹. Therefore, the processing temperature is set just below the onset of melting temperature but above the onset of the crystallisation temperature, known as the 'sintering window'. This is to ensure that the laser only contributes to the remaining energy required to melt the powder particles. If the bed temperature is set too close to the crystallisation temperature, curling will occur causing part distortion due to premature crystallisation. Usually, increasing the temperature slightly may avoid curling, however, if the bed temperature is set too close to the melting temperature it can give rise to lateral growth where powder particles stick on the molten surfaces and reduce the resolution of the part²⁰⁰.

Zhu and Majewski¹⁹¹ investigated the correlation between the energy input and the porosity of HSS parts. The results revealed that parts processed with higher energy inputs showed a decrease in porosity which led to an increase in the ultimate tensile strength. However, if the energy input is too high, it can cause the surrounding powder to become over-sintered making it challenging or unfeasible to remove the parts. Therefore, the processing temperatures selected must be high enough to melt the particles however, not too high to over-sinter the surrounding powder making it not possible to remove the parts.

2.7.2 Part location and orientation in the build platform

The spacing and location of the parts in the bed also has an important effect on the mechanical properties. Studies have confirmed that the outer regions of the build should be avoided as the parts cool down faster than the parts placed in the centre²⁰¹. The orientation of the parts in LS and HSS is important as it can affect part strength

Chapter 2

and flexibility. Previous studies²⁰²⁻²⁰⁵ have reported that parts built in the horizontal direction for both LS and HSS processes have superior ultimate tensile strength, Young's modulus and elongation at break than those built in the vertical direction because the applied force is the same as the layer direction.

2.8 Summary

This Chapter has identified the potential for AM of orbital floor implants to give their potential to manufacture custom-fit implants for the restoration of defects with complex geometries. Various AM techniques are available, however, for this research powder-based AM techniques, LS and HSS, were selected because they can produce parts with a high accuracy, a rough surface and do not require support structures. PA12 was selected as the base polymer as it has the desirable thermal and physical properties to make it an ideal material for processing on both LS and HSS. However, PA12 is bioinert, therefore, different additives were investigated to enhance its osteoconductive and antimicrobial properties. HA was selected as the osteoconductive material because it is closely associated to the natural bone apatite and is the most stable calcium phosphate and Zn was selected as the antimicrobial material because it has a vital role in the development, formation, mineralisation and maintenance of healthy bone. Previous studies which processed HA:PA12 parts by LS generally have low mechanical properties, even though orbital floor implants are non-loadbearing it is important to ensure that the optimal sintering parameters as well as part orientation are selected as they affect the properties of the parts. The LS of polymers with antimicrobial agents remains a fairly novel technique. In addition, HSS of polymers with osteoconductive and antimicrobial properties has not been explored

Chapter 2

in previous literature. Therefore, this research will focus on determining the feasibility of LS and HSS to process polymer parts with osteoconductive and antimicrobial properties.

3 Material and Method

3.1 Material selection

It is evident from the literature that polymer-ceramic composites have gained a lot of interest in bone reconstruction applications especially non-load bearing applications such as orbital floor implants. Some research has been conducted to investigate the feasibility of processing ceramic-polymer composites by laser sintering (LS). However, due to the novelty of high speed sintering (HSS), no research has investigated the processability of ceramic-polymer composites on HSS. In addition, the processability of polymer-ceramic composites with antimicrobial properties using these powder-based additive manufacturing (AM) techniques has also not been explored.

3.1.1 Base polymer

Ceramics, metals and metal oxides generally have high melting temperatures, therefore in order to fabricate sound parts on LS and HSS using these materials, a polymer base has to be selected. As per section 2.6, polyamide 12 (PA12) has the desirable properties making it an ideal material for Laser sintering (LS) and high speed sintering (HSS). In this research, PA12 (PA2200, EOS GmbH) with an average particle size of 56 μm , was selected as the base-polymer. Many industry guidelines recommend the use of 50:50 virgin:aged PA12 to fabricate parts on LS and HSS as it produces denser parts in comparison to virgin PA12. However, virgin PA12 has been shown to have marginally superior mechanical properties²⁰⁶. Additionally, it is difficult

Chapter 3

to know the processing history of the used PA12 powder, thus, 100 wt% virgin PA12 powder was used in this research to ensure better part consistency.

3.1.2 Bioactive material

PA12 has many advantages such as good mechanical strength and biocompatibility, however, it lacks bioactivity. To reduce the risk of implant migration, current polyamide implants require titanium screws to bond the implant to the bone tissue. The use of screws for long-term implantations can cause complications such as implant loosening or wear. Osteoconduction can be improved with the addition of a bioactive ceramic. In this research, commercially available hydroxyapatite (HA) (Plasma Biototal Ltd©. CAPITAL® 30 D50 SD) was selected as the bioactive ceramic due to its spherical particle shape (which is desirable to achieve good flow behaviour in LS and HSS) and particle size similar to that of the base polymer (average particle size of 31.1 µm).

3.1.3 Antimicrobial agent

There are many materials available for orbital floor reconstruction, however, it is evident from the literature review (section 2.3.2) that most of these materials are prone to implant associated infections. The management of infections can be costly and difficult. The addition of an antimicrobial agent to implants have shown a potential in preventing infections and reducing the need for secondary surgeries. Zinc (Zn) has been found to aid in the of bone formation therefore, it is promising antimicrobial agent for bone reconstruction applications.

Chapter 3

3.1.4 Compositions

To assess the processability of HA and PA12 compositions different filler quantities were used. The maximum quantity of HA investigated was 40 wt% as higher quantities of HA would result in less polymer, and hence less sintering, which is likely to impact the mechanical properties of the material. Therefore, for the bioceramic: polymer compositions the ratios investigated were: 0:100, 5:95, 10:90, 20:80, 30:70 and 40:60 wt% HA:PA12.

An ideal concentration of Zn for the optimal antimicrobial properties remains elusive. Prior investigations conducted by group members indicated that a 2:98 Zn:PA12 concentration would be adequate to achieve antimicrobial action whilst preventing cytotoxicity, and due to limited availability of both LS and HSS, this was the only composition investigated.

The final compositions under investigation involved the combination of the optimal HA:PA12 composition for each printer with the selected antimicrobial agent based on the previous investigations. From section 4.6, the optimal HA:PA12 composition for orbital floor reconstruction purposes processed on LS was 20:80 wt% HA:PA12 and 40:60 wt% HA:PA12 for HSS. Therefore, the Zn:HA:PA12 composition selected for LS was 2:19.6:78.4 wt% Zn:HA:PA12 and 2:39.2:58.8 wt% Zn:HA:PA12 for HSS.

Chapter 3

3.1.5 Powder preparation

For each composition, 6 kg of powder was prepared according to the ratios investigated. The compositions were tumbled for 45 minutes to ensure homogeneity. Then the mixed powder was divided in two, where 3 kg were used on LS and 3 kg were used on HSS.

3.2 Powder characterisation

3.2.1 Powder morphology

The powder's extrinsic properties such as particle shape and size have an important role in successful part fabrication in LS and HSS. The powder morphology was investigated using a scanning electron microscope (SEM) (Vega3, Tescan), a widely used technique for material characterisation which can image surfaces at much greater magnifications than optical microscopy. Secondary electron (SE) micrographs were used to evaluate the surface topography of the powders. Additionally, backscattered electron (BSE) micrographs were used to qualitatively measure the homogeneity of additives on the surface of the LS and HSS samples. Energy dispersive X-ray (EDX) were used alongside BSE micrographs to confirm the elemental composition of the printed samples.

The samples were placed on 0.5 inch aluminium stubs (Agar Scientific Ltd) with 12 mm double sided carbon adhesive tabs (Agar Scientific Ltd). Leit-C Plast conductive adhesive paste (Agar Scientific Ltd) was placed on the carbon tab then, the printed discs were pressed on to the adhesive paste. Silver ELECTRODAG 1415 (Agar

Chapter 3

Scientific Ltd) was painted on the side of the disc to further reduce noise and surface charging. The samples were gold coated by a low vacuum sputter coater to produce a conductive layer which- decreases thermal damage and inhibits charging. The samples were analysed at an accelerating voltage of 15.0 kV and a working distance of 10 to 15 mm.

3.2.2 Thermal analysis

Selecting the optimal sintering parameters for LS and HSS is an essential requirement to fabricate parts successfully and is informed by the melting and crystallisation temperatures of the composite in question. A Differential Scanning Calorimeter (DSC) is a thermoanalytical technique which can determine these parameters and is typically used to screen new materials for their potential use in LS and HSS.

DSC measures the heat energy required to keep both the polymer sample pan and the inert reference pan at the same temperature²⁰⁷. The sample pan contains a polymer, thus more heat energy is required to keep the sample pan at the same temperature as the empty reference. During melting, energy is used to melt the crystalline regions of the polymer, thus despite continuous heating, the temperature remains constant in the sample pan. When PA12 is cooled from the melt, the polymer chains realign into crystalline structures. This is an exothermic process, where heat is released, therefore less heat energy is required to keep the sample and reference pan at the same temperature. An example of a typical DSC curve for PA12 is shown by Figure 3.1.

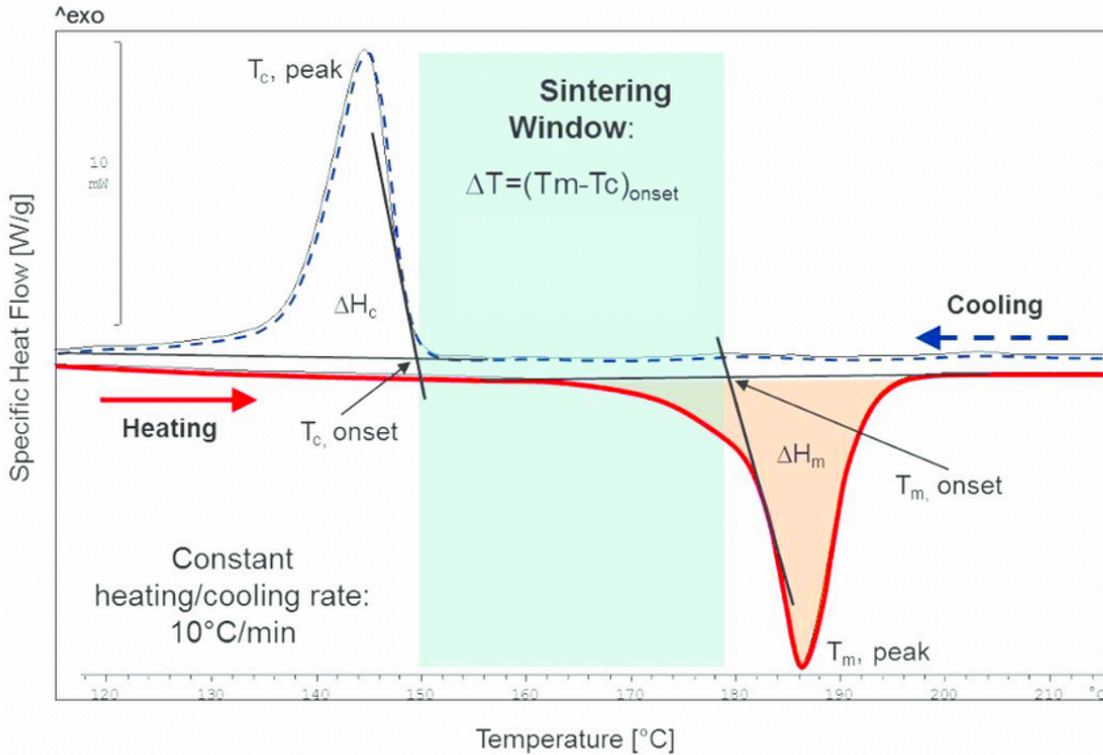


Figure 3.1. A standard differential scanning calorimetry (DSC) curve for polyamide 12 (PA12). The first peak is the crystallisation peak while the second peak is the melting peak. The area in the middle is the sintering. Window also known as the processing window²⁰⁰.

The thermal transitions are determined by plotting heat flow vs temperature values. The area in the middle is the sintering window, also known as the processing window. The flat red line shows the material being heated at a constant rate past the melting temperature (T_m) peak to ensure that all the polymer is melted. Then the polymer is cooled, as shown by the flat blue dotted line until the crystallisation temperature (T_c) peak. The preliminary processing parameters are often set based on DSC results, using the processing window values as a guide. The precise parameters are typically set by trial-and-error builds.

Chapter 3

An average weight of 5.30 mg of the powders investigated were placed in an aluminium pan, closed tightly with a lid and then placed in the DSC (8500, Perkin Elmer). An empty reference aluminium pan also closed tightly with a lid was placed in the reference position. The temperature of the sample was increased from 60 °C to 225 °C at a rate of 10 °C/min. The samples were heated to 225 °C to ensure all the polymer has melted and then cooled to 60 °C at a rate of 10 °C/min. These settings were based on the default parameters for PA12 already established in the Advanced Polymer Sintering laboratory.

3.3 Design of test samples

The first step of additive manufacture (AM) is the generation of 3D computer aided design (CAD) models which were converted into STL format, the standard file type used by most 3D printers. Fusion 360 (Autodesk) was used to generate 3D models of the testing samples.

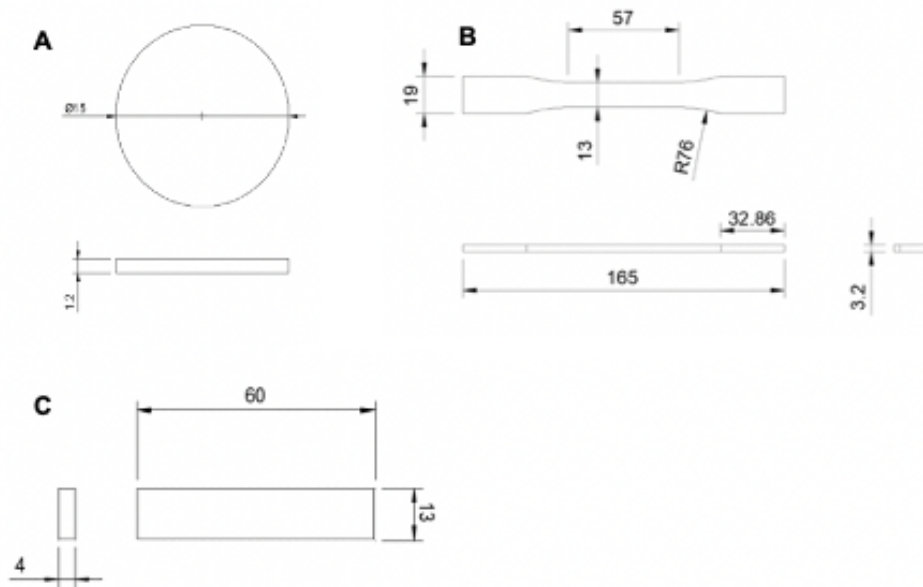


Figure 3.2. Computer aided design (CAD) models showing the dimensions (mm) of (A) discs, (B) tensile test bars and (C) three-point bend bars.

Figure 3.2 (A) shows the dimensions of a disc which was used in material characterisation, cell culture and microbiology tests. The biocompatibility tests were conducted in 24 well plates, therefore, the size and the shape of the discs were fabricated to fit inside these wells. A cylindrical shape was chosen in order to cover the surface area of the 24 well plate. Tensile test bars and three-point bend bars were designed according to ASTM D638 Type 1 and ASTM D790 standards, respectively. The CAD models were converted into STL files and were then sliced into 100 μm layers. As mentioned in section 2.5.1 this forms the printing instructions for the 3D printer.

Chapter 3

3.4 Part fabrication

There are various factors that influence the mechanical properties of LS and HSS including processing conditions and build orientation. Setting the optimal sintering parameters can greatly influence mechanical properties, surface finish and accuracy of the parts.

3.4.1 Laser sintering

LS parameters

Commercial laser sintering system Formiga P100 (EOS GmbH) was used to fabricate the parts. The default processing parameters established by the Advanced Polymer Sintering laboratory at the University were selected. A CO₂ laser with a wavelength of 10.6 μm was used to produce power. The bed temperature was set to 170 °C and a laser power of 21 W was selected. The scan speed and scan spacing were set to 2500 mm/s and 0.25 mm, respectively. A standard layer thickness of 0.1 mm was chosen.

Build setup

The location of the parts in the build is important as highlighted in section 2.7.2. The parts were placed in the centre of the 200 x 250 mm build chamber, avoiding the colder outer corners which could lead to premature recrystallisation thus potentially leading to curling and/or part distortion. The machine underwent a standard warm up cycle of roughly 2 hours where several blank powder layers were spread on the print platform

Chapter 3

without sintering. This helps reduce the shrinkage stresses created during the sintering process which in turn reduces part warpage. Then 12 mm blank unsintered layers were applied to the base of the build before printing to add more heat to the system.

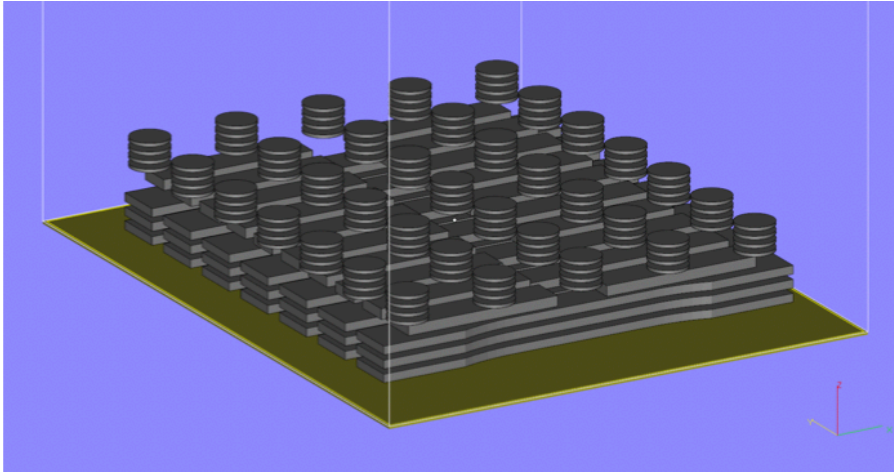


Figure 3.3. LS build set up.

The samples were built in the horizontal orientation as it has shown to produce parts with superior mechanical properties. The build setup (Figure 3.3) contained 181 parts: 21 tensile test bars, 20 3-point bend bars and 140 discs. For the tensile testing, 5 tensile test bars were required, 5 3-point bend bars were needed for 3-point bending, 4 discs were required for every biocompatibility investigation and the discs were needed for antimicrobial investigations. Discs were also used for the physical characterisation of the materials. Extra samples were made for experimental repeats. The build set up was sliced into 0.1 mm series of parallel cross sections. The LS process was briefly described in section 2.5.1 (for a step by step please see Appendix).

Chapter 3

Post-processing

After the print was successfully completed the build chamber was left overnight to cool the powder bed after the printing process. The finished parts were cleaned from the excess powder with compressed air. The samples were stored in sealed bags at room temperature before they were used for testing.

3.4.2 HSS parameters

As mentioned in section 2.5.1, HSS is a prototype and unlike a commercial machine the parameters are likely to change with the development of the machine. The default HSS printing parameters, at the time of use, for processing PA12 were used to high speed sinter all the different compositions. The bed temperature was set to 150 °C. The radiation absorbing material (RAM) (PCO 7774, SunJet) absorbs sufficient thermal energy from the overhead lamp to increase the temperature and transfer it to the powder underneath. The processing parameters used were the default processing parameters established in the Advanced Polymer Sintering laboratory. The overhead initial power was set to 53 % (based on an array of 6 x 300 W ceramic infrared emitters) with a sinter speed and move speed of 120 mm/s and 70 mm/s, respectively. The amount of ink deposited is known as the greyscale. The greyscale has 8 levels excluding 0, where no ink is used. An increase in greyscale number increases the ink deposition. In this project the greyscale was set to 3 drops per drop. As used for LS, the layer thickness was also set to 0.1 mm. All the compositions were processed using the default processing parameters. The HSS process was briefly described in section 2.5.1 (for a step by step please see Appendix).

Chapter 3

Build setup

To ensure consistency between the laser sintering and the high speed sintering set up, the same build was transferred into the high speed sintering build chamber setting, however, the high speed sintering build chamber is rectangular (800 mm in X direction and 200 mm in Y direction) and is not as deep as the LS build chamber meaning the number of test samples that could be produced was slightly lower. This was not an issue as the previous build had many spare samples.

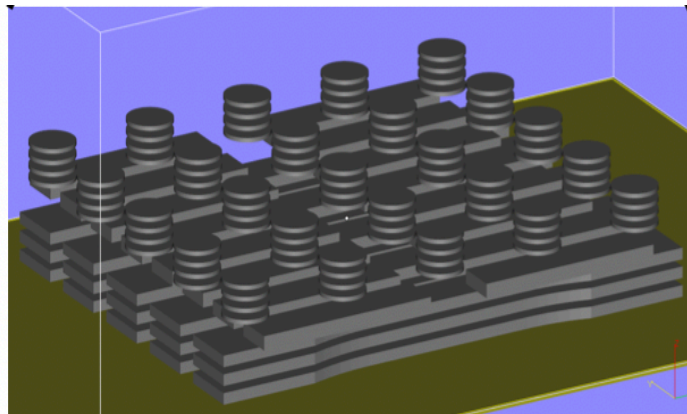


Figure 3.4 High speed sintering build set up.

The build (Figure 3.4) contained 131 parts; 15 tensile test bars, 16 3-point bend bars and 100 discs. The parts were centered in the build platform avoiding the cooler outer edges (the 25 mm around the edges). Like LSS, the HSS machine underwent a standard warm up cycle of roughly 1 hours where several blank powder layers were spread on the print platform. In order to achieve thermal stability before commencing the printing process, 50 standard blank layers were added to the base. This allowed enough time for the target build temperature to be achieved from the lamp moving across the build platform. When the build was complete, the heaters were turned off

Chapter 3

and the build, with the sintered parts and the excess unsintered powder (known as the powder cake), was left to cool in the machine overnight.

Post processing

In HSS, the powder bed was exposed to infrared radiation from the lamp which causes the excess powders around the parts to harden. To remove the excess powder, the parts were blasted with soda-lime glass beads (Honite grade 16, Gyson). The samples were stored in sealed bags, at room temperature, before they were used for testing.

3.5 Effect on the physical and mechanical properties

The physical and mechanical properties of the processed compositions were investigated in terms of dimensional accuracy, surface topography analysis (the methods were discussed in section 3.2.1), additive distribution within the sample, surface area analysis, characterisation of crystal structure, tensile properties and flexural properties. Due to the COVID-19 pandemic there were several restrictions in the laboratories therefore some of the characterisation investigations such as surface area analysis and additive distribution analysis, were not conducted on the LS and HSS Zn:PA12 compositions as well as LS 2:19.6:78.4 wt% Zn:HA:PA12 and HSS 2:39.2:58.8 wt% Zn:HA:PA12.

3.5.1 Dimensional accuracy

When designing patient specific implants any changes in the dimensional accuracy should be compensated for in the design. This is done in order to ensure more

Chapter 3

accurate restoration. The machines are calibrated to PA12 therefore it was expected that different materials may behave differently. The dimensional accuracy of 3-point bend bars was measured for all the compositions that were processed. The width, height and length of a set of 5 three-point bend bars for each composition, were measured in triplicates using Vernier callipers, accurate to 0.01 mm. The percent difference was calculated using (Equation 3.1). These values are useful for determining how the addition of the additives affect the accuracy of the parts.

$$\text{Percent difference (\%)} = \frac{\text{experimental value} - \text{exact value}}{\text{exact value}} \times 100$$

(Equation 3.1.)

3.5.2 Additive distribution

X-ray microcomputed tomography (MicroCT) is a non-destructive imaging technique that produces 3D images from 2D trans-axial slices²⁰⁸. MicroCT was used to analyse the distribution of additives throughout the sample. MicroCT uses a micro-focused X-ray tube to generate X-rays. The X-rays are directed towards the sample which were mounted on a rotating table. Radiation passes through the sample, the attenuation is converted into 2D images by the detector²⁰⁹. The sample is then rotated at a fraction of a degree where another projection image is taken, this is repeated until the sample has turned 360 ° to generate a series of projection images. The X-ray detector converts the incident X-ray photons into collectable electrical charges and digitalises them into 2D slice images that can be reconstructed to form 3D images²¹⁰. Low-density materials

Chapter 3

such as polymers absorb less X-rays and thus leads to poor imaging contrast or fainter images²¹¹, therefore, the information obtained showed mainly HA particles as it is more dense than PA12 thus can attenuate more X-rays.

The discs were placed on a stub and covered with clingfilm to prevent the discs from moving during the process. Clingfilm has low a density, any signals from the clingfilm was digitally filtered out during quantitative analysis of the final image. A 50 kV tube voltage was used. A 0.5 mm aluminium filter was placed in front of the X-ray source to remove lower energy X-rays. The pixel size and the elevation were both set to 10 μm . The rotation step was set to 0.7 $^\circ$. The image files were then reconstructed from TIF to JPEG using NRecon version 1.6.9.8 and the analysis was conducted on CTAn (3D.Suite, Bruker).

3.5.3 Surface area analysis

The surface area of an implant can influence the cell attachment and proliferation. Brunauer-Emmett-Teller (BET) is an adsorption-based technique typically used for measuring the surface area of porous solids and powders. Because the size of nitrogen atoms are well known, it is commonly used as the adsorbate in BET to measure surface area²¹². Firstly, the sample was weighed and a mass range of 0.04-0.08g was used. The sample was then placed under vacuum at 120 $^\circ\text{C}$ to remove gasses and water vapour that may interfere with the surface analysis. The sample was reweighed to obtain the degas weight of the sample. BET analysis was performed at boiling temperature of liquid nitrogen (-196.15 $^\circ\text{C}$). At this temperature the gas molecules can physically be adsorb on the solid surface. The analysis is conducted at

Chapter 3

a relative pressure (P/P_0) typically in the range of 0.05 to 0.30 which is assumed to be the relative pressure for monolayer adsorption²¹². The volume of gas adsorbed is measured at P/P_0 . As the pressure increases, more gas is adsorbed. The volume absorbed can be used to measure the gas molecules in the monolayer. The number of molecules/ atoms required to form a monolayer on the surface can be calculated using the BET equation (Equation 3.2.) , where n is the amount of adsorbent covering the surface at, n_m is monolayer capacity of adsorbed gas, P_0 is the saturation pressure of the nitrogen being adsorbed at the adsorption temperature, P is the pressure and C is the BET constant which is related to the energy of adsorption in the first adsorbed layer²¹³.

$$\frac{P/P_0}{n(1 - P/P_0)} = \frac{1}{n_m C} + \frac{C - 1}{n_m C} \left(\frac{P}{P_0} \right)$$

(Equation 3.2.)

From the BET equation, the surface area (a_s) can then be calculated using (Equation 3.3.) where σ_m is the molecular cross-sectional area, L is Avogadro constant and m is the mass of adsorbent²¹³.

$$a_s = \frac{n_m \cdot L \cdot \sigma_m}{m}$$

(Equation 3.3.)

Chapter 3

3.5.4 Characterisation of crystal structure

X-ray diffraction (XRD) was used in this research for phase identification of materials before and after LS and HSS to determine whether the printing processes effected the crystal structure of the materials.

Crystalline materials are composed of atoms with regular interatomic spacing. When conditions satisfy Bragg's law, X-rays interact with the sample to produce constructive interference, where two of equal amplitudes align to interact and produce a more amplified wave. The diffractions are processed and counted by a detector. The incident X-ray and the crystal plane interact at angle θ which is also equal to the angle between the crystal plane and the diffracted X-ray. The sample is scanned through a range of angle 2θ , which is angle between the incident X-ray and the diffracted X-rays (the angle of the detector).

The diffraction pattern was collected on a Bruker D2 Phaser. CuK_α X-ray wavelength was used with a nickel filter to suppress lower intensity K_β emission. The patterns were obtained from 10 to 80 ° angle 2θ , at a scan speed of 6 ° per minute and a step size of 0.02 °. DIFFRAC.EVA was used to match the diffraction pattern peak positions and intensities against the Inorganic Crystal Structure Database (ICDD).

3.5.5 Tensile properties

Orbital floor implants must be manufactured with adequate mechanical strength to support the orbital content¹⁴⁵. Orbital floor implants may be subject to tension and/or bending, so both tensile testing and 3-point bending were chosen.

Chapter 3

Tensile testing was carried out to determine the Young modulus, tensile strength and the elongation at break of the LS and HSS samples. A 5 kN load cell was used in the tensile test machine (H5K, Tinius Olsen) to test the samples in accordance with ASTM D638²¹⁴ type 1 at a rate of 1 mm/min. Five samples from each composition were tested. The gauge length, the thickness and the width were measured. Reflective tape was placed on either ends of the gauge to enable the laser extensometer to measure the spacing between the tapes and provide a value for the percentage of elongation.

3.5.6 Flexural properties

Three-point bending was used to evaluate the flexural modulus of the LS and HSS samples. A bar with a rectangular cross section, was placed on two supports and was loaded with a 2.5 kN load cell in a three point bend machine (LRX, Lloyd instruments) in accordance to ASTM D790²¹⁵ at rate of 0.1 mm/min. Five samples were tested for each material. The samples were also placed in a bag and picked at random. To ensure that all the data start from the same load, the samples were all preloaded with 5.0 N. The span was set to 50.0 mm and the test was stopped at 10.0 mm deflection.

3.6 Effect of steam sterilisation on the mechanical properties of PA12

Before the printed discs are used in cell culture and antimicrobial investigations, the samples have to be sterilised to reduce contamination. Steam autoclave kills microbes using heat in the form of saturated steam under intense pressure and is a preferred method to sterilise medical and surgical instruments^{216, 217}. It is important that the sterilisation technique does not cause any permanent changes to the mechanical

Chapter 3

properties as it can affect the performance of the samples. The effect of sterilisation on the mechanical properties of PA12 was investigated in collaboration with James Wingham, a PhD researcher at the University of Sheffield. The mechanical properties of PA12 were investigated under the different conditions present in steam autoclave such as high temperature, exposure to moisture/ water or a combination of heat and moisture. Nine sets of five tensile test samples laser sintered from 100 wt% PA12 were tested as printed, after steam autoclave (121 °C for 20 min) and after heat only autoclave (121 °C for 20 min). One set were tested immediately without drying, the second set were air dried for 7 days and the last set were oven dried at 50 °C for 7 days before tensile testing. An overview of the protocol is shown in Figure 3.5. More details can be found in the published paper²¹⁸.

The percentage water content at any given time (w_t) is calculated using Equation 3.4, where (m_t) represents the mass of the sample at time t and. (m_{dried}) is the dried mass of the sample:

$$w_t = \frac{m_t - m_{dried}}{m_{dried}} \times 100$$

(Equation 3.4.)

However, when there was no oven drying before tensile testing, the (m_{dried}) value was not available. Therefore, to calculate the (m_{dried}) (Equation 3.5.) was used. Where (w_{init}) is the initial water content which is assumed to be the same for all the samples because the samples were all fabricated on the same build and (m_{int}) is the initial mass of the samples.

Chapter 3

$$m_{dried} = m_{int} \left(\frac{100}{100 + w_{int}} \right)$$

(Equation 3.5.)

Once the value for (m_{dried}) was calculated, the value for (w_i) was calculated using (Equation 3.4.).

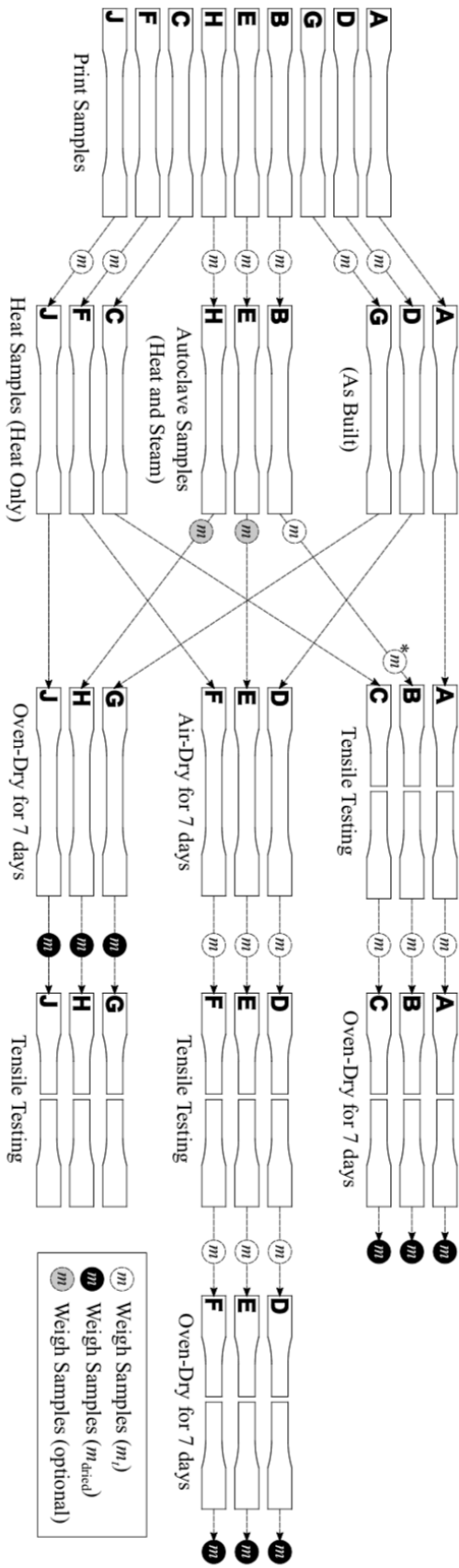


Figure 3.5 Overview of the effect of steam autoclave experiment protocol. The *m was taken due to an 18 h delay between autoclaving and tensile testing.

Chapter 3

3.7 Effect on the biocompatibility

The biocompatibility of the LS and HSS samples were investigated *in vitro* using MG 63 cells (Sigma-Aldrich[®]), a human osteosarcoma-derived osteoblastic cell line. The cells were cultured using the standard media recommended by the supplier: Minimum Essential Medium Eagle (MEME) (Sigma-Aldrich[®]) with 10 vol% fetal calf serum (FCS) (Sigma Aldrich), 1 vol% non-essential amino acids (NEAA) (Sigma-Aldrich[®]), and 1 vol% L-glutamine (LG) (Sigma-Aldrich[®]). In addition, 1 vol% penicillin-streptomycin (P/S) (Sigma-Aldrich[®]) was added to prevent bacterial contamination. An MG 63 (Passage number between 5 to 9) vial with roughly 2 million cells was removed from liquid nitrogen and thawed in a water bath at 37 °C for 30 seconds. The vial was transferred into 10 ml culture medium and centrifuged for 5 minutes at 1000 rpm and 20 °C to remove the dimethylsulfoxide (DMSO) from the thawing process. DMSO is a cryopreservation reagent used to prevent the formation of ice crystals, however it is toxic to cells when they are thawed. Therefore, it must be removed quickly to reduce the exposure of DMSO to the cells. After the centrifuge, the supernatant was removed, and the cell pellet was resuspended with 10 ml culture medium. The cells were then transferred into a T75 flask and incubated at 37 °C with 5 % CO₂. After 24 hours, the medium was replaced with 10 ml of fresh culture medium to ensure that the cell debris and the non-adhered cells were removed. The flask was placed back into the incubator and the medium was changed every two days until the cells reached 70- 80 % confluency and were ready for sub-culturing.

To sub-culture the cells, the media was removed, and the cells were washed three times with sterile phosphate-buffered saline (PBS) (Sigma-Aldrich[®]), a physiological

Chapter 3

buffer used to remove any remaining media. The cells were detached by placing 2 ml trypsin EDTA (Sigma-Aldrich[®]) and incubated for 3 minutes at 37 °C with 5 % CO₂. The cells were suspended with 4 ml culture media and centrifuged for 5 minutes at a speed of 1000 rpm. The supernatant was removed, and the cell pellet was resuspended with 10 ml culture medium. The cells were then counted using a hemocytometer to make up the media with the desired number of cells for further culturing, setting up an experiment or freezing the cells down.

3.7.1 Cell seeding density

Tissue culture plastic (TCPS) is commonly used as a standard control in experiments as its surface has been treated to allow for good surface attachment. However, we cannot use TCPS as a direct control in this experiment as there are differences in surface morphologies of the printed samples and TCPS, which affects both cell growth and attachment. Therefore 100 wt% PA12 was used as the main control. However, it is still useful to use TCPS as a general control to assess how well the samples are performing compare to the TCPS control. It is important to select the optimal seeding density in order to ensure that the cells do not reach over-confluency. When the cells became over-confluent on TCPS, cell clumping, or cell detachment can take place leading to a reduction in the accuracy of the reading. The optimal seeding density on TCPS was assessed by monitoring the rate of cell growth. In a 24 well plate, three repeats of 1×10^4 , 2×10^4 , 3×10^4 , 4×10^4 and 5×10^4 MG 63 cells in 0.5 mL medium were incubated for 7 days on TCPS. The medium was changed every two to three days. An optical microscope with a camera was used to image the cells at days 1,4 and 7.

Chapter 3

3.7.2 Cell viability and DNA quantification

Sterile LS and HSS discs were placed in 24 well plates and weighed down with sterile stainless steel rings with 15 mm outer diameter and a 14 mm inner diameter. Four discs were used for each composition, three discs were suspended with 0.5 ml culture medium containing cells made up as per section 3.7, 0.5 ml media was added to the discs from each composition. TCPS was used as control, sterile surgical grade stainless steel rings were placed in the wells for consistency. The experiment was conducted for 7 days. The media was replaced every two days.

In vitro cell viability of MG 63 cells cultured on LS and HSS discs were assessed using PrestoBlue™, a resazurin based reagent. Non-fluorescent resazurin reduces to strongly fluorescent resorufin in cellular respiration of viable cells²¹⁹. The cell viability was measured at day 1, 4 and 7. However, as with the characterisation investigations (section 3.5), the COVID-19 pandemic lead to restrictions in the tissue culture laboratory therefore, the cell viability was measured only at day 1 and 4 for LS 2:19.6:78.4 wt% Zn:HA:PA12 and HSS 2:39.2:58.8 wt% Zn:HA:PA12. On the following days, the media was removed, the cells were washed twice with sterile PBS, and 0.5 ml of 10 % PrestoBlue™ in culture medium was added to each well. In order to prevent light from breaking down the resazurin, the well plates were wrapped in aluminium foil and incubated for 30-75 min at 37 °C until the assay turned purple/pink in colour. 200 µl of the reduced solutions were pipetted into 96 well plates for the fluorescence to be read at 560 nm using Infinite M200 (Tecan). The fluorescence was normalised to fluorescence produced per minute.

Chapter 3

PicoGreen® dsDNA Assay Kit (ThermoFisher Scientific) was used as a tool to assess cell proliferation on the LS and HSS samples during *in vitro* cell culture. PicoGreen® is a dye which fluoresces when bound to double stranded DNA (dsDNA) ²²⁰. Unlike PrestoBlue™, it is destructive and requires lysed cells. Cell lysis was conducted by placing 250 µl of filter sterilised deionized water in each well to conduct a freeze thaw cycle. It involved placing the well plate in -80 °C for 24 hours before thawing at room temperature. During this process, cells swelled up and ruptured due to the formation of ice crystals and contract when thawed. A pipette was used to scrape the cells attached to the discs and homogenise the cell suspension. The well plate was placed back into -80 °C for another freeze-thaw cycle before DNA quantification.

The PicoGreen® assay was used according to the manufacturer's instructions. In brief: TE buffer (10 mM Tris-HCl, 1 mM EDTA, pH 7.5) was prepared by diluting the TE buffer concentrate to 1 in 20 with deionized water. The dsDNA standard curve solutions were prepared by diluting the DNA stock in TE buffer to make up concentrations ranging from 0-1000 ng/ml. The DNA standard curve concentrations were plated in 100 µl triplicates into a 96 well plate. The provided PicoGreen® stock solution was diluted 200 fold in TE buffer. The reagent was wrapped in aluminium foil to prevent photodegradation. In the 96 well plate 50 µl of distilled water was mixed with 50 µl of the cell suspension. Next, 100 µl of the PicoGreen reagent was added to the samples and the standard curve concentrations. The well plate was wrapped for 4 minutes at room temperature. The fluorescence was quantified using an excitation wavelength of 485 nm at an emission wavelength of 528 nm.

Chapter 3

3.8 Effect on the antibacterial properties

In this research the antibacterial activity of LS and HSS samples were assessed against gram-positive *staphylococcus aureus* (*S. aureus*).

3.8.1 Bacterial culture preparation

S235, a strain of *S. aureus*, was resurrected from frozen stock. A sterile inoculating loop was used to obtain a sample from frozen stock. The bacteria were then suspended in Brain Heart Infusion (BHI) broth and grown overnight in an incubator at 37 °C. The bacterial suspension was diluted to an absorbance of 0.05 at 600 nm in PBS.

3.1.1 Assessing bacterial growth

An experiment was conducted to determine the growth phases of the bacteria over time in PBS. Sterile discs were placed in universal tubes with 5 ml of bacterial suspension. There were 3 repeats for each composition. The universal tubes were placed into a shaking incubator at 200 rpm and 37 °C, overnight to ensure that the disc was submerged with the bacterial suspension. After 24 hours, the bacterial suspension was removed, and the discs were transferred into new universal tubes. The discs were then washed twice with PBS to remove unattached bacteria and resuspended in 5 ml PBS. The discs were shaken on a Vortex for 30 seconds to detach the bacteria attached to the discs.

Bacterial culture dilutions

Chapter 3

Bacterial culture dilutions were required to perform colony counting in order to count the number of bacteria that have been released from the discs. Serial dilutions were performed at 10^0 , 10^{-1} , 10^{-2} , 10^{-3} and 10^{-4} were plated on BHI agar plates (Figure 3.6) to ensure that single colonies could be counted. The bacteria in PBS were plated on agar plates at dilution of 10^{-4} . Two bacterial dilutions were plated up from each disc. The plates were placed into an incubator overnight. The following day, the bacterial colonies were counted. The number of bacterial colonies were counted at the lowest dilution where single colonies could be counted.



Figure 3.6 Agar plate dilutions for colony counting.

Chapter 3

Bacterial colony calculation

The number of colony forming units per ml in the original culture can be calculated by (Equation 3.6.).

$$\text{Colony forming units per ml (CFU/ml)} = \frac{\text{no. of colonies} \times 10^{-(\text{counting dilution})}}{\text{volume of plated dilution}}$$

(Equation 3.6.)

The raw numbers for CFU were converted into log scale and the statistical analysis was carried out as per section 3.9.

3.9 Data analyses

All the data analyses were performed on GraphPad Prism version 7 for Mac OS X. An unpaired T-test was used to analyse whether two sets of samples are statistically different from one another. For tests with three or more sets of samples, one-way ANOVA followed by Tukey's multiple comparison was used.

4 Results and discussion: bioactive ceramic: polymer compositions

This Series was focused on determining the effect of hydroxyapatite (HA) when added to the base polymer PA12 at different wt% and processed on laser sintering (LS) and high speed sintering (HSS). This chapter will discuss the results obtained based on the methodology introduced in Chapter 3. The objectives for this chapter are:

- To investigate the processibility of varying compositions of HA:PA12 in order to establish whether there was an upper limit for the amount of HA which could physically be processed.
- To determine the effect of HA on the physical and mechanical properties for all the compositions that could be processed.
- To identify if the sterilisation technique has an effect on the mechanical properties of the base polymer.
- To determine whether the addition of HA has an impact on the biocompatibility of the processed parts.
- To select the optimal HA:PA12 composition for further investigations into the addition of an antimicrobial agent.

Chapter 4

4.1 Processability

The first objective is to investigate the powder morphology to check for particle sphericity, size (where the optimal particle size ranges between 20- 80 μm) and surface roughness as these factors impact powder processability and cell adhesion. Then the thermal properties of the powder composites were investigated to assess whether the addition of HA affects the melt characteristics of the base polymer which in turn can impact its processability.

4.1.1 Powder morphology

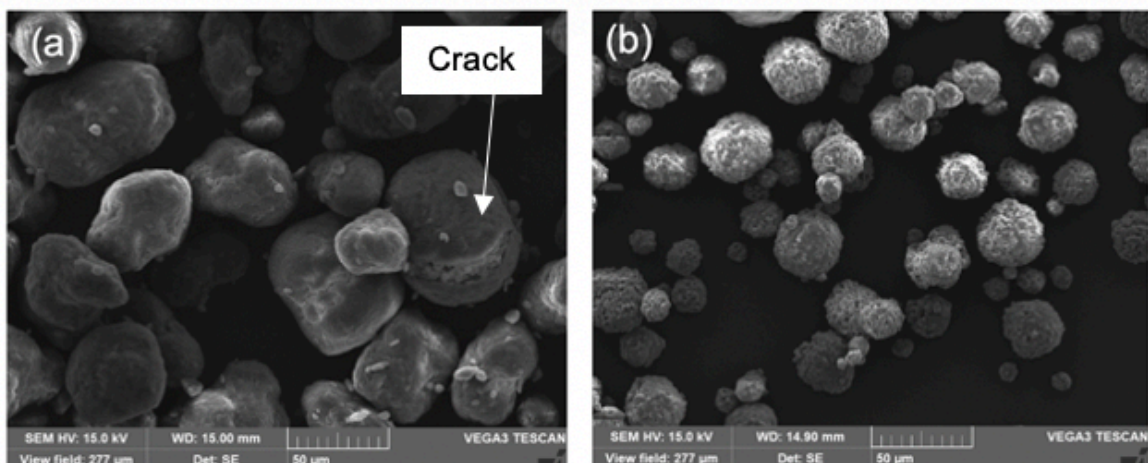


Figure 4.1. Secondary electron (SE)- Scanning electron microscopy (SEM) micrographs of (a) polyamide 12 and (b) hydroxyapatite powders.

The morphology of the powders was assessed using scanning electron microscopy (SEM) as per the method in section 3.2.1. Figure 4.1 (a) shows an SEM micrograph of PA12 particles. The PA12 particles have a near spherical shape and are within the optimal sintering range. The surfaces of PA12 particles appeared relatively smooth with some PA12 particles showing cracks. It has been reported that cracking can

Chapter 4

exists in virgin powders however, aged powders exhibit an increase in cracking as the powders are kept at high temperatures from previous processing²⁰⁶, indicating that cracking is not likely to have a significant effect on the processability. Based on these observations there is no obvious reason why the morphology of PA12 should prevent effective processability.

The HA particles, shown in Figure 4.1 (b), have a spherical shape. The HA particles were generally smaller than the PA12 particles nonetheless they are within the acceptable range for sintering on LS and HSS. HA particles show a higher surface roughness which has been reported to yield a higher degree of cell adhesion and influence proliferation of osteoblasts as it increases the surface area of the samples²²¹⁻²²⁴. As mentioned in the literature, section 2.5.2, a higher surface area is likely to be advantageous as it provides more space for cell attachment which is predicted to be advantageous in this research. Like PA12, the morphology of HA is also not likely to prevent good processability.

4.1.2 Thermal analysis

Thermal analysis of the powders was conducted using differential scanning calorimetry (DSC). As mentioned in section 2.6.1, PA12 has a large sintering window which permits the use of a large variety of processing temperatures²²⁵ on LS and HSS. It is important that when an additive is mixed with PA12, the sintering window does not become smaller. A decrease in the sintering window makes the material more challenging to process as more precise processing parameters would be required.

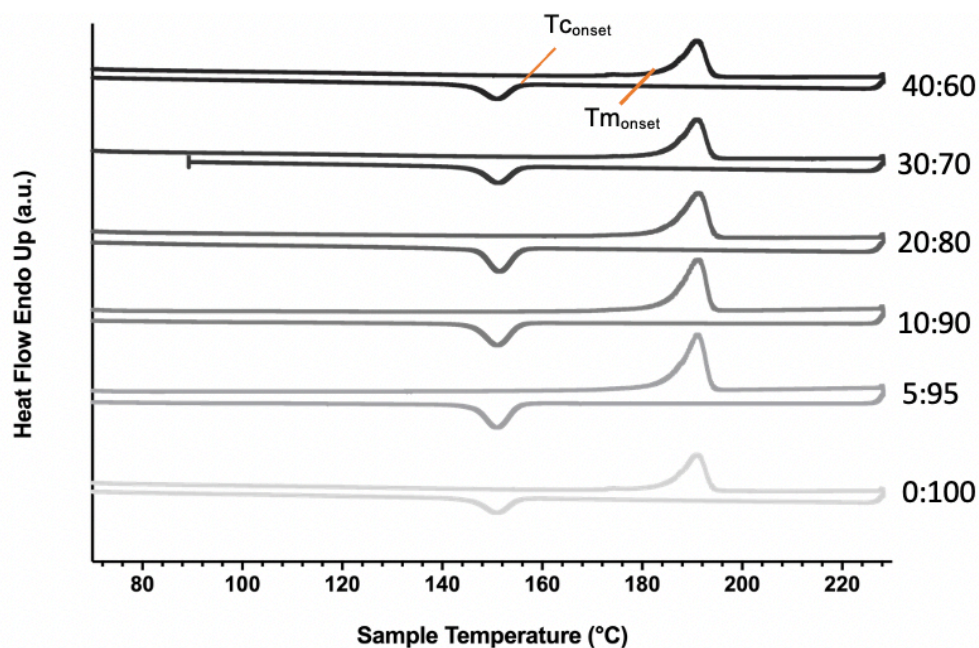


Figure 4.2. Differential scanning calorimeter (DSC) curves of hydroxyapatite: polyamide 12 (HA:PA12) powder compositions, where T_{Conset} is crystallisation temperature onset and T_{monset} is melting temperature onset

Table 4.1. Melt characteristics of hydroxyapatite: polyamide 12 (HA:PA12) powder compositions.

HA:PA12 (wt%)	Melting temperature onset (°C)	Melting temperature (°C)	Crystallisation temperature onset (°C)	Crystallisation temperature (°C)	Processing window (°C)
0:100	181	192	158	150	23
5:95	179	192	158	150	21
10:90	181	192	157	150	24
20:80	181	192	158	151	23
30:70	181	192	158	150	23
40:60	181	192	158	150	23

Chapter 4

Figure 4.2 and Table 4.1 shows the DSC curves and the melt characteristic values, respectively, for the HA:PA12 compositions. All the compositions show a melting and a crystallisation peak with a clear gap between the two peaks. The values for the melting temperature onset ($T_{m\text{onset}}$) range from 179 to 181 °C, the melting temperature (T_m) was 192 °C for all compositions, the crystallisation temperature onset ($T_{c\text{onset}}$) range from 157 to 158 °C and the crystallisation temperature (T_c) range from 150 to 151. The sintering window ranged from 21 to 24 °C, indicating that HA had a marginal effect on the processing window of the material. The values obtained here are comparable to the values reported in the literature for virgin PA12 powder^{184, 226}. HA does not melt in the temperature range analysed as it has a high melting temperature of 1650 °C^{227, 228}, thus it would not be expected to have a big influence on the melt characteristics of the material. Despite slight differences in values between the different compositions, the LS and HSS systems are not accurate enough to input such small changes, indicating that the default processing parameters (for processing PA12 on LS and HSS) can be used in the initial printing trials to process the HA:PA12 compositions.

4.2 Printability

Although the thermal properties did not change, it is still expected that higher concentrations of HA are likely to affect the printability as well as the physical and mechanical properties of the material^{176, 177}. Tensile test samples, 3-point bend bars and discs were printed on LS and HSS using the selected HA:PA12 compositions (as per section 3.1.4).

Chapter 4

4.2.1 Laser sintering

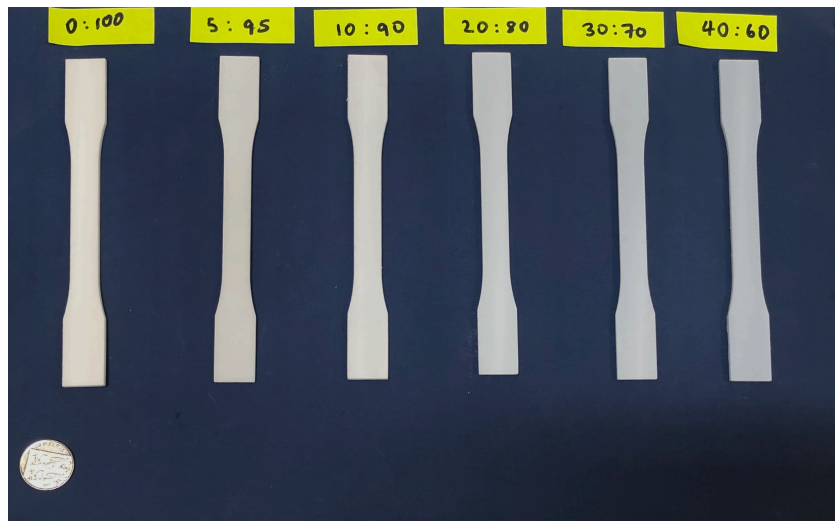


Figure 4.3. Laser sintered tensile test bars made of different wt% of hydroxyapatite: polyamide 12 (HA:PA12). Scale bar= 10p coin.

All the tensile test samples (Figure 4.3) and three-point bend bars were successfully printed by LS, using all the compositions. However, the discs were not successfully printed at 30:70 and 40:60 wt% HA:PA12. At these compositions, some discs curled at the edges during the LS process. The curled discs were dislodged from their position and dragged across the powder bed by the re-coater blade leading to build termination. Often, curling is caused by early crystallisation due to a low bed temperature^{195, 200, 229}, indicating that HA, has an effect on the processability in LS. The reason why the mechanical test specimens were printed successfully but not the discs is not entirely known however one hypothesis is that as the discs are smaller than the tensile test samples therefore less energy from the laser is delivered to sample leading them to cool down at a faster rate. The edges always cool down faster than the centre of the part due to the cold un-sintered powder surrounding it. It is predicted that the steep thermal gradient between the edges and the centre of the part

Chapter 4

gives rise to non-uniform expansion and contraction leading to curling²³⁰⁻²³². A simpler explanation may be that the tensile test specimens and 3-point bend bars have a larger mass than the discs, making them more difficult to drag away in the case of minor curling.

Another reason for the failed discs at higher wt% of HA, is hypothesised to be due to the decrease in polymer particles available to absorb and transmit the energy from the laser. It may reduce the coalescence between polymer particles as there are more HA particles in the way, potentially leading to heterogenous nucleation²³³. In addition, the decrease in polymer particles can result in less energy being absorbed by the polymer grains, potentially leading to poor layer adhesion and thus build failure. Further work is needed to investigate this theory however, it is outside the scope of this research. Due to the build failures at 30:70 and 40:60 wt% HA:PA12, these compositions were not used in any further experimentations, meaning only LS compositions of 20:80 wt% HA:PA12 or below will be included in the remainder of this thesis.

Chapter 4

4.2.2 High speed sintering

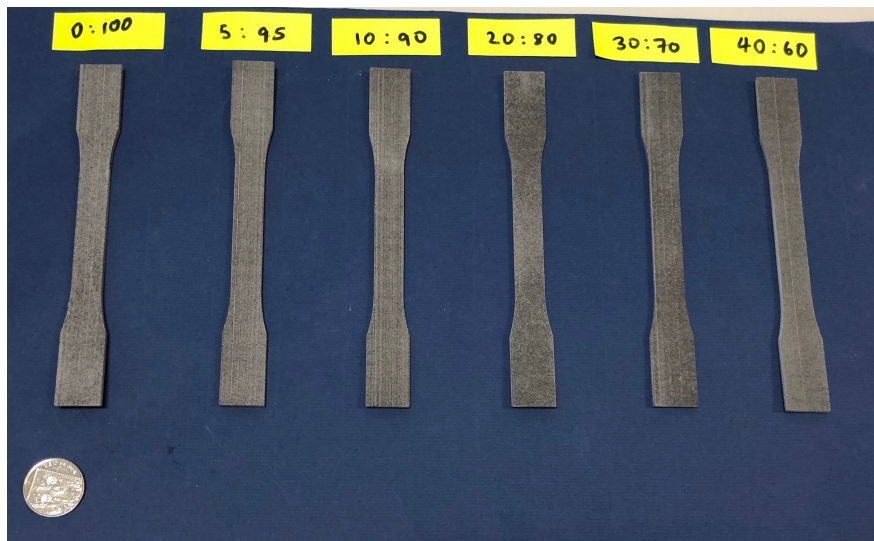


Figure 4.4. High speed sintered tensile test bars made of different wt% of hydroxyapatite: polyamide 12 (HA:PA12). Scale bar= 10p coin.

The HSS of HA:PA12 samples is novel thus far and has not been explored in literature. The results showed that all the tensile test samples (Figure 4.4), 3-point bend bars and discs were printed successfully by HSS using the default processing parameters discussed in section 3.4.2. All the samples were grey/black in colour which was due to the Radiation Absorbing Material (RAM) ink used in the HSS process. The range of compositions which could successfully be built was better in HSS than LS. This was likely to be due to the differences in sintering between the two techniques, where in HSS the infrared lamp passes over the whole powder bed which also heats the surrounding powder, leading to a lower thermal gradient between the edges and the centre of the part. As discussed in section 4.2.1, the thermal gradient can affect the curling and shrinkage of the part thus a reduction in thermal gradient can decrease part failure. Additionally, the energy input is slower which may give more time for the

Chapter 4

particles to melt and coalesce. Unlike LS, no HA:PA12 compositions processed on HSS, were excluded from further experimentations in this thesis.

4.3 Effect on the physical and mechanical properties

The second objective was to assess the effect of the additive on the physical and mechanical properties of the parts produced. The physical properties were investigated in terms of dimensional accuracy, surface topography analysis, additive distribution, surface area analysis and characterisation of the crystal structure. The mechanical properties were assessed by tensile testing and 3-point bending.

4.3.1 Dimensional accuracy

To assess whether the dimensional accuracy was affected by the addition of HA, the dimensions of 3-point bend bars were measured for all the compositions that were processed. The percentage difference was calculated by comparing the values of the samples to the exact values of the CAD dimensions as per Figure 3.2. This information is useful because when real-life parts are produced any significant changes in dimension should be compensated for in the design to ensure a more accurate restoration.

Chapter 4

Table 4.2. Part dimensions of 3-point bend bars composed of different wt% of hydroxyapatite: polyamide 12 (HA:PA12). The expected values were defined in the CAD model. The measurements were conducted on 5 samples.

HA:PA12 (wt%)	Width (mm)	SD	% difference	Thickness (mm)	SD	% error	Length (mm)	SD	% difference
CAD	13.00	-	-	4.00	-	-	60.00	-	-
0:100	13.15	0.10	1.16	4.14	0.05	3.42	60.13	0.05	0.22
5:95	12.68	0.07	2.46	4.24	0.05	5.97	59.80	0.04	0.33
10:90	12.70	0.06	2.34	4.20	0.06	4.95	59.87	0.04	0.22
20:80	12.71	0.05	2.21	4.17	0.05	4.30	59.84	0.08	0.27

Table 4.2 shows the mean part dimensions of 5 LS samples. The width ranges from 12.68 to 13.15 mm, the thickness ranges from 4.14 to 4.24 mm and the length ranges from 59.80 to 60.13 mm. The variance in values for each composition is narrow which shows a homogeneity in production across the prints. The percent difference for the LS samples ranges from 1.16 % to 2.46 % for the width, 3.42 % to 5.97 % for the thickness and 0.22 to 0.33 % for the length. The addition of HA shows a small effect on the accuracy of the parts. As mentioned in section 2.5.2, shrinkage in LS and HSS is well known and can be compensated for in the CAD file. Therefore, when designing real-life parts, test prints are required to check for shrinkage compensation to add into the original CAD file. The results show that implants fabricated from these materials at these processing parameters are likely to have a high dimensional accuracy. Nonetheless, this must be explored further as orbital floor implants have complex shapes which can affect the printability.

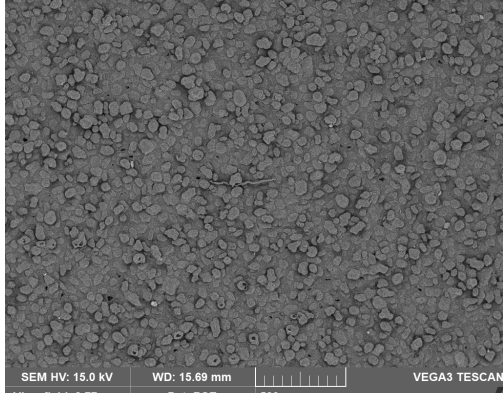
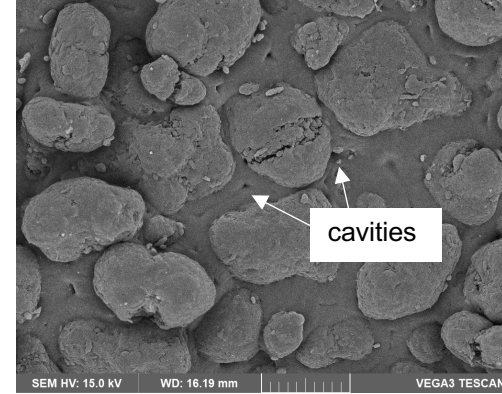
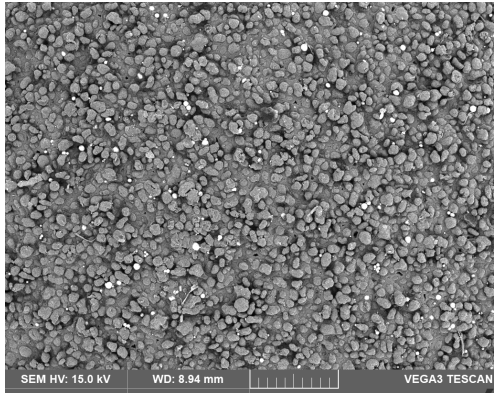
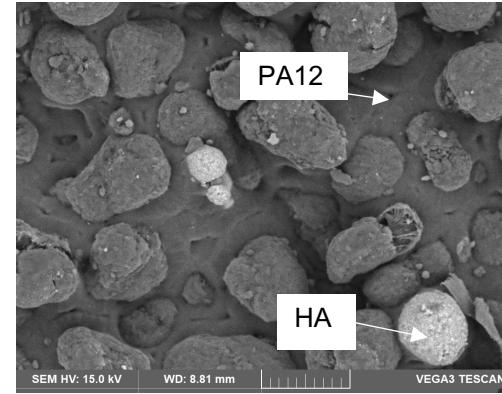
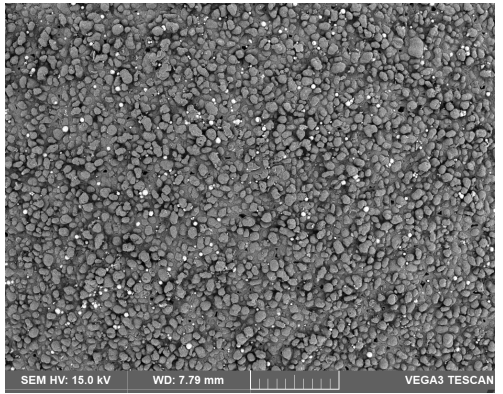
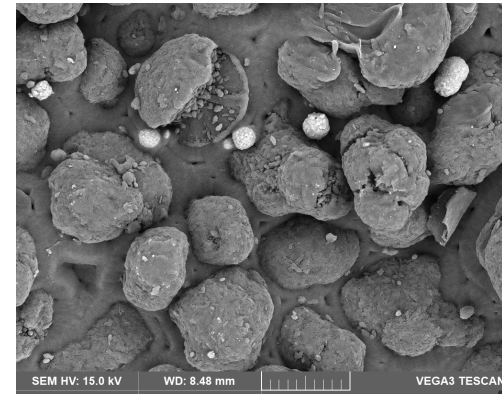
Table 4.3. Part dimensions of high speed sintered 3-point bend bars composed of different wt% of hydroxyapatite: polyamide 12 (HA:PA12). The expected values were defined in the CAD model. The measurements were conducted on 5 samples.

HA:PA12 (wt%)	Width (mm)	SD	% difference	Thickness (mm)	SD	% error	Length (mm)	SD	% difference
CAD	13.00	-	-	4.00	-	-	60.00	-	-
0:100	12.72	0.06	2.18	3.77	0.11	5.85	58.49	0.11	2.52
5:95	12.64	0.09	2.78	3.85	0.07	3.78	58.35	0.23	2.76
10:90	12.70	0.04	2.29	3.81	0.06	4.87	58.30	0.08	2.83
20:80	12.82	0.06	1.37	3.87	0.05	3.17	58.60	0.16	2.33
30:70	12.89	0.05	0.87	3.91	0.04	2.15	58.64	0.18	2.26
40:60	12.80	0.05	1.57	3.86	0.06	3.40	58.59	0.09	2.35

The part dimensions of 3-point bend bars processed by HSS are shown in Table 4.3. The width ranges from 12.64 to 12.89 mm, the thickness ranges from 3.77 to 3.91 mm and the length ranges from 59.30 to 58.64 mm. Like the LS samples, the production was relatively homogeneous for each composition as shown in the narrow variance in values. The percent difference for the average width ranges from 0.87 % to 2.78 %, 2.15 % to 5.85 % for the thickness and 2.33 % to 2.76 % for the length. The percent difference of HSS samples was slightly higher than that of LS samples which was expected as LS is a commercial machine while the HSS machine is still under development. Nonetheless, when designing real-life parts, test prints are required to add the shrinkage compensation into the original CAD model. In addition, the printing of complex shapes must be explored further.

Chapter 4

4.3.2 Surface topography analysis

HA:PA12 (wt%)	x100 (500 μm scalebar)	x1000 (50μm scalebar)
0:100		
5:95		
10:90		

20:80

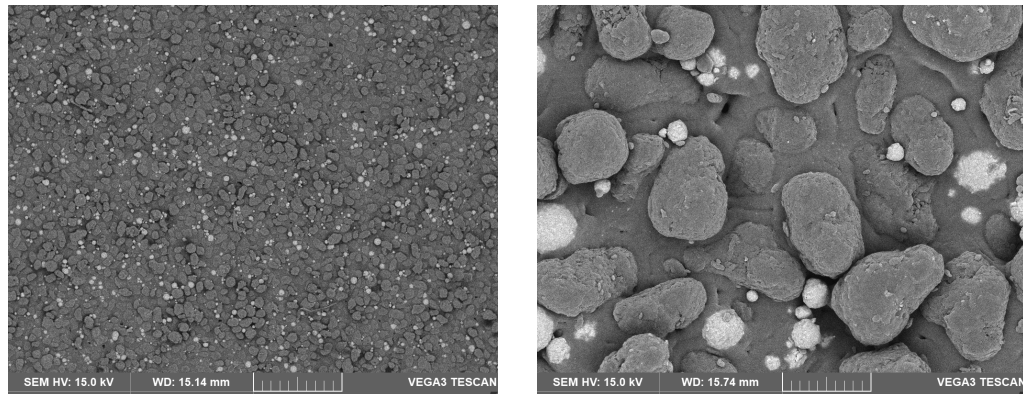


Figure 4.5. Backscattered electron (BSE)- Scanning electron microscopy (SEM) micrographs of laser sintered discs composed of different wt% hydroxyapatite: polyamide 12 (HA:PA12) taken at x100 and x1000 magnifications.

Homogeneous distribution of additives on the surface is generally accepted to be a main priority. Figure 4.5. shows backscattered electron (BSE)-SEM micrographs of LS discs. The PA12 particles are shown in grey. Some PA12 particles appeared to have fully melted while others did not reach full degree of particle melt. As mentioned in section 2.7.1, this is known as 'coring'. An advantage to the cored spherulites is the surface irregularities which leads to a higher degree of surface roughness. Implants with a textured surface have an increased surface area, which is believed to be advantageous in bone reconstruction applications as it increases bone-to-implant contact (BIC)¹⁹⁷⁻¹⁹⁹ thus potentially increasing implant stability.

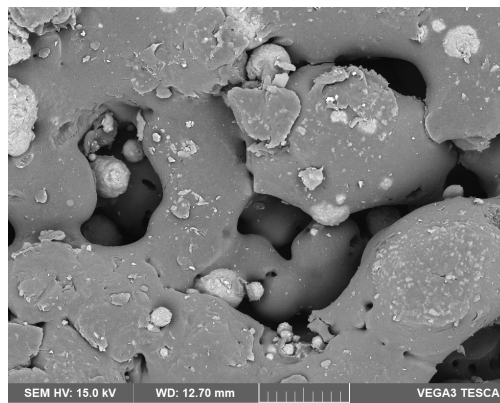
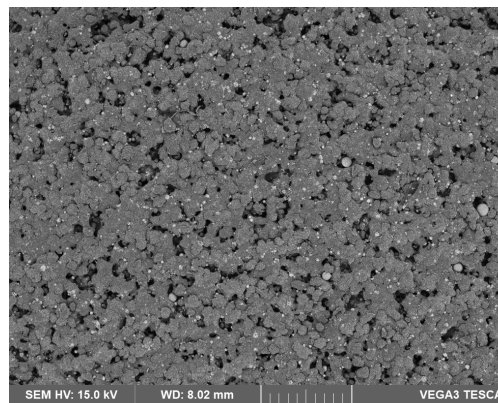
HA particles have a brighter intensity than PA12 particles which correlates to HA's higher average atomic number. The HA particles were found to have retained their shape after sintering as the processing parameters are not high enough to melt the ceramic particles. The PA12 particles melted around the HA particles which held them

Chapter 4

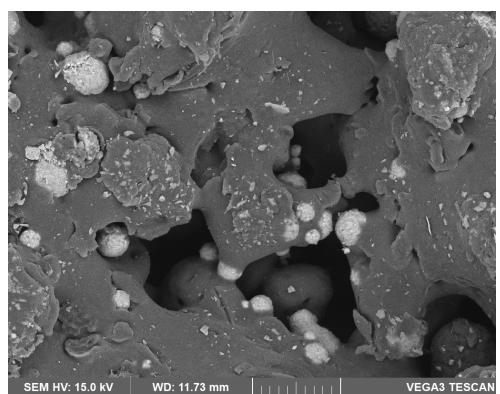
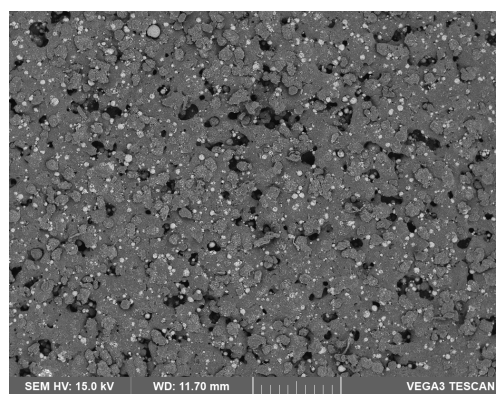
in position, acting like a 'binder'. The x100 magnification images show that HA is relatively well distributed on the surface of the samples with no obvious agglomerations, indicating that the samples are likely to have an even surface interaction with the cells. Additionally, the 100x micrographs indicate that as the concentration of HA increases, more HA is observed at the surface, as would be expected. All the compositions show irregular surface cavities which was also observed by Kinstlinger *et al.*¹³⁵, likely increasing the surface area of the samples and in turn increasing BIC.

HA:PA12	x100	x1000
(wt%)	(500 μm scalebar)	(50 μm scalebar)
0:100		
5:95		
10:90		

20:80



30:70



40:60

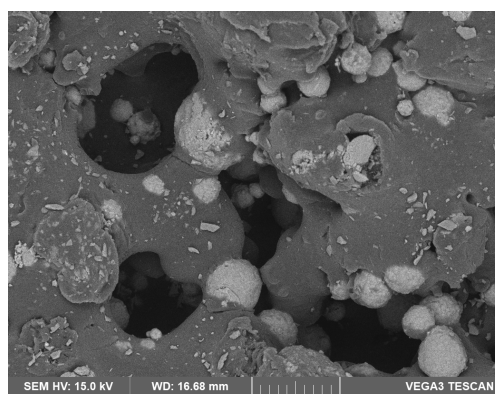
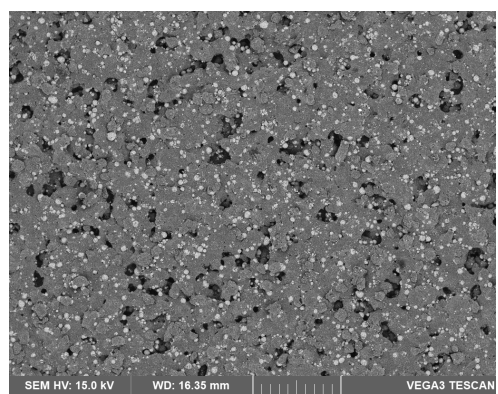


Figure 4.6. Backscattered electron (BSE)- Scanning electron microscopy (SEM) micrographs of high speed sintered discs composed of different wt% of hydroxyapatite: polyamide 12 (HA:PA12) taken at x100 and x1000 magnifications.

Chapter 4

The BSE-SEM micrographs shown in Figure 4.6 are of HSS specimens. HSS samples show less particle coring than LS samples, resulting in smoother surfaces. The HSS samples have a relatively textured surface which is mainly predicted to be a result of the ink (the lighter specks attached to the particles) used during the HSS process. This may be advantageous as it increases the effective surface area, which could result in potentially higher BIC. As expected, the 100x micrographs show that as HA increases, more HA is observed at the surface. The HSS samples have higher porosity compared to LS samples, which may be due to the incomplete melting of the PA12 particles. This is a potential indication that not enough energy was put into HSS to fully melt the particles. The main drawback to increased porosity is the general reduction in mechanical properties²³⁴⁻²³⁷, as pores act as stress concentration sites where cracks can initiate and propagate. However, sufficient porosity has been found to promote bone ingrowth which has been known to increase implant stability^{235, 238, 239}.

Like the LS samples, the HA particles also retained their shape in HSS and were reasonably well distributed on the surface, likely leading to a homogeneous interaction between the surface of the samples and the cells. The micrographs show that the addition of HA increases the porosity which is likely to be advantageous as osteoblasts prefer to grow and proliferate on pore sizes between 100 to 350 μm ^{235, 240-243}, to allow for cell migration, ingrowth and vascularisation. This is roughly similar to the range determined here for 5-40 wt% HA:PA12. The HSS samples appear to have superior porosity than LS samples, indicating that cell viability is likely to be higher on HSS samples. However, increased porosity is predicted to decrease the mechanical properties of the samples. Thus, LS samples are likely to have superior mechanical properties over HSS samples.

4.3.3 Additive distribution

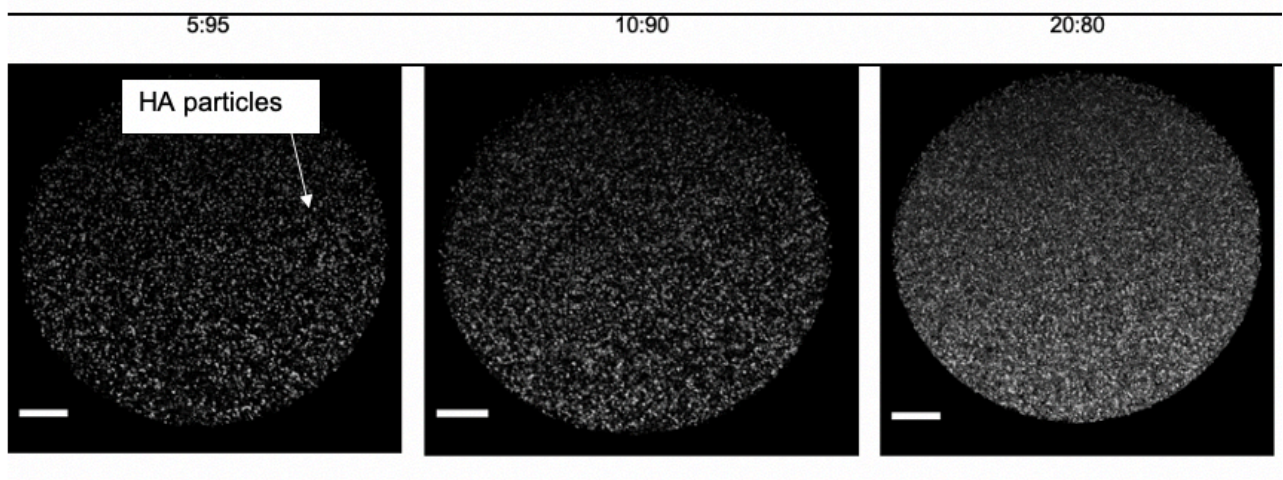


Figure 4.7. 2D cross-sectional images of laser sintered samples composed of different wt% of hydroxyapatite: polyamide 12 (HA:PA12) obtained by micro-CT scanning. Scale bar= 2 mm.

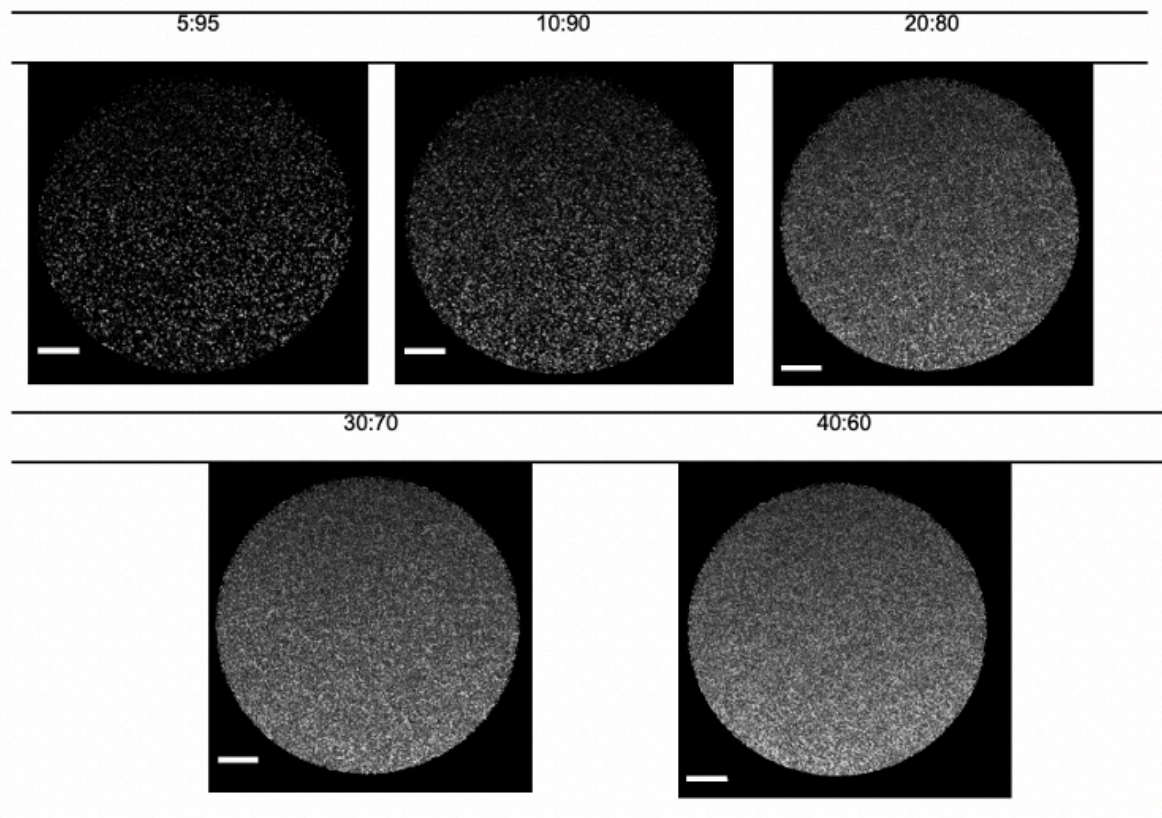


Figure 4.8. 2D cross-sectional images of high speed sintered samples composed of different wt% of hydroxyapatite: polyamide 12 (HA:PA12) obtained by micro-CT scanning. Scale bar= 2 mm.

Additive distribution

Figure 4.7 and Figure 4.8 show 2D cross-sectional images of LS and HSS samples, respectively, obtained by non-destructive X-ray computed micro-tomography (MicroCT) to examine the distribution of additives within the samples. The white specs are the HA particles. The results show that HA is well distributed throughout the LS and HSS samples without any obvious agglomerations, demonstrating that any effect that HA may have on the mechanical properties is predicted to be evenly distributed through the geometry.

4.3.4 Surface area analysis

The specific surface area greatly influences the way osteogenic cells interact with the surface of the scaffold^{155, 244-246}. The specific surface area of the samples was measured by Brunauer-Emmett-Teller (BET) nitrogen adsorption technique as per the method in section 3.5.3.

Chapter 4

Table 4.4. Brunauer-Emmett-Teller (BET) nitrogen adsorption measurements of the specific surface area of laser sintered and high speed sintered samples composed of different wt% of hydroxyapatite: polyamide 12 (HA:PA12).

HA:PA12 (wt%)	Specific surface area (m ² /g)	
	LS	HSS
0:100	20.7	26.4
5:95	21.5	117.6
10:90	40.7	117.7
20:80	77.6	136.4
30:70	-	72.0
40:60	-	121.3

The results in Table 4.4 show the specific surface area values for LS and HSS samples. The values range from 20.7 to 77.6 m²/g for LS samples. The results demonstrate an increase in specific surface with the increase in HA. Various studies comparing the performance of HA based bone substitutes found that materials with increased surface area show greater osseointegration^{155, 156, 247}. The literature theorises that the mechanism of hydroxyapatite induced bone differentiation is caused by the adsorption of native bone morphogenetic proteins (BMPs), osteoblasts and bone marrow cells from the body fluid to the HA-based biomaterial²⁴⁸⁻²⁵⁰. Therefore, materials with a larger surface area have the capacity to adsorb more bone BMPs which can trigger a higher degree of bone formation. BioOss®, a commercial bovine bone substitute with high osteoconductive properties, has been found to have a specific surface area ranging between 60 up to 100 m²/g¹⁵⁵⁻¹⁵⁸. LS 20:80 wt% HA:PA12 had a surface area within the same range indicating that this composition is

Chapter 4

likely to trigger a higher degree of bone formation similar to that of BioOss®. The increase in surface area with the addition of HA was likely to be due to the rougher surfaces of HA particles, as discussed in section 4.1.1.

The values for the specific surface area of HSS samples range from 26.4 to 136.4 m²/g. The results show that the addition of HA led to an increase in specific surface area. However, as the HA content increases there was not a linear increase in specific surface area indicating that higher quantities of HA did not affect the specific surface area of the material. The values for 5:95 wt% HA:PA12 up to 40:60 wt% HA:PA12 were within or marginally higher than the values of BioOss®¹⁵⁵⁻¹⁵⁸, denoting that these samples are predicted to trigger a higher degree of bone formation. It is reasonable to expect the samples to have a higher potential in triggering bone formation. The large increase in specific surface area, with the addition of HA, was predicted to be due to the increase in porosity as seen in section 4.3.2.

4.3.5 Characterisation of crystal structure

X-ray diffraction (XRD) was used to characterise the powders before processing and after processing to gain a deeper understanding of the chemical composition of the material after processing. It was critical that the crystal structure of the HA does not alter during the processing of the materials as it can impact its osteoconductive properties.

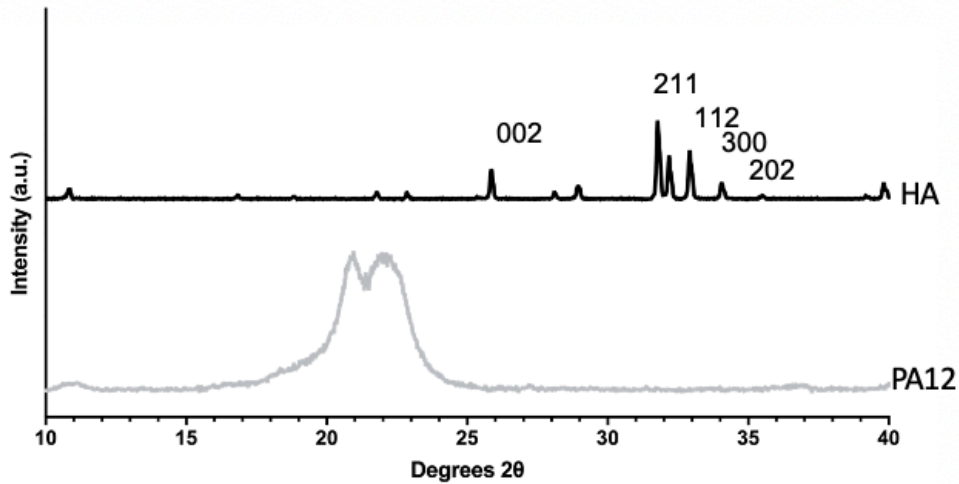


Figure 4.9. Powder X-ray diffraction (XRD) patterns of polyamide 12 (PA12) and hydroxyapatite. (HA) before 3d printing. The XRD pattern of HA is presented with Miller indices (hkl) showing crystal family of planes for each diffraction peak.

The diffraction patterns of the PA12 and HA powders before processing are shown in Figure 4.9. The diffraction patterns agree with the literature which suggests that HA should produce strong peaks at around $2\theta = 25.90, 31.80, 32.91, 32.95, 34.17^\circ$. The orientation of atomic planes in the crystal lattice of HA are represented by the Miller indices (hkl) (002), (211), (112), (300) and (202)^{176, 251-253}. PA12 powder has two crystalline peaks at $2\theta = 20.97$ and 22.27° which is similar to previous studies^{176, 254,}

255.

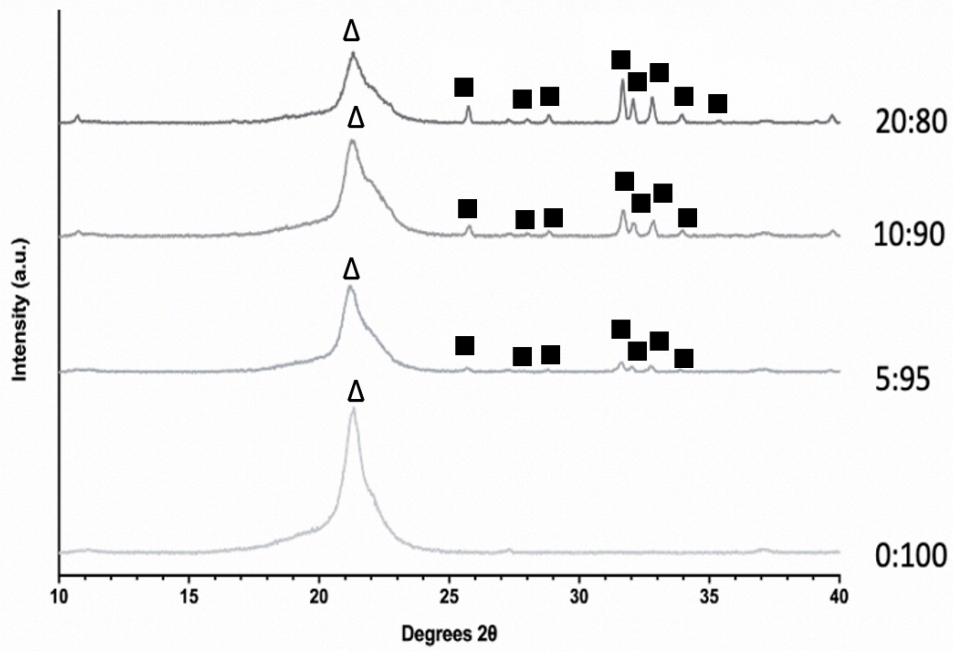


Figure 4.10. XRD patterns of laser sintered discs composed of different wt % of hydroxyapatite: polyamide 12 (HA:PA12). Where Δ represents PA12 and \blacksquare represents HA.

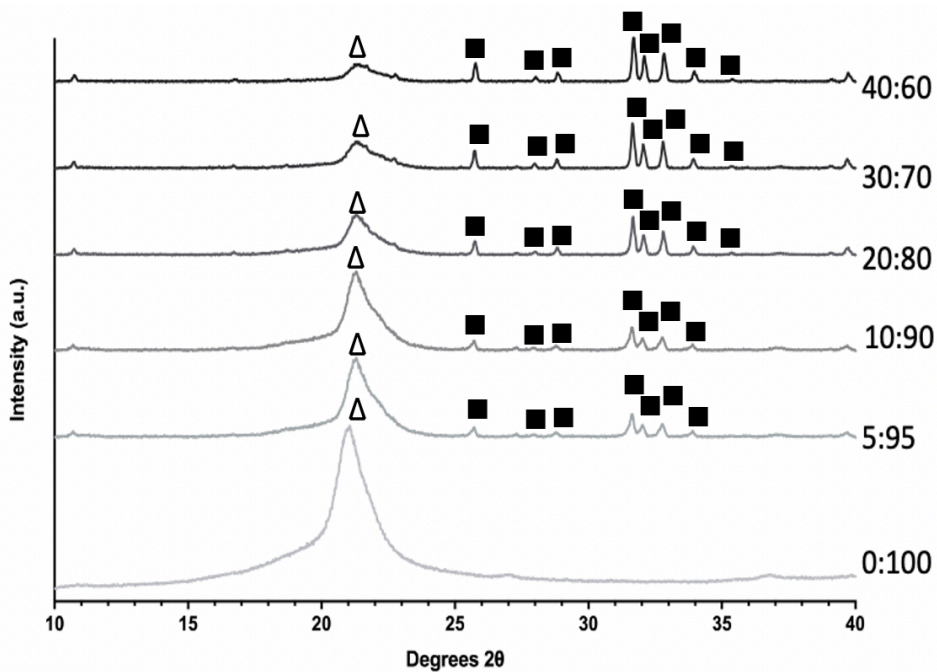


Figure 4.11. XRD patterns of high speed sintered discs composed of different wt % of hydroxyapatite: polyamide 12 (HA:PA12). Where Δ represents PA12 and \blacksquare represents HA.

Chapter 4

The diffraction patterns for the compositions processed by LS and HSS are shown in Figure 4.10 and Figure 4.11, respectively. The diffraction pattern of PA12 after LS and HSS show a single peak at $2\theta = 21.38^\circ$ rather than two peaks at $2\theta = 20.97$ and 22.27° , as seen by PA12 powder before processing (Figure 4.9), indicating that the LS and HSS processes change the crystal structure of PA12. This is a known phenomenon, as mentioned in section 2.6.1, when PA12 is heated from room temperature to its melting point, the triclinic phase of PA12 is replaced by the pseudo-hexagonal crystalline structure. The triclinic phase of PA12 shows two distinct diffractions, as seen by Figure 4.9. During melting, the two diffractions merge into a single broad peak¹⁷⁶. No change is observed to the crystal structure of HA after processing by LS. XRD patterns revealed that the crystalline structure of HA remained the same before and after LS. As with the melt characteristics results in section 4.1.2, it was expected that the LS and HSS processes would not change the crystal structure of the HA as it has extensively high melting temperature, indicating that the osteoconductive properties of HA are not likely to be affected by the printing processes.

4.3.6 Tensile properties

The orbital floor is non-loadbearing therefore, the reconstruction materials used in orbital floor repair are not required to have high mechanical properties nonetheless, the material must possess sufficient mechanical resistance to support the orbital content, which weigh $42.97 \pm 4.05 \text{ g}^{33}$. In addition, during the implantation process, the implant may be subject to bending. The tensile properties and the flexural modulus of LS and HSS samples were tested.

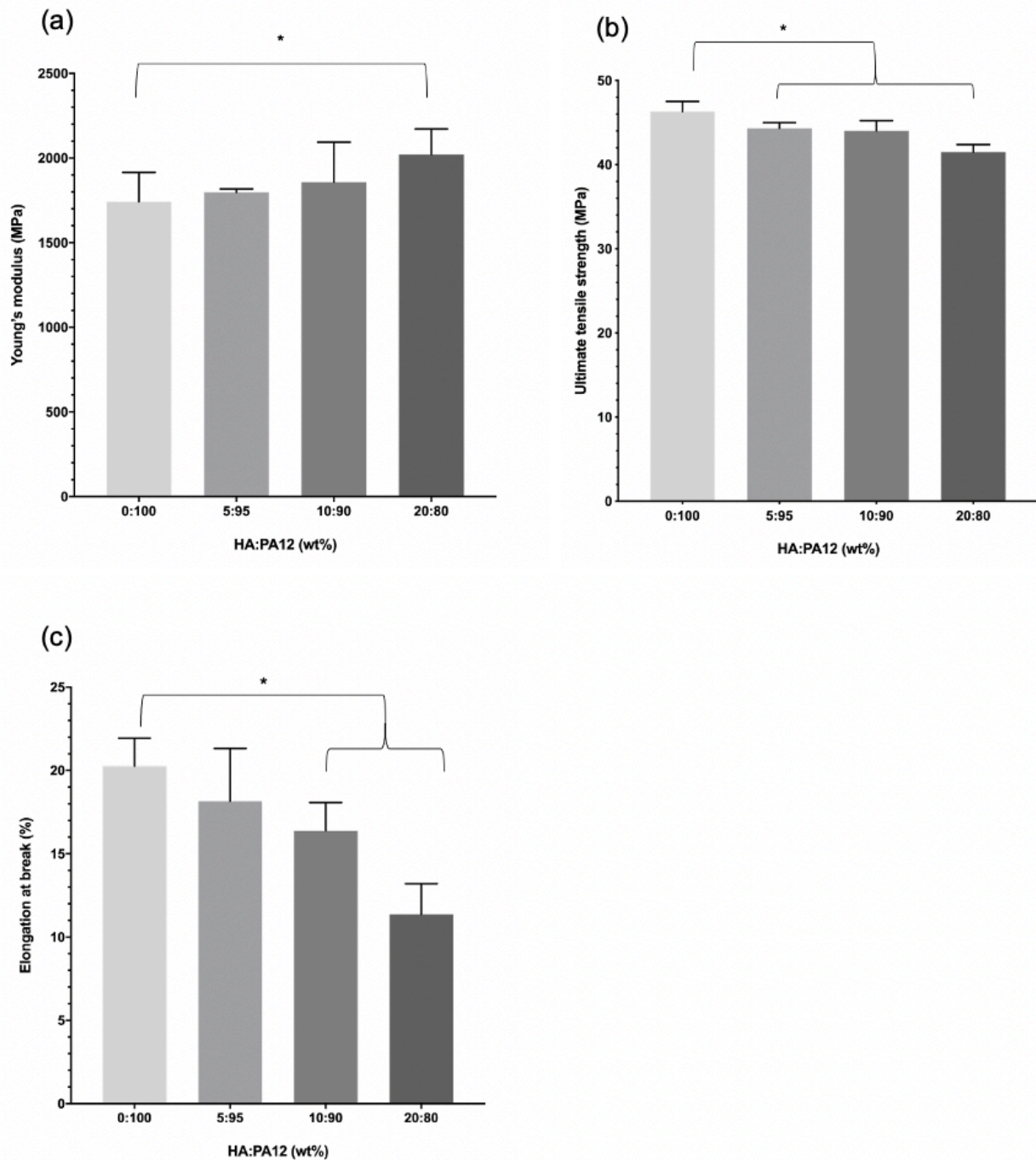


Figure 4.12. The tensile properties: (a) Young's modulus (E), (b) Ultimate tensile strength (σ_{UTS}) and elongation at break (ϵ_{max}) of laser sintered samples composed of different wt% hydroxyapatite: polyamide 12 (HA:PA12). Error bars: \pm SD, n=5. Statistical analysis using one way ANOVA with Tukey's multiple comparison. Statistical significance * $p < 0.05$.

Table 4.5. Tensile properties for laser sintered samples composed of different wt% of hydroxyapatite: polyamide 12.

HA:PA12 (wt%)	E (MPa)	σ_{UTS} (MPa)	ϵ_{max} (%)
0:100	1690± 133	46.3± 1.4	20.3± 0.2
5:95	1804± 15	44.4± 0.7	18.2± 0.2
10:90	1946± 109	44.3± 1.2	16.4± 0.3
20:80	2026± 167	41.7± 0.9	11.4± 0.4

Figure 4.12 and Table 4.5 show the mean (a) Young's modulus (E), (b) ultimate tensile strength (σ_{UTS}) and (c) elongation at break (ϵ_{max}) of 5 LS samples tested as per section 3.5.5. The results show that HA only has a marginal effect on E as the values range from 1690 to 2026 MPa. The increase in HA content gave rise to an increase in E , while only 20:80 wt% HA:PA12 shows as significant difference compared to PA12 control (0:100 wt% HA:PA12). The σ_{UTS} values range from 46.3 to 41.7 MPa, denoting that HA effects the strength of the material. HA has a moderate effect on the ϵ_{max} , as values range 20.3 to 11.4 %. With the increase in HA content there was a decrease in ϵ_{max} , with 10:90 and 20:80 wt% HA:PA12 showing a significant difference compared to the PA12 control. The variance in values is moderate denoting relative homogeneity in the fabrication process across the prints.

In the literature, typically when HA is added to a polymer the E and the σ_{UTS} increases while the ϵ_{max} decreases^{8, 256, 257}. However, Orozco-Diaz *et al.* reported a decrease in E and the σ_{UTS} in samples containing HA compared to the polymer control¹⁶⁶. The results obtained here agree with the research that reported an increase in the E and

Chapter 4

a decrease in ϵ_{\max} with an increase in HA content, denoting a moderate increase in brittleness. Section 2.1 reported that cancellous bone has an ultimate strength of 0.1-30 MPa and a modulus between 10 to 3000 MPa¹¹. The results obtained here were similar to the values as cancellous bone. Section 2.3.2 reported that commercially available Medpor® has a modulus of 30.2 MPa²⁵⁸, which is substantially lower than the values determined here, indicating that implants made of these compositions are likely to be suitable for orbital floor reconstruction. The decrease in σ_{UTS} with increased HA content revealed that HA decreased the strength of the material. Medpor® have been reported to have a σ_{UTS} of 1.85-3 MPa^{258, 259} which is considerably lower than the results obtained by the LS samples, signifying that implants fabricated by LS from these compositions would have enough strength to support the globe and the orbital content. Similar studies have shown a small spread in values, owing at least in part to the homogeneity of the printing in the commercial LS system^{176, 177}. As HA is a brittle material an increase in E is expected with the increase in HA content. The decrease in σ_{UTS} and ϵ_{\max} is predicted to be due to the decrease in 'binder' i.e., PA12 particles available to fuse together as HA content increases.

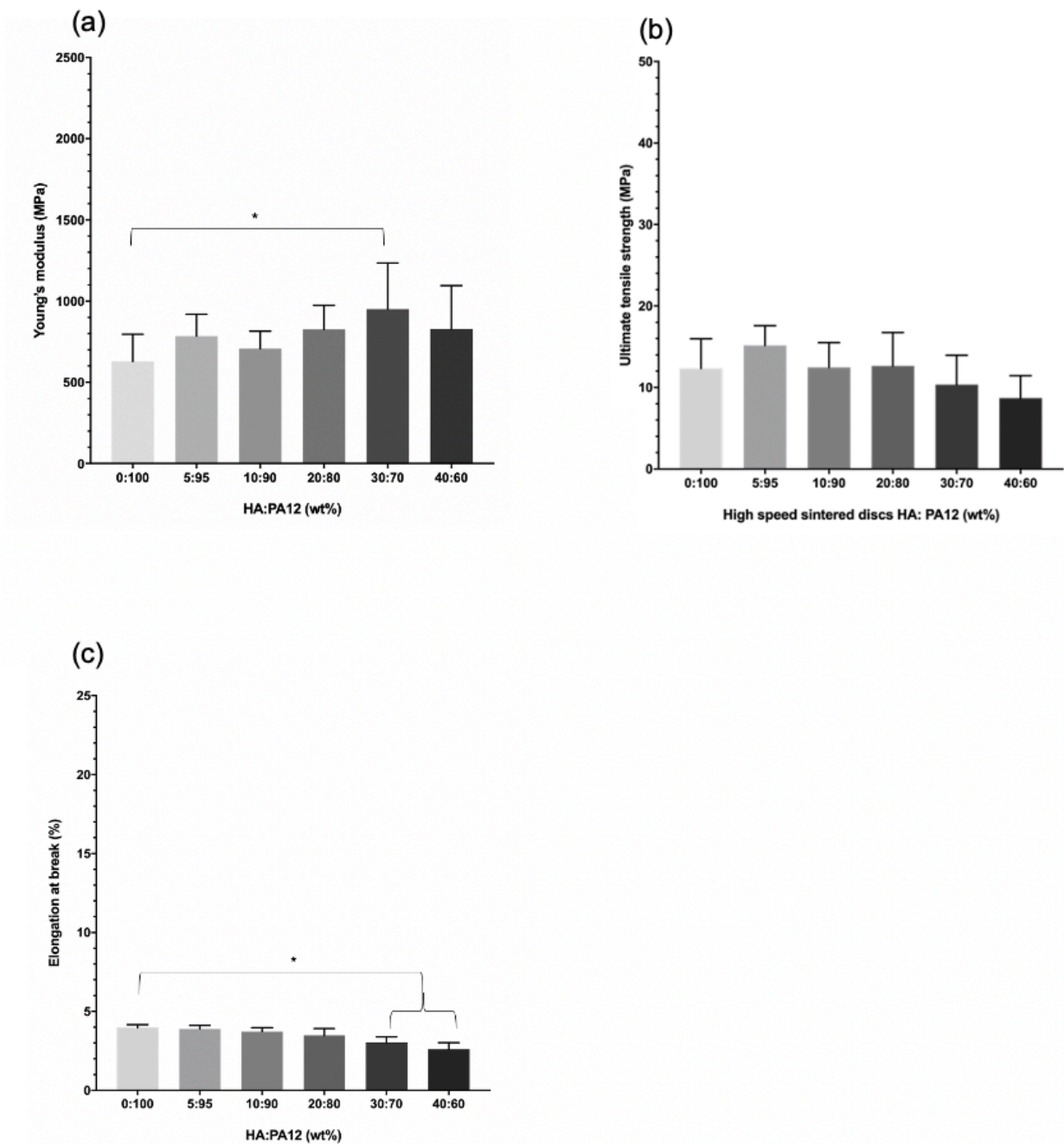


Figure 4.13. The tensile properties: (a) Young's modulus (E), (b) Ultimate tensile strength (σ_{UTS}) and elongation at break (ϵ_{max}) of high speed sintered samples composed of different wt% hydroxyapatite: polyamide 12 (HA:PA12). Error bars: \pm SD, $n=5$. Statistical analysis using one way ANOVA with Tukey's multiple comparison. Statistical significance * $p<0.05$.

Table 4.6 Tensile properties for high speed sintered samples composed of different wt% of hydroxyapatite: polyamide 12 (HA:PA12).

HA:PA12 (wt%)	E (MPa)	σ_{UTS} (MPa)	ϵ_{max} (%)
0:100	639± 168	12.3± 3.3	4.0± 0.2
5:95	813± 134	15.2± 3.3	3.9± 0.2
10:90	705± 107	12.5± 2.9	3.7± 0.3
20:80	822± 147	12.7± 3.7	3.5±0.4
30:70	901± 285	10.4± 3.6	3.0± 0.3
40:60	865± 267	8.7± 2.5	2.6± 0.4

Figure 4.13 and Table 4.6 show the mean (a) E , (b) σ_{UTS} and (c) ϵ_{max} of HSS samples. The results show that HA only has minimal effect on E as the values range from 639 to 901 MPa. The variance for each composition is narrow representing homogeneity in the fabrication process across the prints. As HA content increases, only 30:70 wt% HA:PA12 shows a statistically significant increase in E compared to PA12 control (0:100 wt% HA:PA12). The σ_{UTS} values range from 12.3 to 8.7 MPa, indicating that HA has minimal effect on the strength of the material, with no significant difference observed in the statistical test. As with the E values, the variance across the prints is narrow. HA had a marginal effect on the ϵ_{max} values, decreasing from 4.0 to 2.6 % as the HA content increased. The variance for each composition was relatively narrow as with the E and σ_{UTS} . As the HA content increases, there is a decrease in ϵ_{max} values, although 30:70 and 40:60 wt% HA:PA12 show a significant difference compared to the PA12 control.

Chapter 4

The results obtained here agree with the research that HA increases E and decreases ϵ_{\max} , indicating a minimal increase in brittleness. The modulus values of HSS samples are higher than commercially available Medpor® implants, and were within the values of cancellous bone¹¹, indicating that implants fabricated by HSS from these compositions have suitable stiffness for orbital floor reconstruction applications. The non-linear decrease in σ_{UTS} is not significant and the values obtained are higher than the σ_{UTS} of commercially available Medpor® implants and similar to that of cancellous bone denoting that implant fabricated from these compositions have sufficient strength of support the globe and the orbital content. HSS is not a commercial system, there was a larger spread in values for each composition was expected. Overall, the HSS samples have lower E , σ_{UTS} and ϵ_{\max} compared to LS samples, which is predicted to be due to the considerably higher degree of porosity of HSS samples. It is widely known that increasing the porosity decreases the mechanical properties of the material²⁶⁰⁻²⁶³, as discussed in section 4.3.2.

4.3.7 Flexural properties

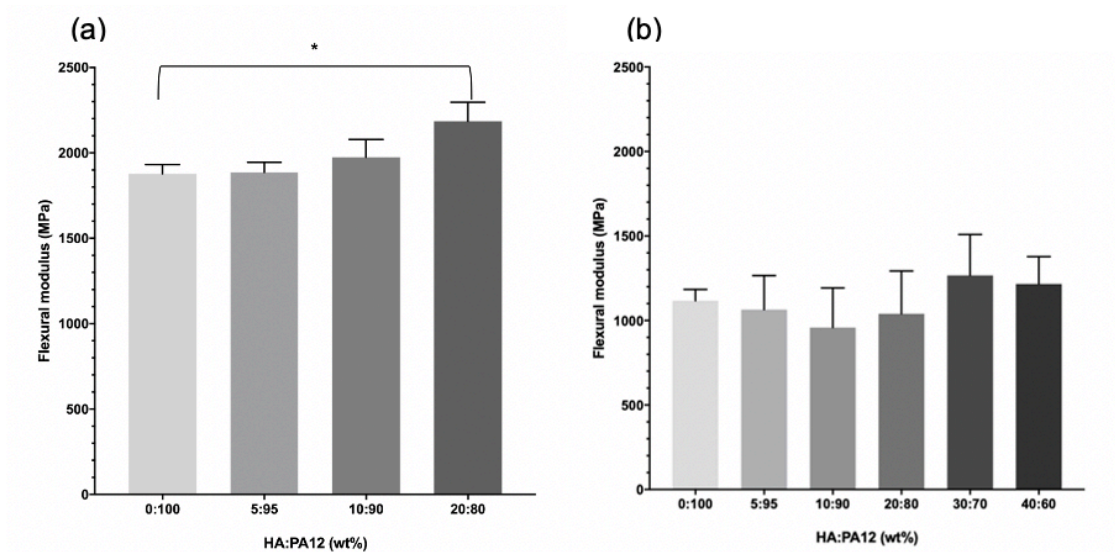


Figure 4.14. Flexural modulus of (a) laser sintered and (b) high speed sintered samples composed of different wt% hydroxyapatite: polyamide 12 (HA:PA12 Error bars: \pm SD, $n=5$. Statistical analysis using one way ANOVA with Tukey's multiple comparison. Statistical significance * $p < 0.05$.

Table 4.7. Flexural modulus values for laser sintered and high speed sintered samples composed of different wt% of hydroxyapatite: polyamide 12 (HA:PA12).

HA:PA12 (wt%)	Flexural modulus (MPa)	
	Laser sintering	High speed sintering
0:100	1878±53	1117±68
5:95	1887±59	1065±201
10:90	1975±101	959±234
20:80	2186±111	1040±254
30:70	-	1267±242
40:60	-	1217±172

Figure 4.14 (a) and Table 4.7 show the mean flexural moduli for 5 LS samples. The values range from 1874 to 2186 MPa, indicating that HA content a minimal effect on the flexural modulus. The variance in values for each composition was moderate indicating homogeneity in samples across the printing. As the HA content increases, an increase in flexural modulus is seen although there was only a statistical difference observed between the PA12 control (0:100 wt% HA:PA12) and 20:80 wt% HA:PA12. A study 3-point tested 15 fresh-frozen orbital floors from cadavers found that the flexural modulus range between 1260 to 4450 MPa^{1, 2}. This is within the range of values determined here, indicating that the LS samples had a similar flexibility to the natural orbital floor. Similar studies have shown a similar small spread in values, owing at least in part to the homogeneity of the printing in the commercial LS system used. A previous study has found that increasing the HA content resulted in a higher flexural modulus for parts produced on FDM and IM²⁶⁴. This trend, also observed here, is likely

Chapter 4

due to a decrease in the degree of particle melt (DPM), as discussed previously in section 4.3.2.

Figure 4.14 (b) and Table 4.7 shows the mean flexural moduli for HSS samples. The values range from 959 to 1267 MPa, like the flexural moduli for LS samples, this indicated that HA had a minimal effect on the flexural modulus. The variance in values for each composition was not as narrow as that of LS samples demonstrating that HSS samples were slightly less homogenous across the printing. As the HA content increases, there was not a linear increase in flexural modulus and no significant difference was observed in the statistical test. The flexural modulus values for HSS samples were marginally lower than that of the natural orbital floor indicating that these samples have increased flexibility while still remaining firm enough to support the globe and the orbital soft tissue contents. As mentioned in 4.3.6, a higher variance in values was expected for the HSS samples as this process is a prototype and is still under development. The increase in HA content also did not have the same effect as with LS samples and the trend observed in the literature.

4.4 Effect of steam sterilisation on the mechanical properties of polyamide 12

In this study the samples have to be sterilised before their use in cell culture and antimicrobial investigations to reduce contamination. Steam autoclave a preferred method to sterilise medical and surgical instruments^{216, 217}. It kills microbes using heat in the form of saturated steam under intense pressure. Therefore, the next objective was to identify the effect of sterilisation on the mechanical properties of the base polymer in order to ensure that it does not negatively impact the material. The results

Chapter 4

obtained are summarised here. More information can be found in the published paper²¹⁸ from this work.

Figure 4.15 and Table 4.8 show the mean (a) E , (b) σ_{UTS} and (c) ϵ_{max} for all combinations of conditioning and drying. E values ranges from 1066 to 1792 MPa, σ_{UTS} ranges from 42.72 to 50.24 and ϵ_{max} ranges from 24.86 to 46.48 %. The results show that steam sterilisation decreases E and σ_{UTS} but increases ϵ_{max} .

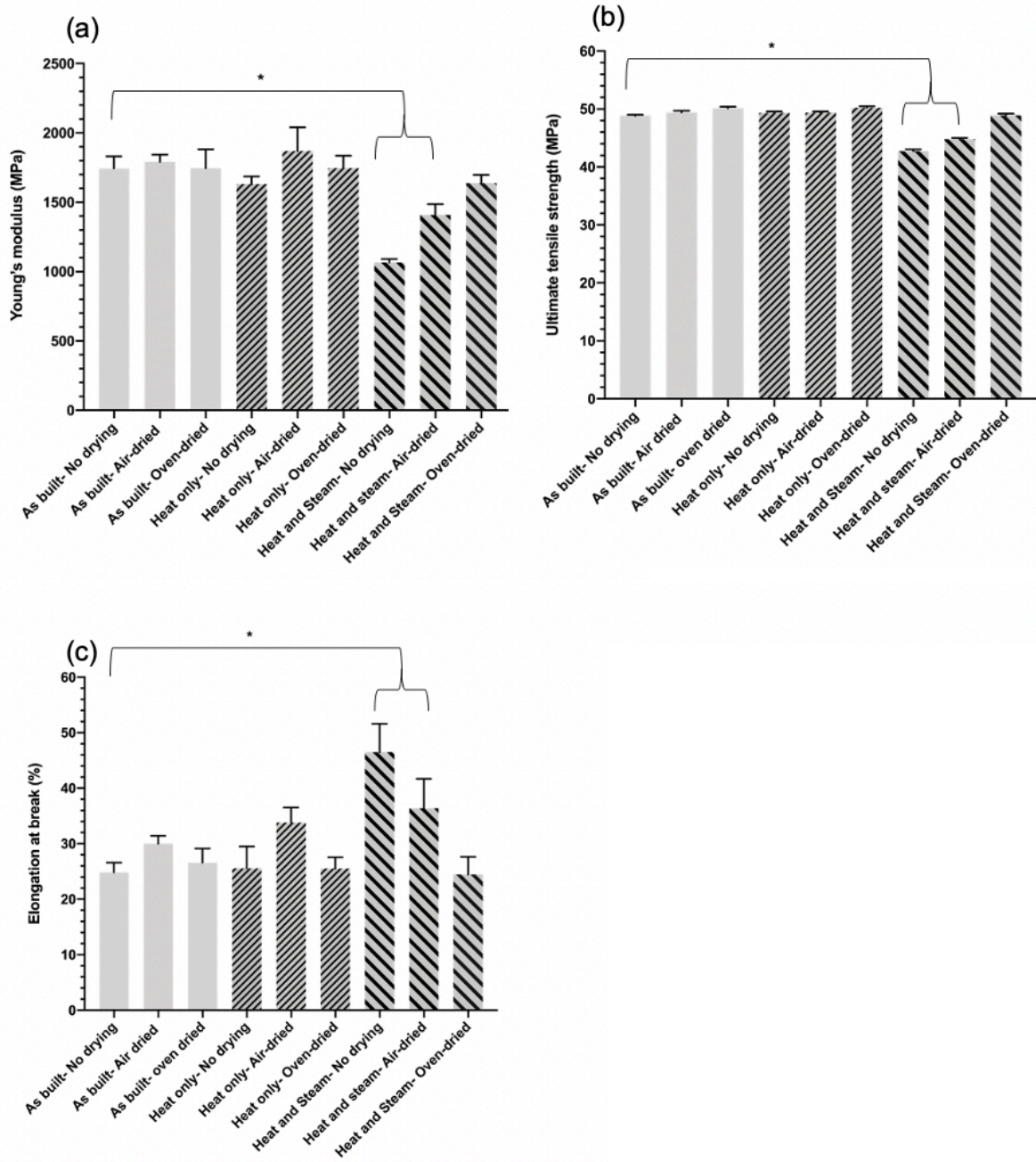


Figure 4.15. The tensile properties: (a) Young's modulus (E), (b) Ultimate tensile strength (σ_{UTS}) and elongation at break (ϵ_{max}) of laser sintered polyamide 12 (PA12) samples for all combinations of conditioning and drying. Error bars: $\pm SD$, $n=5$. Statistical analysis using one way ANOVA with Tukey's multiple comparison. Statistical significance * $p<0.05$.

Table 4.8. The values for the measured tensile properties of all combinations of conditioning and drying.

Sample description		E (MPa)	σ_{UTS} (MPa)	ϵ_{max} (%)
As built	A - No drying	1744	48.9	24.9
	D - Air-dried	1792	49.4	30.0
	G - Oven-dried	1746	50.2	26.6
Heat only	C - No drying	1630	49.3	25.6
	F - Air-dried	1870	49.4	33.8
	J - Oven-dried	1746	50.2	25.5
Heat and steam	B - No drying	1066	42.7	46.5
	E - Air-dried	1408	44.8	36.4
	H - Oven-dried	1638	48.9	24.5

To investigate how moisture effects the tensile properties of the PA12, the water content is measured during testing and then the correlation between water content and mechanical properties is calculated. Table 4.9 shows the values for the measured water content at the time of tensile testing (w_{test}). The effect of water content on the mechanical properties can be seen by Figure 4.16. The linear fit with R^2 shows a moderate correlation between the water content and the Young's modulus ($R^2= 0.86$) as well as the elongation at break ($R^2= 0.87$). There was a strong correlation between the water content and ultimate tensile strength ($R^2= 0.97$) indicating that the changes in mechanical properties are caused by the water content rather than the temperature.

Table 4.9. Measured water content during testing.

Sample description		Water content (%)		
		Pre-test	Post-test	Average
As built	A - No drying	0.13	-0.02	0.05
	D - Air-dried	0.14	0.07	0.11
	G - Oven-dried	0	-	0
Heat only	C - No drying	0.13	-0.03	0.05
	F - Air-dried	0.07	0.06	0.07
	J - Oven-dried	0	-	0
Heat and steam	B - No drying	1.01	0.68	0.84
	E - Air-dried	0.60	0.48	0.54
	H - Oven-dried	0	-	0

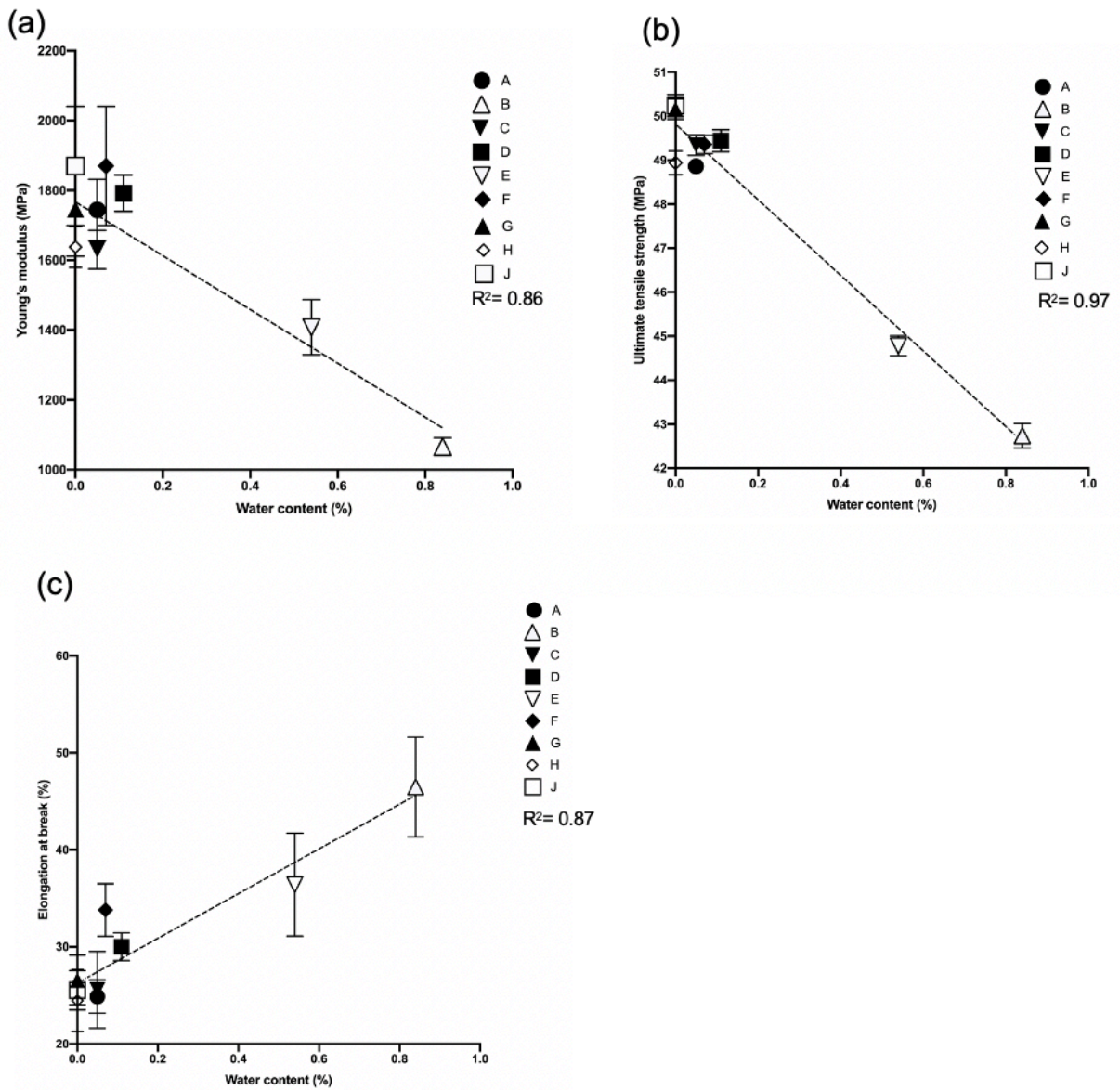


Figure 4.16. Effect of water content on (a) Young's modulus (E), (b) Ultimate tensile strength (σ_{UTS}) and (c) Elongation at break (ϵ_{max}). The measurement of the goodness of fit is shown by the linear fit with the calculated R^2 . There was a strong correlation between the water content and σ_{UTS} and a moderate correlation between water content and E as well as ϵ_{max} .

Chapter 4

The 'Heat and Steam- Oven-dried' show that the changes in mechanical properties are reversible and that steam autoclave can be employed to disinfect the samples in this study without causing permanent changes to the mechanical properties. However, it is important to note that when the implant is inserted *in vivo* it is likely to be absorbing moisture. Therefore, the mechanical properties are likely to change upon implantation. These changes call for further investigation by mechanically testing samples that have been submerged long term in physiological conditions.

4.5 Effect on the Biocompatibility

The last objective of this Series was to determine the effect of HA on the biocompatibility of the parts produced. Prior to these tests a variety of cell seeding densities, commonly used in biocompatibility assessments, were cultured on tissue culture plastic (TCPS) in order to evaluate the optimal seeding density to use in the cell culture investigations.

4.5.1 Cell seeding density

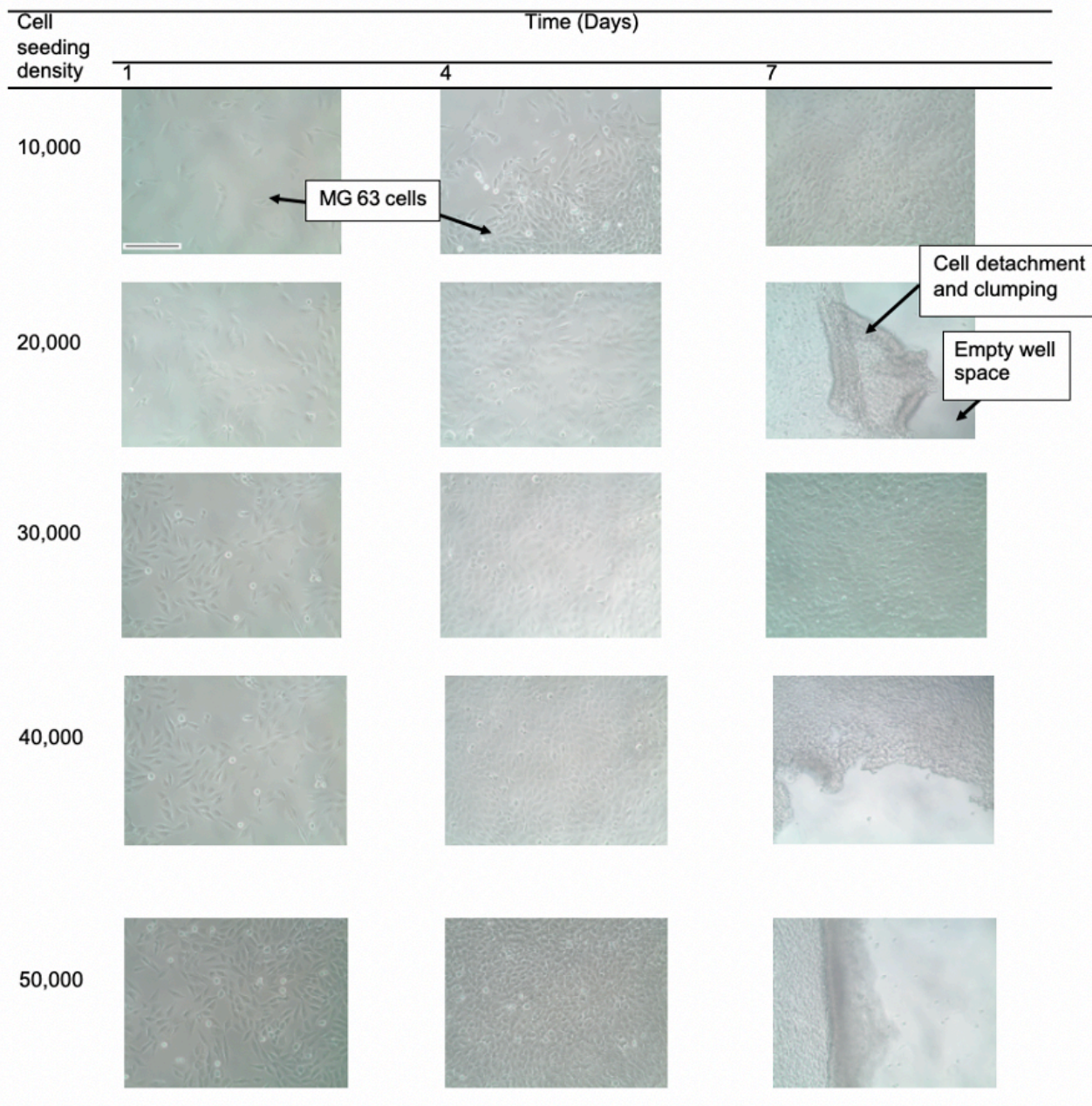


Figure 4.17. Light microscopy of MG 63 cells cultured on tissue culture plastic (TCPS) at different cell densities for 7 days. By day 4, the wells with 30,000 cells or more had reached 100% confluency. The images were acquired at 100x magnification. The images here are a representative of 3 images acquired per sample. Scalebar= 400 μ m and is the same for all images.

Chapter 4

The number of cells used in the cell culture experiments was chosen based on the cell seeding investigation (see section 3.7.1 for full method). In brief, 10,000, 20,000, 30,000, 40,000 and 50,000 MG 63 cells were seeded in 0.5 ml Minimum Essential Medium Eagle (MEME) media into each of n=3 wells in a 24 well plate and grown on TCPS for 7 days. Figure 4.17 shows light microscopy images were taken on days 1, 4 and 7. The wells with 30,000 to 50,000 cells reached almost 100% confluency by day 4. By day 7, the wells with 20,000, 40,000 and 50,000 cells had clumped together and peeled off the edges, which is unfavourable as this is likely to affect the cell viability reading and thus cannot be used as a control or to normalise the data. The wells with 10,000 and 30,000 cells did not show peeling from the edges and appeared to have reached 100% confluency on day 7. Cell detachment and clumping can be caused by various factors such as over-confluency of cells, cell media changes, scraping the cells with the pipette tip during media changes and shaking the well plates during handling. As PA12 is used as a control in this project it is important to have a commonly used control such as TCPS to assess the overall cell viability trend. Kamarajan *et al.*¹⁸⁷ used 10,000 cells in their *in vitro* investigation to evaluate the biocompatibility of LS HA:PA12 composites where no cell clumping or peeling were reported. Therefore, 10,000 cells per well was selected as the cell density. However, after an initial cell viability trial, 10,000 cells per well was too low to obtain a reading for the DNA quantification test. Therefore, 20,000 cells per well was selected as the cell seeding density for this project.

Chapter 4

4.5.2 Cell viability and DNA quantification

The *In vitro* experiments for determining the biocompatibility of LS and HSS samples composed of PA12 and PA12 with different wt% of HA were conducted by measuring the cell viability (metabolic activity) of MG 63 cells using PrestoBlue™ assay and quantifying the DNA content using PicoGreen® dsDNA Assay Kit on day 7. The *in vitro* investigations are limited as they do not give a full idea of how the material will perform *in vivo*, however they are a good starting point to test for the material biocompatibility. It is well known in research that ceramics offer a superior osteoblastic adherence and proliferation²⁶⁵⁻²⁶⁷ therefore a higher percentage of HA present in the samples is likely to be more advantageous when it comes to bone regeneration.

The mean cell viability of MG 63 cells seeded on LS samples is shown in Figure 4.18. The results show an increase in fluorescence over time across all the compositions, denoting that there is an increase in cell viability over time. The variance in fluorescence for each composition is relatively narrow indicating a homogeneity in the surfaces of the samples. There was no statistical difference in the cell viability of the LS PA12 control (0:100 wt% HA:PA12), the rest of the HA:PA12 compositions and TCPS on any of the days, indicating that the addition of HA has a marginal effect the biocompatibility of LS samples. On day 7, there was a reduction in cell viability of TCPS as the MG 63 cells peeled off the edges despite using a low cell seeding density. The results show that the laser sintered samples can support cell viability equivalent to TCPS. Studies using similar quantities of HA in 3D printed scaffolds have also reported no statistical significance in the cell viability with the increase in HA content, incubated for up to 7 days^{166, 268}. The relatively small variance in cell viability for each

composition was likely to be due to the homogeneous surface topography and additive distribution as discussed in section 4.3.2.

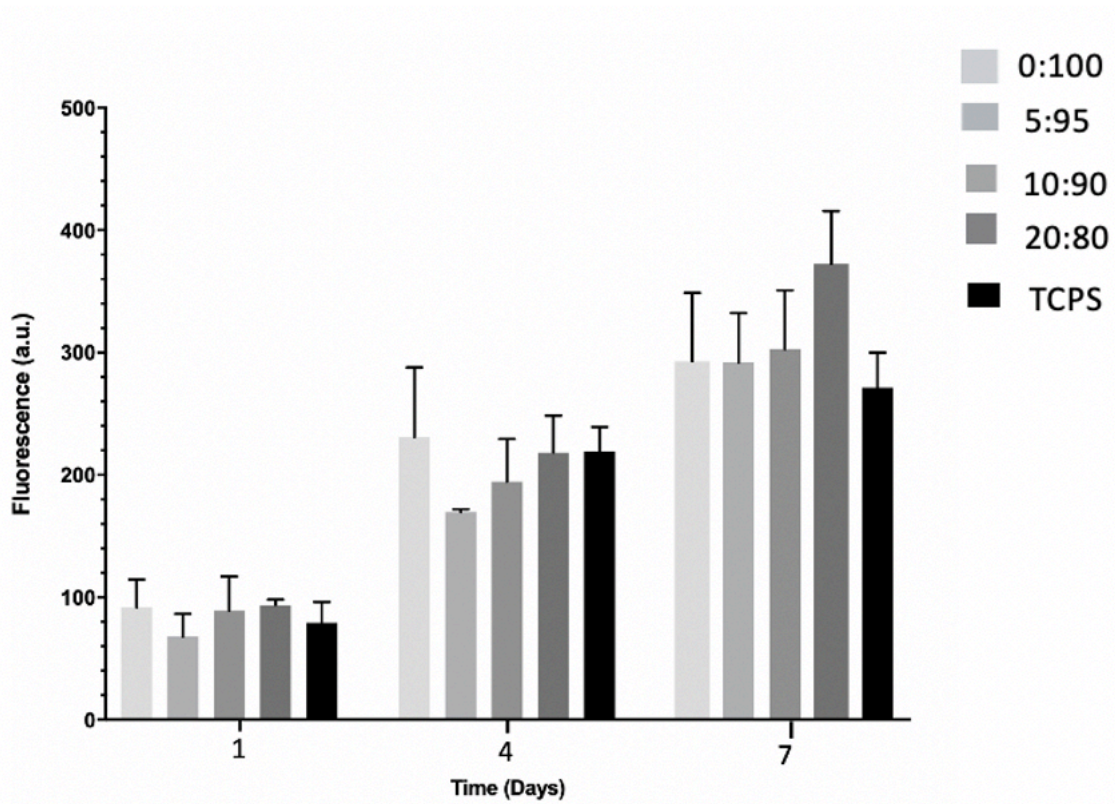


Figure 4.18. Cell viability (MG 63: PrestoBlue™) of laser sintered samples composed of hydroxyapatite: polyamide 12 (HA: PA12) at different weight percentages (wt %). 0:100 HA: PA12 was used as control. Tissue culture plastic (TCPS) was used for comparison. N=1, n=3. Error bars: ±SD. Statistical analysis using one-way ANOVA. Statistical significance * $p < 0.05$.

The amount of DNA recovered from cells, using PicoGreen® dsDNA Assay Kit, after 7 days of culture on LS samples and TCPS is shown in Figure 4.19. The results show no statistical difference in the quantity of DNA in culture between the PA12 control, the HA:PA12 compositions and TCPS. The variance was also narrow for the values presented here. The results not showed no statistical significance in cell viability (Figure 4.18) between the PA12 control and the samples that contained HA. However,

on day 7, there was a marginal non-significant increase for 20:80 wt% HA:PA12. The DNA content results revealed that there was likely the same quantity of DNA per volume, but the cells were more viable on samples containing 20:80 wt% HA:PA12.

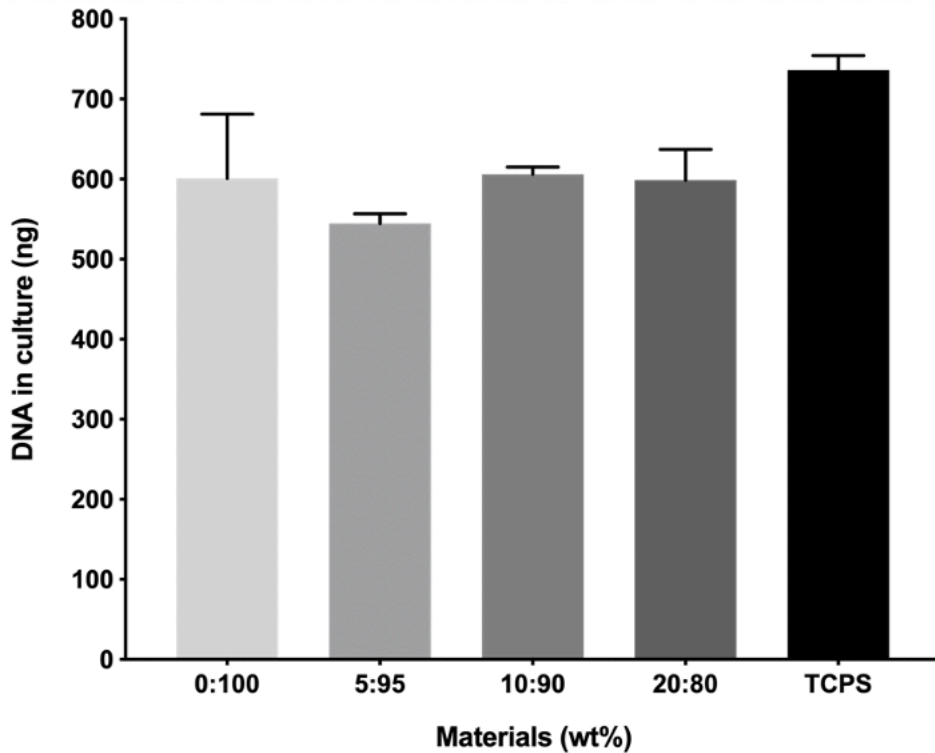


Figure 4.19. DNA content as indication of cell number on laser sintered samples composed of hydroxyapatite: polyamide 12 (HA:PA12) at different weight percentages (wt%) after 7 days of culture. 0:100 HA: PA12 was used as control. Tissue culture plastic (TCPS) was used for comparison. N=1, n=3. Error bars: \pm SD. Statistical analysis using one way ANOVA. Statistical significance * $p < 0.05$.

The mean cell viability of MG 63 cells seeded on HSS samples is shown in Figure 4.20. There was an increase in fluorescence for each composition over time, indicating an increase in cell viability over time. The variance in values for each composition is moderately small indicating homogeneity sample topography across the prints. As HA

Chapter 4

content increases there is an increase in cell viability, although there is only a statistical increase in cells grown on 40:60 wt% HA:PA12 as well as TCPS on day 1, TCPS on day 4 and 40:60 wt% HA:PA12 as well as TCPS on day 7, compared to the PA12 control. The results obtained here show that all the HSS samples generally have lower cell viability than TCPS, with 40:60 wt% HA:PA12 showing the closest cell viability values to TCPS. The cell viability was moderately higher for LS samples than HSS samples, denoting that MG 63 cells prefer to attach and proliferate on LS samples nonetheless all the HSS samples were biocompatible. The variance in HSS samples were similar to that of LS samples, indicating homogeneity of additive distribution and surface topography. Unlike the LS sample and previous studies^{166, 268}, 40:60 wt% HA:PA12 shows a higher fluorescence, demonstrating that implants made from this composition are likely to have increased the cell viability. This trend was expected because as discussed in section 2.4.2, HA has osteoconductive properties which increase the cell viability of the material.

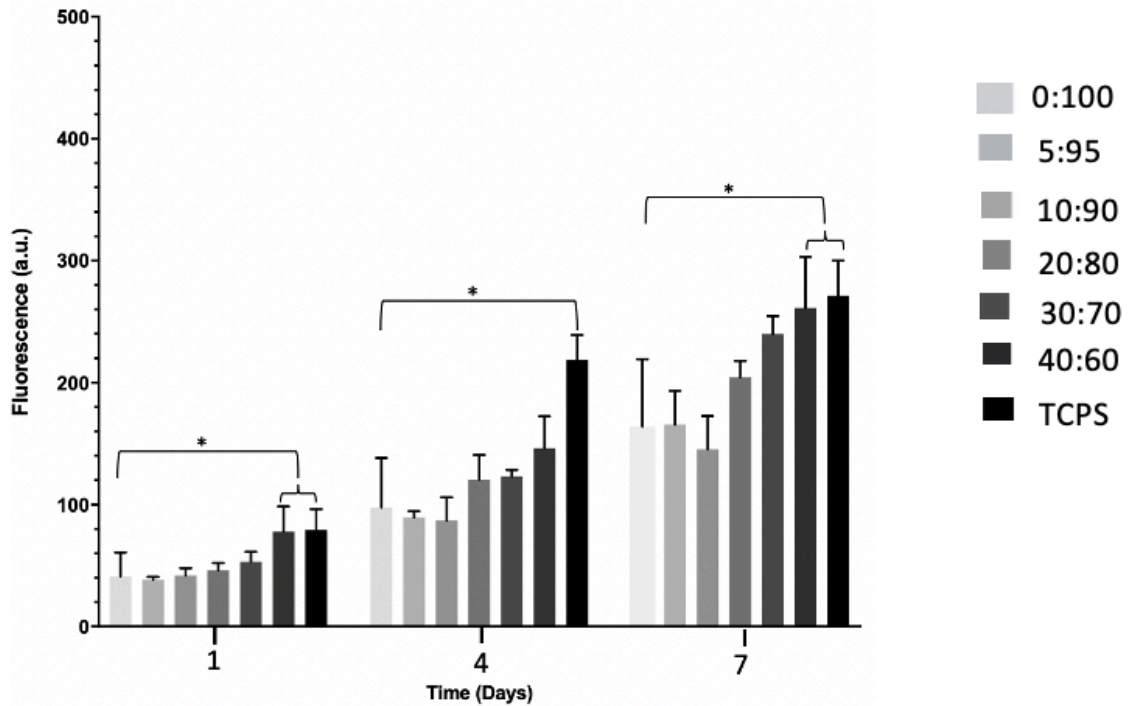


Figure 4.20. Cell viability (MG 63: PrestoBlue™) of high speed sintered (HSS) samples composed of hydroxyapatite: polyamide 12 (HA: PA12) at different weight percentages (wt %). 0:100 HA: PA12 was used as control. Tissue culture plastic (TCPS) was used for comparison. N=1, n=3. Error bars: ±SD. Statistical analysis using one way ANOVA. Statistical significance * p<0.05.

The amount of DNA in 7 days of culture on HSS samples and TCPS is shown in Figure 4.21. The number of DNA in culture were similar between each HA:PA12 composition, signifying that HA did not affect the cell attachment. The variance was relatively small indicating homogeneity in HA distribution and surface topography. The number of cells grown on TCPS was significantly higher than the HA:PA12 samples, indicating that cells prefer to attach to TCPS than the HSS samples. Overall, the number of cells grown on HSS samples is marginally lower than LS samples, demonstrating that cells attachment is better on LS samples. Due to the increase in porosity (as discussed in

Chapter 4

section 4.3.2) and specific surface area (as discussed in section 4.3.4) of HSS samples, an increase in in cells attachment was expected. This discrepancy on the expected outcomes with regards to number of cells grown on the HSS samples could be due to the RAM ink, interfering with the cell attachment mechanisms. This could happen in two ways. If the ink itself interacts with HA and covers it, then the cells have a reduced number of attachment sites, and functionally less attachment area despite roughness. Alternatively, the ink itself could be inhibiting cell attachment or growth in some other way. Both of these would require further investigation. The variance in number of cells grown on HSS samples was relatively small, like the LS results. The cell viability results however showed that on day 7, the cell viability of 40:60 wt% HA:PA12 was similar to that of TCPS. This is an indication that even though fewer cells grew on 40:60 wt% HA:PA12 discs, the cells were more viable on this composition, compared to the cells that grew on TCPS.

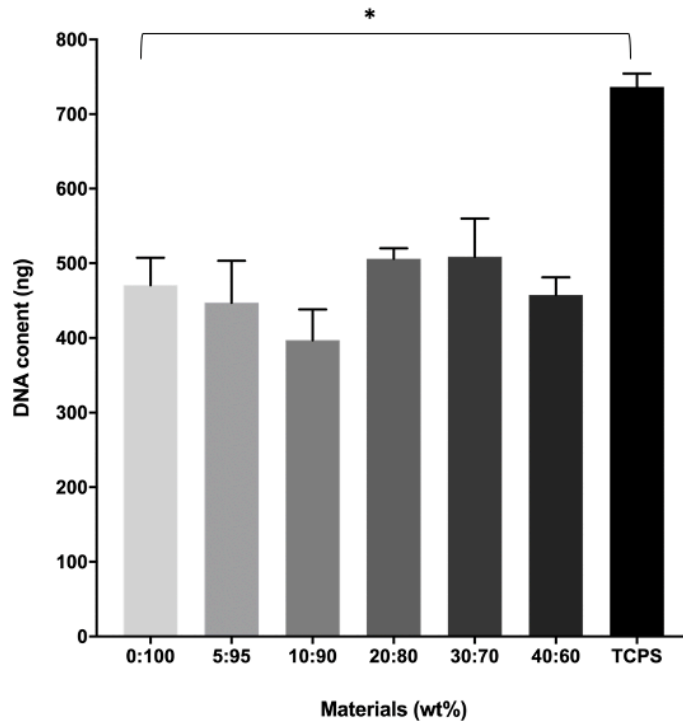


Figure 4.21. DNA content as indication of cell number high speed sintered (HSS) samples composed of hydroxyapatite: polyamide 12 (HA:PA12) at different weight percentages (wt%) after 7 days. 0:100 HA: PA12 was used as control. Tissue culture plastic (TCPS) was used for comparison. N=1, n=3. Error bars: \pm SD. Statistical analysis using one way ANOVA. Statistical significance * $p < 0.05$.

4.6 Summary and composite selection

HA had the desired morphology for processing on LS and HSS. The addition of HA did not seem to affect the melt characteristics of the polymer however, according to the literature a higher concentration of HA is predicted to affect the printability as well as the physical and mechanical properties. For LS the highest concentration of HA that could be processed was 20:80 wt% HA:PA12 and 40:60 wt% HA:PA12 for HSS. Overall, all the parts that could be printed, even the PA12 control, showed a slight

Chapter 4

variation in dimensions compared to the CAD model. Thus, when designing real-life parts, any significant changes should be compensated for in the design.

The analysis of the physical properties such as the additive distribution on the surface and the volume of both LS and HSS samples showed a relatively even distribution of HA. Therefore, any effect that HA may have is likely to be evenly distributed. LS and HSS samples appeared to increase in porosity with the addition of HA however, porosity was higher in HSS samples. An increase in porosity is likely to negatively impact the mechanical properties but overall improve BIC as it increases the surface area of the samples. The surface area results showed that the HSS 5-40 wt% HA:PA12 samples and LS 20:80 wt% HA:PA12 had specific surface area similar or larger than BioOss®¹⁵⁵⁻¹⁵⁸, a commercial bovine bone substitute with high osteoconductive properties. Therefore, it is reasonable to expect the HSS samples and 20:80 wt% HAPA12, to have a higher potential in triggering bone formation. Due to the unchanged crystal structure of HA before and after processing, the samples are predicted to have osteoconductive properties. When the mechanical properties were investigated, as expected, the LS samples had superior mechanical properties to the HSS samples. The addition of HA had more of a significant effect on the LS samples than the HSS samples however, all the samples processed showed higher tensile test values than commercially available Medpor® implants and similar values to cancellous bone¹¹. Therefore, all the processed samples had potentially sufficient tensile properties to potentially be used as orbital floor reconstruction material. In addition, the flexural moduli of the LS samples were all similar to that of the orbital floor bone. The HSS samples however, showed slightly lower values.

Chapter 4

The effects of steam autoclave on the mechanical properties were measured for the PA12 control. The results revealed that steam autoclave did not cause any permanent changes to the mechanical properties. The sterilised samples were then used in *In vitro* cell viability investigations. These investigations showed that all the samples were biocompatible. However, cells grown on LS samples had higher cell viability than those grown on HSS samples. This was predicted to be due to the ink in HSS reducing the number of attachment sites, and functionally less attachment area despite roughness. In addition, the ink may be inhibiting cell attachment or growth in some other way. For the LS samples, the cells on the 20:80 wt% HA:PA12 were marginally more viable than the other samples. For HSS, 40:60 wt% HA:PA12 there was a significant increase in cell viability compared to the PA12 control. Therefore, for LS, 20:80 wt% HA:PA12 and for HSS 40:60 wt% HA:PA12 were selected as the compositions to continue with the investigations.

5 Results and discussion: antimicrobial: polymer compositions

This Chapter was focused on investigating the effect of zinc (Zn) when added to polyamide 12 (PA12) and processed on laser sintering (LS) and high speed sintering (HSS). The results obtained are discussed in this chapter. The objectives were:

- To investigate the processability of Zn in order to assess its suitability for processing on LS and HSS.
- To determine the effect of Zn on the physical and mechanical properties for all the compositions that could be processed.
- To evaluate the antibacterial activity of the parts produced.

5.1 Processability of zinc: polyamide 12 composites

As with Chapter 4 the first objective was to assess particle sphericity and size. Then, the melt characteristics of the composites were investigated as these properties have an effect on the processability of the material.

5.1.1 Powder morphology

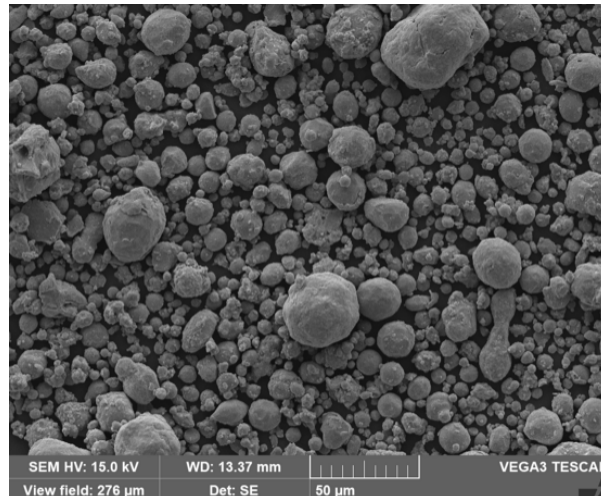


Figure 5.1. Secondary electron (SE)- Scanning electron microscopy (SEM) micrographs of zinc (Zn) powder taken at x1000 magnification.

A scanning electron microscopy (SEM) micrograph of Zn powder is presented in Figure 5.1. The Zn particles appeared to have a near spherical shape. It can be seen the Zn particles are just about within the acceptable range for processing on LS and HSS. Based on this, the powder morphology of Zn was not likely to prevent effective processing.

5.1.2 Thermal analysis

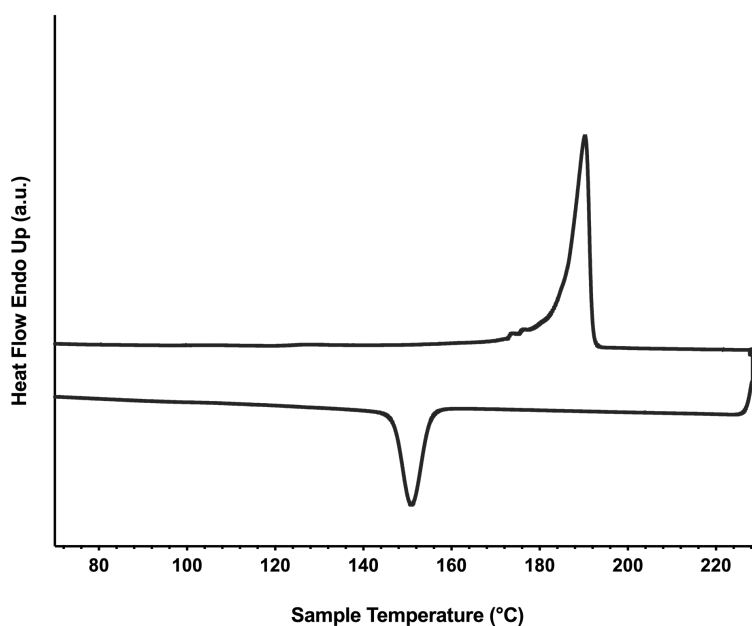


Figure 5.2. Differential scanning calorimeter (DSC) curves of 2:98 wt% zinc: polyamide 12 (Zn:PA12) powder.

Table 5.1. Melting and crystallisation onset temperatures of 2:98 wt% zinc: polyamide 12 (Zn:PA12) powder with pure PA12 for comparison.

Zn:PA12 (wt%)	Melting temperature onset (°C)	Melting temperature (°C)	Crystallisation temperature onset (°C)	Crystallisation temperature (°C)	Processing window (°C)
0:100	181	192	158	150	23
2:98	179	191	157	150	22

Chapter 5

The differential scanning calorimeter (DSC) curve and the melt characteristics for 2:98 wt% Zn:PA12 are shown by Figure 5.2 and Table 5.1, respectively. The value for T_{onset} is 179 °C, T_m is 191 °C, T_{conset} 157 °C and T_c 150 °C. It can be seen that 2:98 wt% Zn:PA12 has a relatively wide processing window of 22 °C, 1 °C lower than the processing window of the PA12 control. As with the HA:PA12 compositions in chapter 4, the default processing parameters could potentially be used to process 2:98 wt% Zn:PA12.

5.2 Printability

The processability of Zn:PA12 samples is novel on both LS and HSS. Test samples were printed on LS and HSS using 0:100 and 2:98 wt% Zn:PA12. The default processing parameters were used for both processes. The HSS parameters changed due to further development on the machine done by the Advanced Polymer Sintering team at the University of Sheffield. The bed temperature was changed from 150 °C to 160 °C. The overhead initial power was kept at 53 % (based on an array of 6 x 300 W ceramic infrared emitters). The sinter speed was decreased from 120 mm/s to 80 mm/s. The recoater speed (move speed) was kept at 70 mm/s. Overall, the new processing parameters delivered higher energy than the old processing parameters (discussed in section 3.4.2). This was predicted to improve the mechanical properties of the samples.

In Chapter 4, the concentrations of HA did not affect the processing window of the material, however, the addition of HA did affect the printability, physical and

Chapter 5

mechanical properties of the samples. Therefore, the addition of Zn was also predicted to have an effect on the overall properties of the material.

5.2.1 Laser sintering

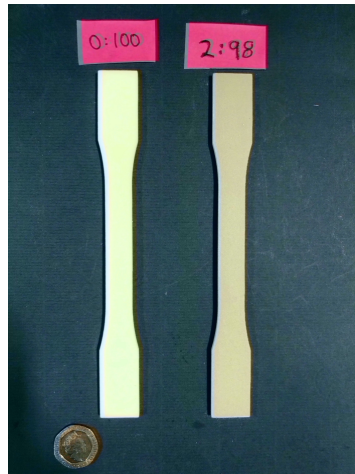


Figure 5.3. Laser sintered tensile test bars made of 0:100 and 2:98 wt% zinc: polyamide 12 (Zn:PA12). Scale bar= 20p coin.

The tensile test samples (Figure 5.3), 3-point bend bars and discs were successfully fabricated on LS using Zn:PA12 compositions, indicating that at this ratio Zn did not affect the printability of the samples.

Chapter 5

5.2.2 High speed sintering

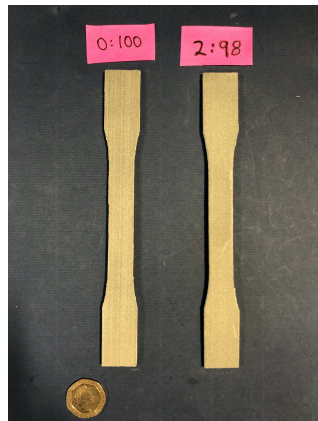


Figure 5.4. High speed sintered tensile test bars made of 0:100 and 2:98 wt% zinc: polyamide 12 (Zn:PA12). Scale bar= 20p coin.

All the tensile test bars (Figure 5.4), 3-point bend bars and discs were produced using 2:98 wt% Zn:PA12 composition on HSS. The new processing parameters resulted in a harder powder cake than the old processing parameters, mentioned in section 3.4.2. However, it was still possible to separate individual parts and removal the surrounding powder completely through bead blasting.

5.3 Effect of Zn on the physical and mechanical properties

The next objective was to assess the effect of Zn on the physical properties of the parts produced. The physical properties were investigated in terms of dimensional accuracy, surface topography analysis and characterisation of the chemical composition. The additive distribution and the surface area analysis could not be conducted for the Zn:PA12 samples due to COVID-19 restrictions. The mechanical properties were assessed by tensile testing and 3-point bending.

Chapter 5

5.3.1 Dimensional accuracy

Table 5.2. Part dimensions of laser sintered 3-point bend bars composed of 0:100 and 2:98 wt% zinc: polyamide 12 (Zn:PA12). The expected values were defined in the CAD model. The measurements were conducted on 5 samples.

Zn:PA12 (wt%)	Width (mm)	SD	% difference	Thickness (mm)	SD	% error	Length (mm)	SD	% difference
CAD	13.00	-	-	4.00	-	-	60.00	-	-
0:100	12.89	0.06	1.42	4.25	0.03	6.13	60.03	0.04	0.06
2:98	12.86	0.05	1.08	4.49	0.05	12.30	60.02	0.07	0.13

The effect of Zn on the dimensional accuracy of the parts was assessed as per the method in section 3.5.1. The results in Table 5.2 show the mean part dimension of LS samples. The width ranged from 12.86 to 12.89 mm, the thickness ranged from 4.25 to 4.49 mm and the length ranged from 60.02 to 60.03 mm. The production was relatively homogeneity as shown by the moderate variance between each composition. The % difference ranges from 1.08 to 1.42 % for the width, 6.13 to 12.30 % for the thickness and 0.06 to 0.13 % for the length. Both the control and the 2:98 wt% Zn:PA12 show a slight variation in the dimensions of the printed samples compared to the CAD model. This was also observed in chapter 4.3.1 for LS HA:PA12 parts.

Chapter 5

Table 5.3. Part dimensions of high speed sintered 3-point bend bars composed of 0:100 and 2:98 wt% zinc: polyamide 12 (Zn:PA12). The expected values were defined in the CAD model. The measurements were conducted on 5 samples.

Zn:PA12 (wt%)	Width (mm)	SD	% difference	Thickness (mm)	SD	% error	Length (mm)	SD	% difference
CAD	13.00	-	-	4.00	-	-	60.00	-	-
0:100	13.07	0.08	0.55	3.98	0.01	0.57	58.70	0.06	2.17
2:98	12.95	0.14	1.01	3.90	0.05	2.48	58.51	0.05	2.48

Table 5.3 shows the mean part dimensions of HSS samples. The width ranges from 12.95 to 13.07 mm, the thickness ranges from 3.90 to 3.98 mm and the length ranges from 58.51 to 58.70 mm. The PA12 control (0:100 Zn:PA12), printed using the new processing parameters shows a reduction in % difference in all dimensions compared to the results presented in section 4.3.1, for the HSS samples. Therefore, the new processing parameters enhanced the dimensional accuracy of the parts.

Similarly to the dimensions of HSS HA:PA12 samples (section 4.3.1), LS Zn:PA12 samples presented here (section 5.3.1), a marginal difference in the dimensions of the HSS Zn:PA12 samples compared to the CAD model is obtained. Therefore, when designing real-life parts, test prints are required to determine shrinkage compensation into the original CAD file.

5.3.2 Surface topography analysis

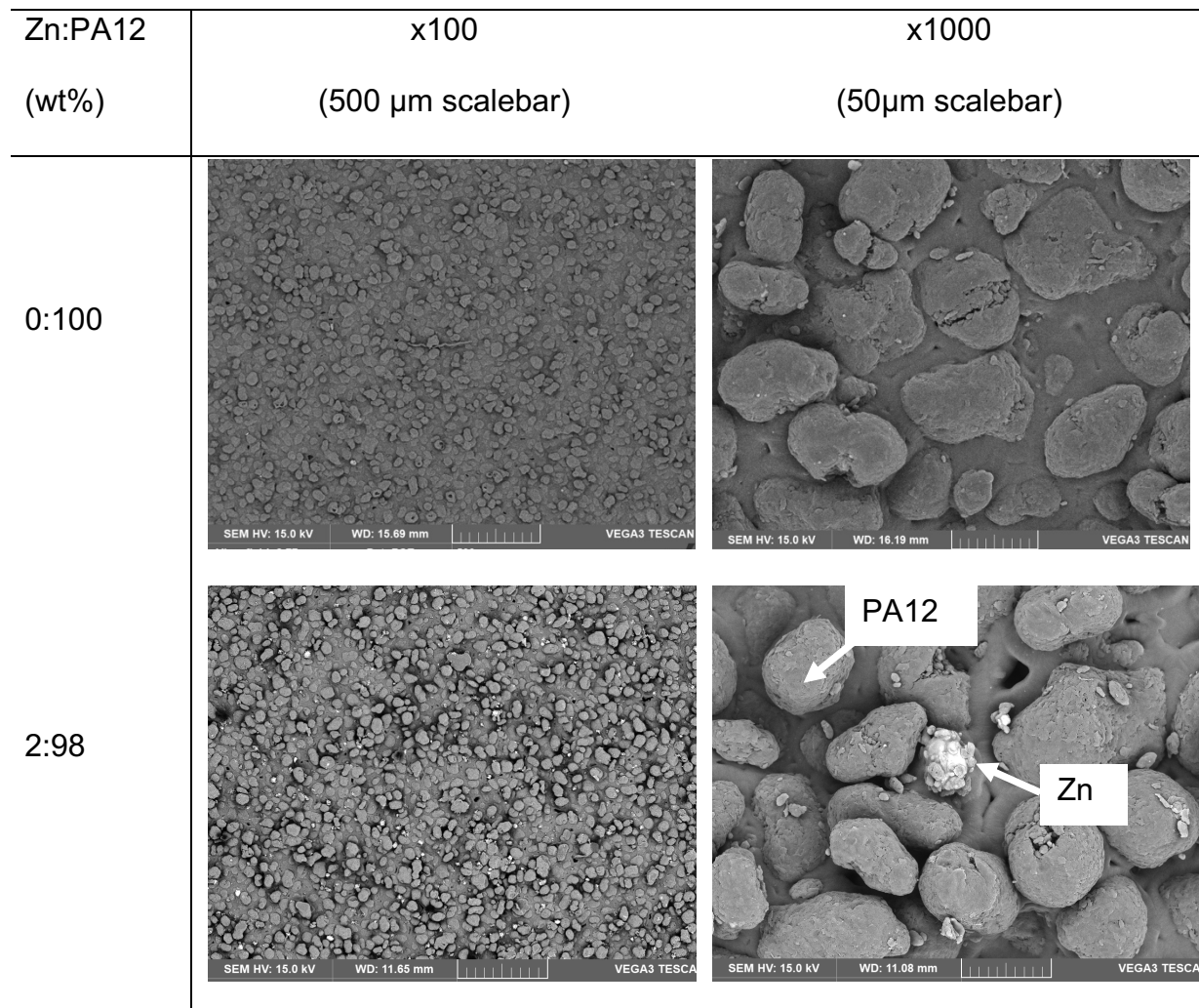


Figure 5.5. Backscattered electron (BSE)- Scanning electron microscopy (SEM) micrographs of laser sintered discs composed of 2:98 wt% zinc: polyamide 12 (Zn:PA12) taken at x100 and x1000 magnifications.

Figure 5.5 shows backscattered electron (BSE)-SEM micrographs of LS 2:98 wt% Zn:PA12 discs. Like HA, the distribution of Zn on the surface of the sample can affect

Chapter 5

both the physical and mechanical properties. For example, a homogeneous distribution of Zn on the surface of the samples can affect the way bacteria interacts with the material. The white particles are the Zn particles, and the grey particles are PA12. The low magnification image show that the Zn was reasonably well distributed on the surface of the discs. Like the HA:PA12 compositions, the surface of the Zn:PA12 discs appeared rough due to particle coring which could potentially increase bone implant contact (BIC) and hence implant stability.

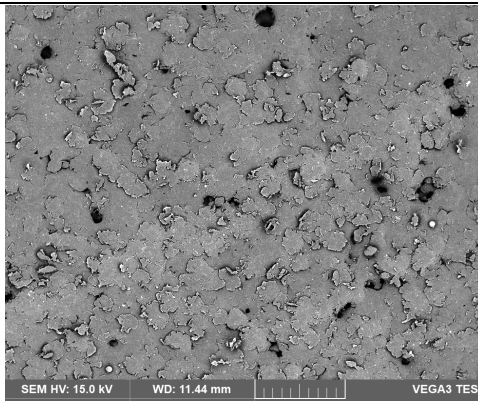
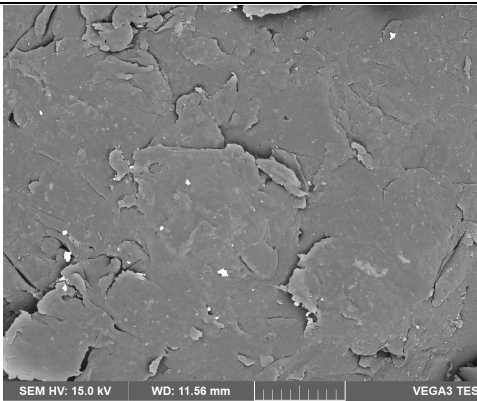
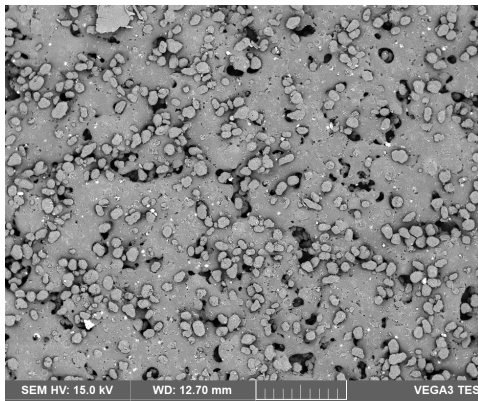
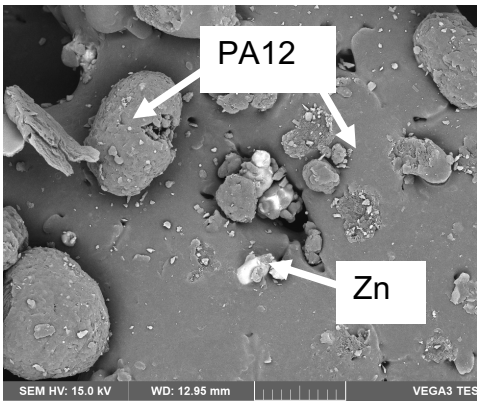
Zn:PA12 (wt%)	Low magnification (500 μm scalebar)	High magnification (50 μm scalebar)
0:100		
2:98		

Figure 5.6. Backscattered electron (BSE)- Scanning electron Scanning electron microscopy (SEM) micrographs of high speed sintered discs composed 2:98 wt% zinc:

Chapter 5

polyamide 12 (Zn:PA12) and 0:100 wt% Zn:PA12 used as comparison. The micrographs were taken at x100 and x1000 magnifications.

The SEM micrographs of HSS samples composed of Zn:PA12 are presented in Figure 5.6. The Zn is relatively well distributed on the surface of HSS samples. As expected, the new processing parameters delivered more energy to the particles which lead to a higher degree of particle melt (DPM) compared to the samples processed using the old HSS processing parameters (shown by

Figure 4.6). As mentioned in section 2.7.1, a higher DPM is predicted to improve the overall mechanical properties of the parts due to the increase in sample densities. The SEM micrographs for 2:98 wt% Zn:PA12 show that the addition of Zn increased the degree of particle coring and increased the porosity compared to the PA12 control which is likely to be advantageous in bone reconstruction application but can have a negative effect on the mechanical properties. The HSS sample appear more porous than the LS sample therefore despite the change in processing parameters the LS samples are predicted to still have superior mechanical properties. Nonetheless as mentioned in section 2.1, porosity is important as it permits bone ingrowth and vascularisation. The pores size of the HSS 2:98 wt% Zn:PA12 are within the optimal range (between 100- 350 μm ^{235, 240-243}) as with the HA:PA12 HSS samples seen in section 4.3.2.

5.3.3 Characterisation of crystal structure

Due to the high melting temperature of Zn (419 °C²⁶⁹) it was expected that the crystal structure would not be affected by the processing parameters. Any changes to the

crystal structure can affect the antimicrobial properties of the material. Therefore, the crystal structure of Zn powder before processing and the crystal structure of the processed LS and HSS samples were assessed by X-ray diffraction (XRD).

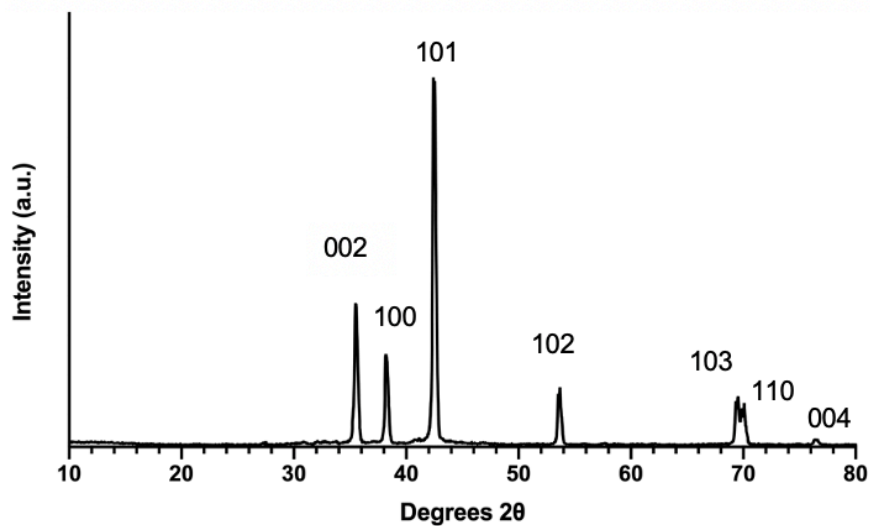


Figure 5.7. Powder X-ray diffraction (XRD) patterns of zinc (Zn) before 3d printing. The XRD pattern of Zn is presented with Miller indices (hkl) showing crystal family of planes for each diffraction peak.

The diffraction pattern for Zn powder is represented in Figure 5.7. Zinc showed diffraction peaks at $2\theta = 35.57, 38.30, 42.52, 53.71, 70.07$ and 70.11° represented (hkl) (002), (100), (101), (102), (103), (110) and (004)²⁷⁰.

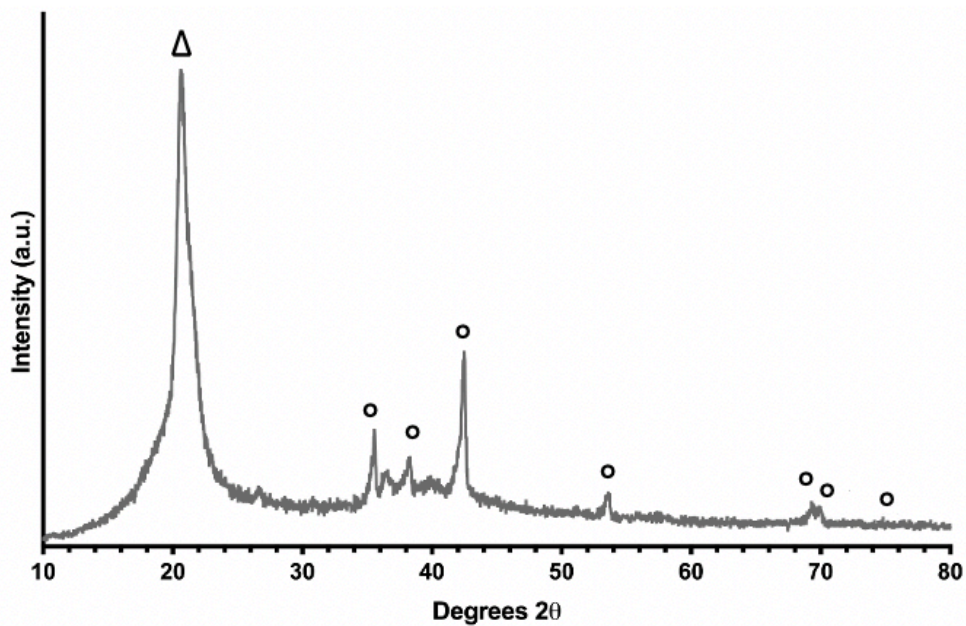


Figure 5.8. X-ray diffraction (XRD) patterns of laser sintered discs composed of 2:98 wt% zinc: polyamide 12 (Zn:PA12). Where Δ represents PA12 and \circ represents Zn.

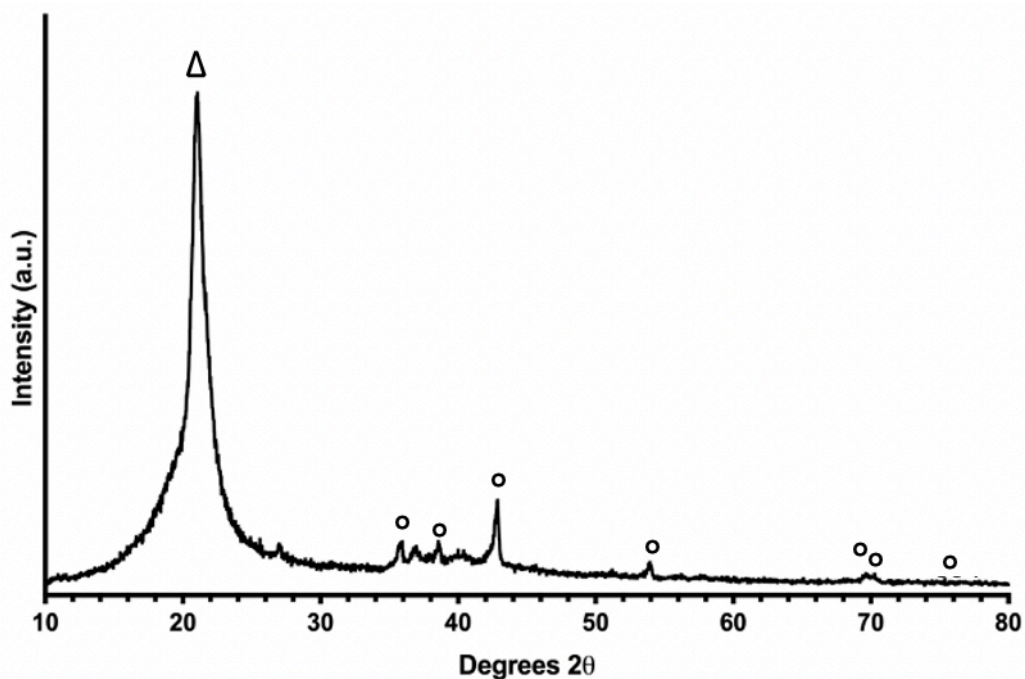


Figure 5.9. X-ray diffraction (XRD) patterns of high speed sintered discs composed of 2:98 wt% zinc: polyamide 12 (Zn:PA12). Where Δ represents PA12 and \circ represents Zn.

Chapter 5

The diffraction patterns for the 2:98 wt% Zn:PA12 samples manufactured by LS is shown by Figure 5.8 and HSS is shown by Figure 5.9. The peak at $2\theta = 21.38^\circ$ is for PA12 and the Zn peaks are shown at $2\theta = 30-80^\circ$. Both graphs confirm the presence of Zn. Similar to the crystal structure of HA:PA12 compositions in section 4.3.5, the processing procedures did not appear to change the crystal structure of Zn therefore, both LS and HSS 2:98 wt% Zn:PA12 samples are predicted to possess antimicrobial properties.

5.3.4 Tensile properties

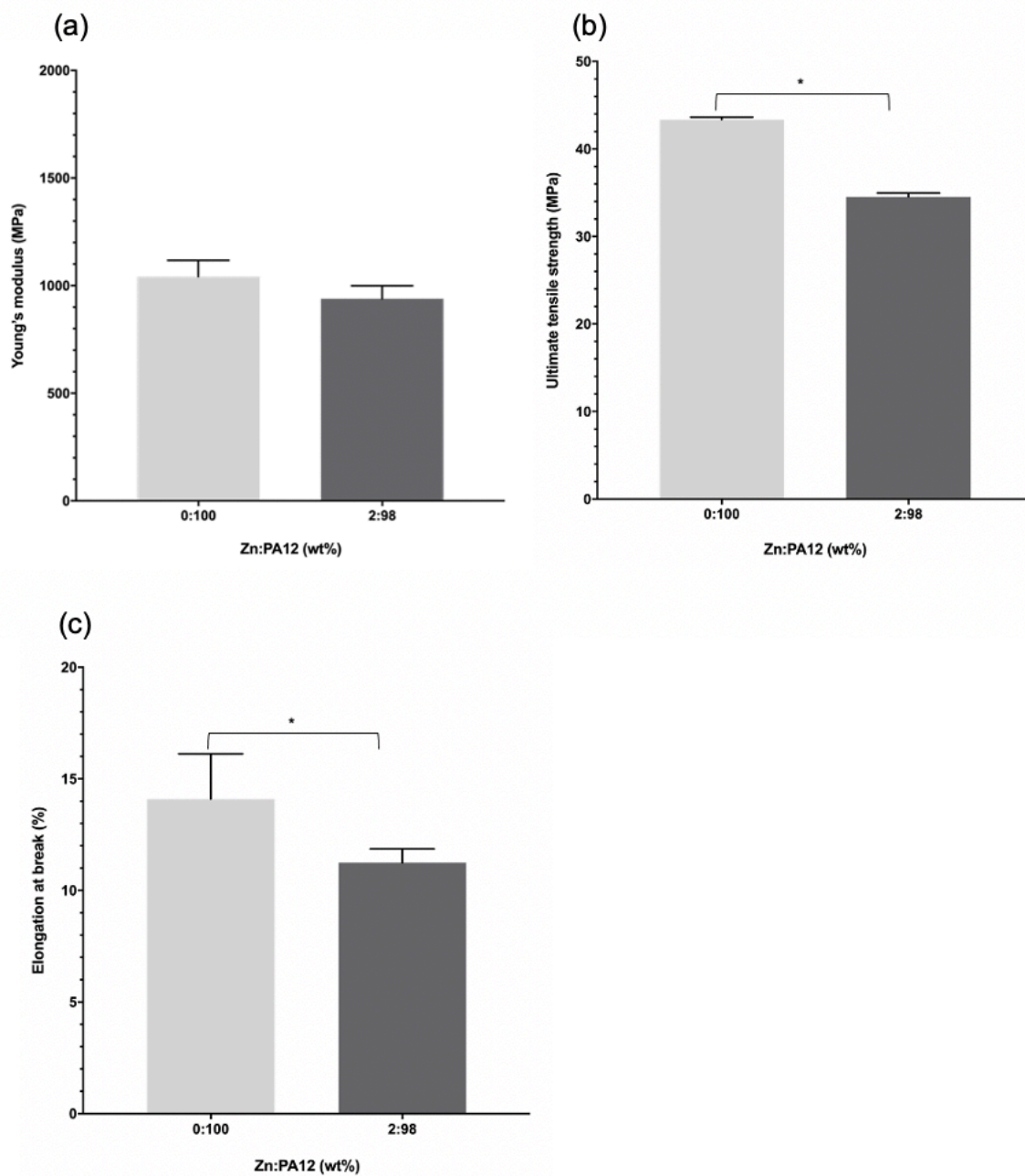


Figure 5.10. The tensile properties: (a) Young's modulus (E), (b) Ultimate tensile strength (σ_{UTS}) and elongation at break (ϵ_{max}) of laser sintered samples composed of 0:100 and 2:98 wt% zinc: polyamide 12 (Zn:PA12). Error bars: \pm SD, n=5. Statistical analysis using an unpaired T-test. Statistical significance * $p < 0.05$.

Table 5.4. Tensile properties for laser sintered samples composed of 0:100 and 2:98 wt% zinc: polyamide 12 (Zn:PA12).

Zn:PA12 (wt%)	E (MPa)	σ_{UTS} (MPa)	ϵ_{max} (%)
0:100	940±94	43.4±0.3	14.1±2.0
2:98	877±124	34.5±0.4	11.2±0.6

Figure 5.10 and Table 5.4 show the mean (a) Young's modulus (E), (b) ultimate tensile strength (σ_{UTS}) and (c) elongation at break (ϵ_{max}) of LS 2:98 wt% Zn:PA12 samples tested as per section 3.5.5. The E ranges from 877 to 940 MPa showing that the addition of Zn had a minimal effect on the stiffness of the material. The σ_{UTS} ranges from 34.2 to 43.4 MPa, showing that Zn significantly decreases the tensile strength of the material. The addition of Zn to PA12 led to a significant decrease in the ϵ_{max} of the material from 14.1 to 11.2 %. All the E , σ_{UTS} and ϵ_{max} have marginally narrow variance representing homogeneity in the fabrication process. The E , σ_{UTS} and ϵ_{max} values presented here, show that the PA12 control (0:100 wt% Zn:PA12) has overall lower values than the LS PA12 control (0:100 wt% HA:PA12) in section 4.3.6. The results presented in section 4.3.6 were obtained one month after printing. However, due to the COVID-restrictions, the results here (section 5.3.4) were obtained, seven months after printing. The decrease in overall tensile properties were predicted to be due to the effect of long-term ageing on the tensile properties of PA12 samples. Goodridge *et al.*²⁷¹ investigated the long-term effect of ageing on the mechanical properties of LS PA12. The results obtained by Goodridge *et al.* did not agree with the results obtained in this study as the results for the samples stored in dry conditions over a 52-week

period showed an increase in the E , σ_{UTS} and ϵ_{max} . Further testing is required in order to determine the reason for the decrease in overall tensile properties.

The results presented in Table 5.5 show that even at a small amount Zn has a bigger effect on the σ_{UTS} and ϵ_{max} compared to the HA:PA12 compositions presented in Table 4.6. This significant decrease in the σ_{UTS} and ϵ_{max} could potentially be due to the wider particle size distribution of Zn:PA12 compositions compared to the HA:PA12 compositions. Hui *et al.*¹⁷⁶ have reported that a large particle size distribution can lead to negative effect on the part density, flowability, surface finish, part accuracy and hence mechanical properties. Nonetheless, despite the reduction in mechanical properties of 2:98 wt% Zn:PA12 the parts possess superior mechanical properties to commercially available Medpor® implants and similar E and σ_{UTS} to cancellous bone¹¹, as reported in section 2.1, therefore LS 2:98 wt% Zn:PA12 are predicted to be strong enough for orbital floor reconstruction application.

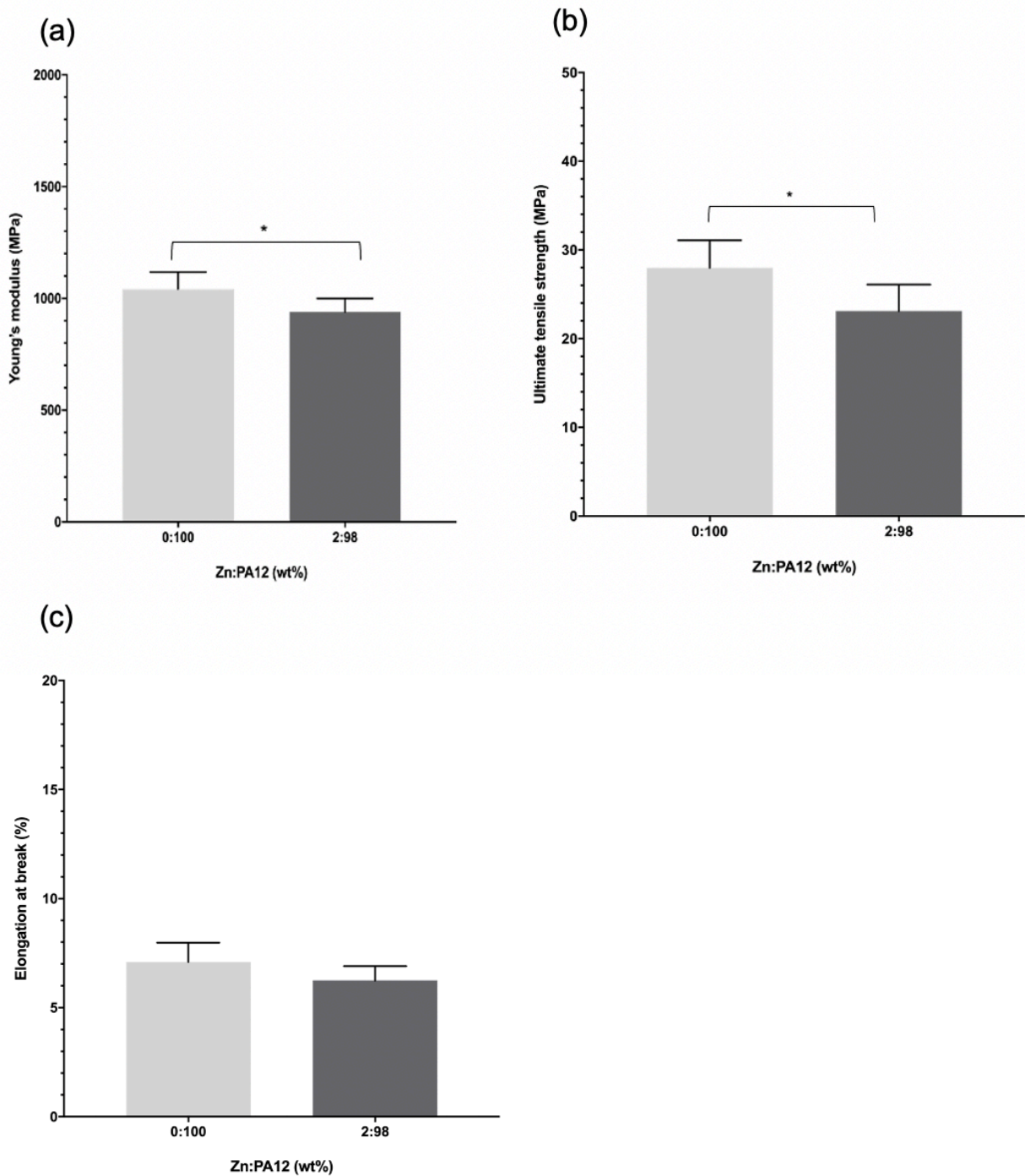


Figure 5.11. The tensile properties: (a) Young's modulus (E), (b) Ultimate tensile strength (σ_{UTS}) and elongation at break (ϵ_{max}) of laser sintered samples composed of 0:100 and 2:98 wt% zinc: polyamide 12 (Zn:PA12). Error bars: $\pm SD$, $n=5$. Statistical analysis using an unpaired T-test. Statistical significance * $p < 0.05$.

Table 5.5. Tensile properties for high speed sintered samples composed of 0:100 and 2:98 wt% zinc: polyamide 12 (Zn:PA12)

Zn:PA12 (wt%)	E (MPa)	σ_{UTS} (MPa)	ϵ_{max} (%)
0:100	1042±76	28.0±3.1	7.1±0.9
2:98	939.0±60	23.1±3.0	6.3±0.7

Figure 5.11 and Table 5.5 show the tensile properties, (a) E , (b) σ_{UTS} and (c) ϵ_{max} , of HSS 0:100 and 2:98 wt% Zn:PA12 samples. The E values ranged from 939 to 1042 MPa, representing that the addition of Zn lead to a significant decrease in the stiffness of the HSS samples. The σ_{UTS} ranged from 23.1 to 28.0 MPa, showing that there is a significant decrease in the tensile strength of the material with the addition of Zn. Zn has a slight effect on the ϵ_{max} which ranged from 6.3 to 7.1 %. The variance is moderate for all the values, showing relative homogeneity in the printing process. As predicted the change in sintering parameters significantly increased the tensile properties in comparison to the mechanical properties of the parts fabricated on HSS using the old processing parameters. In section 4.3.6, the PA12 control had a E of 639.40 MPa, 12.34 MPa σ_{UTS} and 3.98 % ϵ_{max} . The new processing parameters increased the E by 402.6 MPa, the σ_{UTS} by 15.64 MPa and the ϵ_{max} by 3.12. Both the LS and HSS showed a decrease in the E , the σ_{UTS} and ϵ_{max} compared to the PA12 controls. However, HSS 2:98 wt% Zn:PA12 samples have tensile properties higher than that of Medpor® implants and comparable tensile properties of cancellous bone¹¹. Thus, both LS and HSS 2:98 wt% Zn:PA12 have potentially sufficient mechanical strength to support the eye globe and the orbital content.

5.3.5 Flexural properties

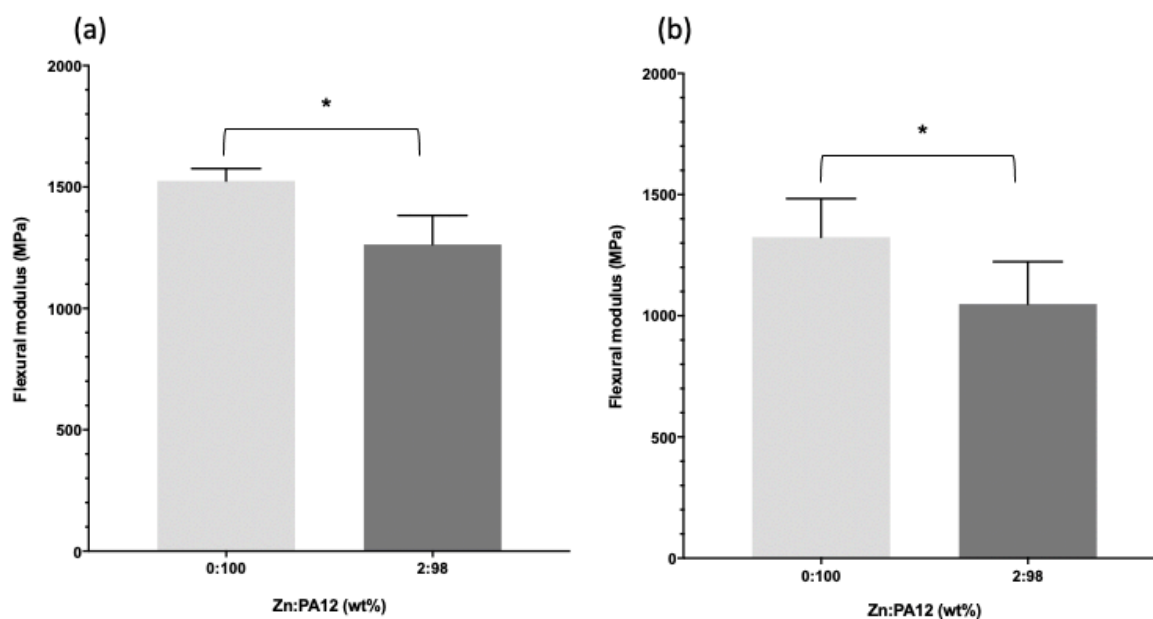


Figure 5.12. Flexural modulus of (a) laser sintered and (b) high speed sintered samples composed of 0:100 and 2:98 wt% zinc: polyamide 12 (Zn:PA12). Error bars: \pm SD, $n=5$. Statistical analysis using unpaired T-test. Statistical significance * $p < 0.05$.

Table 5.6. Flexural modulus values for laser sintered and high speed sintered samples composed of 0:100 and 2:98 wt% zinc: polyamide 12 (Zn:PA12).

Zn:PA12 (wt%)	Flexural modulus (MPa)	
	Laser sintering	High speed sintering
0:100	1525 \pm 51	1324 \pm 160
2:98	1263 \pm 120	1048 \pm 175

Chapter 5

Figure 5.12 (a) and Table 5.6 shows the mean flexural modulus of LS 0:100 and 2:98 wt% ZnO:PA12 samples. The values range from 1263 to 1525 MPa denoting that Zn marginally reduced the flexural modulus of the material. The variance was relatively narrow demonstrating that the LS process produced relatively homogeneous parts. The flexural modulus values for the LS PA12 control (0:100 wt% Zn:PA12) here is 353 MPa lower than the PA12 control in section 4.3.7. Therefore, the effect of polymer aging on the mechanical properties need to be further investigated. Despite the decrease in overall flexural modulus the 2:98 wt% Zn:PA12 samples were similar in flexibility to the natural orbital floor bone^{1, 2} indicating that this composition is likely to be firm enough to support the eye globe and the orbital content. The small spread in values were also observed in previous literature and the results reported in section 4.3.7. In Chapter 4, HA increased the stiffness of the material however, here it can be seen that Zn decreased the stiffness of the material.

Figure 5.12 (b) and Table 5.6 shows the mean flexural modulus of HSS samples. The values range from 1048 to 1324 MPa. The variance in values was slightly larger than the LS samples demonstrating that the HSS prints were marginally less homogeneous than the LS prints. The flexural modulus for the PA12 control (0:100 wt% Zn:PA12) in section 4.3.7 is lower than the flexural modulus of the HSS PA12 control here, showing that the new processing parameters lead to an increase in the flexural modulus of the material. As with the LS samples, the addition of Zn lead to a significant decrease in flexural modulus however, the samples were still within the same flexibility as the natural orbital floor bone^{1, 2}.

5.4 Evaluation of antibacterial properties of Zn:PA12 parts

The last objective for this Series was to evaluate the antibacterial activity of the parts produced against *Staphylococcus aureus* (*S. aureus*). The results are based on the methodology introduced in section 3.8.

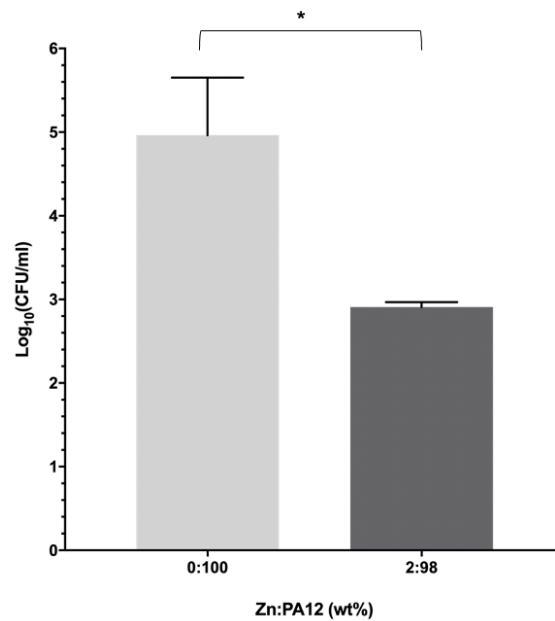


Figure 5.13. Number of viable *Staphylococcus aureus* (*S. aureus*) attached to laser sintered discs composed of 0:100 and 2:98 wt% zinc: polyamide 12 (Zn:PA12) after 24 h incubation. $N=1$, $n=3$. Error bars \pm SD. Statistical analysis using unpaired T-test. Statistical significance * $p < 0.05$.

Figure 5.13 shows a statistically significant 2-log (99 %) reduction in colony forming units (CFU) of *S. aureus* (S235) attached to the discs after 34h incubation compared to the PA12 control (0:100 wt% Zn:PA12). Typically, antibiotics (or bactericidal materials) are required to illicit a ≥ 3 log reduction in number of viable bacteria (≥ 99.9 %). However, the aim of the addition of an antibacterial agent in this research is to

Chapter 5

prevent the growth of bacteria on the implant. Such materials are known as bacteriostatic. Typically, bacteriostatic materials result in a 1 to 2-log reduction (90- 99 %) ^{272, 273} in the CFU measured. Therefore, LS 2:98 wt% ZnO:PA12 demonstrated bacteriostatic effects. Research conducted on Zn/ bioactive glasses have shown that depending on the concentration, the release of Zn²⁺ can take more than 24 hours ²⁷⁴. Therefore, it would be interesting to investigate longer incubation periods to see whether the antibacterial activity of the samples increases over time.

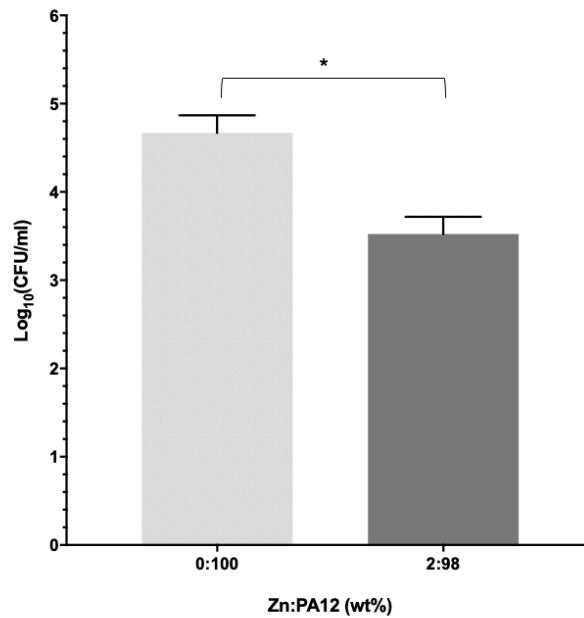


Figure 5.14. Number of viable *Staphylococcus aureus* (*S. aureus*) attached to high speed sintered discs composed of 0:100 and 2:98 wt% zinc: polyamide 12 (Zn:PA12) after 24 h incubation. $N=1$, $n=3$. Error bars \pm SD. Statistical analysis using unpaired *T*-test. Statistical significance * $p<0.05$.

The antibacterial activity of HSS 2:98 wt% Zn:PA12 against *S. aureus* showed a statistically significant 1.2-log reduction in CFU compared to the PA12 control. Like the LS samples, the HSS samples showed a bacteriostatic effect although not as great

Chapter 5

as the LS samples. It has been reported that an increase in surface roughness does not only provide an increase in surface area for cell attachment but also for bacterial colonisation²⁷⁵⁻²⁷⁸. Even though the specific surface area was not measured for the samples in Chapters 5 and 6, it can be assumed from the specific surface area measurements of the HA:PA12 compositions and the SEM micrographs in section 5.3.2, that the HSS samples had a higher surface area than the LS samples. The cell viability and DNA quantification results in section 4.5.2 showed that even though it was expected for the HSS samples to have a higher biocompatibility and DNA content, as indication of cell number, than LS sample due to their higher surface area this was not the case. The HSS samples were covered in Radiation Absorbing Material (RAM) which could be potentially interfering with the antibacterial activity of the Zn. Another potential explanation as to why there is a reduction in the antibacterial activity of HSS samples compared to LS samples may be that the RAM ink covering the particles could be reducing the rate of release of Zn²⁺ therefore once again investigating longer incubation periods may give an indication of the release rate of Zn²⁺ over time.

The LS 2:98 wt% Zn:PA12 samples showed a larger reduction in *S. aureus* attachment than the HSS samples. However, both LS and HSS samples showed a bacteriostatic effect against *S. aureus*. Therefore, the addition of Zn has been found to decrease the attachment of *S. aureus* bacteria and thus potentially decreasing the chances of implant associated infections.

5.5 Summary

Chapter 5

As predicted from the morphology investigations the Zn did not prevent good processability. The dimensional accuracy of the LS and HSS parts showed that all the processed samples had marginally different dimensions compared to CAD model. As with the HA:PA12 samples, further test trials are required to calculate the shrinkage compensation when manufacture of real-life. The characterisation of the crystal structure revealed that the Zn crystal structure remains unchanged after processing. The surface topography analysis showed the addition of Zn was fairly evenly distributed on the surface of both LS and HSS samples which is an indication that the antibacterial properties of Zn was likely to be homogeneous on the surface of the sample. It also showed that the addition of Zn increased the porosity and surface cavities of the samples. The HSS 2:98 wt% Zn:PA12 samples had a porosity within the optimal range^{235, 240-243} to allow for bone ingrowth and vascularisation. However, an increase in porosity affected the mechanical properties of the LS and HSS sample. Nonetheless, the results showed both the LS and HSS 2:98 wt% Zn:PA12 had similar values to modulus and σ_{UTS} to cancellous bone¹¹, higher modulus and σ_{UTS} than commercially available Medpor® implants^{258, 259} and a flexibility comparable to the natural orbital floor bone. This indicates that implants manufactured from these compositions are likely to have a promising potential in orbital floor reconstruction applications.

The antibacterial investigations showed that the LS and HSS 2:98 wt% Zn:PA12 had bacteriostatic effects against *S. aureus* compared to the PA12 control. LS samples showed a larger reduction in *S. aureus* attachment however both LS and HSS samples could potentially be useful in preventing implant associated infections.

6 Results and discussion: antimicrobial: bioactive ceramic: polymer compositions

The final Chapter was focused on determining the effect of the combination of hydroxyapatite (HA) and zinc (Zn) with the polyamide 12 (PA12). The results obtained are discussed in this chapter. The main objectives are:

- To assess the processability of the selected compositions of Zn:HA:PA12 on laser sintering (LS) and high speed sintering (HSS).
- To determine the effect of the combination of HA and Zn on the physical and mechanical properties for all the compositions that could be processed.
- To evaluate the antimicrobial activity of the parts produced.
- To determine whether the addition of HA has an impact on the biocompatibility of the processed parts.

6.1 Processability

Firstly, the thermal characteristics of Zn:HA:PA12 compositions were assessed in order to identify whether the addition of both Zn and HA affect the processing window and thus the processability of the powders.

6.1.1 Thermal analysis

The differential scanning calorimeter (DSC) curve and melt characteristics of the Zn:HA:PA12 compositions are shown in Figure 6.1 and Table 6.1, respectively.

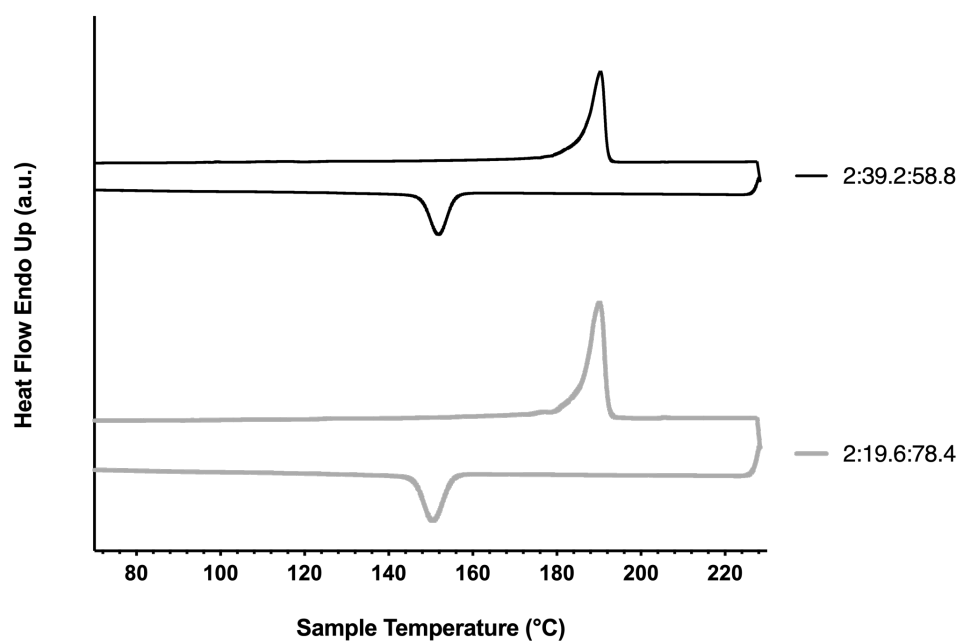


Figure 6.1. Differential scanning calorimeter (DSC) curves of zinc: hydroxyapatite: polyamide 12 (Zn:HA:PA12) powder compositions.

Table 6.1. Melting and crystallisation onset temperatures of zinc: hydroxyapatite: polyamide 12 (Zn:HA:PA12) powder compositions.

Zn:HA:PA12 (wt%)	Melting temperature onset (°C)	Melting temperature (°C)	Crystallisation temperature onset (°C)	Crystallisation temperature (°C)	Processing window (°C)
0:0:100	181	192	158	150	23
2:19.6:78.4	180	191	158	150	23
2:39.2:58.8	180	191	158	151	22

Chapter 6

Both the curves show a gap between the melting and crystallisation peaks. The value for the melting temperature onset ($T_{m_{onset}}$) is 180 °C for 2:19.6:78.4 and 2:39.2:58.8 wt% Zn:HA:PA12, the melting temperature (T_m) is 191 °C for both compositions, the crystallisation temperature onset ($T_{c_{onset}}$) is 158 °C and the crystallisation temperature (T_c) range from 150 to 151 °C. The processing window is 23 °C for 2:19.6:78.4 wt% Zn:HA:PA12 and 22 °C for 2:39.2:58.8 wt% Zn:HA:PA12, only 1 °C lower than the PA12 control, indicating that the combination of Zn and HA has a marginal effect on the melt characteristics of the material. These results were similar to the melt characteristics of HA:PA12 and Zn:PA12, shown in sections 4.1.2 and 5.1.2, respectively, denoting that the default processing parameters for PA12 could potentially be used in the initial printing trials.

6.2 Printability

Despite the additives having a marginal effect on the melt characteristics, it can still be expected that the combination of both the additives can, but is unlikely, to affect the printability of the material. Section 6.2 explores the processability of 2:19.6:78.4 wt% Zn:HA:PA12 by LS and 2:39.2:58.8 wt% Zn:HA:PA12 by HSS.

Chapter 6

6.2.1 Laser sintering



Figure 6.2. Laser sintered tensile test bars composed of 0:100 and 2:19.6:78.4 wt% of zinc: hydroxyapatite: polyamide 12. Scale bar= 20 p coin.

The processability of a polymer with an osteoconductive material and an antimicrobial agent on LS is a novel technique. The results obtained here show that 2:19.6:78.4 wt% Zn:HA:PA12 can be successfully processed using the default processing parameters on LS. The tensile test samples in Figure 6.2 show that the 2:19.6:78.4 wt% Zn:HA:PA12 were grey/blue in colour due to the addition of the Zn and HA.

Chapter 6

6.2.2 High speed sintering

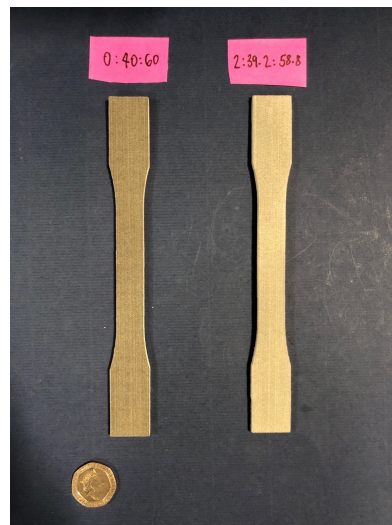


Figure 6.3. High speed sintered tensile test bars composed of 0:100 and 2:39.2:58.8 wt% of zinc: hydroxyapatite: polyamide 12. Scale bar= 20 p coin.

Like LS, the HSS of polymer: osteoconductive material: antimicrobial agent composites have not been previously explored in literature. The results obtained in this section show that 2:39.2:58.8 wt% Zn:HA:PA12 was successfully processed on HSS using the new default processing parameters (discussed in section 5.2). Figure 6.3 shows the 2:39.2:58.8 wt% Zn:HA:PA12 has a lighter grey colour than the PA12 control, which is likely to have been caused by the colour of the additives.

6.3 Effect on the physical and mechanical properties

In order to assess the effect of the additives on the physical and mechanical properties on the samples, the dimensional accuracy, surface topography, characterisation of chemical composition, tensile properties and flexural properties were tested. Due to

Chapter 6

COVID-19 restrictions the additive distribution and the surface area analysis could not be investigated.

6.3.1 Dimensional accuracy

The mean dimensions of 3-point bend bars processed by LS from 0:20:80 and 2:19.6:78.4 wt% Zn:HA:PA12 are shown by Table 6.2 and for HSS from 0:40:80 and 2:39.2:58.8 wt% Zn:HA:PA12 is shown by Table 6.3.

Table 6.2. Part dimensions of laser sintered 3-point bend bars composed of different wt% of zinc: hydroxyapatite: polyamide 12 (Zn:HA:PA12). The expected values were defined in the CAD model. The measurements were conducted on 5 samples.

Zn:HA:PA12 (wt%)	Width (mm)	SD	% difference	Thickness (mm)	SD	% error	Length (mm)	SD	% difference
CAD	13.00	-	-	4.00	-	-	60.00	-	-
0:20:80	12.85	0.09	1.15	4.23	0.04	5.83	60.07	0.05	0.11
2:19.6:78.4	12.93	0.12	0.56	4.46	0.05	10.58	60.17	0.11	0.28

The width, thickness and length range from 12.85 to 12.95 mm, 4.23 to 4.46 mm and 60.07 to 60.17 mm, respectively. The variances in values are moderately small denoting homogeneity in production through the LS prints. The percent difference for the width, thickness and length ranges from 0.66 to 1.15 %, 5.83 to 10.58 % and 0.11 to 0.28 %, respectively. Therefore, the addition of both additives shows a small effect on the accuracy of the parts. A marginal change in dimension was also observed for HA:PA12 parts in 4.3.1 and Zn:PA12 parts in section 5.3.1. As mentioned in section 2.5.2, the accuracy of the parts can be increased by calculating the shrinkage compensation from test trials.

Chapter 6

Table 6.3. Part dimensions of high speed sintered 3-point bend bars composed of different wt% of zinc: hydroxyapatite: polyamide 12 (Zn:HA:PA12). The expected values were defined in the CAD model. The measurements were conducted on 5 samples.

Zn:HA:PA12 (wt%)	Width (mm)	SD	% difference	Thickness (mm)	SD	% error	Length (mm)	SD	% difference
CAD	13.00	-	-	4.00	-	-	60.00	-	-
0:40:60	12.91	0.06	0.88	4.00	0.04	0.63	58.83	0.07	1.95
2:39.2:58.8	12.98	0.12	0.59	3.97	0.04	0.73	58.96	0.16	1.73

The mean width, thickness and length for HSS 3-point bend bars range from 12.89 to 12.91 mm, 3.97 to 4.00 mm and 58.83 to 58.96 mm, respectively. The variance in values across the builds are small, showing the homogeneity of the printing process. The percent difference for the width, thickness and length ranges from 0.59 to 0.88 %, 0.63 to 0.73 % and 1.73 to 1.95 %, respectively, demonstrating that the addition of both the additives have a minor effect on the dimensional accuracy of HSS samples. A minor effect on the dimensional accuracy was also observed above in the chapters 4 for HSS HA:PA12 samples and chapter 5 for HSS Zn:PA12 samples. As mentioned above (section 6.3.1), test trails are required when designing real-life parts to compensate for the shrinkage in the material.

Chapter 6

6.3.2 Surface topography analysis

In order to obtain osteoconductive and antibacterial properties it was important that the additives were evenly distributed on the surface of the samples. The surface distribution of additives was assessed by scanning electron microscopy (SEM).

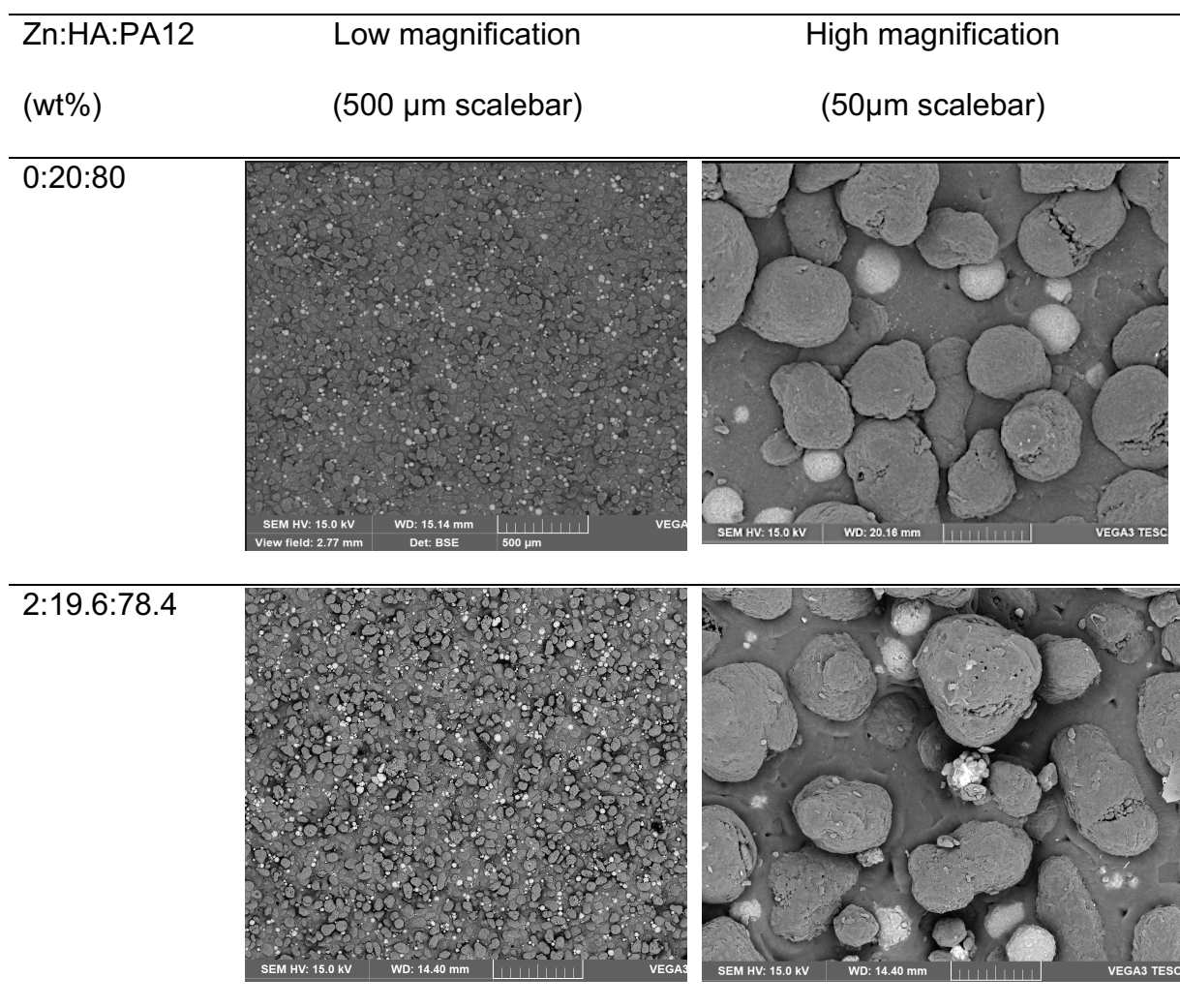


Figure 6.4. Backscattered electrons (BSE)- Scanning electron microscopy (SEM) micrographs of laser sintered discs composed of 2:19.6:78.4 wt% zinc: hydroxyapatite: polyamide 12 (Zn:HA:PA12). Taken at x500 and x1000 magnifications.

Chapter 6

Figure 6.4 shows SEM micrographs taken at x500 and x1000 magnifications of LS 0:20:80 and 2:19.6:78.4 wt% Zn:HA:PA12 discs. The HA and the Zn particles are white in colour while the PA12 are grey in colour. The additives appear relatively well distributed on the surface of LS samples. The additives appeared to increase the surface cavities and particle coring which is likely to increase the surface area of the samples and hence bone-to-implant contact (BIC). A similar trend was also observed in section 4.3.2 and 5.3.2, for HA:PA12 and Zn:PA12, respectively. It is more difficult to distinguish between the Zn and HA particles as both particles have a higher atomic number than PA12 and thus appear brighter. In order to determine the elemental composition of the surface of the samples, SEM-energy dispersive X-ray (EDX) microanalysis was used.

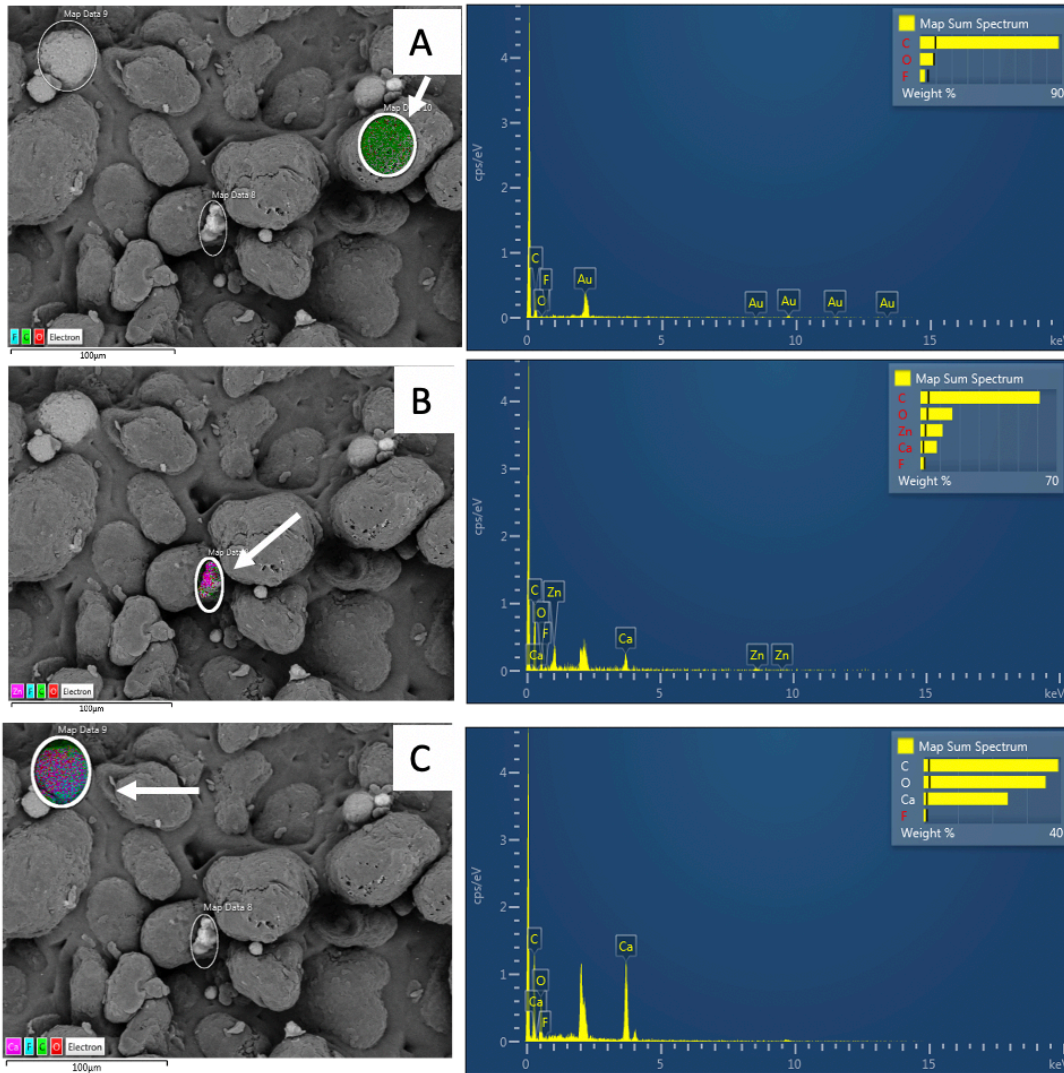


Figure 6.5. Energy Dispersive X-ray (EDX)- Scanning electron microscopy (SEM) analysis of laser sintered 2:19.6:78.4 wt% zinc: hydroxyapatite: polyamide 12 (Zn:HA:PA12).

Figure 6.5 show EDX-SEM micrographs and spectra of LS 2:19.6:78.4 wt% Zn:HA:PA12. Spectrum (A) shows the presence of carbon (C) and oxygen (O) which are elements present in PA12. It also fluorine (F) but it is not significant, which could be a residue from the PA manufacturing machinery. The gold (Au) peaks are predicted to be from the gold coating. Spectrum (B) shows the presence of a Zn indicating that this is a Zn particle. The spectrum also shows the presence of C, O, calcium (Ca)

Chapter 6

which may be residues from the PA12 and HA particles and non-significant F. Spectrum (C) shows the presence of Ca and O, indicating that this is a HA particle. The C can be a residue from the PA12 particles.

Figure 6.6 shows -SEM micrographs of 0:40:60 and 2:39.2:58.8 wt% Zn:HA:PA12.

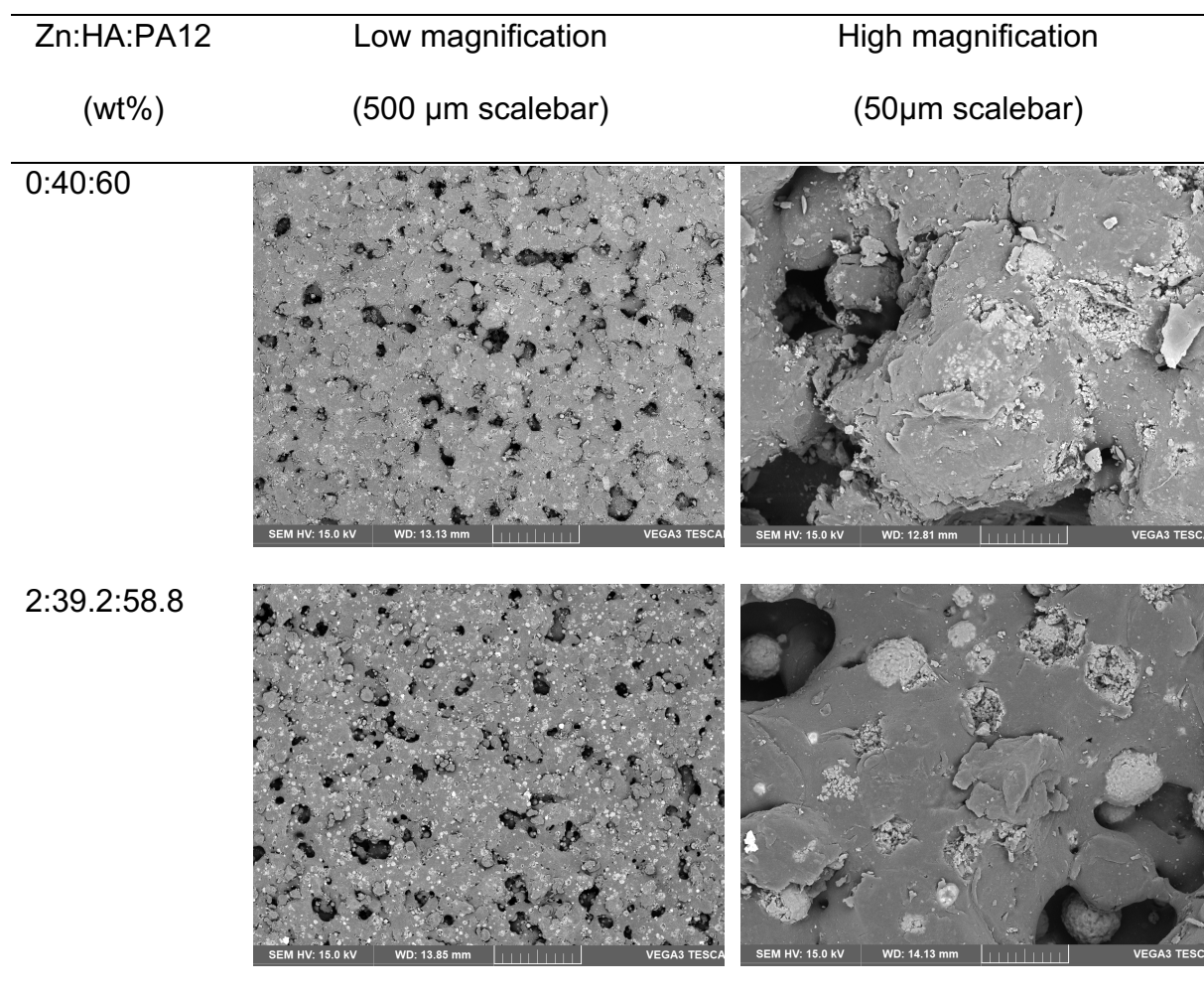


Figure 6.6. Backscattered electron (BSE)- Scanning electron Scanning electron microscopy (SEM) micrographs of high speed sintered discs composed of different wt% zinc: hydroxyapatite: polyamide 12 (Zn:HA:PA12). Taken at x500 and x1000 magnifications.

Chapter 6

The brighter particles show HA and Zn additives while the grey particles are of PA12. The additives appear to be relatively well distributed on the surface. The addition of the additives appears to increase the porosity of the samples. The porosity is overall higher for HSS samples than LS samples, which is likely to increase the surface area of the sample but is predicted to decrease the mechanical properties of the material. This was also observed for the HSS samples in section 4.3.2 for HA:PA12 and section 5.3.2 for Zn:PA12. Like LS, it is difficult distinguish between HA and Zn for the HSS 2:39.2:58.8 wt% Zn:HA:PA12 samples. Therefore, EDX-SEM analysis was conducted to determine the surface elemental composition of 2:39.2:58.8 wt% Zn:HA:PA12.

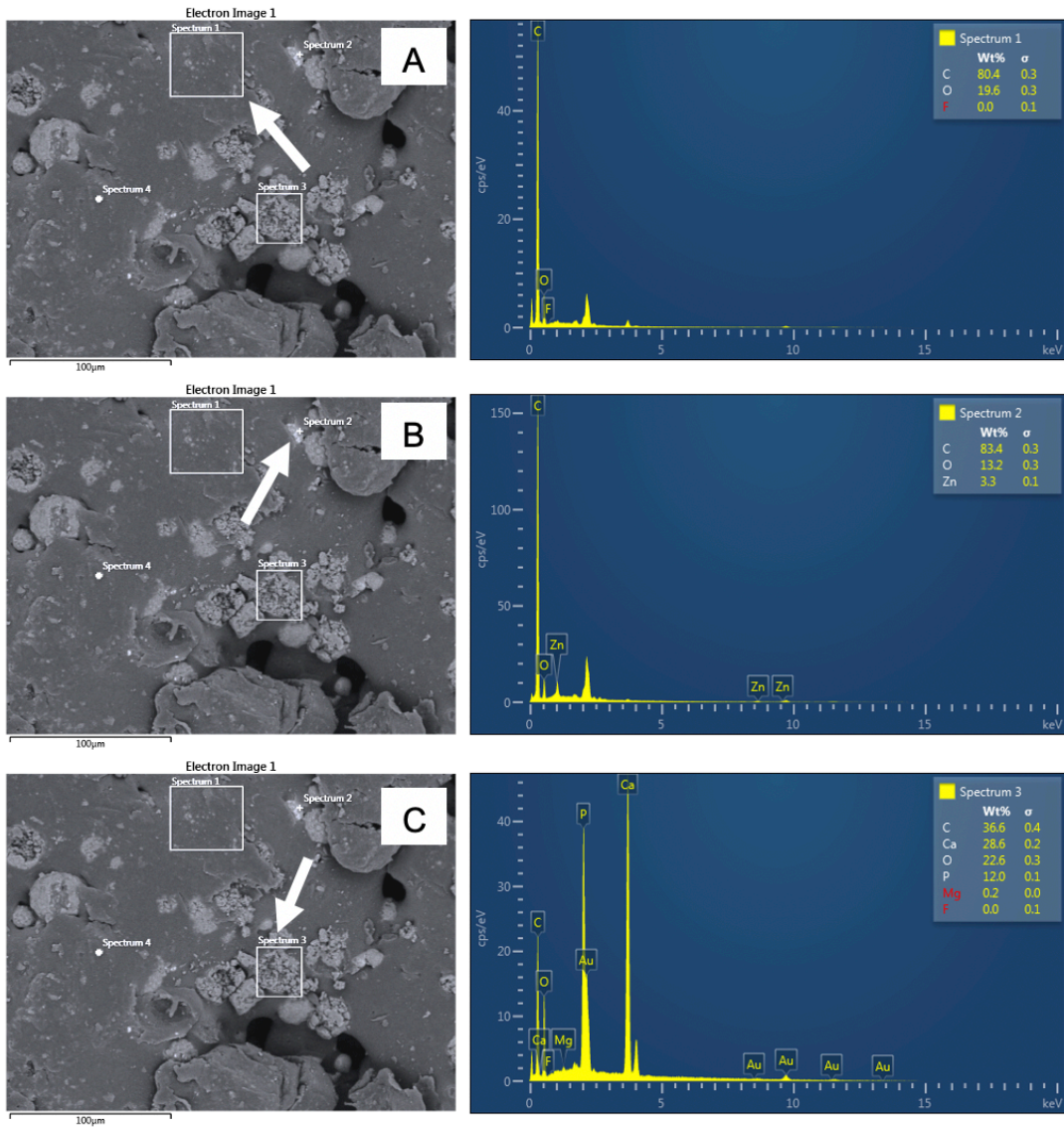


Figure 6.7. Energy Dispersive X-ray (EDX)- Scanning electron microscopy (SEM) analysis of high speed sintered 2:39.2:58.8 wt% zinc: hydroxyapatite: polyamide 12 (Zn:HA:PA12). The arrow points towards the area being analysed.

Figure 6.7 shows EDX-SEM micrographs and spectra of HSS 2:39.2:58.8 wt% Zn:HA:PA12. Spectrum (A) shows the presence of C and O which are present in PA12, indicating that this is a PA12 particle. It also shows the presence of F, however it is not significant. This may be a residue from the PA manufacturing machinery. Spectrum (B) shows the presence of Zn, indicating that this is a Zn particle. It also shows the

presence of C and O which may be residues from the PA12 particles around the Zn particle. Spectrum (C) shows the presence of Ca, O and phosphorus (P) which are present in HA, signifying that this is a HA particle. In the LS spectrum (Figure 6.6 (C)), the HA particle did not show the presence of P. This may be because the LS sample has a smaller quantity of HA and the P may have been undetectable. It also shows the presence of magnesium (Mg) and F, but they are not significant.

6.3.3 Characterisation of crystal structure

X-ray diffraction (XRD) was used to characterise the crystal structure of LS 2:19.6:78.4 wt% Zn:HA:PA12 and HSS 2:39.2:58.8 wt% Zn:HA:PA12.

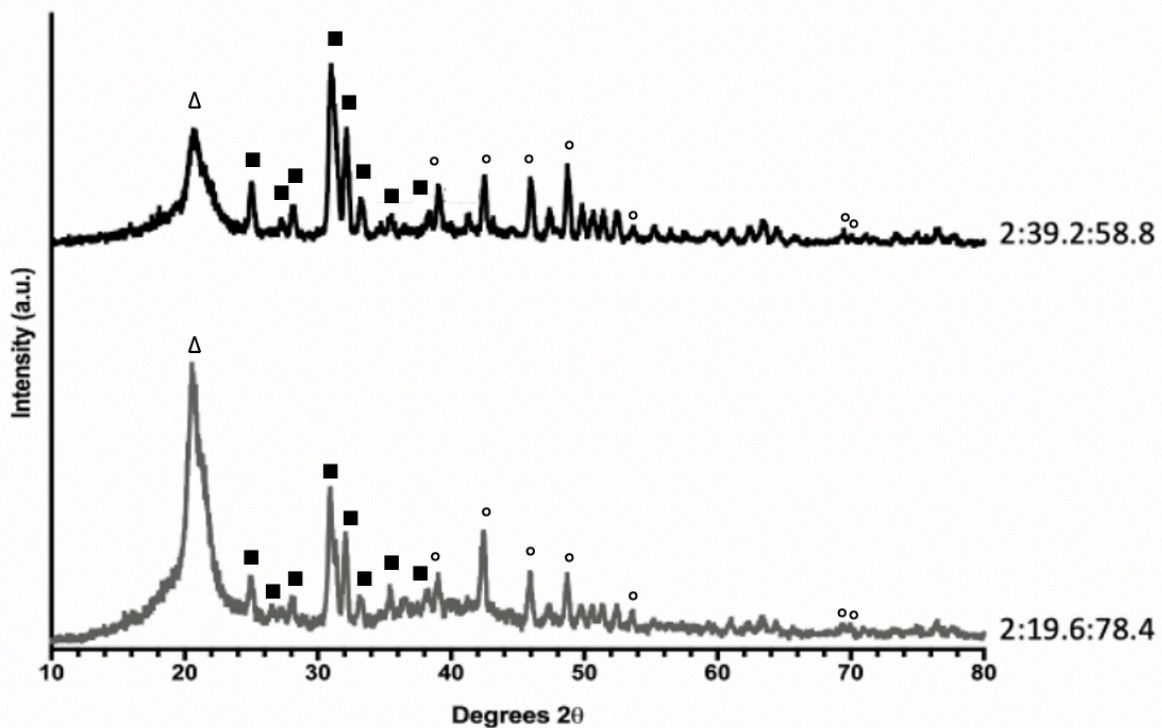


Figure 6.8. Powder X-ray diffraction (XRD) patterns of laser sintered 2:19.6:78.4 wt% zinc: hydroxyapatite: polyamide 12 (Zn:HA:PA12) and high speed sintered 2:39.2:58.8 wt% Zn:HA:PA12. Where Δ represents PA12, \blacksquare represents HA and \circ represents Zn.

Figure 6.8 confirms the presence of PA12, HA and Zn. It can be seen that the PA12 at around $2\theta = 21^\circ$ for LS 2:19.6:78.4 wt% Zn:HA:PA12 is larger than the peak PA12 peak for the HSS sample which correlated to the fact that there was more PA12 present in the LS samples. The diffraction peaks for HA between $2\theta = 25$ to 34° are larger for the HSS samples than the LS samples as there is a higher quantity of HA in the HSS sample. Like the previous results in section 4.3.5 for HA:PA12 samples and section 5.3.3 for Zn:PA12 samples, the crystal structure of the additives is predicted to have stayed the same after processing, indicating the osteoconductive properties of HA and antimicrobial properties of Zn is likely to be present in both LS and HSS samples.

6.3.4 Tensile properties

Figure 6.9 and Table 6.4 show the mean (a) Young's modulus (E), (b) ultimate tensile strength (σ_{UTS}) and (c) elongation at break (ϵ_{max}) of LS 0:0:100, 0:40:60 and 2:19.6:78.4 wt% Zn:HA:PA12 tested seven months after printing due to COVID-19 restrictions.

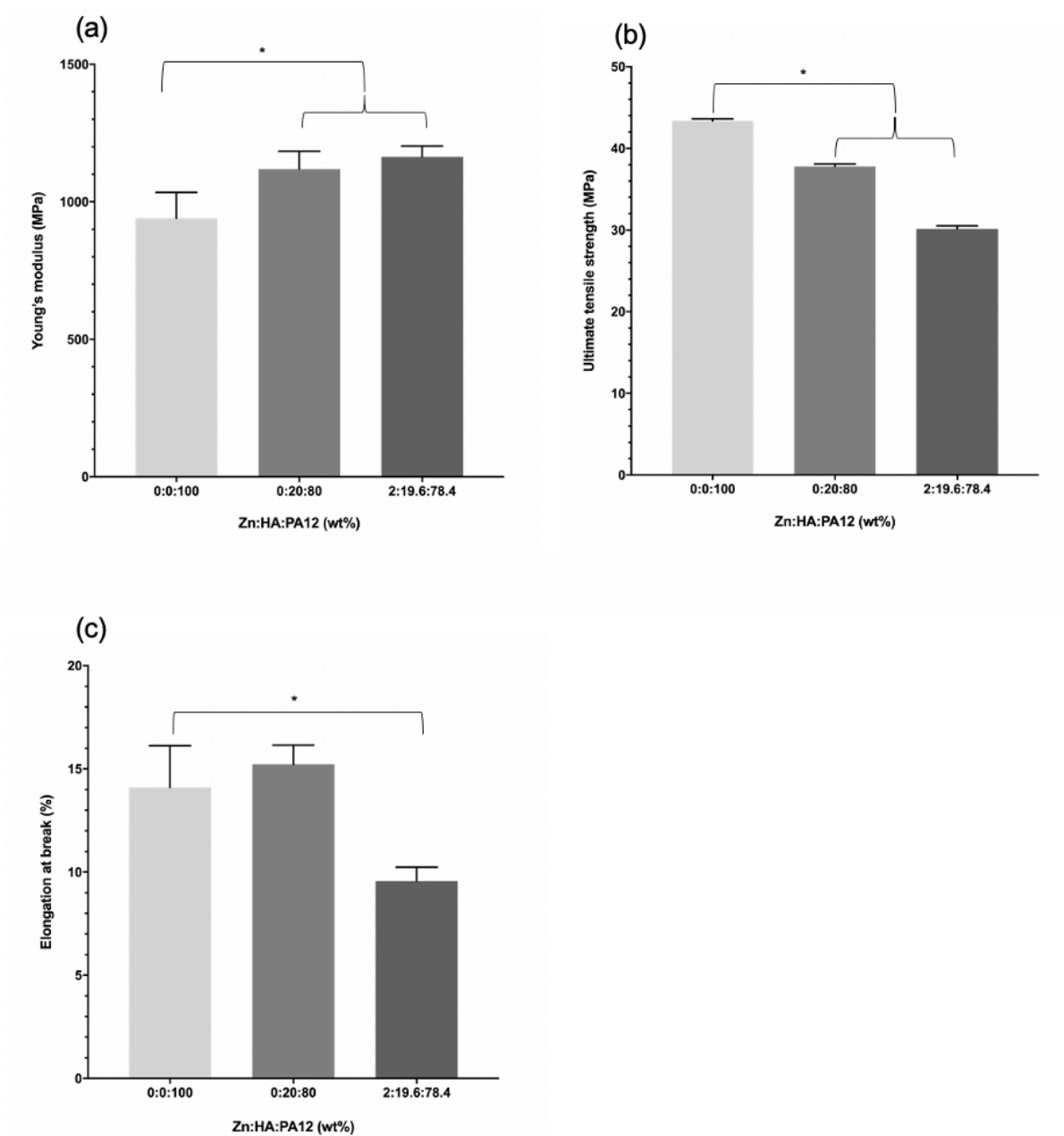


Figure 6.9. The tensile properties: (a) Young's modulus (E), (b) Ultimate tensile strength (σ_{UTS}) and elongation at break (ϵ_{max}) of laser sintered samples composed of different wt% zinc: hydroxyapatite: polyamide 12 (Zn:HA:PA12). Error bars: $\pm SD$, $n=5$. Statistical analysis using an unpaired T-test.

Table 6.4. Tensile properties for laser sintered samples composed of different wt% zinc: hydroxyapatite: polyamide 12 (Zn:HA:PA12).

Zn:HA:PA12 (wt%)	E (MPa)	σ_{UTS} (MPa)	ϵ_{max} (%)
0:0:100	940.0±93.8	43.37±0.3	14.10±2.0
0:20:80	1120±±64.4	37.79±0.3	15.22±0.9
2:19.6:78.4	1164±39.1	30.13±0.4	09.57±0.7

The values for E show a statistically significant increase from 940.0 to 1164 MPa with the addition of the additives, indicating an increase in the material stiffness. The values for σ_{UTS} show a statistically significant decrease from 43.37 to 30.13 MPa with the addition of Zn and HA, signifying that the additives decrease the tensile strength of the material. The values for ϵ_{max} range from 15.22 to 09.57 %, showing a statistically significant decrease with the addition of both Zn and HA. The moderate variance in values of E , σ_{UTS} and ϵ_{max} signifies a relative homogeneity in the fabrication process. Like the tensile properties in section 5.3.4, the E , σ_{UTS} and ϵ_{max} values presented here are lower than the values in 4.3.6, including the values for the PA12 control. Once again this may be due to the ageing of the polymer. Further work is required to investigate the effect of long-term environmental conditions on the mechanical properties of the samples. Nonetheless, the modulus and the tensile strength values were higher than that of commercially available Medpor® implants^{258, 259} and were similar to cancellous bone¹¹, indicating that these materials are potentially strong enough to be used as orbital floor implant materials. As seen in section 4.3.6 the addition of HA led to an increase in E and a decrease in σ_{UTS} and ϵ_{max} , a similar trend

Chapter 6

is seen here, however the decrease ϵ_{\max} for 0:20:80 wt% Zn:HA:PA12 is not statistically significant. A similar to the trend was seen in section 5.3.4 with the addition of Zn. However, here it can be seen that the addition of both the additives further reduces the σ_{UTS} and ϵ_{\max} which is hypothesised to be due a wider particle distribution with the addition of both the additives. In addition, as per section 5.3.2, the additives resulted in more particle coring which, as mentioned in section 2.7.1, is due to incomplete melting of the particles, leading to a reduction in the σ_{UTS} and ϵ_{\max} of the sample.

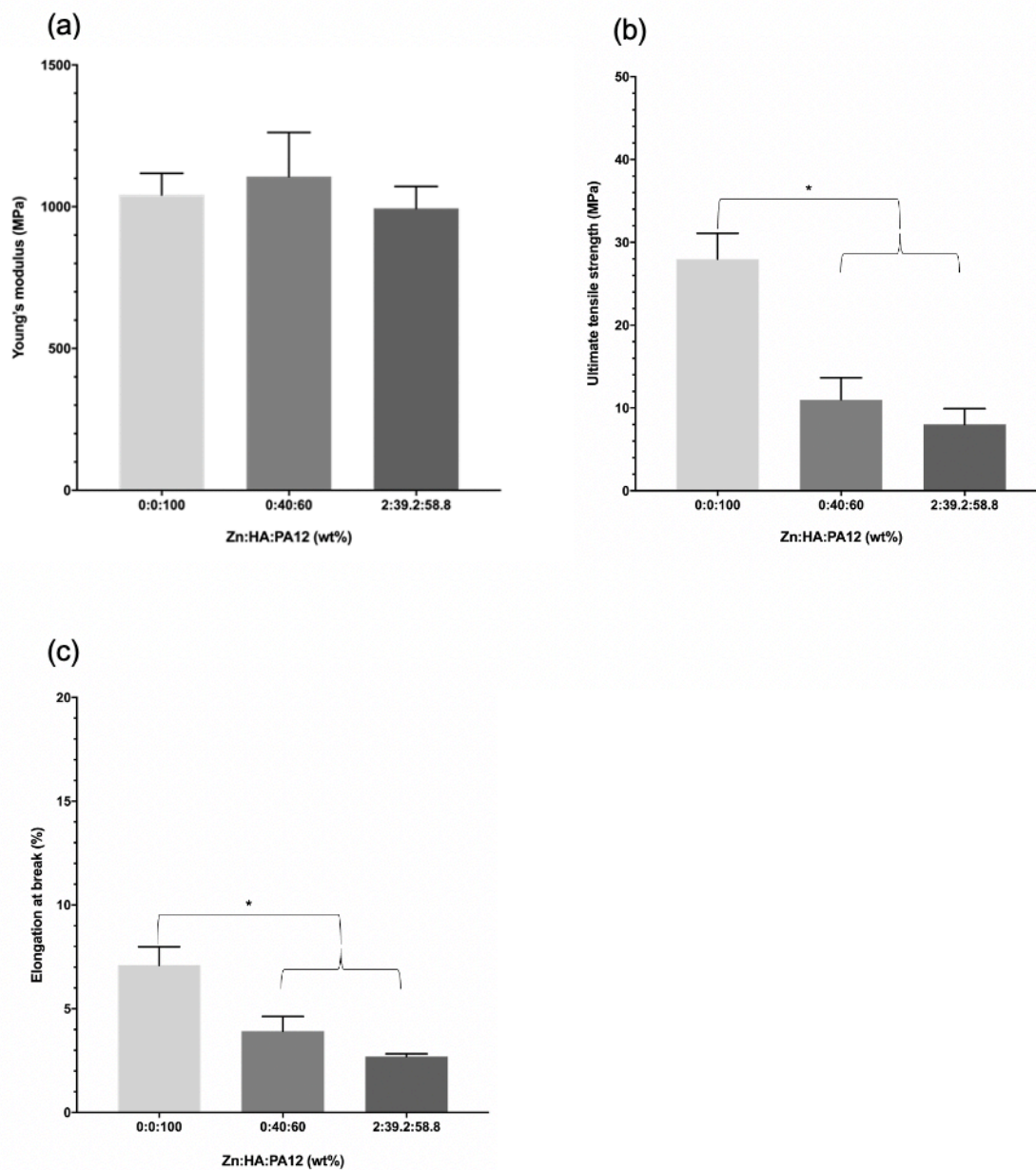


Figure 6.10. The tensile properties: (a) Young's modulus (E), (b) Ultimate tensile strength (σ_{UTS}) and elongation at break (ϵ_{max}) of high speed sintered samples composed of different wt% zinc: hydroxyapatite: polyamide 12 (Zn:HA:PA12). Error bars: \pm SD, $n=5$. Statistical analysis using an unpaired T-test.

Table 6.5. Tensile properties for high speed sintered samples composed of different wt% zinc: hydroxyapatite: polyamide 12 (Zn:HA:PA12).

Zn:HA:PA12 (wt%)	E (MPa)	σ_{UTS} (MPa)	ϵ_{max} (%)
0:0:100	1042±76	28.0±3.1	07.1±0.9
0:40:60	1107±156	11.0±2.6	03.9±0.7
2:39.2:58.8	994.0±78	08.0±1.9	02.7±0.1

Figure 6.10 and Table 6.5 show the tensile properties, (a) E , (b) σ_{UTS} and (c) ϵ_{max} , of HSS 0:0:100, 0:40:60 and 2:39.2:58.8 wt% Zn:HA:PA12. The values of E range from 994 to 1107 MPa, indicating minimal effect on the stiffness of the material. The σ_{UTS} statistically decreased from 28.0 to 08.0 MPa with the addition of both additives. The results also show a statistically significant decreased in ϵ_{max} from 07.1 to 02.7 % with the addition of Zn and HA. The moderate variance in values indicate a rather homogeneous fabrication process. The E values obtained here are similar to the E values of HSS Zn:PA12 seen in section 5.3.4. Like the LS Zn:HA:PA12 samples, the addition of both Zn and HA further reduces the σ_{UTS} and ϵ_{max} values. LS and HSS samples show marginally similar E values. The σ_{UTS} and (c) ϵ_{max} values are higher for LS samples than HSS samples. Nonetheless, both the LS 2:19.6:78.4 and HSS 2:39.2:58.8 wt% Zn:HA:PA12 had higher mechanical properties to some commercially available orbital floor reconstruction materials^{258, 259} and comparable values to cancellous bone¹¹. Therefore, it can be assumed that both the LS 2:19.6:78.4 and HSS 2:39.2:58.8 wt% Zn:HA:PA12 have sufficient strength to potentially be used as orbital floor reconstruction materials.

6.3.5 Flexural properties

The flexural modulus of LS and HSS samples composed of Zn:HA:PA12 were tested on 3-point bending in order to investigate how the addition of Zn and HA affected the way the material deflects during bending.

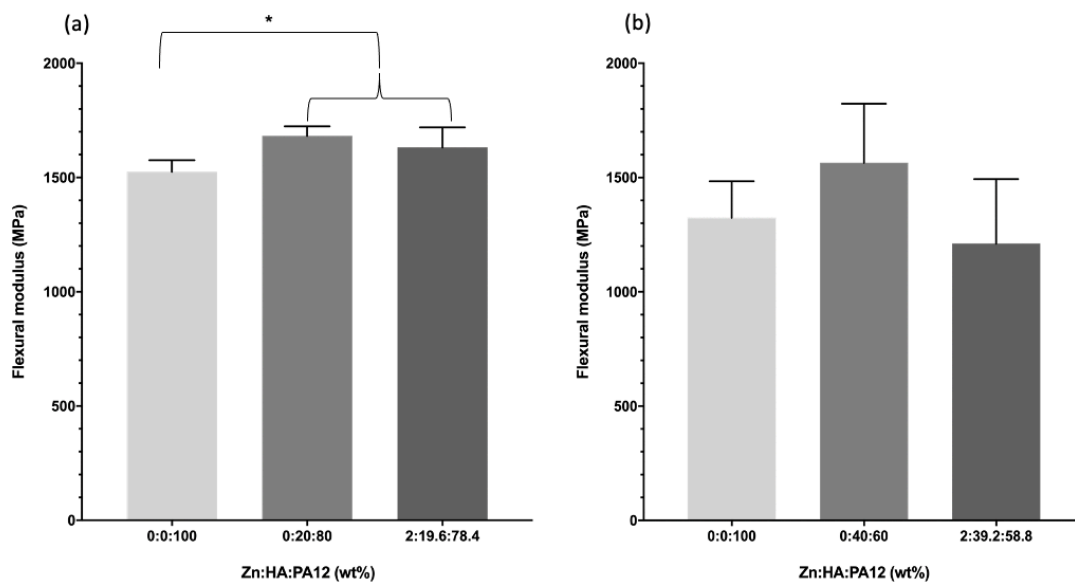


Figure 6.11. Flexural modulus of (a) laser sintered and (b) high speed sintered samples composed of different wt% of zinc: hydroxyapatite: polyamide 12 (Zn:HA:PA12). Error bars: \pm SD, $n=5$. Statistical analysis using one way ANOVA with Tukey's multiple comparison.

Table 6.6. Flexural modulus values for laser sintered and high speed sintered samples composed of different wt% zinc: hydroxyapatite: polyamide 12 (Zn:HA:PA12).

Zn:HA:PA12 (wt%)	Flexural modulus (MPa)	
	Laser sintering	High speed sintering
0:0:100	1525±51	1324±160
0:20:90	1682±42	1564±259
2:19.6:78.4	1632±87	-
2:39.2:58.8	-	1211±283

Figure 6.11(a) and Table 6.6 show the mean flexural modulus of LS Zn:HA:PA12 compositions. The results show that the addition of Zn and HA resulted in a statistically significant increase in flexural modulus from 1525 to 1682 MPa, indicating that the addition of both the additives have marginal effect on the flexural modulus of the material. There is a moderate variance in values for LS samples, representing relative homogeneity of the printing process across the builds. As mentioned in section 4.3.7, the tested flexural modulus of the orbital floor bone ranges from 1260 to 4550 MPa^{1, 2}. The results for LS 2:19.6:78.4 wt% Zn:HA:PA12 is within that range therefore implants made from this material are likely to have similar flexibility to the natural orbital floor. The results obtained here show a similar trend to the flexural modulus of HA:PA12 samples (sections 4.3.7), and unlike the Zn:PA12 samples (section 5.3.5), the addition of both additives led to an increase in the flexural modulus compared to the PA12 control.

Chapter 6

Figure 6.11(b) and Table 6.6 show the mean flexural modulus of HSS Zn:HA:PA12 compositions. The flexural modulus ranges from 1211 to 1564 MPa, showing that the addition of both additives have a minimal effect on the flexural modulus of the material. The variance in values is moderate, showing slightly reduced homogeneity in the printing process across the prints. The flexural modulus values for HSS 2:39.2:58.8 wt% Zn:HA:PA12 are similar to the natural orbital floor bone therefore, implants fabricated from this material are likely to be firm enough to support the orbital content and the eye globe. The spread in values obtained here were similar to the spread in values for the HSS samples in section 5.3.5. The variance is larger for HSS samples than LS samples which is likely to be due to the LS machine being a commercial system. The flexural modulus values for HSS Zn:HA:PA12 samples did not show a trend with the addition of the additives which was also seen in section 4.3.7 for HSS HA:PA12 samples.

6.4 Evaluate the antimicrobial properties of Zn:HA:PA12

The next objective of this Chapter is to evaluate the antimicrobial properties of the LS and HSS Zn:HA:PA12 parts against *Staphylococcus aureus* (*S. aureus*) after 24 h of incubation.

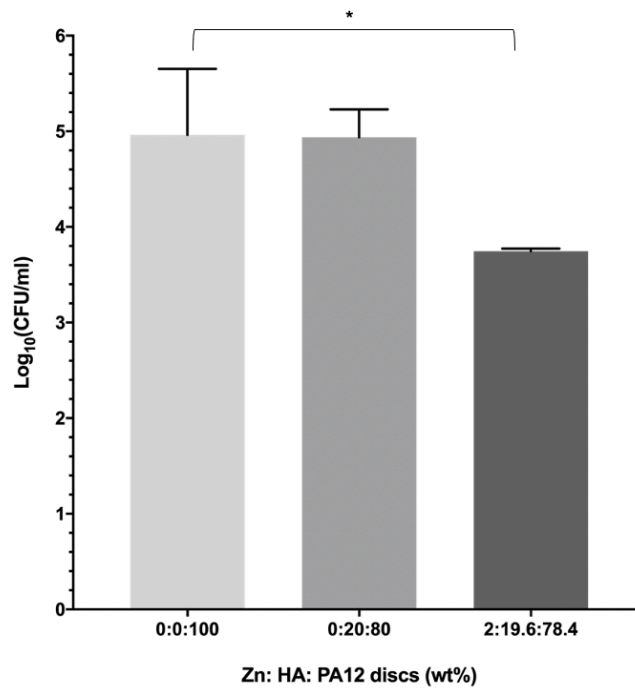


Figure 6.12. Number of viable *Staphylococcus aureus* attached to laser sintered discs composed of zinc: hydroxyapatite: polyamide 12 (Zn:HA:PA12) at different weight percentages (wt%) after 24 h incubation. $N=1$, $n=3$. Error bars \pm SD. Statistical analysis using one way ANOVA with Tukey's multiple comparison. Statistical significance * $p<0.05$.

Figure 6.12 shows a statistically significant 1.2-log reduction in colony forming units (CFU) of *S. aureus* for 2:19.6:78.4 wt% Zn:HA:PA12 compared to the PA12 control. There is not a significant reduction in CFU of *S. aureus* for 0:20:80 wt% Zn:HA:PA12 compared to the control. This indicates that only 2:19.6:78.4 wt% Zn:HA:PA12 has the bacteriostatic effect required. In section 5.4, LS 2:98 wt% Zn:PA12 samples showed a 2-log reduction in CFU of *S. aureus* attached to the discs compared to the PA12 control. The combination of Zn and HA appears to decrease the antimicrobial properties of the material. An increase in surface area has been found to increase

Chapter 6

bacterial colonisation, leading to potentially more bacterial attachment on Zn:HA:PA12 discs compared to the Zn:PA12 discs, however, this requires further investigation. Another hypothesis is that the HA may be reducing the toxicity of Zn but this also requires further investigation.

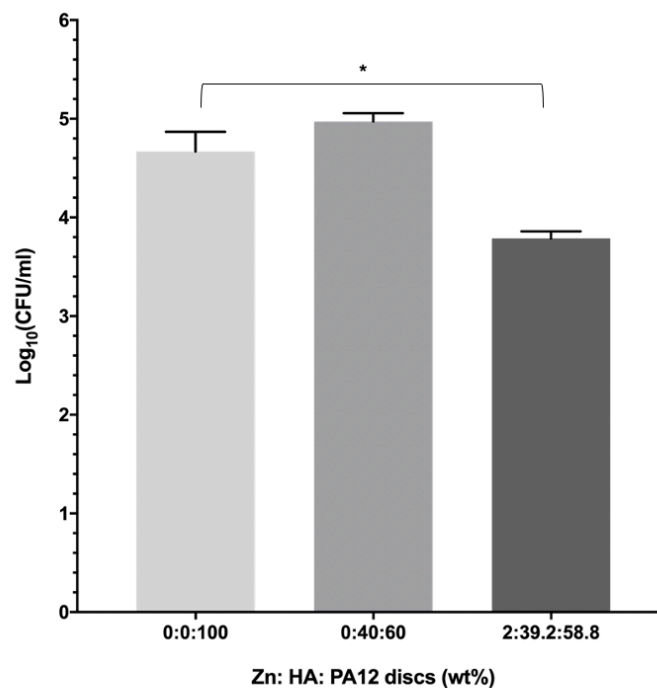


Figure 6.13. Number of viable *Staphylococcus aureus* attached to high speed sintered discs composed of zinc: hydroxyapatite: polyamide 12 (Zn:HA:PA12) at different weight percentages (wt%) after 24 h incubation. $N=1$, $n=3$. Error bars \pm SD. Statistical analysis using one way ANOVA with Tukey's multiple comparison. Statistical significance * $p<0.05$.

Figure 6.13 shows that, as expected, 0:40:60 wt% Zn:HA:PA12 did not reduce the attachment of CFU of *S. aureus* compared to the PA12 control. Despite 2:39.2:58.5 wt% Zn:HA:PA12 showing a statistically significant 0.9-log reduction in CFU of *S. aureus*, the material does not possess the bacteriostatic effect required. Section 5.4

Chapter 6

revealed that the antibacterial properties of HSS samples were lower than that of LS samples which is also observed here. This was predicted to be due to the ink which may be interfering with either the release of Zn^{2+} or the interaction of antibacterial activity of Zn.

6.5 Effect on the biocompatibility

The last objective for this Chapter was to assess how the addition of the antimicrobial agent to the bioceramics-polymer composite influences the cytotoxicity of the samples. Due to COVID-19 restrictions a higher cell seeding density (50000 cells per well) was selected to ensure less time was required for the PrestoBlue™ analysis. The results were all divided by the incubation time therefore this change was not likely to effect overall results. However ideally the same cell seeding density should have been used.

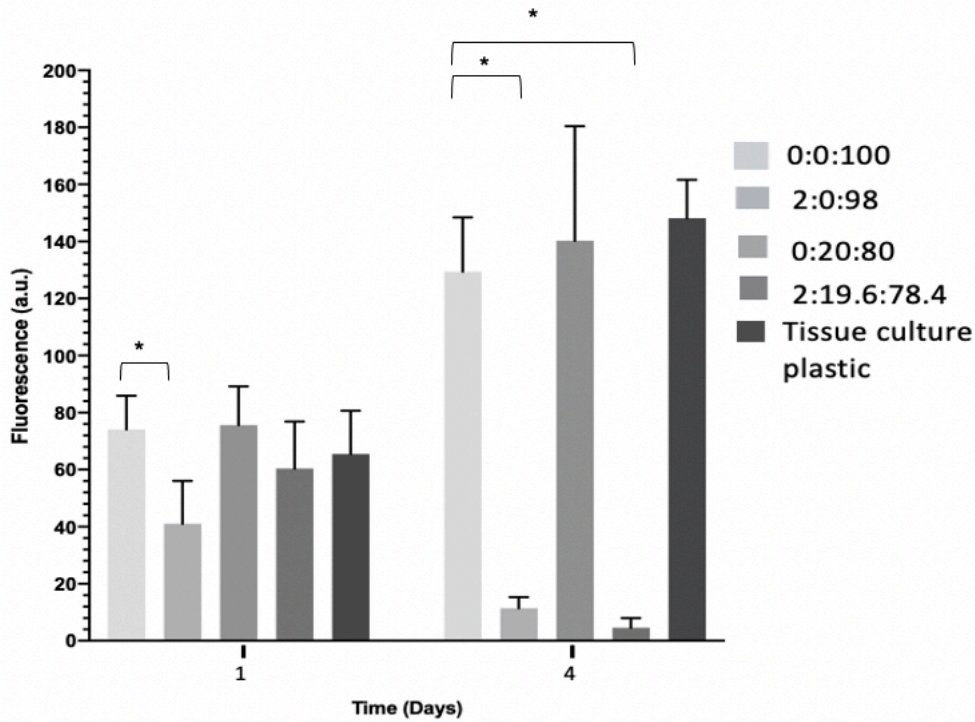


Figure 6.14. Cell viability (MG 63: PrestoBlue™) of laser sintered samples composed of zinc: hydroxyapatite: polyamide 12 (Zn:HA:PA12) at different weight percentages (wt %). 0:0:100 HA: PA12 was used as control. N=3, n=3. Error bars: \pm SD. Statistical analysis using one way ANOVA with Tukey's multiple comparison. Statistical significance * $p < 0.05$.

The mean cell viability of MG 63 cells seeded on LS Zn:HA:PA12 discs is shown in Figure 6.14. The results show a statistically significant decrease in fluorescence for 2:0:98 wt% Zn:HA:PA12 compare to the PA12 control on day 1. There is an increase in fluorescence over time for 0:0:100, 0:20:80 wt% Zn:HA:PA12 and tissue culture plastic (TCPS) and a statistically significant reduction in fluorescence over time for 2:0:98 and 2:19.6:78.4 wt% Zn:HA:PA12, indicating that Zn reduces the viability of the material. The variance in values is moderate indicating a relatively homogenous interaction between the cells and the sample. The fluorescence values for the PA12

Chapter 6

control and 0:20:80 were relatively similar to results obtained for the same compositions in section 4.5.2, indicating that the change in cell seeding density did not have a significant effect on the results. A similar spread in values was also obtained for LS HA:PA12 samples, denoting a homogeneity in the interaction between the cells and the sample. As mentioned in section 5.4, the literature suggests that it can take more than 24 h for the Zn^{2+} ions to get released and exhibit cytotoxic effects²⁷⁴ which is what was seen in the results here. The release of Zn^{2+} can have an effect on the pH of the media. Changes in the pH can be toxic to cells however, this has to be tested further. Additionally, further investigations are required to test whether there is an ideal concentration of Zn that is both biocompatible and bacteriostatic. Nevertheless, this is a proof of concept of the processability of these materials. This research has shown that these materials can be processed successfully. At this stage, it may not be used in orbital floor reconstruction applications however, it may be useful in applications such as antimicrobial surfaces.

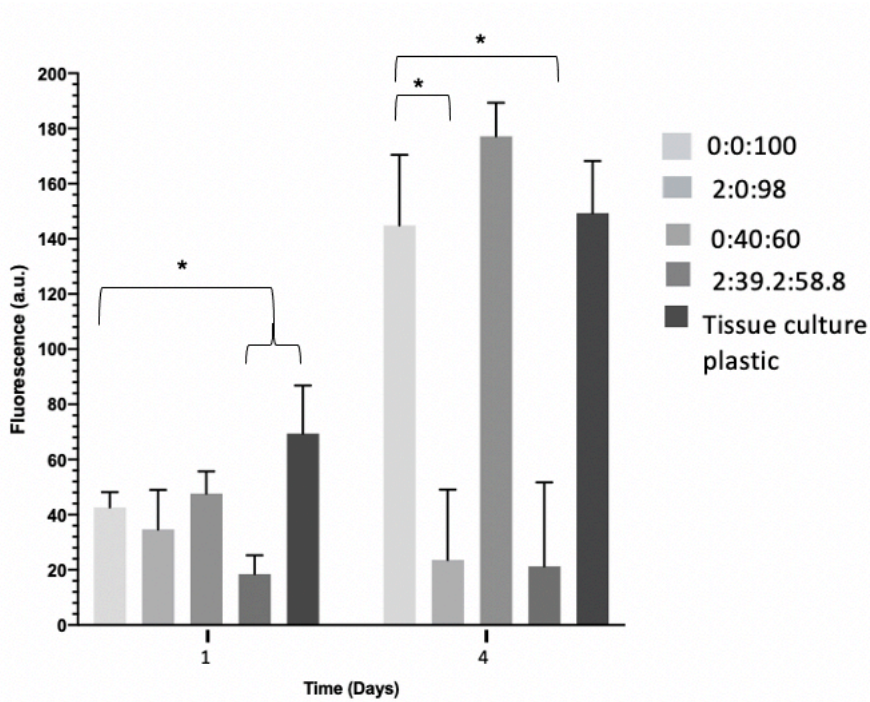


Figure 6.15. Cell viability (MG 63: PrestoBlue™) of high speed sintered samples composed of zinc: hydroxyapatite: polyamide 12 (Zn:HA:PA12) at different weight percentages (wt %). 0:0:100 HA: PA12 was used as control. N=3, n=3. Error bars: \pm SD. Statistical analysis using one way ANOVA with Tukey's multiple comparison. Statistical significance * $p < 0.05$.

Figure 6.15 shows the cell viability of MG 63 cells seeded on different compositions of Zn:HA:PA12 fabricated by HSS. On day 1, there is a statistically significant decrease in fluorescence for 2:29.2:58.8 wt% Zn:HA:PA12 compared to the control. The results show an increase in fluorescence over time for 0:0:100, 0:40:80 wt% Zn:HA:PA12 and TCPS and a statistically significant reduction in fluorescence over time for 2:0:98 and 2:39.2:58.8 wt% Zn:HA:PA12, denoting a reduction in cell viability due to the presence of Zn. The values show a relatively moderate variance, representing a moderate homogeneity in the interaction between the cells and the samples. As with the fluorescence values for the LS, the fluorescence values for the PA12 control and

Chapter 6

0:40:60 were comparable to the values obtained for the same compositions in section 4.5.2. Overall, the fluorescence values obtained for the HSS samples were lower than LS samples, indicating that LS samples are more viable than the HSS samples. A similar spread in values was obtained for HSS HA:PA12 samples, denoting a homogeneity in the interaction between the cells and the sample. Unfortunately, at this wt% of Zn, the HSS samples are not bacteriostatic nor biocompatible. The antimicrobial property investigation in Chapter 6, showed that HSS Zn:PA12 samples showed a bacteriostatic effect. Therefore, this material may not be able to be used *in vivo* at this stage but can potentially be used in other applications that require antimicrobial properties.

6.6 Summary

The default processing parameters were used to fabricate the different Zn:HA:PA12 compositions on LS and HSS. The physical and the mechanical properties of all the processed Zn:HA:PA12 samples were investigated. The dimensional accuracy investigations revealed that all the LS and HSS parts had marginally different dimensions compared to the CAD model. Thus, when printing real-life parts, test prints are required to calculate the shrinkage compensation in order to rescale the original CAD model. The surface topography analysis showed that the Zn and HA additives were relatively evenly distributed on the surface of both LS and HSS compositions, which suggests this approach is suitable for compositing. It can be predicted from the XRD results that the crystal structure of Zn and HA after processing, by LS and HSS, remained unchanged thus the samples are predicted to have osteoconductive and antibacterial properties, that are relatively well distributed on the material's surface (as

Chapter 6

seen from the SEM micrographs). The addition of Zn and HA increased the porosity of the materials which in turn led to a decrease in tensile strength and elongation at break of the LS and HSS. LS 2:19.6:78.4 and HSS 2:39.2:58.8 wt% Zn:HA:PA12 had similar E values but LS 2:19.6:78.4 Zn:HA:PA12 had superior σ_{UTS} and ϵ_{max} than HSS 2:39.2:58.8 wt% Zn:HA:PA12 samples. Nonetheless, both LS and HSS samples had a higher modulus and σ_{UTS} and then commercially available Medpor® implants^{258, 259} and similar values to cancellous bone¹¹, denoting that both these materials are likely to be suitable for orbital floor reconstruction. In addition, the flexural modulus of both LS and HSS Zn:HA:PA12 samples were similar to that of the natural orbital floor indicating that implants manufactured from these materials are likely to be firm enough to support the eye globe and the orbital content.

The antibacterial investigations showed that the LS 2:19.6:78.4 wt% Zn:HA:PA12 had a bacteriostatic effect against *S. aureus*. However, HSS 2:39.2:58.8 wt% Zn:HA:PA12 did not have a bacteriostatic effect against *S. aureus*. *In vitro* cell viability investigation revealed that both LS 2:19.6:78.4 wt% and HSS 2:39.2:58.8 wt% Zn:HA:PA12 samples had a cytotoxic effect on MG 63 cells.

7 Summary discussion and conclusions

The aim of this research was to investigate the potential use of powdered-polymer Additive Manufacturing processes (specifically laser sintering and high speed sintering) for orbital floor reconstruction applications. To achieve this, the selected materials must be readily available and able to be processed on LS and HSS into patient-specific geometries with the required dimensions. In order for a material to be suitable for orbital floor implant applications it must also have sufficient mechanical properties, ability to be sterilised before implantation and biocompatibility. Desirable properties include porosity, ideal specific surface area, osteoconductivity and antimicrobial properties. This research was set out to address each of these requirements by the inclusion of additives, such as HA and Zn, which potentially could induce the required and desirable properties in PA12 additively manufactured parts., as summarised in the following sections.

7.1 Processability on LS and HSS

In order to assess the processability, the powder morphology was evaluated, and the thermal properties of the compositions were investigated. Processing of hydroxyapatite (HA) on HSS is a novel technique that has not been explored previously in the literature. The results obtained here show that a wider range of compositions were capable of being processed on HSS than LS, where the upper limit for the quantity of HA which could be physically processed on LS was 20:80 wt%

Summary discussion and conclusions

HA:PA12 and 40:60 wt% HA:PA12 for HSS. Nonetheless, both processes were shown to be capable of producing parts at the appropriate size for orbital floor reconstruction.

7.2 Additive distribution, porosity and specific surface area

The distribution of the additive within the sample was assessed using microcomputed tomography (MicroCT) while the distribution of the additives on the surface and the porosity were assessed using scanning electron microscopy (SEM). The additives were relatively well distributed within and on the surface of the samples therefore, any effect on the properties was predicted to be evenly distributed through the geometry. The addition of the additives increased the porosity. Unlike LS samples, all the HSS samples (except the PA12 control) had pores within the optimal range for cell ingrowth (between 100- 350 μm ^{235, 240-243}). An increase in porosity increased the specific surface area. The investigations revealed that HSS 5- 40 wt% HSS HA:PA12 samples and LS 20:80 wt% HA:PA12 had a surface area similar to that of BioOss® (60 - 100 m^2/g ¹⁵⁵⁻¹⁵⁸) which is likely to trigger a higher degree of bone-to-implant contact (BIC). Thus, implants manufactured from LS 20:80 wt% HA:PA12 and HSS 5-40 wt% HA:PA12 compositions are predicted to be less likely to lead to implant migration from the fracture site^{235, 238, 239}.

7.3 Mechanical properties

The mechanical properties of the processed compositions were assessed by tensile testing and 3-point bending. An increase in porosity negatively impacted the mechanical properties of the samples due to pores acting as stress concentration sites

Summary discussion and conclusions

where cracks can initiate and propagate²³⁴⁻²³⁷. The addition of the additives led to a decrease in the ultimate tensile strength (σ_{UTS}) and elongation at break (ϵ_{max}). The LS samples had a higher modulus, σ_{UTS} and ϵ_{max} than HSS samples. However, all the processed samples both LS and HSS had comparable values to cancellous bone (ultimate strength between 0.1- 30 MPa and a modulus between 10 to 3000 MPa¹¹). In addition, the 3-point bend results showed that both processes produced parts with similar flexibility to the natural orbital floor bone (between 1260 to 4450 MPa^{1, 2}), indicating that all the compositions were more likely to be firm enough to support the eye globe and the orbital content.

7.4 Sterilisability

Implant sterilisation is an important criterion for orbital floor implants. The sterilisation investigations were conducted on LS 100% PA12 samples and showed that the samples could be steam autoclaved without permanently affecting the mechanical properties of the parts. However, the investigations revealed that moisture does affect the mechanical properties of the material. Therefore, in order to gain a better understanding of how the mechanical properties would change after implantation, further tests are required where the samples are submerged long term in physiological conditions.

7.5 Chemical composition

Analysing the chemical structure of the processed samples gives an idea of what materials are present and hence what properties are expected of the samples. The X-

Summary discussion and conclusions

ray diffraction (XRD) analysis confirmed the presence of the additives and showed that the crystal structure of the additives appeared to remain unchanged after processing. Therefore, any effects of HA and zinc (Zn), such as osteoconductive and antimicrobial properties, were likely to be present in both LS and HSS samples.

7.6 Antimicrobial capabilities

The antibacterial investigations revealed that LS 2:98 wt% Zn:PA12 was more effective against *Staphylococcus aureus* (*S. aureus*) than the HSS 2:98 wt% Zn:PA12. Nonetheless, both LS and HSS 2:98 wt% Zn:PA12 samples had a bacteriostatic effect against *S. aureus*. However, when Zn was combined with HA:PA12 samples there was a reduction in the antimicrobial activity where only LS 2:19.4:78.6 wt% Zn:HA:PA12 had a bacteriostatic effect. Therefore, implants made from this material on LS are likely to be more effective against infections than HSS samples.

7.7 Biocompatibility

In vitro cell viability tests showed that all the LS and HSS HA:PA12 samples were biocompatible, but the cell viability was higher for LS samples than HSS samples. However, when Zn was added to HA:PA12 samples, both the LS and HSS samples showed cytotoxic effects against MG 63 cells, meaning that they cannot be used in safely *in vivo*. This research is a proof of concept that HA and Zn can successfully be processed with PA12 on both LS and HSS, however, further research is required before this approach can be applied in practice.

Summary discussion and conclusions

Table 7.1 provides an overview of the compositions processed and whether they met the implant requirements or not while. Table 7.2 provides a summary of these main findings, in order to form a conclusion as to the viability of this approach for use in orbital floor reconstructions.

Table 7.1. Overview of the compositions and whether they met the implant requirements. Where ✓ means they did, ★ means some of the compositions did, ✗ means they did not and - means it was not tested.

Requirements	Process	Compositions			
		PA12	HA:PA12	Zn:PA12	Zn:HA:PA12
Processing	LS	✓	★	✓	✓
	HSS	✓	✓	✓	✓
Additive distribution	LS	-	✓	✓	✓
	HSS	-	✓	✓	✓
Porosity	LS	✗	✗	✗	✗
	HSS	✗	✓	✓	✓
Specific surface area	LS	✗	★	-	-
	HSS	✗	✓	-	-
Mechanical properties	LS	✓	✓	✓	✓
	HSS	✓	✓	✓	✓
Sterilisation	LS	✓	-	-	-
	HSS	-	-	-	-
Antimicrobial properties	LS	✗	✗	✓	✓
	HSS	✗	✗	✓	✗

Summary discussion and conclusions

Biocompatibility	LS	✓	✓	✗	✗
	HSS	✓	✓	✗	✗

Table 7. 2 Implant requirements and summary conclusions

Requirement	LS	HSS	Recommendation
Processability on LS and HSS (ESSENTIAL)	Can produce readily available samples to the required accuracy for this application but only up to 20 wt% HA.	Can produce readily available samples to the required accuracy for this application up to 40 wt% HA.	Both processes suitable but choose HSS if higher HA concentrations required.
Additive distribution (ESSENTIAL)	Additives well distributed within and on the surface of the samples.	Additives well distributed within and on the surface of the samples.	Both suitable processes.
Porosity (DESIRABLE)	The pores were smaller than the optimal pore size required for bone reconstruction applications (100- 350 µm).	The porosity of the samples was within the optimal pore size required for bone reconstruction applications (100- 350 µm).	Consider HSS if bone-implant integration is highly important. Changing processing parameters may allow tailored pore size on either process.
Specific surface area (DESIRABLE)	Only 20 wt% HA:PA12 showed a specific surface area likely to trigger a higher degree of bone formation (between 60 - 100 m ² /g).	All the HA:PA12 samples had a specific surface area which was likely to trigger a higher degree of bone formation (between 60 - 100 m ² /g).	Consider HSS if bone-implant integration is highly important. Changing processing parameters may allow tailored specific surface area on either process.
Mechanical properties (ESSENTIAL)	All samples had comparable values to cancellous bone (ultimate strength between 0.1- 30 MPa and a modulus between 10 to 3000 MPa and flexibility similar to the natural orbital floor bone (between 1260 to 4450 MPa), indicating that the samples are likely to be firm and flexible enough for orbital floor reconstruction applications.		Both processes are suitable.
Sterilisation (ESSENTIAL)	Could be sterilised without permanently effecting the mechanical properties of the samples.	Not been tested but we can assume from the investigations on LS samples that they could be sterilised without permanently effecting the mechanical properties.	Both likely to be suitable processes.
Antimicrobial properties (DESIRABLE)	All the samples showed a bacteriostatic effect against <i>S. aureus</i> .	The Zn:HA:PA12 samples did not show a bacteriostatic effect against <i>S. aureus</i> .	LS is more suitable at this stage but with further development on HSS and perhaps the use of different inks or antimicrobial agent this process may be suitable.
Biocompatibility (ESSENTIAL)	The non-Zn containing samples were biocompatible. The samples that contained Zn were cytotoxic against MG 63 cells therefore further work is required. The non-Zn containing samples were biocompatible. The samples that contained Zn were cytotoxic against MG 63 cells therefore further work is required		Investigate changing the ratios of the composition or the use of a different antimicrobial agents.

Summary discussion and conclusions

It is evident from Table 7.1 and Table 7.2 that PA12 and HA:PA12 compositions produced by both LS and HSS met all the essential criteria assessed in this work to be used in orbital floor implants indicating that both LS and HSS processes have shown a clear potential in the fabrication of an implant for orbital floor reconstruction application. As the LS Zn:HA:PA12 samples have shown bacteriostatic effects but were cytotoxic, further work can be conducted to investigate whether there is an optimal Zn:HA:PA12 ratio that has a bacteriostatic effect and is biocompatible. Specific suggestions for further work can be found in Section 7.8.

7.8 Future work

1. Properties of LS and HSS parts are known to change with time and due to environmental conditions. Longer-term studies of mechanical properties of these parts when subject to conditions simulating orbital floor environments will provide further confidence in the suitability of this approach.
2. Investigate whether there is an ideal Zn:HA:PA12 composition or other antimicrobial agents that are both biocompatible and exhibits a bacteriostatic effect on LS.
3. Investigate the time it takes for the Zn to be released from the processed samples to gain a better understanding of how long it may take for the samples to exhibit their optimal antimicrobial effect and whether the antimicrobial effects will provide suitable protection under the relevant timescales for this application.

Summary discussion and conclusions

4. Test the antimicrobial samples against a wider array of bacteria to identify the antimicrobial effect of the material on both Gram positive and Gram negative bacteria.
5. Investigate pre-conditioning of the samples such as placing them in media or simulated body fluid (SBF) for a period of time before the cell viability investigations to assess whether this may reduce the cytotoxic effects of Zn on cells.
6. Investigate the use of other inks in HSS which may improve cell attachment or is less likely to interfere with the performance of the additives
7. Designing implants from patient scan data and printing them to assess the feasibility of printing of complex structures.

8 Outputs

8.1 Publication

J.R. Wingham, M. Omran, J. Shepherd, C. Majewski. Effect of steam autoclave in laser sintered polyamide 12. *Rapid Prototyping Journal*. 2020.

8.2 Conferences

M. Omran, C. J. Wilcock, K. Mumtaz, R. Moorehead and C. Miller. "Development of Additively Manufactured Stratified Custom Ceramic Implants for Orbital Floor Reconstruction". Poster at Advanced Biomanufacturing Conference, United Kingdom, Sheffield, 22-23 May 2017.

M. Omran, C. J. Wilcock, K. Mumtaz, R. Moorehead and C. Miller. "The relationship between the viscoelasticity and printability of hydroxyapatite/agarose pastes" poster at Polymer Process Engineering (PPE) 2017, United Kingdom, Bradford, 25-27 July 2017.

M. Omran, I. Varley, C. J. Wilcock, C. Majewski, R. Moorehead and C.A. Miller. "Additively Manufactured Polyamide Scaffolds for Maxillofacial Reconstruction" poster at MeDe Innovation Annual Conference, United Kingdom, Sheffield, 18 January 2018.

M. Omran, C.J. Wilcock, R. Moorehead, C. Majewski, I. Varley and C.A. Miller. "Incorporating antimicrobial agents into polyamide scaffolds for orbital floor implants"

Outputs

Poster at United Kingdom Society of Biomaterials Conference, United Kingdom, Bath, 28-29 June 2018.

M. Omran, C.J. Wilcock, R. Moorehead, C. Majewski, I. Varley and C.A. Miller. "Evaluating two powder-based 3d printing techniques for the manufacture of implants for orbital floor repair" Presentation at Tissue and Cell Engineering Society and the United Kingdom Society for Biomaterials Conference, United Kingdom, Nottingham, 11-13 June 2019.

8.3 Awards

The University of Sheffield Kroto Research Inspiration: My Research Story Video Competition. 24 October 2018.

The University of Sheffield Post Graduate Research Day: Gone in 60 Seconds Prize winner. 28 March 2019.

9 References

1. Vehmeijer M, van Eijnatten M, Liberton N, Wolff J. A Novel Method of Orbital Floor Reconstruction Using Virtual Planning, 3-Dimensional Printing, and Autologous Bone. *Journal of Oral and Maxillofacial Surgery* 2016; **74** (8): 1608-1612.
2. Ong H. Biomechanical properties of the human orbital floor for selection of reconstruction materials using mathematical engineering model. , University Medical Center Groningen, 2012.
3. Weatherholt AM, Fuchs RK, Warden SJ. Specialized Connective Tissue: Bone, the Structural Framework of the Upper Extremity. *Journal of Hand Therapy* 2012; **25** (2): 123-132.
4. Velasco MA, Narváez-Tovar CA, Garzón-Alvarado DA. Design, materials, and mechanobiology of biodegradable scaffolds for bone tissue engineering. *BioMed research international* 2015; **2015**: 729076-729076.
5. Neto A, Ferreira J. Synthetic and Marine-Derived Porous Scaffolds for Bone Tissue Engineering. *Materials (Basel)* 2018; **11** (9): 1702.
6. Rho JY, Kuhn-Spearing L, Zioupos P. Mechanical properties and the hierarchical structure of bone. *Medical Engineering & Physics* 1998; **20** (2): 92-102.
7. Daniel M-M, Ylva D, Shoujin S, Rodney AS. Exploring Macroporosity of Additively Manufactured Titanium Metamaterials for Bone Regeneration with Quality by Design: A Systematic Literature Review. *Materials* 2020; **13** (21): 4794.
8. Wang M. Hydroxyapatite-polyethylene composites for bone substitution: effects of ceramic particle size and morphology. *Biomaterials* 1998; **19** (24): 2357-2366.

References

9. Rezwan K, Chen QZ, Blaker JJ, Boccaccini AR. Biodegradable and bioactive porous polymer/inorganic composite scaffolds for bone tissue engineering. *Biomaterials* 2006; **27** (18): 3413-3431.
10. Kokubo T, Kim H-M, Kawashita M. Novel bioactive materials with different mechanical properties. *Biomaterials* 2003; **24** (13): 2161-2175.
11. Morgan EF, Unnikrisnan GU, Hussein AI. Bone Mechanical Properties in Healthy and Diseased States. *Annu Rev Biomed Eng* 2018; **20** (1): 119-143.
12. Kalfas IH. Principles of bone healing. *Neurosurgical focus* 2001; **10** (4): E1-E1.
13. Long F, Ornitz DM. Development of the Endochondral Skeleton. *Cold Spring Harbor Perspect Biol* 2013; **5** (1).
14. Ratner BD. Biomaterials science : an introduction to materials in medicine. 3rd ed. edn. Kidlington, Oxford: Kidlington, Oxford : Academic/Elsevier, 2013, 2013.
15. Roberts S, Ke H. Anabolic Strategies to Augment Bone Fracture Healing. *Current Osteoporosis Reports* 2018; **16** (3): 289-298.
16. Calori GM, Mazza EL, Mazzola S, et al. Non- unions. *Clinical cases in mineral and bone metabolism : the official journal of the Italian Society of Osteoporosis, Mineral Metabolism, and Skeletal Diseases* 2017; **14** (2): 186-188.
17. Marsell R, Einhorn TA. The biology of fracture healing. *Injury* 2011; **42** (6): 551-555.
18. Oryan A, Monazzah S, Bigham-Sadegh A. Bone Injury and Fracture Healing Biology. *Biomedical and Environmental Sciences* 2015; **28** (1): 57-71.
19. Keramaris NC, Calori GM, Nikolaou VS, Schemitsch EH, Giannoudis PV. Fracture vascularity and bone healing: A systematic review of the role of VEGF. *Injury* 2008; **39** (2): S45-S57.

References

20. Brady SM, McMann MA, Mazzoli RA, Bushley DM, Ainbinder DJ, Carroll RB. The diagnosis and management of orbital blowout fractures: Update 2001. *American Journal of Emergency Medicine* 2001; **19** (2): 147-154.
21. Gunderson LL, Tepper JE. Clinical radiation oncology. Fourth edition. edn. Philadelphia, PA: Philadelphia, PA : Elsevier, 2016, 2016.
22. Joseph JM, Glava IP. Orbital fractures: A review. *Clinical Ophthalmology* 2011; **5** (1): 95-100.
23. Balaji SM. Residual diplopia in treated orbital bone fractures. *Annals of maxillofacial surgery* 2013; **3** (1): 40-5.
24. Siemionow MZ, Eisenmann-Klein M. Plastic and Reconstructive Surgery. Plastic and Reconstructive Surgery. London: Springer, 2010.
25. Waterhouse N, Lyne J, Urdang M, Garey L. An investigation into the mechanism of orbital blowout fractures. *British Journal of Plastic Surgery* 1999; **52** (8): 607-612.
26. Mok D, Lessard L, Cordoba C, Harris PG, Nikolis A. A review of materials currently used in orbital floor reconstruction. *The Canadian journal of plastic surgery = Journal canadien de chirurgie plastique* 2004; **12** (3): 134-140.
27. Tang D, Lalonde J, Lalonde D. Delayed immediate surgery for orbital floor fractures: Less can be more. *Can J Plast Surg* 2011; **19** (4): 125-128.
28. Athanasiov PA, Prabhakaran VC, Selva D. Non- traumatic enophthalmos: a review. Vol. 86. Oxford, UK, pp. 356-364, 2008.
29. Araslanova R, Allen L, Rotenberg BW, Sowerby LJ. Silent sinus syndrome after facial trauma: A case report and literature review. *The Laryngoscope* 2017; **127** (7): 1520-1524.

References

30. Ceylan OM, Uysal Y, Mutlu FM, Tuncer K, Altinsoy HI. Management of diplopia in patients with blowout fractures. *Indian Journal of Ophthalmology* 2011; **59** (6): 457-460.
31. Somogyi MMD, Vrcek IMD, Nakra TMD, Durairaj VMD. Orbital Floor Fracture Management. *Advances in ophthalmology and optometry* 2017; **2** (1): 409-420.
32. Dubois L, Steenen SA, Gooris PJJ, Mourits MP, Becking AG. Controversies in orbital reconstruction-I. Defect-driven orbital reconstruction: A systematic review. *International Journal of Oral and Maxillofacial Surgery* 2015; **44** (3): 308-315.
33. Haug RH, Nuveen E, Bredbenner T. An evaluation of the support provided by common internal orbital reconstruction materials. *Journal of Oral and Maxillofacial Surgery* 1999; **57** (5): 564-570.
34. Kim HS, Jeong EC. Orbital Floor Fracture. *Archives of craniofacial surgery* 2016; **17** (3): 111-118.
35. Mims MM, Wang EW. Cost Analysis of Implants in the Surgical Repair of Orbital Floor Fractures. *Ann Otol Rhinol Laryngol* 2019; **129** (5): 000348941989435-461.
36. Baino F. Biomaterials and implants for orbital floor repair. *Acta Biomaterialia* 2011; **7** (9).
37. Kulinets I. Biomaterials and their applications in medicine 2014.
38. Hussein KH, Saleh T, Ahmed E, et al. Biocompatibility and hemocompatibility of efficiently decellularized whole porcine kidney for tissue engineering. *Journal of Biomedical Materials Research Part A* 2018; **106** (7): 2034-2047.
39. Do Prado Ribeiro DC, De Abreu Figueira L, Mardegan Issa JP, Dias Vecina CA, Josédias F, Da Cunha MR. Study of the osteoconductive capacity of hydroxyapatite implanted into the femur of ovariectomized rats. *Microscopy Research and Technique* 2012; **75** (2): 133-137.

References

40. Mahanty S, Prigent A, Garraud O. Immunogenicity of infectious pathogens and vaccine antigens. *BMC Immunol* 2015; **16** (1): 31-31.
41. Albrektsson, Johansson. Osteoinduction, osteoconduction and osseointegration. *European Spine Journal* 2001; **10** (2): S96-S101.
42. Dimitriou R, Jones E, McGonagle D, Giannoudis PV. Bone regeneration: current concepts and future directions. *Bmc Medicine* 2011; **9**.
43. Totir M, Ciuluvica R, Dinu I, Careba I, Gradinaru S. Biomaterials for orbital fractures repair. *Journal of medicine and life* 2015; **8** (1): 41-3.
44. Sheikh Z, Hamdan N, Ikeda Y, Gryn timer M, Ganss B, Glogauer M. Natural graft tissues and synthetic biomaterials for periodontal and alveolar bone reconstructive applications: a review. *Biomaterials research* 2017; **21** (1): 9-9.
45. Jones JR, Lin S, Yue S, et al. Bioactive glass scaffolds for bone regeneration and their hierarchical characterisation. *Proceedings of the Institution of Mechanical Engineers Part H-Journal of Engineering in Medicine* 2010; **224** (H12): 1373-1387.
46. Baino F, Hamzehlou S, Kargozar S. Bioactive Glasses: Where Are We and Where Are We Going? *Journal of functional biomaterials* 2018; **9** (1).
47. Oh J-h. Recent advances in the reconstruction of cranio-maxillofacial defects using computer-aided design/computer-aided manufacturing. *Maxillofacial Plastic and Reconstructive Surgery* 2018; **40** (1): 1-7.
48. Herford AS, Miller M, Lauritano F, Cervino G, Signorino F, Maiorana C. The use of virtual surgical planning and navigation in the treatment of orbital trauma. *Chinese Journal of Traumatology* 2017; **20** (1): 9-13.
49. Pettersson ABV, Salmi M, Vallittu P, Serlo W, Tuomi J, Mäkitie AA. Main Clinical Use of Additive Manufacturing (Three-Dimensional Printing) in Finland

References

Restricted to the Head and Neck Area in 2016–2017. *Scandinavian Journal of Surgery* 2020; **109** (2): 166-173.

50. Pereira T, Kennedy JV, Potgieter J. A comparison of traditional manufacturing vs additive manufacturing, the best method for the job. *Procedia Manufacturing* 2019; **30**: 11-18.

51. Jeong J, Kim JH, Shim JH, Hwang NS, Heo CY. Bioactive calcium phosphate materials and applications in bone regeneration. *Biomater Res* 2019; **23** (1): 4-11.

52. Aitasalo K, Kinnunen I, Palmgren J, Varpula M. Repair of orbital floor fractures with bioactive glass implants. *Journal of Oral and Maxillofacial Surgery* 2001; **59** (12): 1390-1395.

53. Kinnunen I, Aitasalo K, Pöllönen M, Varpula M. Reconstruction of orbital floor fractures using bioactive glass. *J Craniomaxillofac Surg* 2000; **28** (4): 229-234.

54. Silbert DI, Matta NS, Singman EL. Diplopia Secondary to Orbital Surgery. *Am Orthopt J* 2012; **62** (1): 22-28.

55. Rai A, Datarkar A, Arora A, Adwani DG. Utility of High Density Porous Polyethylene Implants in Maxillofacial Surgery. *J Maxillofac Oral Surg* 2013; **13** (1): 42-46.

56. Sevin K, Askar I, Saray A, Yormuk E. Exposure of high-density porous polyethylene (Medpor (R)) used for contour restoration and treatment. *British Journal of Oral & Maxillofacial Surgery* 2000; **38** (1): 44-49.

57. Ng SGJ, Madill SA, Inkster CF, Maloof AJ, Leatherbarrow B. Medpor porous polyethylene implants in orbital blowout fracture repair. *Eye (Lond)* 2001; **15** (5): 578-582.

References

58. Rubin PA, Bilyk JR, Shore JW. Orbital reconstruction using porous polyethylene sheets. *Ophthalmology : journal of the American Academy of Ophthalmology* 1994; **101** (10): 1697-1708.
59. Jung S-K, Cho W-K, Paik J-S, Yang S-W. Long-term surgical outcomes of porous polyethylene orbital implants: a review of 314 cases. *British Journal of Ophthalmology* 2012; **96** (4): 494-498.
60. Ridwan-Pramana A, Wolff J, Raziei A, Ashton-James CE, Forouzanfar T. Porous polyethylene implants in facial reconstruction: Outcome and complications. *Journal of Cranio-Maxillo-Facial Surgery* 2015; **43** (8): 1330-1334.
61. Villarreal PM, Monje F, Morillo AJ, Junquera LM, Gonzalez C, Barbon JJ. Porous polyethylene implants in orbital floor reconstruction. *Plastic and Reconstructive Surgery* 2002; **109** (3): 877-885.
62. Lin IC, Liao S-L, Lin LLK. Porous polyethylene implants in orbital floor reconstruction. *Journal of the Formosan Medical Association* 2007; **106** (1): 51-57.
63. Mok D, Lessard L, Cordoba C, Harris PG, Nikolis A. A review of materials currently used in orbital floor reconstruction. *The Canadian journal of plastic surgery = Journal canadien de chirurgie plastique* 2004; **12** (3): 134-40.
64. Dedhia R, Tollefson TT. Delayed Periorbital Abscess after Silicone Implant to Orbital Floor Fracture. *Craniomaxillofacial trauma & reconstruction* 2016; **9** (2): 185-187.
65. Son S-R, Linh N-TB, Yang H-M, Lee B-T. In vitro and in vivo evaluation of electrospun PCL/ PMMA fibrous scaffolds for bone regeneration. *Science and Technology of Advanced Materials* 2013; **14** (1).
66. Rashid H, Sheikh Z, Vohra F. Allergic effects of the residual monomer used in denture base acrylic resins. *Eur J Dent* 2015; **9** (4): 614-619.

References

67. Jiang H-J, Xu J, Qiu Z-Y, et al. Mechanical Properties and Cytocompatibility Improvement of Vertebroplasty PMMA Bone Cements by Incorporating Mineralized Collagen. *Materials* 2015; **8** (5): 2616-2634.
68. Groth MJ, Bhatnagar A, Clearihue WJ, Goldberg RA, Douglas RS. Long-term efficacy of biomodeled polymethyl methacrylate implants for orbitofacial defects. *Archives of Facial Plastic Surgery* 2006; **8** (6): 381-389.
69. Majmundar MV, Hamilton JS. Repair of orbital floor fractures with SupraFOIL smooth nylon foil. *Archives of Facial Plastic Surgery* 2007; **9** (1): 64-65.
70. Babar S, Iliff NT, Macquaid E. Secondary infection affecting one of two simultaneously placed orbital wall implants. *Craniofacial trauma & reconstruction* 2009; **2** (2): 113-115.
71. Park DJJ, Garibaldi DC, Iliff NT, Grant MP, Merbs SL. Smooth nylon foil (SupraFOIL) orbital implants in orbital fractures: A case series of 181 patients. *Ophthalmic Plastic and Reconstructive Surgery* 2008; **24** (4): 266-270.
72. Pihlajamaki HK, Salminen ST, Tynninen O, Bostman OM, Laitinen O. Tissue Restoration After Implantation of Polyglycolide, Polydioxanone, Polylevolactide, and Metallic Pins in Cortical Bone: An Experimental Study in Rabbits. *Calcified Tissue International* 2010; **87** (1): 90-98.
73. Seeck NGK, Springer I, Becker S, Kandzia C, Gierloff M, Wiltfang J. Orbital Floor Reconstruction With Resorbable Polydioxanone Implants. *Journal of Craniofacial Surgery* 2012; **23** (1): 161-164.
74. Becker ST, Terheyden H, Fabel M, Kandzia C, Moller B, Wiltfang J. Comparison of Collagen Membranes and Polydioxanone for Reconstruction of the Orbital Floor After Fractures. *Journal of Craniofacial Surgery* 2010; **21** (4): 1066-1068.

References

75. Baumann A, Burggasser G, Gauss N, Ewers R. Orbital floor reconstruction with an alloplastic resorbable polydioxanone sheet. *International Journal of Oral and Maxillofacial Surgery* 2002; **31** (4): 367-373.
76. Kontio R, Suuronen R, Salonen O, Paukku P, Konttinen YT, Lindqvist C. Effectiveness of operative treatment of internal orbital wall fracture with polydioxanone implant. *International Journal of Oral and Maxillofacial Surgery* 2001; **30** (4): 278-285.
77. Chiono V, Carmagnola I, Hatton PV, Gentile P, Hatton P. An Overview of Poly(lactic-co-glycolic) Acid (PLGA)-Based Biomaterials for Bone Tissue Engineering. *International journal of molecular sciences* 2014; **15** (3): 3640-3659.
78. Hatton PV, Walsh J, Brook IM. The response of cultured bone cells to resorbable polyglycolic acid and silicone membranes for use in orbital floor fracture repair. *Clinical Materials* 1994; **17** (2): 71-80.
79. Novaes Jr AB, de Souza SLS, de Barros RRM, Pereira KKY, Iezzi G, Piattelli A. Influence of implant surfaces on osseointegration. *Brazilian Dental Journal* 2010; **21** (6): 471-481.
80. Hollier LH, Rogers N, Berzin E, Stal S. Resorbable mesh in the treatment of orbital floor fractures. *Journal of Craniofacial Surgery* 2001; **12** (3): 242-246.
81. Walsh WR, Pelletier MH, Bertollo N, Christou C, Tan C. Does PEEK/HA Enhance Bone Formation Compared With PEEK in a Sheep Cervical Fusion Model? *Clin Orthop Relat Res* 2016; **474** (11): 2364-2372.
82. Parthasarathy J. 3D modeling, custom implants and its future perspectives in craniofacial surgery. *Annals of maxillofacial surgery* 2014; **4** (1): 9-18.
83. Kim MM, Boahene KDO, Byrne PJ. Use of Customized Polyetheretherketone (PEEK) Implants in the Reconstruction of Complex Maxillofacial Defects. *Archives of Facial Plastic Surgery* 2009; **11** (1): 53-57.

References

84. Chepurnyi Y, Chernogorskyi D, Kopchak A, Petrenko O. Clinical efficacy of peek patient-specific implants in orbital reconstruction. *J Oral Biol Craniofac Res* 2020; **10** (2): 49-53.
85. Rakhmatia YD, Ayukawa Y, Furuhashi A, Koyano K. Current barrier membranes: Titanium mesh and other membranes for guided bone regeneration in dental applications. *Journal of Prosthodontic Research* 2013; **57** (1): 3-14.
86. Strong EB, Fuller SC, Wiley DF, Zumbansen J, Wilson MD, Metzger MC. Preformed vs Intraoperative Bending of Titanium Mesh for Orbital Reconstruction. *Otolaryngology-Head and Neck Surgery* 2013; **149** (1): 60-66.
87. Schubert W, Gear AJL, Lee C, et al. Incorporation of titanium mesh in orbital and midface reconstruction. *Plastic and Reconstructive Surgery* 2002; **110** (4): 1022-1030.
88. Popov Jr VV, Muller-Kamskii G, Kovalevsky A, et al. Design and 3D-printing of titanium bone implants: brief review of approach and clinical cases. *Biomedical Engineering Letters* 2018; **8** (4): 337-344.
89. Mauriello JA, Hargrave S, Yee SY, Mostafavi R, Kapila R. INFECTION AFTER INSERTION OF ALLOPLASTIC ORBITAL FLOOR IMPLANTS. *American Journal of Ophthalmology* 1994; **117** (2): 246-252.
90. Dwyer DJ, Collins JJ, Kohanski MA. How antibiotics kill bacteria: from targets to networks. *Nature reviews* 2010; **8** (6): 423-435.
91. Gold K, Slay B, Knackstedt M, Gaharwar AK. Antimicrobial Activity of Metal and Metal- Oxide Based Nanoparticles. *Advanced Therapeutics* 2018; **1** (3): n/a-n/a.
92. Puzari M, Chetia P. RND efflux pump mediated antibiotic resistance in Gram-negative bacteria *Escherichia coli* and *Pseudomonas aeruginosa*: a major issue worldwide. *World J Microbiol Biotechnol* 2017; **33** (2): 1-8.

References

93. Shepherd J. Best served small: nano battles in the war against wound biofilm infections. *Emerging Topics in Life Sciences* 2020; **4** (6): 567-580.
94. Dizaj SM, Lotfipour F, Barzegar-Jalali M, Zarrintan MH, Adibkia K. Antimicrobial activity of the metals and metal oxide nanoparticles. *Materials Science & Engineering C* 2014; **44**: 278-284.
95. Sims J. CLASSIC PAGES IN OBSTETRICS AND GYNECOLOGY - ON THE TREATMENT OF VESICOVAGINAL FISTULA. *Am J Obstet Gynecol* 1995; **172** (6): 1936-1937.
96. Raghunath A, Perumal E. Metal oxide nanoparticles as antimicrobial agents: a promise for the future. *International Journal of Antimicrobial Agents* 2017; **49** (2): 137-152.
97. Sirelkhatim A, Mahmud S, Seeni A, et al. Review on Zinc Oxide Nanoparticles: Antibacterial Activity and Toxicity Mechanism. *Nano-Micro Letters* 2015; **7** (3): 219-242.
98. Espitia P, Soares Nd, Coimbra J, Andrade N, Cruz R, Medeiros E. Zinc Oxide Nanoparticles: Synthesis, Antimicrobial Activity and Food Packaging Applications. *An International Journal* 2012; **5** (5): 1447-1464.
99. Kasemets K, Ivask A, Dubourguier H-C, Kahru A. Toxicity of nanoparticles of ZnO, CuO and TiO₂ to yeast *Saccharomyces cerevisiae*. *Toxicology in Vitro* 2009; **23** (6): 1116-1122.
100. Mijndonckx K, Leys N, Mahillon J, Silver S, Van Houdt R. Antimicrobial silver: uses, toxicity and potential for resistance. *Biometals* 2013; **26** (4): 609-621.
101. Vincent M, Duval RE, Hartemann P, Engels-Deutsch M. Contact killing and antimicrobial properties of copper. Vol. 124, pp. 1032-1046, 2018.

References

102. Balasubramanian P, Strobel Leonie A, Kneser U, Boccaccini Aldo R. Zinc-containing bioactive glasses for bone regeneration, dental and orthopedic applications. *Biomedical Glasses* 2015; **1** (1).
103. Park JK, Kim YJ, Yeom J, et al. The Topographic Effect of Zinc Oxide Nanoflowers on Osteoblast Growth and Osseointegration. *Advanced Materials* 2010; **22** (43): 4857-4861.
104. Kono M, Mori R, Uchio Y. Bone Screws Have Advantages in Repair of Experimental Osteochondral Fragments. *Clin Orthop Relat Res* 2012; **470** (7): 2043-2050.
105. Banica B, Ene P, Vranceanu D, Ene R. Titanium preformed implants in orbital floor reconstruction - case presentation, review of literature. *Maedica (Buchar)* 2013; **8** (1): 34-39.
106. Xie S, Manda K, Pankaj P. Time-dependent behaviour of bone accentuates loosening in the fixation of fractures using bone-screw systems. *Bone Joint Res* 2018; **7** (10): 580-586.
107. Ohtsuki C, Kamitakahara M, Miyazaki T. Bioactive ceramic- based materials with designed reactivity for bone tissue regeneration. *Journal of the Royal Society, Interface* 2009; **6 suppl 3** (3): S349-S360.
108. Dorozhkin S. Calcium Orthophosphates in Nature, Biology and Medicine. *Materials* 2009; **2** (2): 399-498.
109. Wu C, Chang J. A review of bioactive silicate ceramics. Vol. 8, pp. 032001, 2013.
110. Xidaki D, Agrafioti P, Diomatari D, et al. Synthesis of Hydroxyapatite, β -Tricalcium Phosphate and Biphasic Calcium Phosphate Particles to Act as Local

References

Delivery Carriers of Curcumin: Loading, Release and In Vitro Studies. *Materials (Basel, Switzerland)* 2018; **11** (4).

111. Mistry S, Kundu D, Datta S, Basu D. Effects of bioactive glass, hydroxyapatite and bioactive glass - Hydroxyapatite composite graft particles in the treatment of infrabony defects. *Journal of Indian Society of Periodontology* 2012; **16** (2): 241-246.

112. Kattimani VS, Kondaka S, Lingamaneni KP. Hydroxyapatite— Past, Present, and Future in Bone Regeneration. *Bone and Tissue Regeneration Insights* 2016; **7**.

113. Attaran M. The rise of 3-D printing: The advantages of additive manufacturing over traditional manufacturing. *Business Horizons* 2017; **60** (5): 677-688.

114. ASTM, F2792-12a. Standard Terminology for Additive Manufacturing Technologies. Vol. 10.04.2012.

115. Hoang D, Perrault D, Stevanovic M, Ghiassi A. Today surgical applications of three- dimensional printing: A review of the current literature & how to get started. *Annals of Translational Medicine* 2016; **4** (23): <xocs:firstpage xmlns:xocs=""/>.

116. Tofail SAM, Koumoulos EP, Bandyopadhyay A, Bose S, O'Donoghue L, Charitidis C. Additive manufacturing: scientific and technological challenges, market uptake and opportunities. *Materials Today* 2018; **21** (1): 22-37.

117. Szilvsi-Nagy M, Mátyási G. Analysis of STL files. *Mathematical and Computer Modelling* 2003; **38** (7): 945-960.

118. Peltola SM, Melchels FPW, Grijpma DW, Kellomaki M. A review of rapid prototyping techniques for tissue engineering purposes. *Annals of Medicine* 2008; **40** (4): 268-280.

119. Yuan B, Zhou S-y, Chen X-s. Rapid prototyping technology and its application in bone tissue engineering. *Journal of Zhejiang University-Science B* 2017; **18** (4): 303-315.

References

120. Jingchao J, Xun X, Jonathan S. Support Structures for Additive Manufacturing: A Review. *Journal of Manufacturing and Materials Processing* 2018; **2** (4): 64.
121. Farre-Guasch E, Wolff J, Helder MN, Schulten EAJM, Forouzanfar T, Klein-Nulend J. Application of Additive Manufacturing in Oral and Maxillofacial Surgery. *Journal of Oral and Maxillofacial Surgery* 2015; **73** (12): 2408-2418.
122. Rider P, Kačarević ŽP, Alkildani S, Retnasingh S, Schnettler R, Barbeck M. Additive Manufacturing for Guided Bone Regeneration: A Perspective for Alveolar Ridge Augmentation. *International journal of molecular sciences* 2018; **19** (11).
123. Mondschein RJ, Kanitkar A, Williams CB, Verbridge SS, Long TE. Polymer structure- property requirements for stereolithographic 3D printing of soft tissue engineering scaffolds. *Biomaterials* 2017; **140**: 170-188.
124. Hao L, Tang D, Sun T, et al. Direct Ink Writing of Mineral Materials: A review. *INTERNATIONAL JOURNAL OF PRECISION ENGINEERING AND MANUFACTURING-GREEN TECHNOLOGY* 2020.
125. Lewis JA, Smay JE, Stuecker J, Cesarano J, III. Direct ink writing of three-dimensional ceramic structures. *Journal of the American Ceramic Society* 2006; **89** (12): 3599-3609.
126. Lin K, Sheikh R, Romanazzo S, Roohani I. 3D Printing of Bioceramic Scaffolds—Barriers to the Clinical Translation: From Promise to Reality, and Future Perspectives. *Materials (Basel)* 2019; **12** (17): 2660.
127. Sivandzade F, Cucullo L. In-vitro blood–brain barrier modeling: A review of modern and fast-advancing technologies. *J Cereb Blood Flow Metab* 2018; **38** (10): 1667-1681.
128. Vyavahare S, Teraiya S, Panghal D, Kumar S. Fused deposition modelling: a review. *Rapid Prototyping Journal* 2020; **26** (1): 176-201.

References

129. Danforth S. Fused Deposition of Ceramics: A New Technique for the Rapid Fabrication of Ceramic Components. *Materials Technology* 1995; **10** (7-8).
130. Rubio-Perez I, Diaz Lantada A. Surgical Planning of Sacral Nerve Stimulation Procedure in Presence of Sacral Anomalies by Using Personalized Polymeric Prototypes Obtained with Additive Manufacturing Techniques. *Polymers (Basel)* 2020; **12** (3): 581.
131. Msallem B, Sharma N, Cao S, Halbeisen FS, Zeilhofer H-F, Thieringer FM. Evaluation of the Dimensional Accuracy of 3D-Printed Anatomical Mandibular Models Using FFF, SLA, SLS, MJ, and BJ Printing Technology. *Journal of clinical medicine* 2020; **9** (3): 817.
132. Chen Z, Li Z, Li J, et al. 3D printing of ceramics: A review. *Journal of the European Ceramic Society* 2019; **39** (4): 661-687.
133. Solís Pinargote NW, Smirnov A, Peretyagin N, Seleznev A, Peretyagin P. Direct Ink Writing Technology (3D Printing) of Graphene-Based Ceramic Nanocomposites: A Review. *Nanomaterials (Basel, Switzerland)* 2020; **10** (7): 1300.
134. formlabs. 3D Printing Technology Comparison: FDM vs. SLA vs. SLS. Also available at: <https://formlabs.com/uk/blog/fdm-vs-sla-vs-sls-how-to-choose-the-right-3d-printing-technology/> (accessed 20/12).
135. Kinstlinger IS, Bastian A, Paulsen SJ, et al. Open-Source Selective Laser Sintering (OpenSLS) of Nylon and Biocompatible Polycaprolactone. *PloS one* 2016; **11** (2): e0147399-e0147399.
136. Norazman F, Hopkinson N. Effect of Sintering Parameters and Flow Agent on the Mechanical Properties of High Speed Sintered Elastomer. *Journal of Manufacturing Science and Engineering-Transactions of the Asme* 2014; **136** (6): 6.

References

137. Ellis A, Noble C, Hartley L, Lestrangle C, Hopkinson N, Majewski C. Materials for high speed sintering. *Journal of Materials Research* 2014; **29** (17): 2080-2085.
138. Ellis A, Hartley L, Hopkinson N. Effect of Print Density on the Properties of High Speed Sintered Elastomers. *Metallurgical and Materials Transactions A: Physical Metallurgy and Materials Science* 2015; **46** (9).
139. Majewski CE, Hobbs BS, Hopkinson N. Effect of bed temperature and infra-red lamp power on the mechanical properties of parts produced using high-speed sintering. *Virtual and Physical Prototyping* 2007; **2** (2): 103-110.
140. Griffith ML, Halloran JW. Freeform Fabrication of Ceramics via Stereolithography. *Journal of the American Ceramic Society* 1996; **79** (10): 2601-2608.
141. Wu H, Li D, Tang Y, Sun B, Xu D. Rapid fabrication of alumina-based ceramic cores for gas turbine blades by stereolithography and gelcasting. *Journal of Materials Processing Tech* 2009; **209** (18): 5886-5891.
142. Allen Brady G, Halloran JW. Stereolithography of ceramic suspensions. *Rapid Prototyping Journal* 1997; **3** (2): 61-65.
143. Seitz H, Rieder W, Irsen S, Leukers B, Tille C. Three-dimensional printing of porous ceramic scaffolds for bone tissue engineering. *J BIOMED MATER RES B* 2005; **74** (2): 782-788.
144. Zakeri S, Vippola M, Levänen E. A comprehensive review of the photopolymerization of ceramic resins used in stereolithography. *Additive Manufacturing* 2020; **35**.
145. Geven MA, Varjas V, Kamer L, et al. Fabrication of patient specific composite orbital floor implants by stereolithography. *Polymers for Advanced Technologies* 2015; **26** (12): 1433-1438.

References

146. Gentry SP, Halloran JW. Depth and width of cured lines in photopolymerizable ceramic suspensions. *Journal of the European Ceramic Society* 2013; **33** (10): 1981-1988.
147. Schwarzer E, Götz M, Markova D, Stafford D, Scheithauer U, Moritz T. Lithography-based ceramic manufacturing (LCM) – Viscosity and cleaning as two quality influencing steps in the process chain of printing green parts. *Journal of the European Ceramic Society* 2017; **37** (16): 5329-5338.
148. Schmidleithner C, Malferarri S, Palgrave R, Bomze D, Schwentenwein M, Kalaskar DM. Application of high resolution DLP stereolithography for fabrication of tricalcium phosphate scaffolds for bone regeneration. *Biomedical materials (Bristol, England)* 2019; **14** (4): 045018.
149. Czekanska E, Stoddart M, Richards RG, Hayes J. IN SEARCH OF AN OSTEOBLAST CELL MODEL FOR IN VITRO RESEARCH. *Eur Cells Mater* 2012; **24**: 1-17.
150. Cesarano J, King BH, Denham HB. Recent developments in robocasting of ceramics and multimaterial deposition. In: 9th Solid Freeform Fabrication (SFF) Symposium, Aug 10-12, Univ Texas, Austin, Tx, 1998.
151. Cesarano J, Dellinger JG, Saavedra MP, et al. Customization of Load-Bearing Hydroxyapatite Lattice Scaffolds. *International journal of applied ceramic technology* 2005; **2** (3): 212-220.
152. Simon JL, Michna S, Lewis JA, et al. In vivo bone response to 3D periodic hydroxyapatite scaffolds assembled by direct ink writing. *J BIOMED MATER RES A* 2007; **83** (3): 747-758.

References

153. Tan KH, Chua CK, Leong KF, et al. Scaffold development using selective laser sintering of polyetheretherketone- hydroxyapatite biocomposite blends. *Biomaterials* 2003; **24** (18): 3115-3123.
154. Maazouz Y, Montufar EB, Guillem-Marti J, et al. Robocasting of biomimetic hydroxyapatite scaffolds using self-setting inks. *Journal of Materials Chemistry B* 2014; **2** (33): 5378-5386.
155. Figueiredo M, Henriques J, Martins G, Guerra F, Judas F, Figueiredo H. Physicochemical characterization of biomaterials commonly used in dentistry as bone substitutes—Comparison with human bone. *Journal of Biomedical Materials Research Part B: Applied Biomaterials* 2010; **92** (2): 409-419.
156. Lambert F, Bacevic M, Layrolle P, Schupbach P, Drion P, Rompen E. Impact of biomaterial microtopography on bone regeneration: comparison of three hydroxyapatites. *Clinical Oral Implants Research* 2017; **28** (10): E201-E207.
157. Weibrich G, Trettin R, Gnoth SH, Götz H, Duschner H, Wagner W. [Determining the size of the specific surface of bone substitutes with gas adsorption]. *Mund-, Kiefer- und Gesichtschirurgie : MKG* 2000; **4** (3): 148-152.
158. Fonseca RJ. *Oral and Maxillofacial Surgery Vol. 1*. Missouri: Elsevier, 2017.
159. Vandeperre LJ, De Wilde AM, Luyten J. Gelatin gelcasting of ceramic components. *Journal of materials processing technology* 2003; **135** (2): 312-316.
160. Abdullah AM, Rahim TNAT, Hamad WNF, Mohamad D, Akil HM, Rajion ZA. Mechanical and cytotoxicity properties of hybrid ceramics filled polyamide 12 filament feedstock for craniofacial bone reconstruction via fused deposition modelling. *Dent Mater* 2018; **34** (11): e309-e316.

References

161. Kim J, McBride S, Tellis B, et al. Rapid-prototyped PLGA/beta-TCP/hydroxyapatite nanocomposite scaffolds in a rabbit femoral defect model. *Biofabrication* 2012; **4** (2).
162. Jiao Z, Luo B, Xiang S, Ma H, Yu Y, Yang W. 3D printing of HA / PCL composite tissue engineering scaffolds. *Advanced Industrial and Engineering Polymer Research* 2019; **2** (4): 196-202.
163. Spanou A, Diez-Escudero A, Persson C, Wu D. 3D-printed PLA/HA composite structures as synthetic trabecular bone: A feasibility study using fused deposition modeling. *Journal of the mechanical behavior of biomedical materials* 2020; **103**: 103608.
164. Niaza KV, Senatov FS, Kaloshkin SD, Maksimkin AV, Chukov DI. 3D-printed scaffolds based on PLA/HA nanocomposites for trabecular bone reconstruction. Vol. 741: IOP Publishing, pp. 012068, 2016.
165. Li Y, Wu Z-g, Li X-k, et al. A polycaprolactone-tricalcium phosphate composite scaffold as an autograft-free spinal fusion cage in a sheep model. *Biomaterials* 2014; **35** (22): 5647-5659.
166. Amnael Orozco-Díaz C, Moorehead R, Reilly GC, Gilchrist F, Miller C. Characterization of a composite polylactic acid-hydroxyapatite 3D-printing filament for bone-regeneration. 2020.
167. Pitjamit S, Thunsiri K, Nakkiew W, Wongwichai T, Pothacharoen P, Wattanuchariya W. The Possibility of Interlocking Nail Fabrication from FFF 3D Printing PLA/PCL/HA Composites Coated by Local Silk Fibroin for Canine Bone Fracture Treatment. *Materials (Basel)* 2020; **13** (7): 1564.
168. Mohan Pandey P, Venkata Reddy N, Dhande SG. Slicing procedures in layered manufacturing: a review. *Rapid prototyping journal* 2003; **9** (5): 274-288.

References

169. Garg A, Bhattacharya A, Batish A. On Surface Finish and Dimensional Accuracy of FDM Parts after Cold Vapor Treatment. *Materials and Manufacturing Processes* 2016; **31** (4): 522-529.
170. Chua CK, Leong KF, Tan KH, Wiria FE, Cheah CM. Development of tissue scaffolds using selective laser sintering of polyvinyl alcohol/hydroxyapatite biocomposite for craniofacial and joint defects. *Journal of Materials Science-Materials in Medicine* 2004; **15** (10): 1113-1121.
171. Eosoly S, Vrana NE, Lohfeld S, Hindie M, Looney L. Interaction of cell culture with composition effects on the mechanical properties of polycaprolactone-hydroxyapatite scaffolds fabricated via selective laser sintering (SLS). *Materials Science & Engineering C-Materials for Biological Applications* 2012; **32** (8): 2250-2257.
172. Hao L, Savalani MM, Zhang Y, Tanner KE, Harris RA. Effects of material morphology and processing conditions on the characteristics of hydroxyapatite and high-density polyethylene biocomposites by selective laser sintering. *Proceedings of the Institution of Mechanical Engineers Part L-Journal of Materials-Design and Applications* 2006; **220** (L3): 125-137.
173. Hao L, Savalani MM, Zhang Y, Tanner KE, Harris RA. Selective laser sintering of hydroxyapatite reinforced polyethylene composites for bioactive implants and tissue scaffold development. *Proceedings of the Institution of Mechanical Engineers Part H-Journal of Engineering in Medicine* 2006; **220** (H4): 521-531.
174. Zhou WY, Wang M, Cheung WL, Ip WY. Selective Laser Sintering of Poly(L-Lactide)/Carbonated Hydroxyapatite Nanocomposite Porous Scaffolds for Bone Tissue Engineering. *Tissue Engineering* 2010: 179-204.

References

175. Song X, Li W, Song P, et al. Selective laser sintering of aliphatic-polycarbonate/hydroxyapatite composite scaffolds for medical applications. *International Journal of Advanced Manufacturing Technology* 2015; **81** (1-4): 15-25.
176. Hui D, Goodridge RD, Scotchford CA, Grant DM. Laser sintering of nano-hydroxyapatite coated polyamide 12 powders. *Additive Manufacturing* 2018; **22** (C): 560-570.
177. Dabbas F, Stares SL, Mascheroni JM, Hotza D, Salmoria GV. Selective Laser Sintering of Polyamide/Hydroxyapatite Scaffolds. *Proceedings of the 3rd Pan American Materials Congress* 2017: 95-103.
178. Chung H, Das S. Functionally graded Nylon-11/silica nanocomposites produced by selective laser sintering. *Materials Science & Engineering A* 2008; **487** (1): 251-257.
179. Kumaresan T, Gandhinathan R, Ramu M, Ananthasubramanian M, Pradheepa KB. Design, analysis and fabrication of polyamide/hydroxyapatite porous structured scaffold using selective laser sintering method for bio-medical applications. *Journal of Mechanical Science and Technology* 2016; **30** (11): 5305-5312.
180. Sagar MB, Elangovan K. Consolidation & Factors Influencing Sintering Process in Polymer Powder Based Additive Manufacturing. In: International Conference on Materials, Alloys and Experimental Mechanics (ICMAEM), 2017 Jul 03-04, Narsimha Reddy Engn Coll, INDIA, 2017.
181. Brighenti R, Cosma MP, Marsavina L, Spagnoli A, Terzano M. Laser-based additively manufactured polymers: a review on processes and mechanical models. *Journal of Materials Science* 2021; **56** (2): 961-998.

References

182. Yan C, Shi Y, Hao L. Investigation into the Differences in the Selective Laser Sintering between Amorphous and Semi-crystalline Polymers. *International Polymer Processing* 2011; **26** (4): 416-423.
183. Feng L, Wang Y, Wei Q. PA12 Powder Recycled from SLS for FDM. *Polymers* 2019; **11** (4).
184. Schmid M, Kleijnen R, Vetterli M, Wegener K. Influence of the Origin of Polyamide 12 Powder on the Laser Sintering Process and Laser Sintered Parts. *Applied Sciences* 2017; **7** (5): 462.
185. Wolanov Y, Feldman AY, Harel H, Marom G. Amorphous and crystalline phase interaction during the Brill transition in nylon 66. *Express polymer letters* 2009; **3** (7): 452-457.
186. Xiao D, Cui X, Li W, Yan D. Investigation on the Brill transition of polyamide 618. *Selected Publications from Chinese Universities* 2007; **2** (1): 6-12.
187. Kamarajan BP, Murugan R, Ananthasubramanian M, Dinakar R, Mathialagan V, S S. Evaluation of selective laser sintered polyamide/hydroxyapatite composite compositions –in vitro and in vivo. *International Journal of Biomedical Research* 2017; **8** (08): 467-474
188. Saldaña L, Bensiamar F, Boré A, Vilaboa N. In search of representative models of human bone- forming cells for cytocompatibility studies. *Acta Biomaterialia* 2011; **7** (12): 4210-4221.
189. Segnani C, Ippolito C, Antonioli L, et al. Histochemical Detection of Collagen Fibers by Sirius Red/ Fast Green Is More Sensitive than van Gieson or Sirius Red Alone in Normal and Inflamed Rat Colon. *PLoS One* 2015; **10** (12): e0144630.

References

190. Turner RD, Wingham JR, Paterson TE, Shepherd J, Majewski C. Use of silver-based additives for the development of antibacterial functionality in Laser Sintered polyamide 12 parts. 2020.
191. Zhu Z, Majewski C. Understanding pore formation and the effect on mechanical properties of High Speed Sintered polyamide-12 parts: A focus on energy input. *Materials & design* 2020; **194**: 108937.
192. Pilipović A, Brajlilić T, Drstvenšek I. Influence of Processing Parameters on Tensile Properties of SLS Polymer Product. *Polymers (Basel)* 2018; **10** (11): 1208.
193. Majewski C, Zarringhalam H, Hopkinson N. Effect of the degree of particle melt on mechanical properties in selective laser-sintered Nylon-12 parts. *Proceedings of the Institution of Mechanical Engineers, Part B: Journal of Engineering Manufacture* 2008; **222** (9): 1055-1064.
194. Zarringhalam H, Majewski C, Hopkinson N. Degree of particle melt in Nylon-12 selective laser-sintered parts. *Rapid Prototyping Journal* 2009; **15** (2): 126-132.
195. Gu H, AlFayez F, Ahmed T, Bashir Z. Poly(ethylene terephthalate) powder-a versatile material for additive manufacturing. *Polymers* 2019; **11** (12).
196. Dupin S, Lame O, Barrès C, Charneau J-Y. Microstructural origin of physical and mechanical properties of polyamide 12 processed by laser sintering. *European Polymer Journal* 2012; **48** (9): 1611-1621.
197. Shalabi MM, Gortemaker A, Hof MAVt, Jansen JA, Creugers NHJ. Implant Surface Roughness and Bone Healing: a Systematic Review. Vol. 85, pp. 496-500, 2006.
198. Buser D, Schenk RK, Steinemann S, Fiorellini JP, Fox CH, Stich H. INFLUENCE OF SURFACE CHARACTERISTICS ON BONE INTEGRATION OF

References

TITANIUM IMPLANTS - A HISTOMORPHOMETRIC STUDY IN MINIATURE PIGS.

Journal of Biomedical Materials Research 1991; **25** (7): 889-902.

199. Nanci A, Puleo D. Understanding and controlling the bone–implant interface.

Biomaterials 1999; **20** (23-24): 2311-2321.

200. Schmid M, Wegener K. Additive Manufacturing: Polymers applicable for Laser Sintering (LS). *International Conference on Manufacturing Engineering and Materials, Icmem 2016* 2016; **149**: 457-464.

201. Josupeit S, Schmid H-J. Temperature history within laser sintered part cakes and its influence on process quality. *Rapid Prototyping Journal* 2016; **22** (5): 788-793.

202. Ellis A, Brown R, Hopkinson N. The effect of build orientation and surface modification on mechanical properties of high speed sintered parts. *Surface Topography: Metrology and Properties* 2015; **3** (3).

203. Gibson I, Shi D. Material properties and fabrication parameters in selective laser sintering process. *Rapid Prototyping Journal* 1997; **3** (4): 129-136.

204. Hofland EC, Baran I, Wismeijer DA. Correlation of Process Parameters with Mechanical Properties of Laser Sintered PA12 Parts. *Advances in Materials Science and Engineering* 2017.

205. Ellis A, Brown R, Hopkinson N. The effect of build orientation and surface modification on mechanical properties of high speed sintered parts. *Surface Topography-Metrology and Properties* 2015; **3** (3).

206. Dadbakhsh S, Verbelen L, Verkinderen O, Strobbe D, Van Puyvelde P, Kruth J-P. Effect of PA12 powder reuse on coalescence behaviour and microstructure of SLS parts. *European Polymer Journal* 2017; **92**: 250-262.

207. Using Differential Scanning Calorimetry to Measure Changes in Enthalpy. *Journal of Visualized Experiments* 2019.

References

208. Boerckel JD, Mason D, McDermott A, Alsberg E. Microcomputed tomography: approaches and applications in bioengineering. *Stem Cell Res Ther.* Vol. 52014.
209. du Plessis A, Broeckhoven C, Guelpa A, le Roux SG. Laboratory x-ray micro-computed tomography: a user guideline for biological samples. *GigaScience* 2017; **6** (6): 1-11.
210. Li H, Zhang H, Tang Z, Hu G. Micro-computed tomography for small animal imaging: Technological details. *Progress in Natural Science* 2008; **18** (5): 513-521.
211. Crica LE, Wengenroth J, Tiainen H, Ionita M, Haugen HJ. Enhanced X- ray Absorption for Micro- CT Analysis of Low Density Polymers. *Journal of Biomaterials Science, Polymer Edition* 2016; **27** (9): 1-54.
212. Sinha P, Datar A, Jeong C, Deng X, Chung YG, Lin LC. Surface Area Determination of Porous Materials Using the Brunauer-Emmett-Teller (BET) Method: Limitations and Improvements. *Journal of Physical Chemistry C* 2019; **123** (33): 20195-20209.
213. Ambroz F, Macdonald TJ, Martis V, Parkin IP. Evaluation of the BET Theory for the Characterization of Meso and Microporous MOFs. *Small Methods* 2018; **2** (11): n/a-n/a.
214. ASTM. Standard test method for tensile properties of plastics. West Conshohocken, PA.: ASTM International,2014.
215. ASTM. Standard Test Methods for Flexural Properties of Unreinforced and Reinforced Plastics and Electrical Insulating Materials. West Conshohocken, PA,: ASTM International2017.
216. Jarvis WR. Bennett & Brachman's Hospital Infections: Wolters Kluwer, 2013.

References

217. Rutala WA, Weber DJ, Healthcare, Committee ICPA. Guideline for Disinfection and Sterilization in Healthcare Facilities. 2008. Also available at: <https://www.cdc.gov/infectioncontrol/guidelines/disinfection/>.
218. Wingham JR, Omran M, Shepherd J, Majewski C. Effect of steam autoclaving on laser sintered polyamide 12. 2020.
219. Xu M, McCanna DJ, Sivak JG. Use of the viability reagent PrestoBlue in comparison with alamarBlue and MTT to assess the viability of human corneal epithelial cells. *Journal of Pharmacological and Toxicological Methods* 2015; **71**: 1-7.
220. Holden MJ, Haynes RJ, Rabb SA, Satija N, Yang K, Blasic JR. Factors affecting quantification of total DNA by UV spectroscopy and PicoGreen fluorescence. *Journal of agricultural and food chemistry* 2009; **57** (16): 7221-7226.
221. Montanaro L, Arciola CR, Campoccia D, Cervellati M. In vitro effects on MG63 osteoblast-like cells following contact with two roughness-differing fluorohydroxyapatite-coated titanium alloys. *Biomaterials* 2002; **23** (17): 3651-3659.
222. Romero-Ruiz MM, Gil-Mur FJ, Ríos-Santos JV, Lázaro-Calvo P, Ríos-Carrasco B, Herrero-Climent M. Influence of a Novel Surface of Bioactive Implants on Osseointegration: A Comparative and Histomorfometric Correlation and Implant Stability Study in Minipigs. *International journal of molecular sciences* 2019; **20** (9).
223. Wennerberg A, Hallgren C, Johansson C, Danelli S. A histomorphometric evaluation of screw-shaped implants each prepared with two surface roughnesses. *Clinical Oral Implants Research* 1998; **9** (1): 11-19.

References

224. Komasa S, Nishizaki M, Zhang H, et al. Osseointegration of Alkali-Modified NANOZR Implants: An In Vivo Study. *International journal of molecular sciences* 2019; **20** (4).
225. Berretta S, Evans KE, Ghita OR. Predicting processing parameters in high temperature laser sintering (HT-LS) from powder properties. *Materials & Design* 2016; **105** (C): 301-314.
226. Yuan S, Bai J, Chua C, Wei J, Zhou K. Material Evaluation and Process Optimization of CNT-Coated Polymer Powders for Selective Laser Sintering. *Polymers (Basel)* 2016; **8** (10): 370.
227. Tõnsuaadu K, Gross KA, Plūduma L, Veiderma M. A review on the thermal stability of calcium apatites. *Journal of thermal analysis and calorimetry* 2012; **110** (2): 647-659.
228. Shuai C, Zhou Y, Yang Y, et al. Biodegradation resistance and bioactivity of hydroxyapatite enhanced Mg-Zn composites via selective laser melting. *Materials (Basel)* 2017; **10** (3): 307.
229. Brandt M. Laser additive manufacturing : materials, design, technologies, and applications. Amsterdam: Amsterdam : Elsevier, 2017, 2017.
230. Mugwagwa L, Dimitrov D, Matope S, Muvunzi R. Residual Stresses and Distortions in Selective Laser Melting- A Review. . 7th International conference of the Rapid Product Development Association of South Africa. Vaal2016.
231. Cheng B, Chou K. Thermal Stresses Associated with Part Overhang Geometry in Electron Beam Additive Manufacturing: Process Parameter Effects. Conference: 25th Annual International Solid Freeform Fabrication Symposium - An Additive Manufacturing Austin, TX, USA2004.

References

232. Ali H, Ghadbeigi H, Mumtaz K. Effect of scanning strategies on residual stress and mechanical properties of Selective Laser Melted Ti6Al4V. *Materials Science & Engineering A* 2018; **712** (C): 175-187.
233. Gránásy L, Tóth GI, Warren JA, et al. Phase-field modeling of crystal nucleation in undercooled liquids – A review. *Progress in materials science* 2019; **106**: 100569.
234. Prasad S, Wong RCW. Unraveling the mechanical strength of biomaterials used as a bone scaffold in oral and maxillofacial defects. *Oral Science International* 2018; **15** (2): 48-55.
235. Abbasi N, Hamlet S, Love RM, Nguyen NT. Porous scaffolds for bone regeneration. *Journal of Science: Advanced Materials and Devices* 2020.
236. Zugic R, Szpunar B, Krstic VD, Erb U. Effect of porosity on the elastic response of brittle materials: An embedded-atom method approach. *Philosophical Magazine a-Physics of Condensed Matter Structure Defects and Mechanical Properties* 1997; **75** (4): 1041-1055.
237. Liu D, Savija B, Smith GE, Flewitt PEJ, Lowe T, Schlangen E. Towards understanding the influence of porosity on mechanical and fracture behaviour of quasi-brittle materials: experiments and modelling. *International Journal of Fracture* 2017; **205** (1): 57-72.
238. Bobbert FSL, Zadpoor AA. Effects of bone substitute architecture and surface properties on cell response, angiogenesis, and structure of new bone. *J Mater Chem B* 2017; **5** (31): 6175-6192.
239. Van Der Stok J, Van Der Jagt OP, Amin Yavari S, et al. Selective laser melting-produced porous titanium scaffolds regenerate bone in critical size cortical bone defects. *Journal of Orthopaedic Research* 2013; **31** (5): 792-799.

References

240. Puwanun S. Developing a tissue engineering strategy for cleft palate repair: University of Sheffield; Faculty of Engineering (Sheffield); Materials Science and Engineering (Sheffield); 2014. 2014.
241. Rainer A, Mozetic P, Giannitelli SM, et al. Computer-aided tissue engineering for bone regeneration: IEEE, pp. 473-476, 2012.
242. Lim TC, Chian KS, Leong KF. Cryogenic prototyping of chitosan scaffolds with controlled micro and macro architecture and their effect on in vivo neo-vascularization and cellular infiltration. *J Biomed Mater Res A* 2010; **94A** (4): 1303-1311.
243. Murphy CM, Haugh MG, O'Brien FJ. The effect of mean pore size on cell attachment, proliferation and migration in collagen–glycosaminoglycan scaffolds for bone tissue engineering. *Biomaterials* 2010; **31** (3): 461-466.
244. Schwartz Z, Kieswetter K, Dean DD, Boyan BD. Underlying mechanisms at the bone-surface interface during regeneration. *Journal of Periodontal Research* 1997; **32** (1): 166-171.
245. Li X, van Blitterswijk CA, Feng Q, Cui F, Watari F. The effect of calcium phosphate microstructure on bone-related cells in vitro. *Biomaterials* 2008; **29** (23): 3306-3316.
246. Hannink G, Arts JJC. Bioresorbability, porosity and mechanical strength of bone substitutes: What is optimal for bone regeneration? *Injury* 2011; **42** (2): S22-S25.
247. Jensen S, Aaboe M, Pinholt E, Hjørting-Hansen E, Melsen F, Ruyter I. Tissue Reaction and Material Characteristics of Four Bone Substitutes. *The International journal of oral & maxillofacial implants* 1996; **11** (1): 55-66.

References

248. Yuan H, Zou P, Yang Z, Zhang X, De Bruijn J, De Groot K. Bone morphogenetic protein and ceramic-induced osteogenesis. *Official Journal of the European Society for Biomaterials* 1998; **9** (12): 717-721.
249. Yang Z, Yuan H, Tong W, Zou P, Chen W, Zhang X. Osteogenesis in extraskeletally implanted porous calcium phosphate ceramics: variability among different kinds of animals. *Biomaterials* 1996; **17** (22): 2131-2137.
250. Ripamonti U. Osteoinduction in porous hydroxyapatite implanted in heterotopic sites of different animal models. *Biomaterials* 1996; **17** (1): 31-35.
251. Shahabi S, Najafi F, Majdabadi A, et al. Effect of gamma irradiation on structural and biological properties of a PLGA-PEG-hydroxyapatite composite. *TheScientificWorldJournal* 2014; **2014**: 420616-420616.
252. Ozeki K, Aoki H, Fukui Y. Effect of pH on crystallization of sputtered hydroxyapatite film under hydrothermal conditions at low temperature. *Journal of Materials Science* 2005; **40** (11): 2837-2842.
253. Huang D, Yin M, Lin Q, et al. Aligned hydroxyapatite nano-crystal formation on a polyamide surface. *RSC Adv* 2017; **7** (68): 43040-43046.
254. Van Hooreweder B, Moens D, Boonen R, Kruth J-P, Sas P. On the difference in material structure and fatigue properties of nylon specimens produced by injection molding and selective laser sintering. *Polymer Testing* 2013; **32** (5): 972-981.
255. Xu F, Yan C, Shyng Y-T, Chang H, Xia Y, Zhu Y. Ultra-toughened nylon 12 nanocomposites reinforced with IF-WS sub(2). *Nanotechnology* 2014; **25** (32): 1-10.
256. Kim J-W, Shin K-H, Koh Y-H, Hah MJ, Moon J, Kim H-E. Production of poly(ϵ -caprolactone)/hydroxyapatite composite scaffolds with a tailored macro/micro-porous structure, high mechanical properties, and excellent bioactivity. *Materials (Basel)* 2017; **10** (10): 1123.

References

257. Nathanael AJ, Mangalaraj D, Chen PC, Ponpandian N. Enhanced mechanical strength of hydroxyapatite nanorods reinforced with polyethylene. *Journal of Nanoparticle Research* 2011; **13** (5): 1841-1853.
258. Xu P, Feng X, Zheng H, et al. A tarsus construct of a novel branched polyethylene with good elasticity for eyelid reconstruction in vivo. *Regenerative biomaterials* 2020; **7** (3): 259-269.
259. Kim CS, Jung K-H, Kim H, Kim C-B, Kang I-K. Collagen-grafted porous HDPE/PEAA scaffolds for bone reconstruction. *Biomaterials Research* 2016; **20** (3): 191-199.
260. Chen X, Wu S, Zhou J. Influence of porosity on compressive and tensile strength of cement mortar. *Construction and Building Materials* 2013; **40**: 869-874.
261. Gustavo Waldemar M, Daniel Oscar T, Julio César C, Aulio César G. Effect of porosity on the tensile properties of low ductility aluminum alloys. *Materials Research* 2004; **7** (2): 221-229.
262. Liu D, Šavija B, Smith G, Flewitt P, Lowe T, Schlangen E. Towards understanding the influence of porosity on mechanical and fracture behaviour of quasi-brittle materials: experiments and modelling. *International Journal of Fracture* 2017; **205** (1): 57-72.
263. Bin L, Xin-Gang W, Yong T, Wei Y, Chao-Bin F, Zhen-Ping W. Experimental Study on the Tensile Property of a Novel Oriented Linear Porous Metal. *Advances in Materials Science and Engineering* 2016; **2016**.
264. Rahim TNAT, Abdullah AM, Akil HM, Mohamad D, Rajion ZA. The improvement of mechanical and thermal properties of polyamide 12 3D printed parts by fused deposition modelling. *eXPRESS Polymer Letters* 2017; **11** (12): 963-982.

References

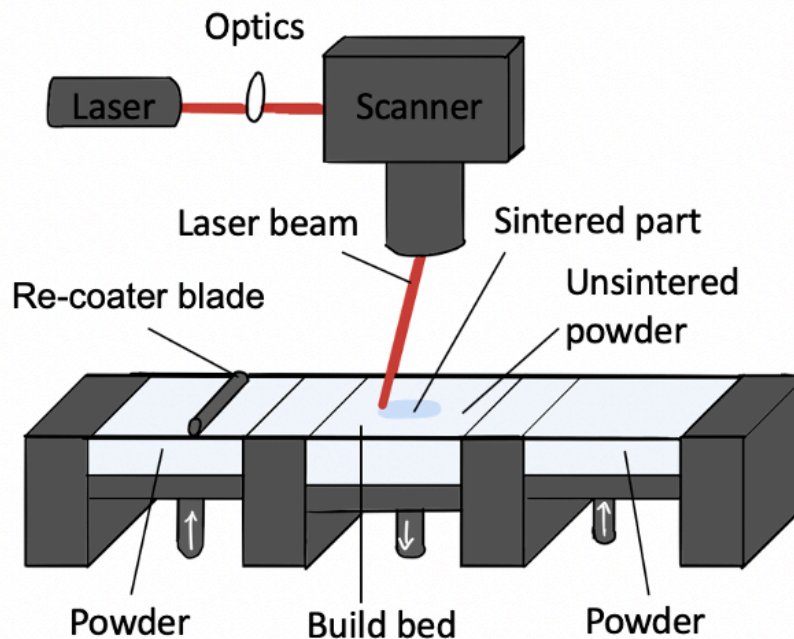
265. Ghassemi T, Shahroodi A, Ebrahimzadeh MH, Mousavian A, Movaffagh J, Moradi A. Current concepts in scaffolding for bone tissue engineering. *Archives of bone and joint surgery* 2018; **6** (2): 90-99.
266. Stevens B, Yang Y, Mohandas A, Stucker B, Nguyen KT. A review of materials, fabrication methods, and strategies used to enhance bone regeneration in engineered bone tissues. *J Biomed Mater Res B Appl Biomater* 2008; **85B** (2): 573-582.
267. Ducheyne P. Bioactive ceramics: the effect of surface reactivity on bone formation and bone cell function. *Biomaterials* 1999; **20** (23-24): 2287-2303.
268. Pradheepa KB, Ramu M, Ananthasubramanian M, Dinakar R, Vignesh M, Shanthakumari S. Evaluation of selective laser sintered polyamide/hydroxyapatite composite compositions –in vitro and in vivo. *International Journal of Biomedical Research* 2017; **8** (08): 467-474
269. Zhu L, Honrao S, Rijal B, Hennig RG, Manuel MV. Phase equilibria and diffusion coefficients in the Fe-Zn binary system. *Materials & design* 2020; **188** (C): 108437.
270. Ullah S, Badshah A, Ahmed F, Raza R, Altaf AA, Hussain R. Electrodeposited zinc electrodes for high current Zn/AgO bipolar batteries. *International Journal of Electrochemical Science* 2011; **6** (9): 3801-3811.
271. Goodridge RD, Hague RJM, Tuck CJ. Effect of long-term ageing on the tensile properties of a polyamide 12 laser sintering material. *Polymer Testing* 2010; **29** (4): 483-493.
272. Pankey GA, Sabath LD. Clinical Relevance of Bacteriostatic versus Bactericidal Mechanisms of Action in the Treatment of Gram-Positive Bacterial Infections. *Clin Infect Dis* 2004; **38** (6): 864-870.

References

273. Thijssen EGJ, van Gestel NAP, Bevers R, et al. Assessment of Growth Reduction of Five Clinical Pathogens by Injectable S53P4 Bioactive Glass Material Formulations. *Frontiers in bioengineering and biotechnology* 2020; **8**: 634-634.
274. Aina V, Perardi A, Bergandi L, et al. Cytotoxicity of zinc-containing bioactive glasses in contact with human osteoblasts. *Chem Biol Interact* 2007; **167** (3): 207-218.
275. Mediaswanti K. Influence of Physicochemical Aspects of Substratum Nanosurface on Bacterial Attachment for Bone Implant Applications. *Journal of nanotechnology* 2016; **2016**: 1-6.
276. Ivanova EP, Truong VK, Wang JY, et al. Impact of Nanoscale Roughness of Titanium Thin Film Surfaces on Bacterial Retention. *Langmuir* 2010; **26** (3): 1973-1982.
277. Bollen CML, Lambrechts P, Quirynen M. Comparison of surface roughness of oral hard materials to the threshold surface roughness for bacterial plaque retention: A review of the literature. *Dent Mater* 1997; **13** (4): 258-269.
278. Bollen CML, Papaioanno W, Van Eldere J, Schepers E, Quirynen M, Van Steenberghe D. The influence of abutment surface roughness on plaque accumulation and peri-implant mucositis. *Clin Oral Implants Res* 1996; **7** (3): 201-211.

10 Appendix A

Laser sintering process

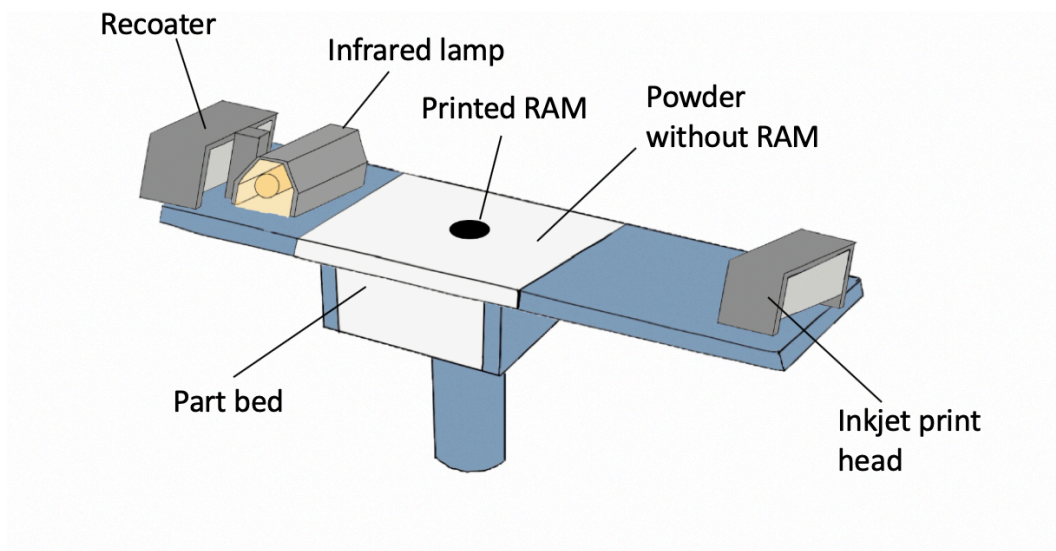


1. The powder was placed into the machine.
2. A re-coater blade was used to spread a thin layer of powder on the build platform. The powder was heated using a heater throughout the process.
3. CO₂ laser sinter was used to fuse powder particles in specific areas according to cross sectional data from the STL file.
4. The build platform moved down one layer (0.1 mm).
5. A new layer of powder was spread on top of the previous layer by the re-coater blade.
6. The laser scanned the successive cross section according to the STL file.
7. Steps 5-7 were repeated until the print was completed.

Appendix A

8. After the print was completed the build was removed. Compressed air was used to remove the excess powder from the discs, tensile test bars and 3-point bending bars.

High speed sintering process



1. The fresh powder was placed in the powder chamber of the machine.
2. The build platform was lowered to one layer thickness.
3. The feed hopper was filled with powder.
4. The infrared (IR) lamp and the roller, attached together in a moving carriage, moved transversely across the build platform. The roller deposited the powder while the IR lamp preheated powder on the build platform.
5. The inkjet print-head moved across the build platform depositing RAM in the desired cross-section according to the STL file.

Appendix A

6. The IR lamp carriage passed across the build platform, the areas with the ink, absorbed higher thermal energy to sinter the underlying powder. The powder without the ink was not sintered and acted as support material.
7. Steps 4-7 were repeated until the print was completed.
8. When the print was completed, the parts were removed from the machine and left to cool at room temperature overnight.
9. In HSS, the powder bed is exposed to infrared radiation from the lamp which causes the excess powders around the parts to become solid and can only be removed by blasting the parts with soda-lime glass beads (Honite grade 16, Gyson).